# Modélisation et optimisation d'actionneurs électrostatiques à membrane

Cesary Maj


# THÈSE

**En vue de l'obtention du**

## DOCTORAT DE L'UNIVERSITÉ DE TOULOUSE

**Délivré par** *INSA de Toulouse*
**Discipline ou spécialité :** *conception des circuits microelectroniques et microsystemes*

---

**Présentée et soutenue par** *Cezary MAJ*
**Le** *8 juillet 2009*

**Titre :** *Modelling and optimization of electrostatic membrane-based actuators*

---

**JURY**
*Jean Yves FOURNIOLS, president*
*Sylvain BALLANDRAS, rapporteur*
*Jan DZIUBAN, examinateur*
*Andrzej NAPIERALSKI, directeur de these*
*Patrick PONS, directeur de these*
*Robert PUERS, rapporteur*

---

**Ecole doctorale :** *GEET*
**Unité de recherche :** *LAAS-CNRS*
**Directeur(s) de Thèse :** *Patrick PONS*
*Andrzej NAPIERALSKI*
**Rapporteurs :** *Sylvain BALLANDRAS*
*Robert PUERS*

# Acknowledgments

This work has been carried out at the Laboratory of Analysis and Architecture of Systems of the French National Research Center (LAAS-CNRS) within the framework of the project CAPTAM. I wish to express my gratitude to the successive directors of the LAAS-CNRS, Mr. Malik Ghallab and Mr. Raja Chatila, for the facilities provided in the laboratory.

This thesis was conducted as a part of a cotutelle agreement between Technical University of Lodz and Institut National des Sciences Appliquées of Toulouse. It was partially financed by the Cotutelle PhD Scholarship from the French Ministry of Foreign Affairs.

I owe my sincere thanks to my thesis supervisor, Mr. Patrick Pons, without whom this thesis would not be possible. I appreciate his vast knowledge and I am most grateful to him for offering me the opportunity of working in the interesting area of research, for his guidance, advice and time he devoted to read my thesis.

I am also deeply grateful to my second supervisor, Mr. Andrzej Napieralski, for his many helpful suggestions and constant encouragement during the course of this work and I want to thank him for his expertise, understanding and patience.

I wish to express my gratitude to Mr. Michal Olszacki and Mr. Mohamad Al Bahri for their excellent team-work and support. I want to thank also all other persons involved in the project CAPTAM.

I would like to thank all members of the M2D and MINC groups for accepting me in their midst and providing a friendly atmosphere during my work at LAAS-CNRS. I would especially like to acknowledge Mr. Hikmat Achkar and Mr. David Peyrou for their insightful comments on my work.

I have also benefited from many valuable discussions with my colleagues Piotr Zajac and Lucjan Janowski.

I would like to thank also all persons from Departement of Microelectronics and Computer Science for their support during the stay at Poland.

Finally, I would like to thank my family and also Natalia for their personal support.

# RESUME DE THESE EN FRANCAIS

Table des matières

# Introduction générale

MEMS est l'abréviation de microsystèmes électromécaniques. Ces sont des dispositifs de taille micrométrique qui intègrent des composants électriques et mécaniques (poutres, diaphragmes, ponts, ressorts, etc..) fabriqués en utilisant les microtechnologies.

La technologie MEMS est utilisée presque partout. Elle est le plus populaire pour le marché automobile des capteurs (airbags, systèmes de sécurité, suspension, échappement). Elle est utilisée aussi pour le marché industriel (détection des tremblements de terre, perception de choc, robots, etc.), le marché domestique (ordinateurs, portables, systèmes de navigation, etc.) et militaire (chars, avions, équipements des soldats). Le domaine le plus promoteur concerne les applications biomédicales. Les capteurs peuvent être utilisés pour mesurer la pression, ou les contraintes comme dans les instruments chirurgicaux. Les actionneurs comme les micro-pompes sont utilisées en dosage des médicaments et les analyseurs de DNA existent même sur le marché. La liste des applications est très longue.

De nombreux MEMS intègrent des micro-actionneurs pour actionner des pièces mobiles. De nombreuses méthodes existent générer cet actionnement parmi lesquelles l'actionnement électrostatique est le plus utilisé à cause de sa simplicité de mise en oeuvre. Il suffit juste d'appliquer une tension entre deux électrodes dont une est mobile. Alors, l'énergie électrostatique est simplement transformée en mouvement.

Ce mémoire porte sur l'étude d'un actionneur électrostatique pour l'auto-calibration in situ d'un capteur de pression. Ces travaux ont été réalisés au LAAS (Toulouse, France) dans le cadre d'un projet de l'Agence nationale de la Recherche (CAPTAM :CApteur de Pression Télémétrique Auto-étalonnable Miniature pour la mesure de fonctions physiologiques sur l'homme). L'objectif de ce projet était de développer un capteur de pression fortement miniaturisé utilisable aussi bien pour la mesure de la pression artérielle que de la pression intracrânienne, intégrant la mesure de température, auto-étalonnable in situ et utilisable à terme sur l'Homme. Le projet était réalisé en collaboration avec Hemodia (Labège, France), le Centre Hospitalier Universitaire de Toulouse (CHU Toulouse, France) et l'Université de Picardie Jules Verne (UPJV, Amiens, France). La tache réalisée par le LAAS concernait le développement de la cellule sensible à la pression et la température. En raison de l'application, les dimensions de cellule étaient fixées à 2400 μm × 740 μm. Cette cellule comprend une membrane avec quatre jauges de contrainte implantée en configuration de pont de Wheatstone. Le principe de fonctionnement est présenté sur la Figure 1. La membrane est

placée au-dessus d'une cavité, obtenue par la soudure de deux plaquettes de silicium. La pression constante dans la cavité est la pression de référence ($P_{ref}$). La différence entre la pression extérieure ($P_{ext}$) et la pression de référence entraîne la déflexion de la membrane ($\Delta w$). Une contrainte mécanique ($\Delta\sigma$) apparait alors dans la membrane et est transformée en signal électrique ($\Delta V_{out}$) en raison du changement de résistance des jauges ($R+\Delta R$). Le matériau utilisé pour fabrication de la membrane était le silicium de type N dans le plan (100). La membrane est fabriquée dans la direction <110> pour obtenir la plus haute valeur de coefficient de piézorésistivité. L'épaisseur de la membrane était fixée à 5 µm en prenant en compte la sensibilité du capteur, les limites technologiques et la disponibilité des plaquettes SOI au marché. Les dimensions de la membrane était fixées à 300 µm × 300 µm ou 900 µm × 300 µm. Le générateur de pression électrostatique intégré est obtenu par une contre électrode déposée au fond de la cavité. L'électrode est simplement obtenue par utilisation de silicium comme le substrat. La tension disponible, qui permettra l'auto-étalonnage, est limitée à 6 V maximum.

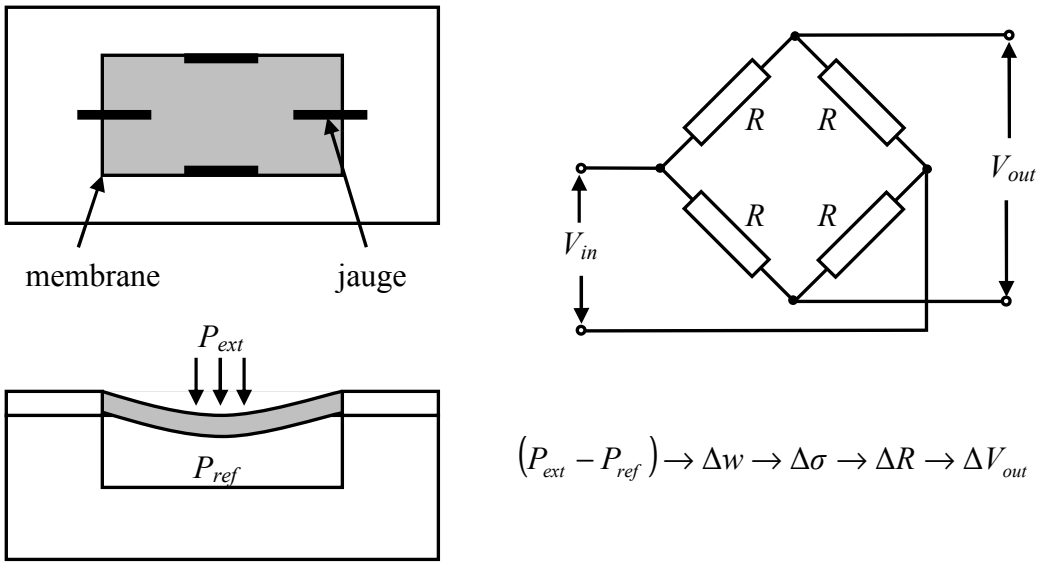


**Figure 1: Schéma du capteur de pression et son principe de fonctionnement.**

La première partie de ce mémoire porte sur la théorie des actionneurs électrostatique à membrane dans laquelle nous présentons les modèles analytiques développés. Dans la seconde partie nous exposons l'outil de simulation développé pour réaliser l'optimisation de l'actionneur et l'analyse statistique des performances. Le troisième chapitre porte sur la fabrication et la caractérisation des structures de tests.

# Chapitre F-1 Modélisation actionneur électrostatique

### *Comportement mécanique de la membrane*

Nous considérons la plaque mince avec le rapport longueur-épaisseur (*a*/*h*) de 10 à 80. Cette plaque sera appelée la membrane. La déformation dune membrane rectangulaire sous l'action d'une pression hydrostatique est donnée par l'équation Newton-Lagrange en coordonnées cartésienne :

$$D\left(\frac{\partial^4 w_1(x,y)}{\partial x^4}+2\alpha\frac{\partial^4 w_1(x,y)}{\partial x^2\partial y^2}+\frac{\partial^4 w_1(x,y)}{\partial y^4}\right)=P \qquad \textbf{Equation 1}$$

où $w_1$ est la déflexion de la membrane en raison de pression appliquée $P$, α est le coefficient d'anisotropie, $D_0$ est la rigidité de la membrane et $D$ est la rigidité à la flexion décrit par l'Equation 2:

$$D=D_0h^3,\qquad D_0=\frac{E}{12\left(1-\nu^2\right)} \qquad \textbf{Equation 2}$$

où $E$ est le module d'Young et $v$ le coefficient de Poisson. En réalité la membrane est stressée initialement. Ces contraintes s'appellent les contraintes résiduelles et elles sont causées usuellement pendant le procédé technologique. Ces contraintes en cas de compression peuvent causer la déflexion initiale de la membrane. Puis, en prenant sur compte les phénomènes mentionnés, l'Equation 1 prend la forme suivante :

$$D\Delta\Delta\left(w(x,y)-w_0(x,y)\right)+\sigma_0h\Delta w(x,y)=P \qquad \textbf{Equation 3}$$

où $w_0$ est la déflexion initiale de la membrane, $\sigma_0$ est la contrainte résiduelle (la valeur négative et positive indique la compression et la tension, respectivement), Δ est l'operateur Laplacien et ΔΔ est l'operateur suivant :

$$\Delta\Delta=\frac{\partial^4}{\partial x^4}+2\alpha\frac{\partial^4}{\partial x^2\partial y^2}+\frac{\partial^4}{\partial y^4}$$

L'Equation 3 est solutionnée en utilisant la méthode de Galerkin en prenant la solution sous la forme suivante :

$$w(u,v)=\left(1-u^2\right)^2\left(1-v^2\right)^2\sum_{i,j=0}^{n}K_{ij}u^{2i}v^{2j} \qquad \textbf{Equation 4}$$

où $u$ et $v$ sont les coordonnées normalisées à la longueur $a$ et à la largeur $b$ de la membrane, respectivement. Les coefficients inconnus $K_{ij}$ sont calculés à partir de l'équation suivante :

$$\mathbf{K}=\left(D\frac{16}{a^2b^2}\mathbf{A_1}+\sigma_0h\frac{4}{ab}\mathbf{A_2}\right)^{-1}\left(P+P_{w0}\right)\mathbf{B} \qquad \textbf{Equation 5}$$

où $P_{wo}$ est la pression qui provoque la déflexion initiale de la membrane, $\mathbf{A_1}$ et $\mathbf{A_2}$ sont les matrices des éléments constants qui sont calculées analytiquement.

La dépendance de la déflexion de la membrane à la pression appliquée est linéaire. Donc, on peut réduire le modèle de la forme linéaire suivante :

$$k_{mem} w_{\max} = P + P_{w0\_\max}, \qquad k_{mem} = C_1 \frac{D}{b^4} + C_2 \frac{\sigma_0 h}{b^2} \qquad \textbf{Equation 6}$$

où $C_1$ et $C_2$ sont les constantes qui dépendent du rapport $R=b/a$ de la membrane et $C_1$ du coefficient d'anisotropie. Ce modèle réduit utilise juste la déflexion maximale de la membrane. Donc, il ne donne pas d'information sur la forme de la membrane et la forme normalisée doit être utilisée. Les simulations ont montrés que la forme de la membrane dépendait de la contrainte résiduelle. Donc, le modèle réduit est précis juste pour des contraintes résiduelles relativement faibles.

### *Actuation électrostatique*

L'équation d'équilibre de la membrane sous la pression électrostatique générée par l'application de la tension $V$ entre la membrane et l'électrode parallèle à la membrane est donnée par :

$$D\Delta\Delta\big(w(x,y) - w_0(x,y)\big) + \sigma_0 h \Delta w(x,y) = P + \varepsilon \frac{V^2}{2\big(d - w(x,y)\big)^2} \qquad \textbf{Equation 7}$$

où $d$ est la distance entre la membrane et l'électrode. La solution de cette équation est la même que pour la pression uniforme. Donc, la méthode de Galerkin mène à l'équation suivante :

$$\mathbf{K} = \left( D \frac{16}{a^2 b^2} \mathbf{A_1} + \sigma_0 h \frac{4}{ab} \mathbf{A_2} \right)^{-1} \left( (P + P_{w0}) \mathbf{B} + \varepsilon \frac{V^2}{2} \mathbf{B_1} \right) \qquad \textbf{Equation 8}$$

où $\mathbf{B_1}$ est le vecteur donné par :

$$\iint_{\Omega} \frac{1}{(d-w)^2} \varphi_{i,j} \, du dv \qquad \textbf{Equation 9}$$

Il n'y a pas de solution analytique pour ces intégrales. Il faut donc les calculer numériquement ce qui prends beaucoup de temps. Puis, comme ces éléments sont dépendants de la déflexion de la membrane, la solution doit être itérative. Ainsi, l'usage du modèle réduit est intéressant car il réduit les temps de calcul :

$$k_{mem} w_{\max} = P_h + \varepsilon \frac{V^2}{2\big(d - w_{\max}\big)^2} \qquad \textbf{Equation 10}$$

Les simulations ont montrés que ce modèle n'est pas très précis (Figure 1).

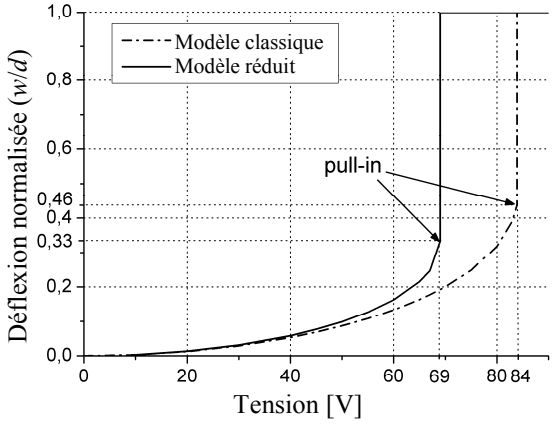


**Figure 1: Comparaison entre le modèle réduit et classique pour l'actuation électrostatique.**

Afin de corriger ce modèle réduit nous avons introduit deux termes supplémentaires dans l'Equation 10 :

$$k_{mem} w_{\max} = P_h + B\varepsilon \frac{V^2}{2(d - Aw_{\max})^2} \qquad \textbf{Equation 11}$$

Les coefficients $A$ et $B$ sont calculés à partir du modèle classique et permettent une première correction. Toutefois, la forme de la caractéristique $w$=f($V$) n'est pas correcte et elle doit être corrigée aussi. Ceci est obtenu en introduisant les fonctions de correction de la Figure 2 qui dépendent du rapport $P_h/P_{max}$ ($P_h$ est la pression hydrostatique qui cause la déflexion de la membrane égale à la profondeur de la cavité $d$).

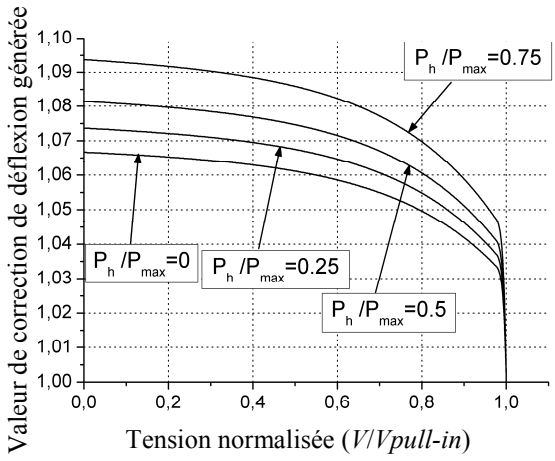


**Figure 2: Fonction de correction de la déflexion générée.**

Les simulations FEM ont montrées que la correction du modèle réduit pour l'actuation électrostatique est précis et que les résultats sont comparable avec les résultats obtenues avec la simulation FEM. De plus, le temps de calcul du modèle développé est beaucoup plus faible que celui obtenu avec la simulation FEM (environ 50 ms au lieu de 6 minutes pour tracer la

pleine caractéristique qui comprend 50 points). C'est le grand avantage, spécialement en phase d'optimisation. Toutefois le modèle développé, a des limitations (le plus importante est l'encastrement idéal de la membrane) qui limitent l'usage de ce modèle.

# Chapitre F-2 Optimisation et approche statistique

La phase d'optimisation d'un capteur est très importante parce qu'elle affecte la réussite d'un projet (durée, coût, …). Cette phase doit donc utiliser des simulations pour diminuer le nombre de vérifications expérimentales. Le modèle analytique développé, qui simple et rapide, permet ainsi de mener à bien cette phase d'optimisation. La possibilité d'effectuer de nombreuses simulations dans un temps très court permet également d'estimer l'influence de procède technologique sur la performance des capteurs.

Des simulations FEM sont réalisées uniquement à la fin de cette phase pour vérifier les résultats obtenus. La procédure d'optimisation qui a été développée sous MATLAB® est décrite sur la Figure 1.

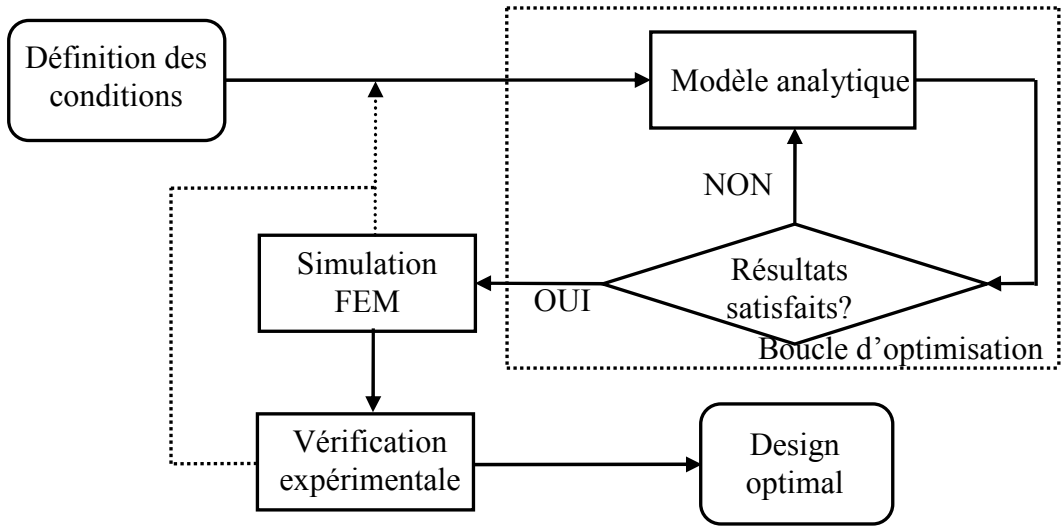


**Figure 1: Procédure d'optimisation.**

# Chapitre F-3 Fabrication et caractérisation des structures de test

Les actionneurs électrostatiques ont été fabriques en utilisant deux plaquettes de silicium. La première (Figure 1a), est une plaquette de type P oxydée (Figure 1b). Les cavités sont formées par gravure chimique de l'oxyde (Figure 1c). Puis, le fond de la cavité est oxydé pour éviter les courts circuits (Figure 1d). La plaquette est ensuite soudée avec une deuxième plaquette SOI de type N (Figure 1e). La soudure est réalisée sous vide pour assurer une pression nulle dans les cavités. La partie massive du SOI (Figure 1f) et l'oxyde (Figure 1g) sont supprimés pour libérer les membranes. Après, les cellules sont séparées par gravure RIE du SOI (Figure 1h). L'implantation N++ du contact est réalisé (Figure 1i), et l'accès à la contre électrode de Silicium inférieure est obtenue par gravure RIE (Figure 1j). Finalement les contacts électriques sont métallisés (Figure 1k).

La caractérisation du procède se concentre sur :

- la mesure de la courbure des plaquettes avant soudure en utilisant le profilomètre mécanique. Ce paramètre est important car il conditionne la qualité de la soudure. La vérification du procédé de soudure est réalisée en utilisant une camera infrarouge.
- la mesure des dimensions des cavités et de l'épaisseur des membranes en utilisant le profilomètre optique. La sensibilité de l'actionneur électrostatique est en effet très sensible à ces paramètres géométriques.

La méthodologie de caractérisation des performances des actionneurs est décrite dans ce qui suit. Au début, la déflexion initiale de la membrane est mesurée en plaçant l'échantillon une enceinte à vide pour obtenir une pression différentielle nulle. Puis, la déflexion de la membrane sous pression hydrostatique est mesurée pour estimer la contrainte résiduelle en faisant varier la pression dans l'enceinte. Finalement, la réponse sous la pression électrostatique est mesurée et est comparée avec le modèle analytique. Les mesures se basent sur la mesure de la déflexion de la membrane en utilisant le profilomètre optique ou sur la mesure de la résistance de jauge implantées dans la membrane.

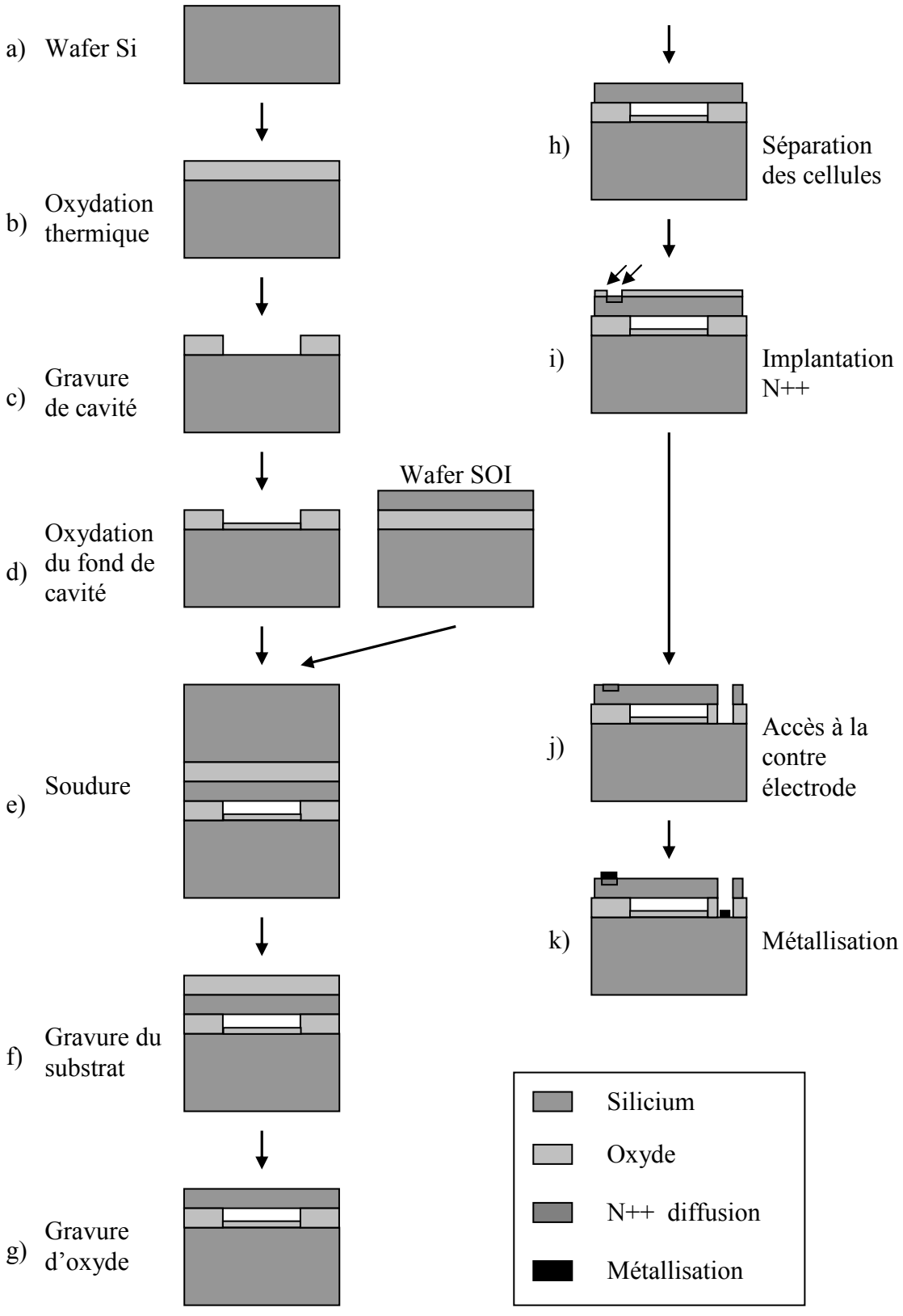


**Figure 1: Procédé technologique.**

Les structures de test ont été fabriquées sur cinq plaquettes en utilisant différentes conditions présentées dans le Tableau 1 :

**Tableau 1: Conditions de fabrication des actionneurs sur différentes plaquettes.**

| Wafer | 1 | 2 | 3 | 4 / 5 |
|---|---|---|---|---|
| Courbature Si [µm] | ⌒ 17.7 | ⌒ 12.5 | ⌣ 5.8 | ⌣ 0.7 / 0.8 |
| Compensation Si | aucun | aucun | aucun | aucun |
| Courbature SOI [µm] | ⌒ 16.3 | ⌒ 33.2 | ⌒ 82.5 | ⌒ 83.3 / 81.2 |
| Compensation SOI | aucun | aucun | $SiO_2$ (côté bulk) ⌣ 1.2 | $SiO_2$ (côté bulk) ⌣ 3 / 2.5 |
| Température de soudure [˚C] | 150 | 20 | 150 | 150 |
| Température de traitement d'implantation [˚C] | 1000 | 1000 | 1200 | 1000 |
| Profondeur de cavité [µm] | 1.25 | 1.25 | 2 | 2 |

### *Plaquette 1*

Les membranes carrées ont été caractérisées. La déflexion initiale varie de -291 nm à 126 nm (la valeur négative indique que la membrane est gonflée). La membrane n'est pas flambées ce qui a été vérifié par la mesure sous la pression hydrostatique. De plus, la contrainte résiduelle varie de -5 MPa à -33 MPa.

Les caractéristiques $w$=f($V$) obtenues sont présentées sur Figure 2. Les résultats sont similaires pour toutes les structures. Le modèle analytique surestime de 13% maximum la déflexion pour les grandes tensions. Pour les faibles tension la différence est plus grande (de -16% à 18%) car l'incertitude de mesure est plus grande. De plus, il n'a y pas d'influence de déflexion initiale et la contrainte résiduelle sur le comportement de l'actionneur.

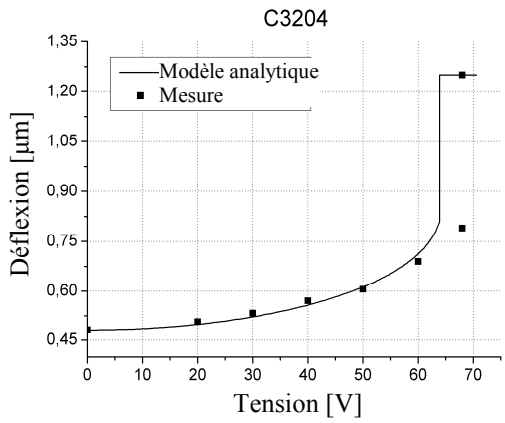
C3204
Modèle analytique
Mesure
Déflexion [µm]
Tension [V]

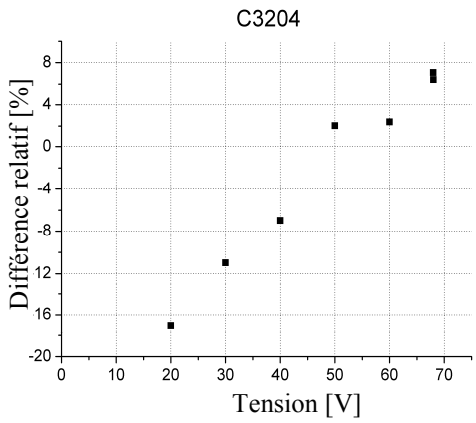
C3204
Différence relatif [%]
Tension [V]

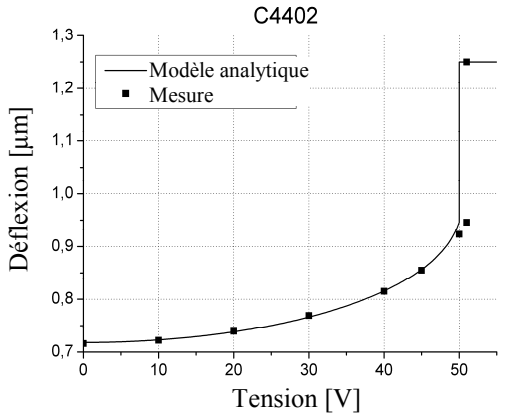
C4402
Modèle analytique
Mesure
Déflexion [µm]
Tension [V]

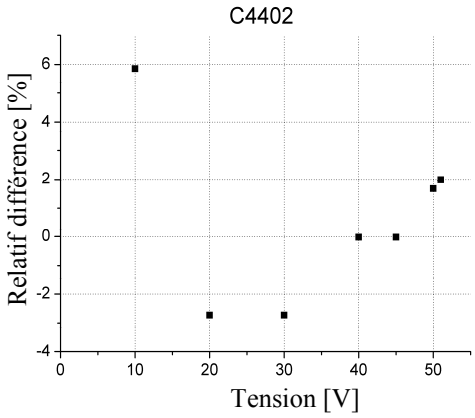
C4402
Relatif différence [%]
Tension [V]

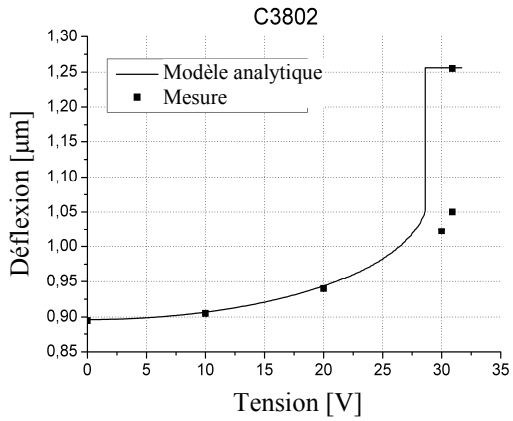
C3802
Modèle analytique
Mesure
Déflexion [µm]
Tension [V]

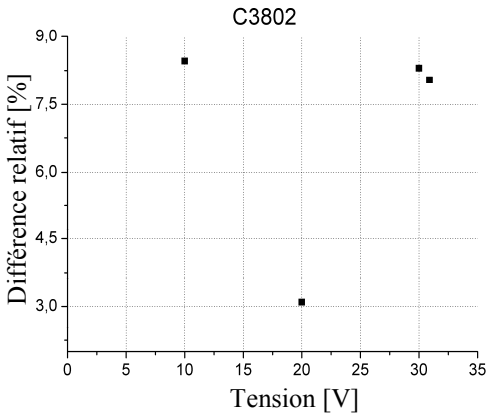
C3802
Différence relatif [%]
Tension [V]

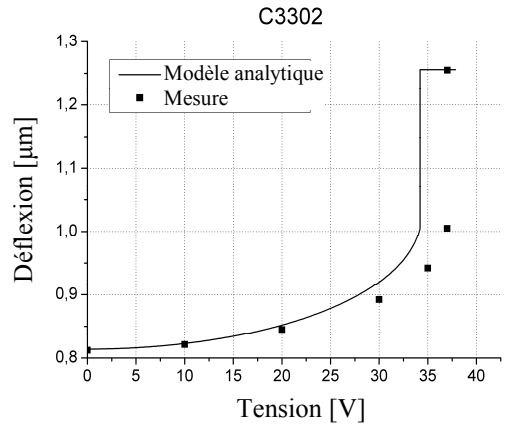
C3302
Modèle analytique
Mesure
Déflexion [µm]
Tension [V]

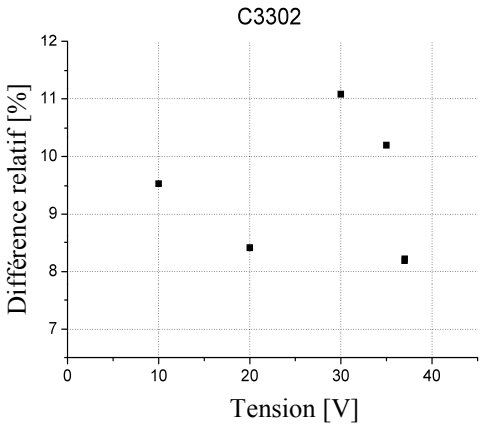
C3302
Différence relatif [%]
Tension [V]

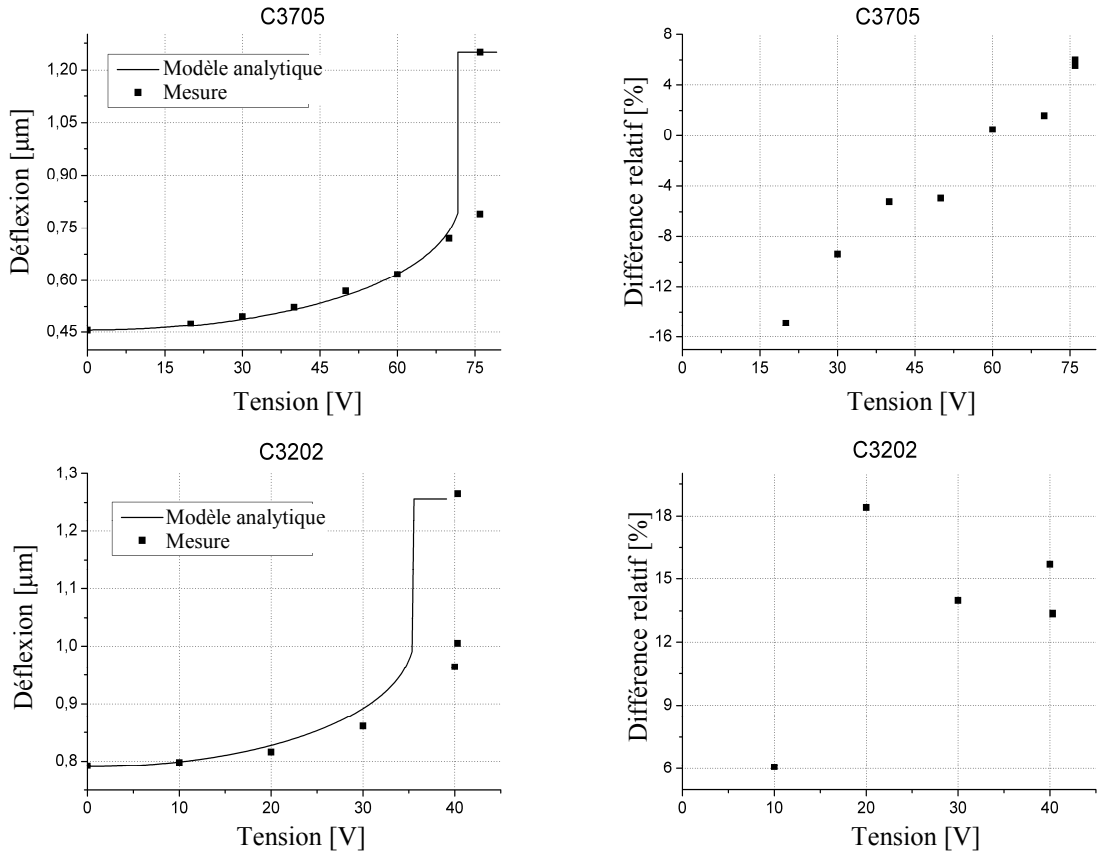


**Figure 2: Caractéristiques *w*=f(*V*) et les différences relatives des structures de wafer 1.**

### *Plaquette 2*

La déflexion initiale varie de -480 nm à 290 nm. La contrainte résiduelle est reproductible (environ -25 MPa). Les caractéristiques *w*=f(*V*) sont présentées sur Figure 3. Pour cette plaquette, nous avons obtenu une sous-estimation de 10% maximum. Pour une structure la différence entre les mesures et le modèle est de 14%, ce qui peut être causé par une zone de soudure incorrecte. Pour les faibles tensions, la différence peut être beaucoup est plus grande (60%) à cause de l'incertitude sur la mesure de la déflexion.

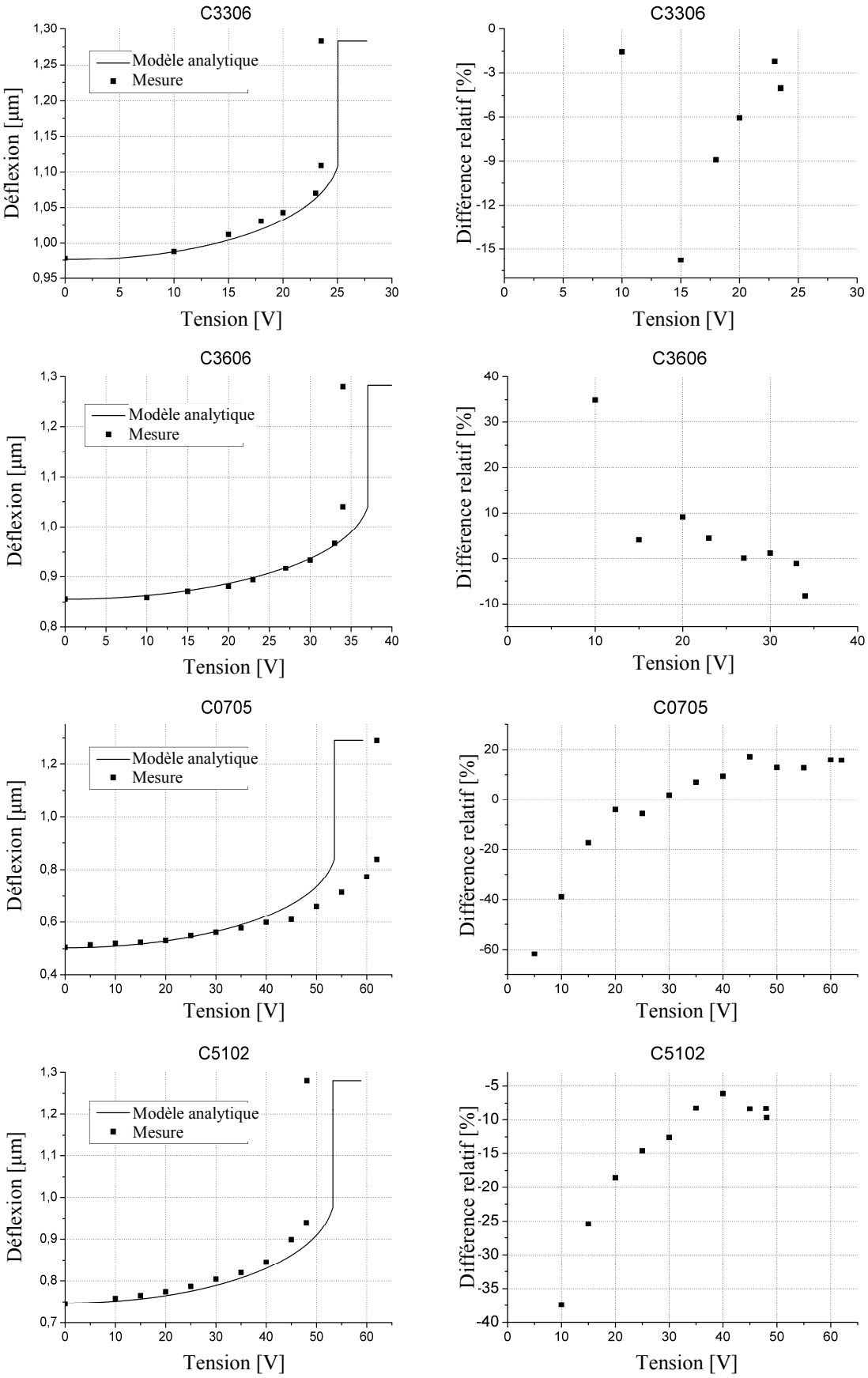


**Figure 3: Caractéristiques *w*=f(*V*) et les différences relatives des structures de wafer 2.**

### *Plaquette 3*

Pour cette plaquette, nous avons obtenu une déflexion initiale dans une seule direction (de -153 nm à -260 nm). Ceci indique que la soudure est plus reproductible pour cette plaquette. De plus, la contrainte résiduelle est reproductible (-93 MPa à -127 MPa). Les caractéristiques $w$=f($V$) sont présentées sur Figure 4. Le modèle analytique surestime de 20% maximum les déflexions. Pour les deux structures (C0806 and C0205) pour laquelle la contrainte résiduelle est plus faible, la différence est plus petite (7%). Il faut souligner que la contrainte résiduelle plus grande est probablement causée par les conditions du procédé de fabrication. Toutefois, le modèle analytique est toujours comparable avec les mesures.

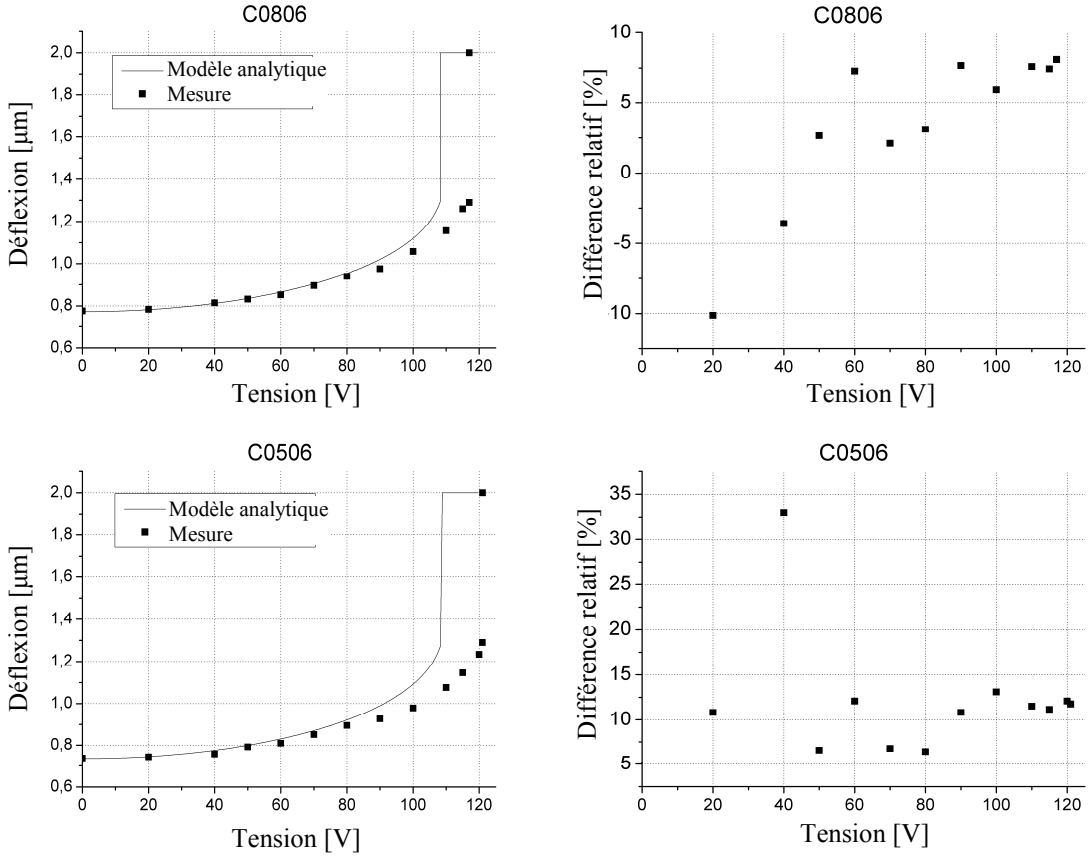

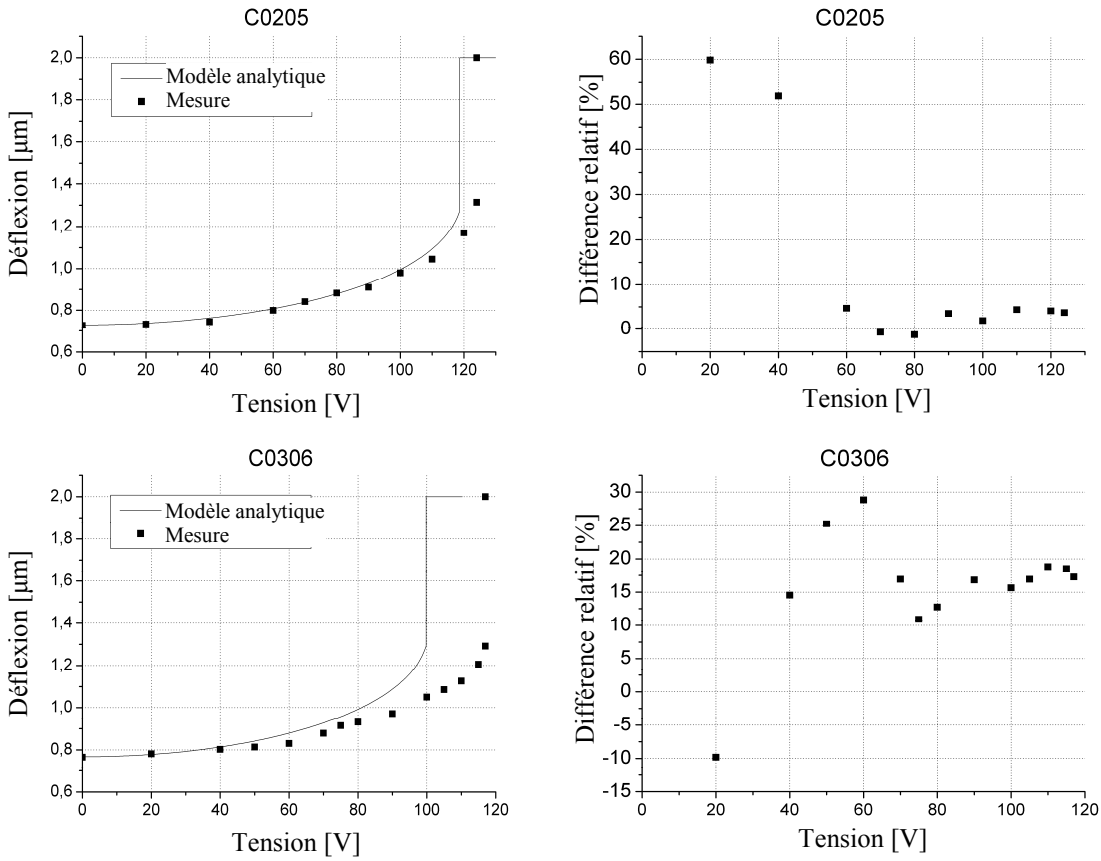


**Figure 4: Caractéristiques *w*=f(*V*) et les différences relatives des structures de wafer 3.**

### *Plaquette 4*

Cette plaquette a permis de mesurer des membranes carrées et rectangulaires. Toutes les membranes carrées sont gonflées (environ de -100 nm). Pour les membranes rectangulaires les résultats ne sont pas reproductibles. Ils varient de -180nm à 80nm. La contrainte résiduelle est reproductible pour les deux types de membranes (-30 MPa et -50 MPa pour les membranes carrées et rectangulaires respectivement). Les caractéristiques *w*=f(*V*) sont présentées sur Figure 5. Les résultats obtenus pour les membranes carrées sont très proche des modèles analytiques (surestimation de 5%). Pour les membranes rectangulaires ils sont surestimés de 12%.

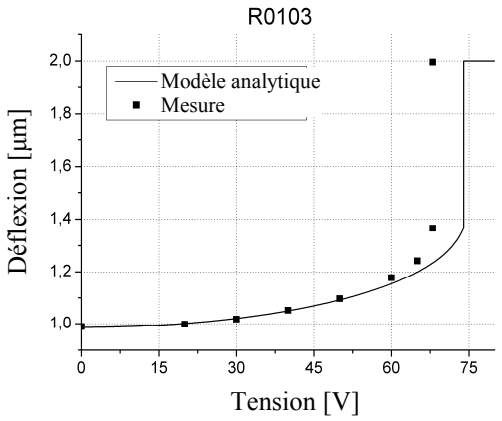
R0103
Modèle analytique
Mesure
Déflexion [µm]
Tension [V]

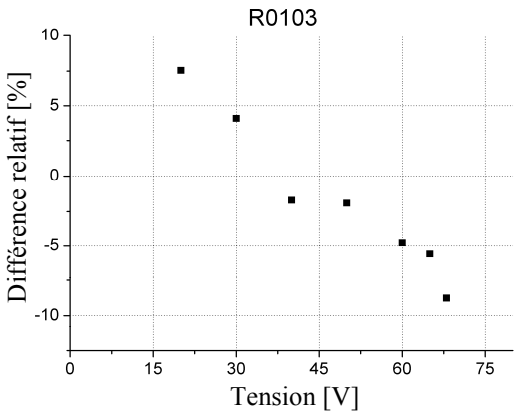
R0103
Différence relatif [%]
Tension [V]

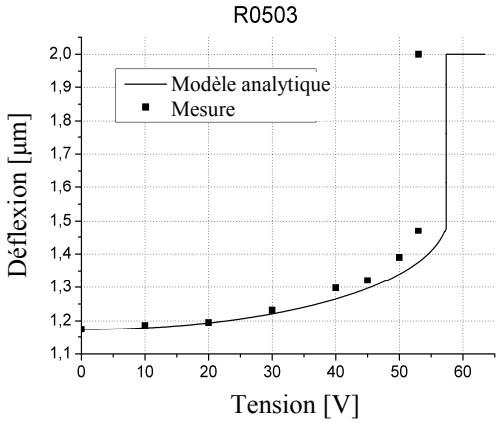
R0503
Modèle analytique
Mesure
Déflexion [µm]
Tension [V]

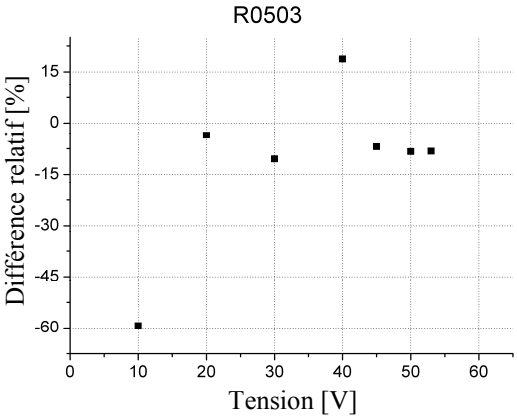
R0503
Différence relatif [%]
Tension [V]

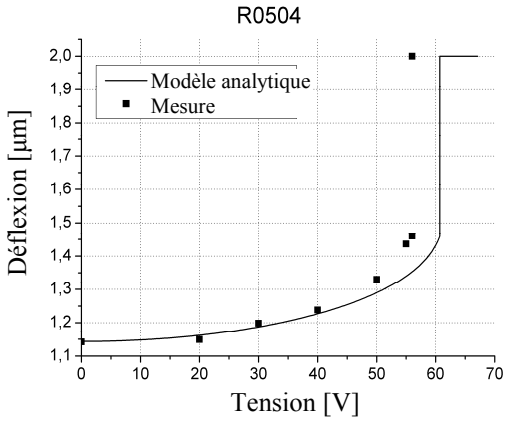
R0504
Modèle analytique
Mesure
Déflexion [µm]
Tension [V]

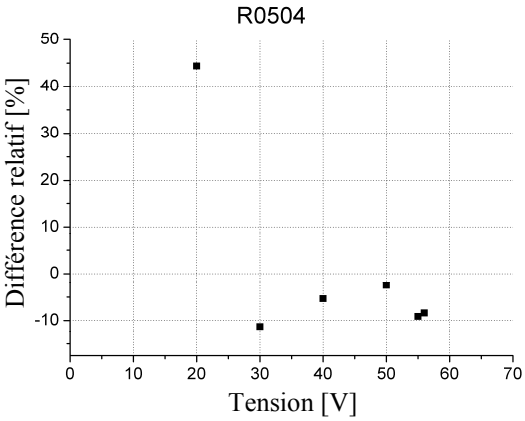
R0504
Différence relatif [%]
Tension [V]

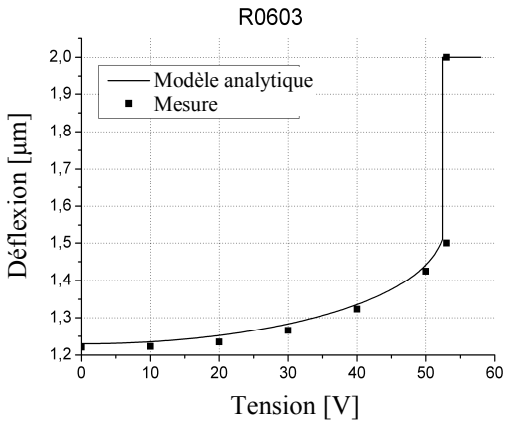
R0603
Modèle analytique
Mesure
Déflexion [µm]
Tension [V]

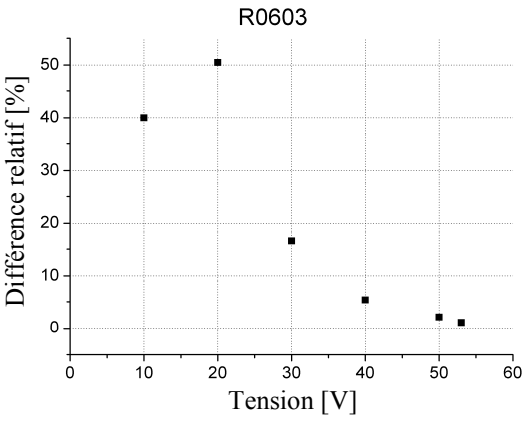
R0603
Différence relatif [%]
Tension [V]

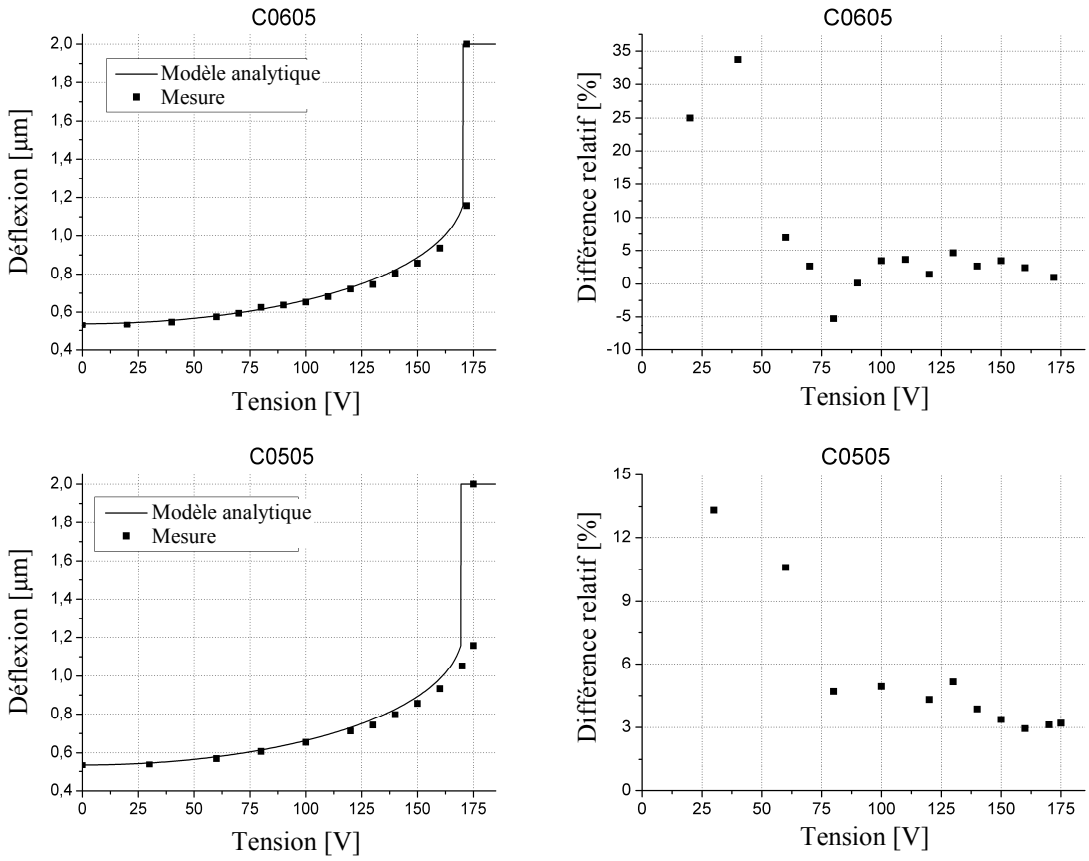


**Figure 5: Caractéristiques *w*=f(*V*) et les différences relatives des structures de wafer 4.**

### *Mesure de résistance*

La plaquette 5 a été caractérisée par la mesure de résistance implantée sur la membrane. C'est la méthode qui sera utilisée pour l'auto-étalonnage du capteur. De plus, cette méthode est plus précise pour les petites tensions que la mesure de la mesure de déflexion. Nous avons mesuré deux structures avec la membrane carrée. La déflexion initiale est égale à -100 nm et la contrainte résiduelle environ de -50 MPa. Les variations de la résistance en fonction de la tension appliquée sont présentées sur Figure 6. Pour les tensions importantes la différence entre le modèle analytique et les mesures est plus petite que 3%. Pour les faibles tensions, elle est plus grande et arrive à 14%.

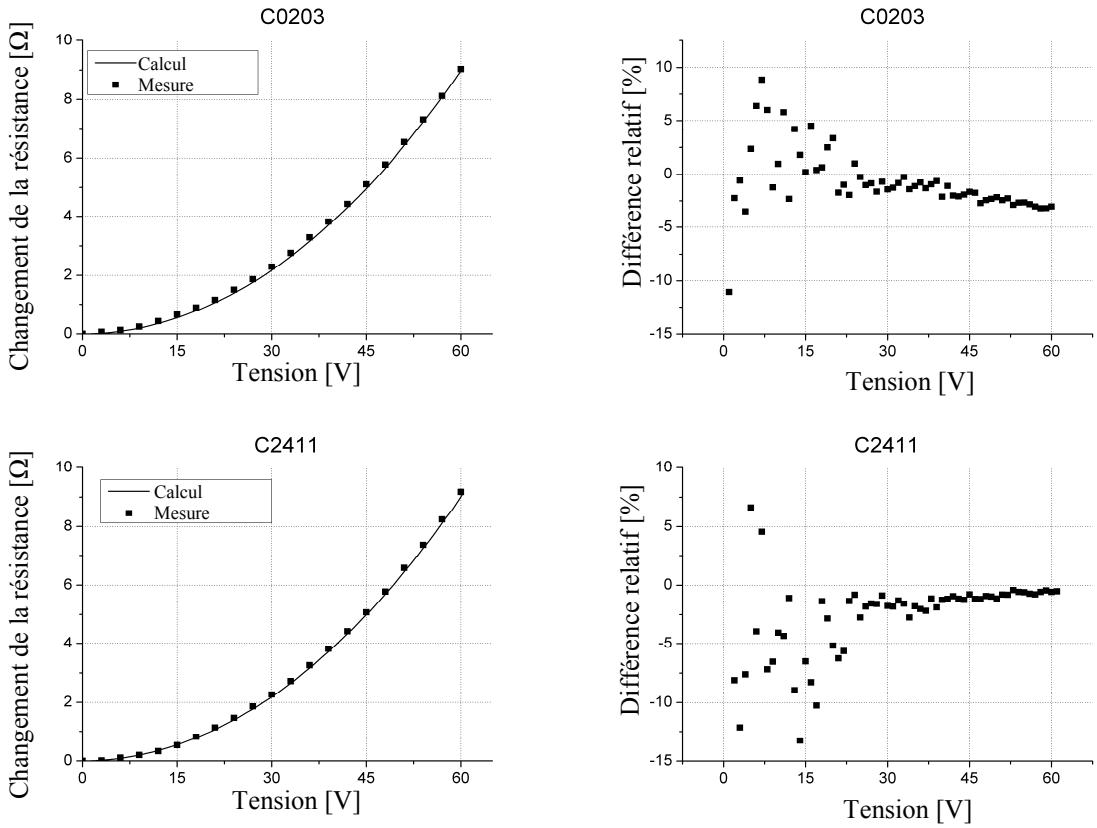


**Figure 6: Caractéristiques $\Delta R$=f($V$) pour la structure de wafer 5.**

# Chapitre F-4 Conclusion

L'objectif de ce mémoire était de développer un modèle complet pour simuler et optimiser un actionneur électrostatique. La voie choisie à consister à privilégier un modèle analytique qui est beaucoup plus rapide et qui permettra ainsi de réaliser une phase d'optimisation plus facilement et de produire des analyses statistiques pour estimer le rendement de fabrication en fonction des dispersions technologiques.

Le modèle analytique est basé sur l'équation Newton-Lagrange qui a été modifiée pour prendre en compte les contraintes résiduelles et la déflexion initiale de la membrane qui sont souvent présentes dans les microstructures. Après, ce modèle a été réduit pour éliminer les calculs intégraux complexes. La comparaison avec la simulation FEM a monté que le modèle donne les résultats corrects et qu'il est beaucoup plus rapide. La plus importante source des erreurs est l'hypothèse d'encastrement parfait. Il produit une erreur de 10% en déflexion et de 20% en contrainte.

Le modèle analytique complet a été développé sous MATLAB. Il comprend un module d'optimisation et d'analyse statistique.

Des structures de test ont été fabriquées pour vérifier le modèle analytique. Ces structures sont basées sur l'assemblage d'une plaquette de silicium présentant une cavité en SiO2 et d'une plaquette SOI.

La caractérisation de ces structures de tests a été menée en mesurant la déflexion des membranes au profilomètre optique. La différence entre le modèle analytique et les mesures est globalement inférieure à 20%. Les erreurs sont surtout importantes pour les faibles tensions à cause de l'incertitude sur la mesure de la déflexion. Dans des conditions de mesure plus favorables, l'écart est généralement inférieur à 10%% ce qui correspond aux limites du modèle qui considère un encastrement parfait de la membrane.

Les modèles présentés dans ce mémoire seront utilisés dans le projet CAPTAM. L'objective de ce projet est l'optimalisation du capteur de pression qui intègre le générateur de pression électrostatique. Ainsi, l'optimisation doit être couplée pour obtenir la sensibilité désirée du capteur et la performance désirée du générateur. Donc, le modèle analytique développé sera très utile dans cette tache complexe numériquement.

# Table of contents

# Notations

| | |
|---|---|
| $\mu$ | Expected value |
| $a$ | Membrane length |
| $A, B$ | Correction coefficients of classical model |
| $\mathbf{A_1}$, $\mathbf{A_2}$ | Matrices of constants in Galerkin equation |
| $a1_{ij}$, $a2_{ij}$ | Elements of matrices $\mathbf{A_1}$ and $\mathbf{A_2}$ |
| $b$ | Membrane width |
| $\mathbf{B}$ | Vector of constants in Galerkin method |
| $b_i$ | Elements of vector $\mathbf{B}$ |
| $\mathbf{C}$ | Stiffness matrix |
| $C$ | Capacitance |
| $C_1$, $C_2$ | Coefficients of proportionality |
| $C_{gen}$ | Capacitance generated electrostatically |
| $d$ | Distance between the electrodes |
| $D$ | Flexural rigidity |
| $D_0$ | Rigidity |
| $E$ | Energy |
| $E$ | Young's modulus |
| $E'_x$, $E'_y$, $E''$, $G$ | Constants characterizing the elastic properties of an anisotropic material (Young's modulus and shear modulus) |
| $F_e$ | Electrostatic force |
| $F_{sp}$ | Spring force |
| $G$ | Shear modulus |
| $h$ | Membrane thickness |
| $\mathbf{K}$ | Vector of coefficients $K_{ij}$ |
| $k_e$ | Coulomb constant |
| $K_{ij}$ | Coefficients of equation describing the membrane form |
| $k_{ij}$ | Coefficients of equation describing the membrane form normalized to maximal deflection |
| $k_{sp}$ | Spring constant |
| $M_x$, $M_y$, $M_{xy}$ | Bending and twisting moments |
| $P_e$ | Electrostatic pressure |
| $P_{e\_av}$ | Average value of electrostatic pressure acting on the membrane |
| $P_{gen}$ | Pressure generated electrostatically |
| $P_h$ | Sum of uniform pressure $P$ and $P_{w0\_max}$ |
| $P_{w0}$ | Pressure corresponding to the initial deflection of the membrane |
| $P_{w0\_max}$ | Pressure corresponding to the maximal initial deflection of the membrane |
| $q$ | Electric charge |
| $R$ | $b/a$ ratio |
| $r$, $\theta$ | Polar coordinates |

| | |
|---|---|
| $R_0$ | Radius |
| $r_e$ | Distance between two charges |
| $R_h$ | $a/h$ ratio |
| $S$ | Electrode surface |
| $\mathbf{S}$ | Compliance matrix |
| $t_{ox}$ | Oxide thickness |
| $V$ | Voltage |
| $Vol_{gen}$ | Volume generated electrostatically |
| $V_{pull\text{-}in}$ | Pull-in voltage |
| $V_{pull\text{-}out}$ | Pull-out voltage |
| $w$ | Deflection / displacement |
| $w_{0\_max}$ | Initial deflection in the centre of the membrane |
| $w_1$ | Change of the membrane deflection due to applied pressure |
| $w_{1\_max}$ | Maximal change of the membrane in its centre due to applied pressure |
| $w_{eff}$ | Effective membrane deflection |
| $w_{gen}$ | Deflection generated electrostatically |
| $w_{max}$ | Total deflection in the centre of the membrane |
| $w_{pull\text{-}in}$ | Pull-in deflection / displacement |
| $x$, y, $z$ | Cartesian coordinates |
| $\alpha$ | Coefficient of anisotropy |
| $\varepsilon$ | Strain |
| $\varepsilon_0$ | Vacuum permittivity |
| $\varepsilon_{ox}$ | Oxide permittivity |
| $\nu$ | Poisson ratio |
| $\sigma$ | Stress |
| $\sigma$ | Standard deviation |
| $\sigma_0$ | Residual stress |
| $\sigma_{cr}$ | Critical residual stress |
| $\sigma_{gen}$ | Stress generated electrostatically |
| $\sigma_{vM}$ | Von Mises stress |
| $\Omega$ | Integration limit |
| $u$, $v$ | Coordinates normalized to membrane dimmensions |

# Introduction

### *Introduction to MEMS*

The term MEMS is the abbreviation of Micro Electro-Mechanical Systems. They are small devices in range of millimetre to nanometre level that integrates mechanical and electrical components. These systems extend the fabrication techniques in order to combine the electrical components with the mechanical ones such as beams, gears, diaphragms, bridges, springs etc.

The invention of the transistor in 1947 began fast growing of microelectronic technology. In 1958 the first integrated circuit was built by Jack Kilby that consisted of one transistor, three resistors and one capacitor. Then, the first MEMS device was published in 1967 [1], which was a gold resonating MOS gate structure. The evolution of micromachining owed also to the silicon as an electronic material. Its wide abilities from sand ($SiO_2$), high Young modulus and no mechanical hysteresis resulted in potentially lower costs and better properties than other semiconductors. In order to fabricate the integrated circuits, several techniques were developed. The first one is the bulk micromachining [2] in which the crucial process is etching, which allows forming the desired geometries. Two kinds of etching were developed, isotropic in 1960s and anisotropic in 1967. Subsequently, various etch-stop techniques were developed to provide further flexibility of the process. In the same decade the sacrificial layer technique was demonstrated in 1965 [3], which initiated the development of the surface micromachining. In 1982 the term micromachining came into use to describe the fabrication of micromechanical parts such as diaphragms and suspension beams. The turning point was reached in 1987 when the techniques for integrated fabrication of mechanisms using volume and surface micromachining were demonstrated. Then, the term MEMS saw the light.

The MEMS technology is used almost everywhere. They are most popular in automotive market as various kind of sensors (airbags, door locks, lights, security systems, suspension, exhaust etc.). They are also used in industry market (earthquake detection, gas shutoff, shock and tilt sensing, robots etc.), consumer market (domestic appliances, computers, mobiles, navigation systems etc.) and military (tanks, planes, equipment for soldiers). The most promising domain concerns the biomedical applications. Sensors are used in pressure monitoring, strain gauges may be helpful in automatic surgery, actuators such as micro-pumps are used in drugs dosage and even DNA analysers exist on the market. The list is very long. The shortened classification of MEMS applications by type and domain is presented in Figure 1:

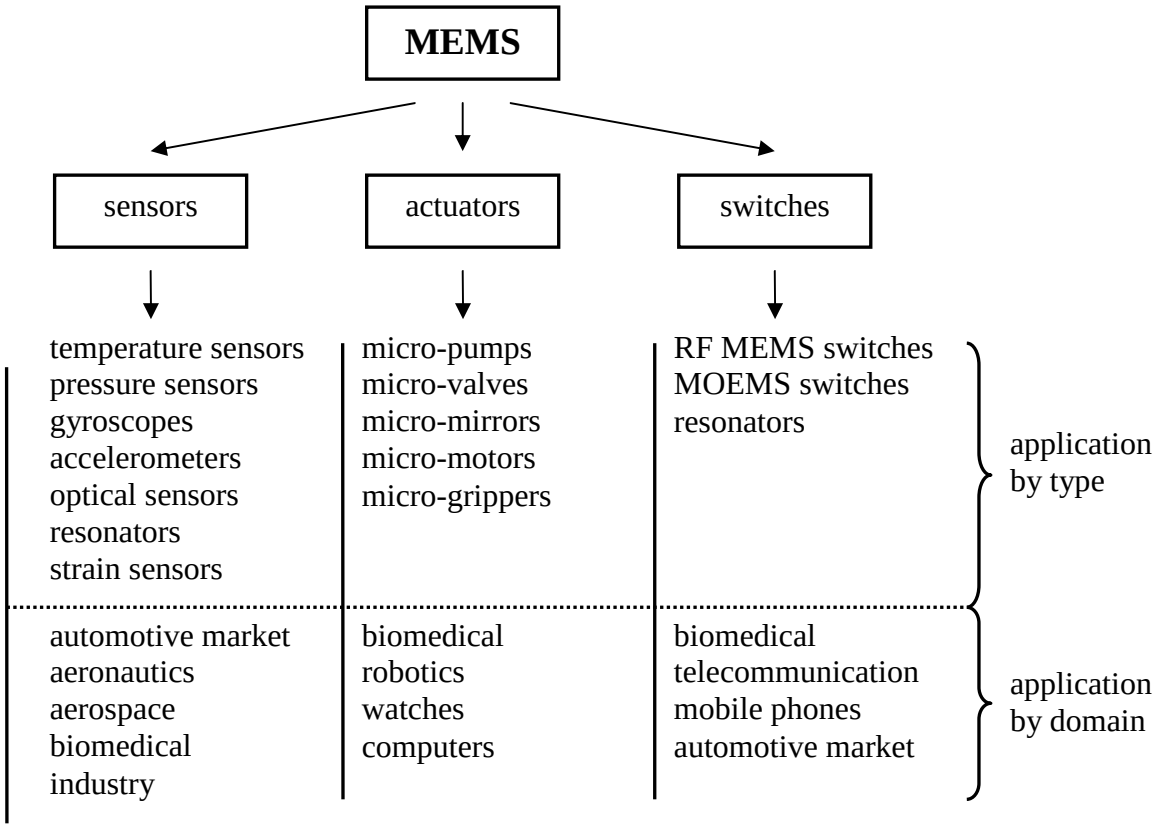


**Figure 1: MEMS applications sorted by type and domain.**

The MEMS market is very open. From day to day, MEMS with theirs applications appear into the new domains of our life. Thus, more and more money is allocated for development of MEMS technology. The growth of the market marks out new challenges and requirements that concern the reliability and precision.

### *Actuation methods*

MEMS often integrate the micro-actuators. In other words they involve movable parts. They can rotate, vibrate, translate etc. However, to get the movement of the actuator, an energy needs to be provided. There are a lot of methods to provide it, namely:

- pneumatic actuation – The pneumatic energy can be brought by a gas under pressure. This method is used in various kinds of membrane-based pressure sensors [4][5]. However, in these applications the external pressure is a measured value. In other cases, when a specific actuation needs to be performed, we need to apply a pressure provided with a pump what could be inconvenient.
- piezoelectric actuation – When a piezoelement is placed under the electrostatic field, the strain is induced within it. This effect is useful only in a microscale. It has excellent operating bandwidth and generates large forces in a compact size. However, its small generated displacement, nonlinear working zones, high temperature sensitivity and

hysteresis are serious drawbacks [13]. Examples of applications are beam actuation [6] and actuation in microscopy [7].

- thermal actuation – The current, passing through a material, generates the heat according to the Joule's law. Then, due to thermal expansion, the element becomes bigger and proper design of a structure allows the movement of elements [8][12]. However, there are some difficulties with isolating the temperature changes to a fixed area and interferences with control electronics.
- electromagnetic actuation – This kind of actuation is performed by generating a magnetic field by the current flow. Then, the magnetic element is deformed. The applications are limited due to the construction difficulties [9], but some applications exist [10][11].
- shape memory alloys – The materials with the specific property that they can "remember" their shape. They are deformable at low temperatures and they return to their original shape when heated [14].
- optical actuation – The actuation is achieved by the optical pressure phenomenon [15]. Although some working devices exist [16], the fabrication is very difficult due to the necessity of integrating the light source and building the reflecting surface.
- electrostatic actuation – This is the most interesting method because it avoids all above-mentioned problems. It needs only to apply a voltage between two elements, from which one is movable. Then, the electrostatic energy is simply converted into the motion [17]. Furthermore, the realization is very simple as most devices are powered electrically and any other electronic circuits can be easily integrated with MEMS technology. The main drawback of electrostatic effect is that it is inversely proportional to the square of distance between two charged bodies. However, this property has smaller influence in microscale, because most structures have much smaller gap distance in relation to their surface. Nevertheless, the list of applications is very long. The electrostatic actuation is used in resonators [18], optical switches [19], micro-grippers [20], micro force gauges [21], micro-pumps [22], gyroscopes [23], pressure sensors [24], RF switches [25] and microscopy [26].

### *Design methods*

The choice of proper design method is very important for the project. It affects on crucial factors such as project duration, cost and even its success. The main steps performed in the project are calculations and experimental verification. Nowadays, when cost and time to market are crucial factors, the calculations should be as precise as possible limiting the

number of experimental verifications. In 1943 finite element analysis (FEA or FEM) was first developed by R. Courant. It was a turning point in the numerical analysis. It uses a system of nodes forming elements, which imitate an analyzed structure. These elements contain the material and structural properties, which define how the structure will react to certain loading conditions. This allows the simulation of structure of almost every size and shape. Furthermore, it combines many domains (mechanical, electrical, thermal etc.) and it allows performing various kinds of analysis (structural, vibrational, transient, thermal etc.). Thank to these advantages, the FEM is commonly used in new project design and in refining the existing product or structure. Moreover, continuous growth of computer market gives an opportunity of FEM use for everyone without possessing supercomputer. However, is it always necessary to use the FEM? The answer is no. When the structure is simple (basic shapes), there is no need to perform meshing and analytical model can be used. Then, the solution reduces to solving one or a few equations, which significantly shortens calculation time. Moreover, the results are usually similar to those obtained with FEM. These features of analytical modelling are especially useful in optimization phase in which several single simulations need to be performed. The above-mentioned facts indicate that the analytical modelling may be a good alternative to the FEM in specific cases.

### *CAPTAM project*

The work presented in this dissertation was realized in LAAS laboratory (Toulouse, France) within the framework of the CAPTAM project (“CApteur de Pression Télémétrique Auto-étalonnable Miniature pour la mesure de fonctions physiologiques sur l'homme”). The aim of this project was to develop a highly miniaturized pressure sensor usable for measurement of arterial and intracranial pressure in a human, which integrates the temperature sensor and has a feature of autocalibration. The project was realized in collaboration with Hemodia (Labège, France), Centre Hospitalièr Universitaire de Toulouse (CHU Toulouse, France) and Université de Picardie Jules Verne (UPJV, Amiens, France). The task realized in LAAS concerned the development of a cell sensitive to the pressure and the temperature. Due to the specific application, the cell size was set to 2400 μm × 740μm. It consists of a membrane with four implanted strain gauges in configuration of Wheatstone bridge. The principle of operation is very simple (Figure 2). The membrane is placed above the cavity, which is formed by the bonding of two wafers. The constant pressure inside the cavity is used as the reference pressure ($P_{ref}$). The difference between external ($P_{ext}$) and reference pressure is converted into the change of membrane deflection ($\Delta w$). The stress ($\Delta\sigma$)

induced within the membrane is converted into the electrical signal ($\Delta V_{out}$) due to change of gauges resistance ($R+\Delta R$).

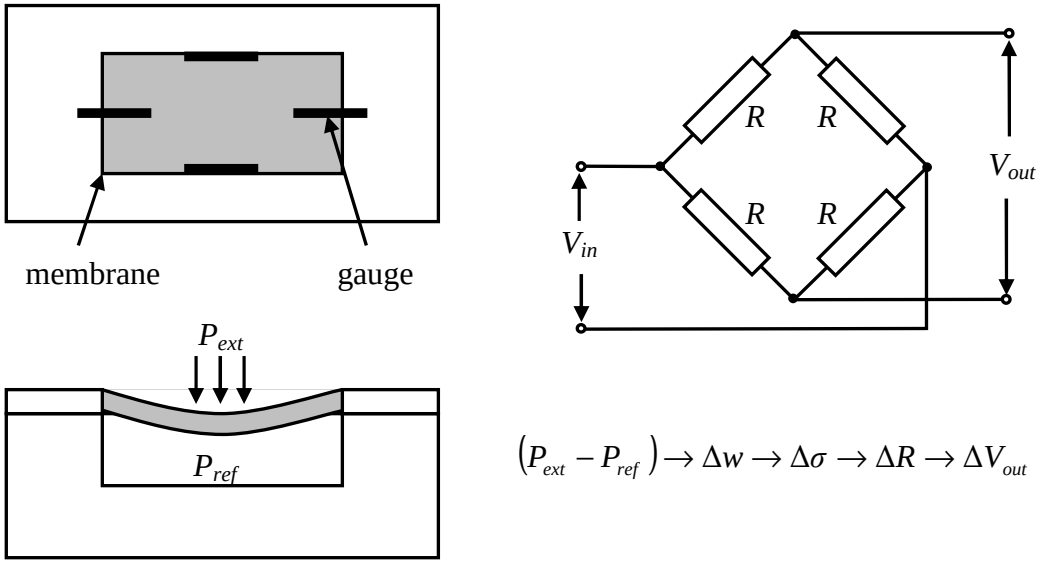


**Figure 2: Schema of the pressure sensor and its principle of operation.**

The material used for membrane fabrication was N-type silicon in (100) plane. The membrane was fabricated in <110> direction, which gives the highest value of piezoresistivity coefficient. The membrane thickness was set to 5 μm taking into consideration the sensor sensitivity, technological limits and availability of SOI wafers on the market. The membrane size was set to 300 μm × 300 μm and 900 μm × 300 μm. The integrated electrostatic pressure generator, which will allow the autocalibration, is limited on applied voltage to 6 V maximum. The generator is obtained by placing the electrode under the membrane. The electrode is simply obtained by using the silicon as a substrate. The work in the field of pressure sensor development concerned its optimization in order to satisfy the project requirements such as minimal pressure sensitivity and generated electrostatic pressure. This dissertation focuses only on the electrostatic pressure generator.

### *Thesis layout*

The objectives of this dissertation are to investigate the analytical methods of modelling the electrostatic membrane-based actuators in terms of precision and calculation time and develop the complete model that takes into consideration all basics phenomena induced during the fabrication process. This should allow a fast simulation and optimization of this type of structures. The dissertation is divided into three main parts.

In the first chapter, the analytical description of membrane behaviour under the hydrostatic and electrostatic load is analysed including the residual stress and initial deflection

of the membrane. According to the project assumptions, only thin plates in range of small deflection will be taken into account. The developed analytical model is also compared to the FEM simulations in terms of precision and calculation time.

The second chapter concerns the optimization. It describes the possible design paths and principles of optimization using analytical modelling. Next, the statistical approach is presented in order to characterize the fabrication process.

The last chapter focuses on the experimental work, which will allow the validation of analytical results. It describes the realization of test samples: the technological process, process characterization and techniques of measurement. Next, it presents the experimental results obtained from measurement of membranes actuated electrostatically. These results are compared with the theory and mismatch hypotheses are described.

Chapter 1

# Electrostatic membrane-based actuator theory

## 1.1. Electrostatic actuator principles

The fundamental phenomenon used in electrostatic actuators is an electrostatic attraction between electric charges. This phenomenon was first observed by ancient Greeks. However, until XVIII century there was no scientific description of it. In 1780 Charles Coulomb has developed the law describing the electrostatic force. It says that the magnitude of electrostatic force $F_e$ on a charge $q_1$ due to presence of a second charge $q_2$ (Figure 1-1) is directly proportional to the product of the magnitudes of the charges and inversely proportional to the square of the distance between the charges. The relation describing the law is as follows:

$$F_e = k_e \frac{q_1 q_2}{r_e^2}, \qquad k_e = \frac{1}{4\pi\varepsilon_0} \qquad \textbf{Equation 1-1}$$

where $r_e$ is a distance between the two charges, $k_e$ is proportionality constant (Coulomb constant) and $\varepsilon_0$ is a vacuum permittivity.

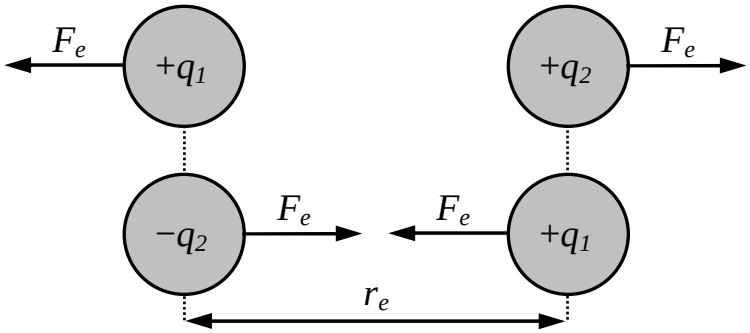


**Figure 1-1: Interaction of electric charges.**

When talking about a structure, this force can be produced by applying the voltage between two elements which cause the mutual attraction between them. Furthermore, the force can be used in actuation when one element of the structure is not fixed.

Let us consider the simplest model of the electrostatic actuator (Figure 1-2) [1], where the bottom electrode of surface $S$ is fixed and the top electrode is attached to a spring.

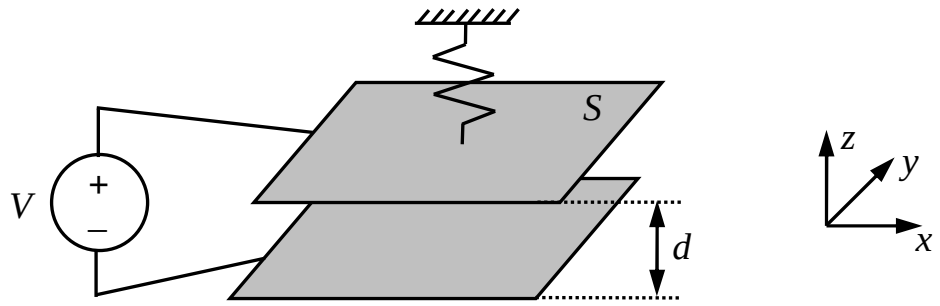


**Figure 1-2: Model of electrostatic actuator.**

When the voltage *V* is applied, the electrostatic force is produced between the electrodes. This force can be calculated using Equation 1-1. However, it needs to know the charge distribution. It is easier to use the energy *E* stored in the structure [28] expressed with the following formula:

$$E = \frac{1}{2} C V^2, \qquad C = \varepsilon_0 \frac{S}{d} \qquad \textbf{Equation 1-2}$$

where C is the capacitance. The magnitude of force is then:

$$F_e = \frac{\partial E}{\partial z} = \varepsilon \frac{V^2 S}{2 d^2} \qquad \textbf{Equation 1-3}$$

As electrostatic force cause attraction of electrodes, the initial distance between electrodes *d* reduces to *d-w*, where *w* is the electrode displacement and the spring force $F_{sp}$ is trying to counteract the electrostatic force. The equation describing the system is as follows:

$$F_e = F_{sp}$$
$$\varepsilon \frac{V^2 S}{2(d-w)^2} = k_{sp} w \qquad \textbf{Equation 1-4}$$

As one can see, the spring force is proportional to the displacement and the electrostatic force is inversely proportional in square. Thus, the system is not linear and we need to study the equilibrium positions. Figure 1-3 shows the exemplary dependence between the spring force and electrostatic force for various voltages:

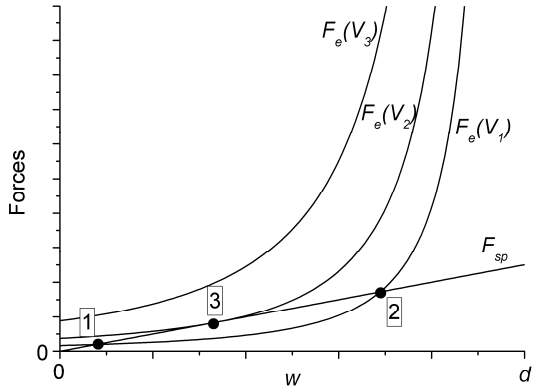


**Figure 1-3: Dependence between electrostatic and spring force**

When the voltage $V_1$ is applied, there are two equilibrium positions. The first one (1) is stable because at each position around it the reacting force is directed into the stable position. The second one (2) is unstable because the reacting force is directed inversely. When the voltage increases up to $V_2$, only one equilibrium position exists (3) and it is the maximal applied voltage when the system is stable. When this voltage is exceeded ($V_3$), there are no equilibrium positions and the movable electrode is pulled down to the fixed electrode. This effect is called the pull-in effect and occurs when the applied voltage is higher then pull-in voltage ($V_{pull\text{-}in}$). In the above example the pull-in voltage is equal to $V_2$. To avoid short circuit when the pull-in effect occurs, the bottom electrode has to be insulated. The value of pull-in voltage is calculated from Equation 1-4 that can be transformed into following form:

$$w(d-w)^2 = \varepsilon \frac{V^2 S}{2k_{sp}} \qquad \textbf{Equation 1-5}$$

The graphical representation of this equation is presented in Figure 1-4:

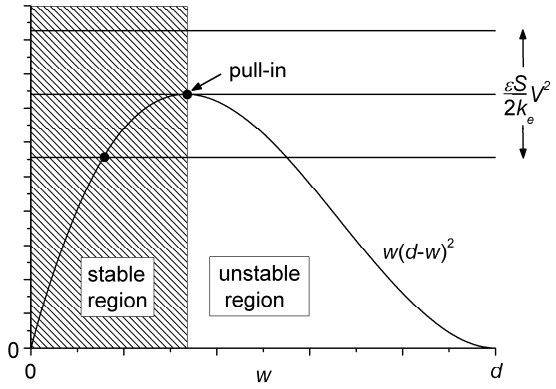


**Figure 1-4: Graphical representation of equilibrium equation**

The pull-in occurs when the function on the left side of Equation 1-5 has a maximum, which leads to the following relations [29]:

$$\frac{\partial}{\partial w} w(d-w)^2 = 0 \qquad \Rightarrow \qquad w_{pull-in} = \frac{1}{3} d \qquad \textbf{Equation 1-6}$$

$$V_{pull-in} = \sqrt{\frac{8}{27} \frac{k_e d^3}{\varepsilon_0 S}} \qquad \textbf{Equation 1-7}$$

When the electrodes stick together, the electrostatic force raises to very large value, as the distance between electrodes is equal to oxide thickness. Thus, to separate the electrodes the voltage has to be reduced to pull-out voltage ($V_{pull-out}$) [30]. This situation is shown in Figure 1-5:

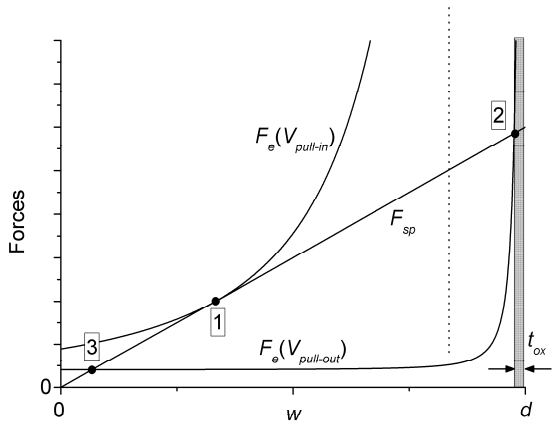


**Figure 1-5: Dependence between electrostatic and spring force for pull-out state**

For voltages higher than pull-in voltage, the electrostatic force is much greater than spring force (this stable point is not shown in the figure) and is expressed with the following formula:

$$F_{el} = \varepsilon_{ox} \frac{V^2 S}{2t_{ox}^2}, \qquad V > V_{pull-in} \qquad \textbf{Equation 1-8}$$

To separate the electrodes, the voltage has to be reduced to the level wherein the electrostatic force is not greater than the spring force (position 2). Then the system goes to stable position (3). The pull-out voltage is calculated from following relation valid for pull-in state:

$$F_{el} = F_{sp}$$

$$\varepsilon_{ox} \frac{V_{pull-out}^2 S}{2t_{ox}^2} = k_{sp}\left(d - t_{ox}\right)$$

$$V_{pull-out} = \sqrt{\frac{2k_{sp}t_{ox}^2\left(d - t_{ox}\right)}{\varepsilon_{ox}S}}$$

$$V_{pull-out} \approx \sqrt{\frac{2k_{sp}t_{ox}^2 d}{\varepsilon_{ox}S}}, \qquad d >> t_{ox}$$

**Equation 1-9**

Summarizing, we can determine four cycles of operation, which form the hysteresis loop, presented in Figure 1-6:

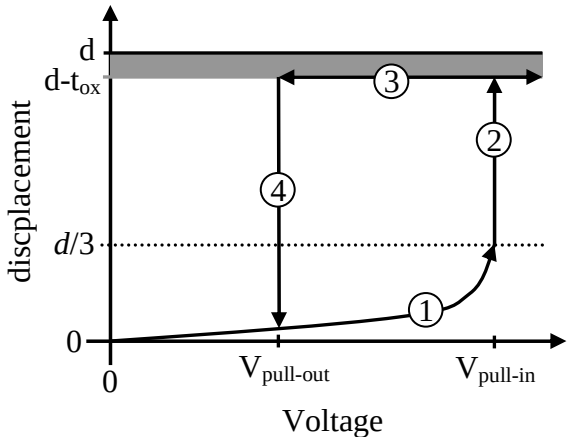


**Figure 1-6: Cycles of electrostatic actuator operation**

1. normal operation ($V<V_{pull-in}$) – electrode position varies with applied voltage
2. pull-in effect ($V>V_{pull-in}$)
3. movable electrode touches the oxide layer on fixed electrode ($V>V_{pull-out}$)
4. pull-out effect ($V<V_{pull-out}$)

Actuator, presented above, is the simplest structure because both electrodes are flat. This simplifies the modelling due to fact that the electrostatic force is constant at each point of electrode. In next sections, we will focus on more complex structure, in which the movable electrode is made of a membrane.

## *1.2. Membrane mechanical behaviour*

### 1.2.1. Material properties

In further discussion, we will take into consideration a membrane made of silicon, a material that is commonly used in microsystems. We assume that the material is linearly elastic, which is usually true for relatively small deformations and that body is homogeneous and continuously distributed over its volume. As silicon is an orthotropic material, one has to precise the crystallographic orientation of the membrane. In technology, silicon cut in plane (100) aligned in two basics directions <100> and <110> is commonly used. Additionally, in model description, an isotropy will be taken into consideration. Basics of linear elasticity and mechanical properties of silicone are described in APPENDIX A.

### 1.2.2. Membrane bending

Before we start describing the membrane bending we have to define what exactly the membrane is. Generally, a structure of a cuboid shape with dimensions of length *a*, width *b* and constant thickness *h*, which is relatively small compared to other dimensions, is called a plate (Figure 1-7).

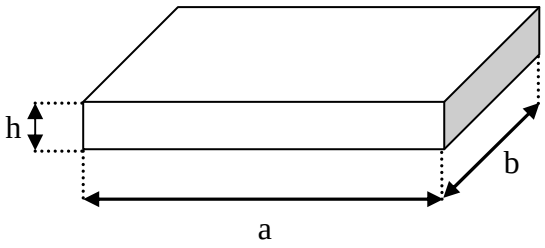


**Figure 1-7: Scheme of plate.**

There are three kinds of plates, which are defined by a ratio $R_h$ of the length of the shorter side to the thickness [36]:

$$R_h = \frac{a}{h}, \qquad a < b \qquad \textbf{Equation 1-10}$$

1. thick plates – $8<R_h<10$
2. thin plates – $10<R_h<80$
3. membranes – $R_h>80$

This classification results from bending properties, which depends on ratio $R_h$. When it becomes larger some assumptions can be applied which simplify the calculation. From this moment we will use the theory of thin plates and as a membrane we will mean a thin plate.

A lot of work has been done in investigation of plate bending starting from Euler (1766) and Bernoulli (1789) [37]. Germain (1826) developed a plate differential equation, which was corrected by Lagrange (1828) and named as Germain-Lagrange equation [38]. Then, Kirchoff (1850) published his thesis, wherein some assumptions, valid for small deflections, were made (Kirchoff's hypotheses), which are fundamental in the theory of thin plates [39]. Timoshenko (1913) provided a boost to this theory. He gave a solution for large deflection of plates, circular plates and he considered the elastic stability problems [40] resulting in a textbook written together with Woinowski-Kreiger (1959) that is fundamental in plates bending analysis [41]. The assumptions of theory of thin plates are as follows [43]:

- There is no deformation in the middle plane of the plate. This plane remains neutral during bending.
- Points of the plate laying initially on a normal to the middle plane of the plane remain on the normal to the middle surface of the plane after bending.
- The normal stresses in the direction transverse to the plate are small in relation to the others and can be neglected.

Then, using the two dimensional function of deflection $w(x,y)$, which satisfies the differential equation and boundary conditions, one can define all stress components at any point of the plate. It must be emphasized that above-mentioned assumptions are valid only when the deflection of the plate $w$ is small in comparison with the thickness of the plate $h$ (small deflection, $w/h \leq 0.3$ [42]). In other case (large deflection) [41], the first assumption is not valid and supplementary stresses must be taken into account in deriving the differential equation of the plates. However, we will use only the theory of thin plates for small deflections. In next sections we will describe the bending of the circular and the rectangular membrane separately.

## 1.2.3. Rectangular membrane

### 1.2.3.1. Membrane bending by laterally distributed load

Let us consider a rectangular membrane with dimensions of length $a$, width $b$ and thickness $h$, placed in Cartesian coordinates system with its origin (0,0) in the middle of the membrane, as shown in Figure 1-8:

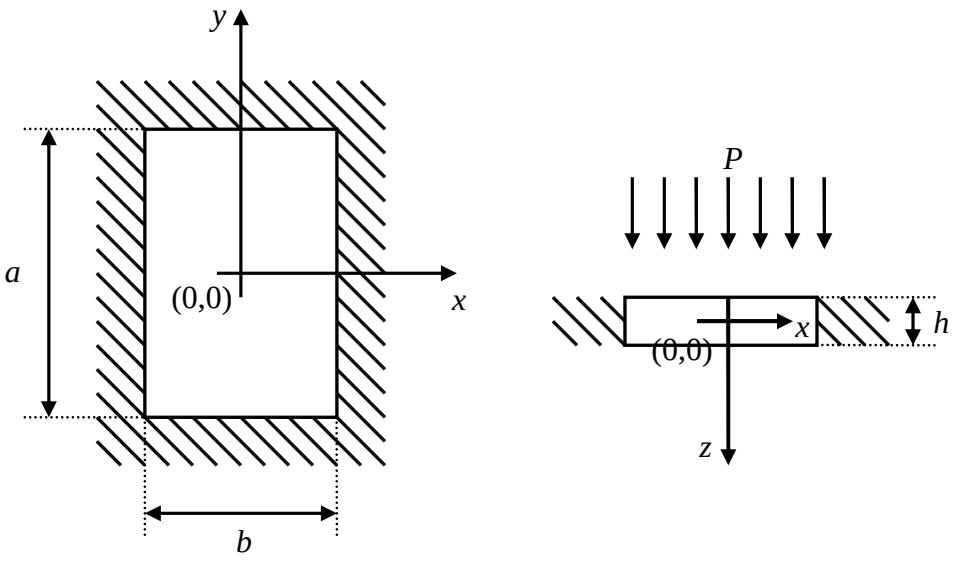


**Figure 1-8: Definition of geometric parameters. Top view is on the left and section on the right.**

We assume that width *b* is smaller or equal to the length *a* and we introduce a membrane ratio *R*:

$$R = \frac{a}{b}, \qquad R \geq 1 \qquad \textbf{Equation 1-11}$$

The external pressure *P* is distributed over the whole membrane. Taking into consideration the anisotropy [44], the equation of equilibrium of the loaded membrane for small deflections is as follows [41] (derivation of this equation is shown in APPENDIX B.1):

$$D\left(\frac{\partial^4 w_1(x,y)}{\partial x^4} + 2\alpha\frac{\partial^4 w_1(x,y)}{\partial x^2 \partial y^2} + \frac{\partial^4 w_1(x,y)}{\partial y^4}\right) = P \qquad \textbf{Equation 1-12}$$

where $w_1$ is a change of membrane deflection due to applied load, $D_0$ is a membrane rigidity and *D* is a membrane flexural rigidity described with Equation 1-13:

$$D = D_0 h^3, \qquad D_0 = \frac{E}{12\left(1-\nu^2\right)} \qquad \textbf{Equation 1-13}$$

where *E* is a Young Modulus and *v* is a Poisson ratio. To simplify the notation, we introduce the following operator:

$$\Delta\Delta = \frac{\partial^4}{\partial x^4} + 2\alpha\frac{\partial^4}{\partial x^2 \partial y^2} + \frac{\partial^4}{\partial y^4}$$

and Equation 1-12 takes the following form:

$$D\Delta\Delta w_1(x,y) = P \qquad \textbf{Equation 1-14}$$

### 1.2.3.2. Residual stress

In theory, when no external forces are acting on the membrane, there is no stress within it. However, in many cases, the membrane is initially stressed. This kind of stress is called residual stress. By definition the residual stress remains in the material after the cause of external stress (external force, heat gradient) is removed. Residual stresses occur for variety of reasons. In case of microsystems, the main source is a technological process in which the heat treatment is performed. Basic technological phases when the residual stress can be introduced are deposition, oxidation or plastic deformation. There are two kinds of residual stress:

- compressive – stress resulting in compaction of the material (decrease of volume)
- tensile – stress resulting in stretching of the material (increase of volume)

In modelling of the residually stressed rectangular membrane, we assume that this stress is uniformly distributed within the membrane and has equal values of components in *x* and *y* axis [45]. Thus, the residual stress can be expressed as a result of a force acting transversally and uniformly on the membrane edges as shown in Figure 1-9:

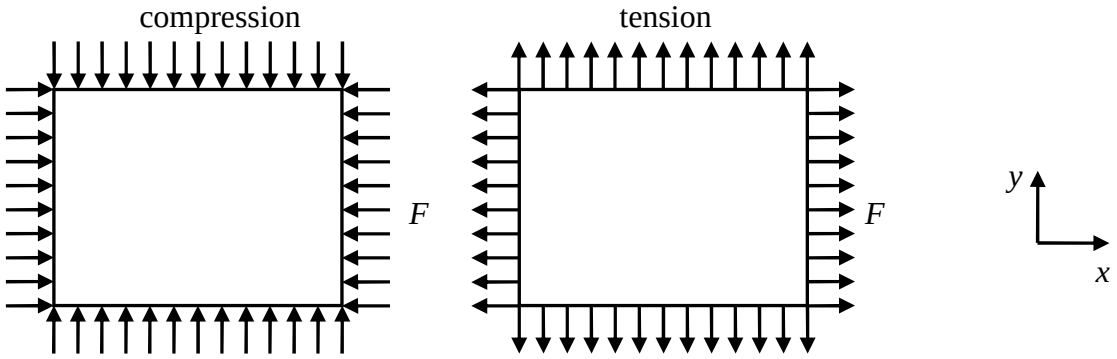


**Figure 1-9: Compressive and tensile residual stresses in rectangular membrane.**

The term describing the residual stress in the membrane is [45]:

$$\sigma_0 h\left(\frac{\partial^2 w_1(x,y)}{\partial x^2}+\frac{\partial^2 w_1(x,y)}{\partial y^2}\right) \qquad \textbf{Equation 1-15}$$

or in the simplest form by introducing the Laplace operator:

$$\sigma_0 h\Delta w_1(x,y), \qquad \Delta=\frac{\partial^2}{\partial x^2}+\frac{\partial^2}{\partial y^2} \qquad \textbf{Equation 1-16}$$

where $\sigma_0$ is the residual stress. Its negative value corresponds to compression and positive to tension.

### 1.2.3.3. Initial deflection

There is another phenomenon, which can be observed in real microstructures. As it was presented before, the membrane can be residually stressed. In case of tensile stress when the membrane is stretched, there is no reason why the membrane could not be flat. If the membrane is compressed, it can be proved (by equating the term from Equation 1-15 to zero) that the membrane remains flat if a critical residual stress is not exceeded (it will be precisely described in paragraph 1.2.5). However, real structures are not usually symmetric so that membrane deflects, producing the initial deflection $w_0$ (Figure 1-10) [46]. The direction of the initial deflection of the membrane depends on the geometry of the structure.

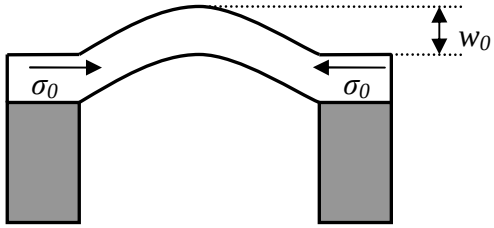


**Figure 1-10: Membrane with initial deflection.**

The initial deflection of the membrane has no effects on bending moments meaning that the change of the deflection due to external load remains the same. Thus, Equation 1-14 is still valid and the total deflection $w$ of the membrane is a sum of initial deflection $w_0$ and deflection $w_1$ induced by applied load. If lateral loads are acting on the membrane (e.g. due to residual stress), the initial deflection produces additional forces acting in the middle of plane. Then, this effect has to be taken into account by using the total deflection $w$ in the term in Equation 1-15 [45]. This implies the assumption, that the curvature of an initially deformed membrane is the same as for a membrane deflected under the load of uniform pressure.

### 1.2.3.4. Classical equation of equilibrium

Combining the equation of membrane bending, the term describing the existence of residual stress and taking into account the initial deflection of the membrane, we get the final equation of equilibrium:

$$D\Delta\Delta w_1(x,y) + \sigma_0 h\Delta w(x,y) = P \qquad \textbf{Equation 1-17}$$

To simplify the calculations, the deflection $w_1$ is replaced with the deflection $w$:

$$w_1 = w - w_0 \qquad \textbf{Equation 1-18}$$

Then, the equation of equilibrium has only one unknown $w$:

$$D\Delta\Delta\big(w(x,y) - w_0(x,y)\big) + \sigma_0 h\Delta w(x,y) = P \qquad \textbf{Equation 1-19}$$

### 1.2.3.5. Solution for rectangular membrane

We consider a rectangular membrane under the uniformly distributed pressure (e.g. hydrostatic pressure) as shown on Figure 1-8. The integration limit Ω is [-*a*/2, *a*/2]×[-*b*/2, *b*/2]. We assume that the membrane is perfectly clamped on its edges. Thus, the boundary conditions are as follows [47]:

$$w(\partial\Omega) = 0$$
$$\left.\frac{\partial w}{\partial z}\right|_{\partial\Omega} = 0 \qquad \textbf{Equation 1-20}$$

where dΩ are points on the membrane edges. First equation indicates that membrane edges do not move vertically, the second one indicates that direction of membrane edges is always horizontal.

Using Vashy-Buckingham theory [54], Equation 1-19 can be expressed without dimensions, using the following transformation:

$$u = \frac{2x}{a}$$
$$v = \frac{2y}{b} \qquad \textbf{Equation 1-21}$$
$$R = \frac{b}{a}$$

The integration limit Ω becomes non-dimensional [-1, 1]×[-1, 1] and Equation 1-19 takes the following form:

$$D\frac{16}{a^2b^2}\left(R^2\frac{\partial^4(w-w_0)}{\partial u^4} + 2\alpha\frac{\partial^4(w-w_0)}{\partial u^2\partial v^2} + \frac{1}{R^2}\frac{\partial^4(w-w_0)}{\partial v^4}\right) + \sigma_0 h\frac{4}{ab}\left(R\frac{\partial^2 w}{\partial u^2} + \frac{1}{R}\frac{\partial^2 w}{\partial v^2}\right) = P \qquad \textbf{Equation 1-22}$$

where *w* and $w_0$ are functions of variables *u* and *v*. To simplify the calculation we assume that the initial deflection $w_0$ can be expressed as an additional pressure $P_{w0}$:

$$P_{w0} = D\frac{16}{a^2b^2}\left(R^2\frac{\partial^4 w_0}{\partial u^4} + 2\alpha\frac{\partial^4 w_0}{\partial u^2\partial v^2} + \frac{1}{R^2}\frac{\partial^4 w_0}{\partial v^4}\right) \qquad \textbf{Equation 1-23}$$

Equation 1-22 is then:

$$D\frac{16}{a^2b^2}\left(R^2\frac{\partial^4 w}{\partial u^4} + 2\alpha\frac{\partial^4 w}{\partial u^2\partial v^2} + \frac{1}{R^2}\frac{\partial^4 w}{\partial v^4}\right) + \sigma_0 h\frac{4}{ab}\left(R\frac{\partial^2 w}{\partial u^2} + \frac{1}{R}\frac{\partial^2 w}{\partial v^2}\right) = P + P_{w0} \qquad \textbf{Equation 1-24}$$

### *Choice of approximation function*

To solve Equation 1-24 we need to know the function $w(x,y)$ describing the membrane form which fits the boundary conditions. However, there is no simple analytical solution [55]. Thus, the approximated solution has to be used. In our discussion we take into consideration the rectangular membrane with ratio $R$ up to 3 (see paragraph 1.2.3.6). Many works have been done to find the best function. The approximation using trigonometric functions was presented by Timoshenko [41] and used by Allen [56]. This membrane form was not optimal [57] and Maier-Schneider presented the expanded form of this function [58]. The other form of trigonometric approximation was presented by Kerrour [59]. The other way is to use a polynomial approximation. The simplest form was presented by Ko [60], the other form was presented by Vlassak [61] and the extended function was presented by Naciri [62]. All above-mentioned solutions are listed in Table 1-1, wherein $K$ are coefficients to be determined, $u$ and $v$ are coordinates normalized to membrane length $a$ and width $b$, respectively.

**Table 1-1: Functions describing the membrane form**

| Author | Function |
|---|---|
| Timoshenko | $w(u,v) = K_0 \cos\left(\frac{\pi u}{4}\right)\cos\left(\frac{\pi v}{4}\right)$ **Equation 1-25** |
| Maier-Schneider | $w(u,v) = \left[K_0 + K_1\left(u^2+v^2\right)+K_2\left(u^2v^2\right)\right]\cos\left(\frac{\pi u}{4}\right)\cos\left(\frac{\pi v}{4}\right)$ **Equation 1-26** |
| Kerrour | $w(u,v) = \left(1-u^2\right)^2\left(1-v^2\right)^2\sum_{i,j=0}^{n} K_{ij}\cos^2\left(\frac{(4i+1)\pi u}{4}\right)\cos^2\left(\frac{(4j+1)\pi v}{4}\right)$ **Equation 1-27** |
| Ko | $w(u,v) = K_0\left(1-u^2\right)\left(1-v^2\right)$ **Equation 1-28** |
| Vlassak | $w(u,v) = \left(1-u^2\right)\left(1-v^2\right)\left[K_0 + K_1\left(u^2+v^2\right)\right]$ **Equation 1-29** |
| Naciri | $w(u,v) = \left(1-u^2\right)^2\left(1-v^2\right)^2\sum_{i,j=0}^{n} K_{ij}u^{2i}v^{2j}$ **Equation 1-30** |

The simplest functions (Equation 1-25 and Equation 1-28) are valid only for square membranes. The functions from Equation 1-26 and Equation 1-29 have not enough terms and cannot model correctly edges of rectangular membranes (Figure 1-11).

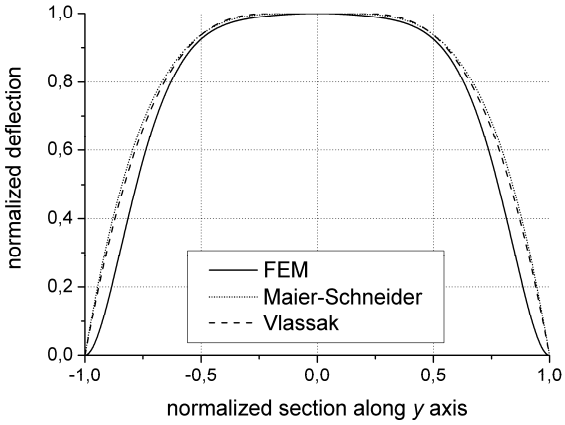


**Figure 1-11: Comparison between membrane forms obtained from analytical solutions and FEM simulation (1) for membrane ratio *R*=3.**

The last ones (Equation 1-27 and Equation 1-30) have variable number of terms, so they are applicable for membranes with almost any membrane ratio *R*. Theirs comparison show that the polynomial function is closer to the form obtained by FEM simulation (Figure 1-12).

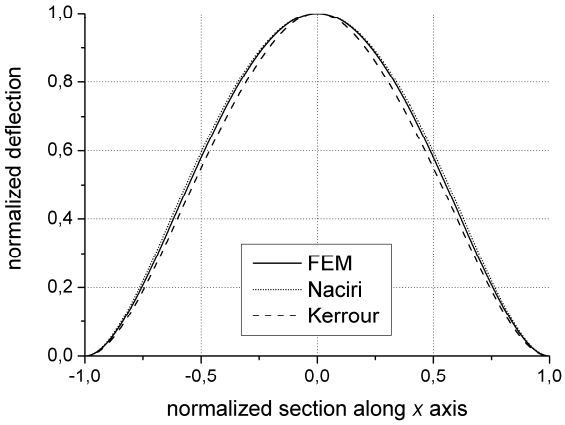


**Figure 1-12: Comparison between membrane forms obtained from analytical solutions and FEM simulation (2) for membrane ratio *R*=1.**

Finally, for further calculations we have chosen the function from Equation 1-30. The number of coefficients was limited to 9 ($n$=3), which is suitable for rectangular membranes with ratio *R* up to 3 [65]. In [63] it was shown that the function from Equation 1-30 is not an ideal solution. If we analyze all terms of this function, we can clearly see that not all space is filled (Figure 1-13) what can cause erroneous results. To compensate this lack of functions, one can introduce other types of functions what was shown in [63]. However, the comparison from Figure 1-12 shows that the differences are not critical and can be neglected.

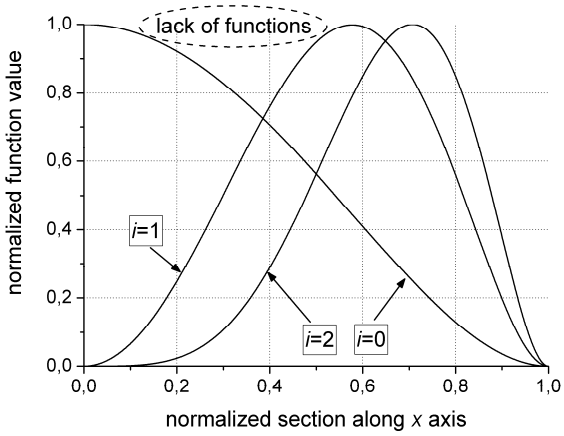


**Figure 1-13: Terms of polynomial function for *n*=3.**

### *Galerkin method*

Equation 1-24 is a differential equation whose simple solution does not exist. In solving such problems, Galerkin method [64] is used which converts a continuous operator problem to a discrete problem and transform the equation into the weak formulation. This leads to a system of linear equations.

Let us transform Equation 1-30 into the following form:

$$w(u,v)=\sum_{i,j=0}^{n}K_{ij}\varphi_{ij} \qquad \textbf{Equation 1-31}$$

where:

$$\varphi_{ij}=\left(1-u^2\right)^2 u^{2i}\left(1-v^2\right)^2 v^{2j} \qquad \textbf{Equation 1-32}$$

Then, the system of Galerkin equations can be written as follows:

$$\iint_{\Omega} D\frac{16}{a^2b^2}\left(R^2\frac{\partial^4 w}{\partial u^4}+2\alpha\frac{\partial^4 w}{\partial u^2\partial v^2}+\frac{1}{R^2}\frac{\partial^4 w}{\partial v^4}\right)\varphi_{ij}dudv+$$
$$+\iint_{\Omega}\sigma_0 h\frac{4}{ab}\left(R\frac{\partial^2 w}{\partial u^2}+\frac{1}{R}\frac{\partial^2 w}{\partial v^2}\right)\varphi_{ij}dudv=\iint_{\Omega}\left(P+P_{w0}\right)\varphi_{ij}dudv,\qquad i,j=0,1,2$$

**Equation 1-33**

Substituting Equation 1-31 into Equation 1-33 and calculating the integrals, we get the system of linear equations in matrix form (see APPENDIX C.1):

$$D\frac{16}{a^2b^2}\mathbf{A_1K}+\sigma_0 h\frac{4}{ab}\mathbf{A_2K}=\left(P+P_{w0}\right)\mathbf{B} \qquad \textbf{Equation 1-34}$$

where **K** is a (9×1) vector of unknown coefficients $K_{ij}$, $\mathbf{A_1}$, $\mathbf{A_2}$ are (9×9) matrices and **B** is a (9×1) vector. Coefficients of matrices $\mathbf{A_1}$, $\mathbf{A_2}$ and vector **B** are calculated analytically and are presented in APPENDIX D.1. The vector **K** is calculated as follows:

$$\mathbf{K} = \left( D\frac{16}{a^2 b^2}\mathbf{A_1} + \sigma_0 h\frac{4}{ab}\mathbf{A_2} \right)^{-1} (P + P_{w0})\mathbf{B} \qquad \textbf{Equation 1-35}$$

The last unknown term is the pressure $P_{w0}$, which can be calculated from Equation 1-23. Knowing the normalized coefficients $k_{ij}$ (coefficients $K_{ij}$ normalized to $K_{00}$ - see next paragraph) and the coefficient $K_{00}$ (equal to $w_0$) we have all coefficients of matrix **K** and one can easily calculate $P_{w0}$ from transformed Equation 1-34:

$$P_{w0} = D\frac{16}{a^2 b^2}\mathbf{A_1}\mathbf{K}\mathbf{B}^{-1} \qquad \textbf{Equation 1-36}$$

### 1.2.3.6. Membrane deflection

The typical graphical representation of the membrane deflection described by Equation 1-30 for various membrane ratios is presented in Figure 1-14 to Figure 1-16:

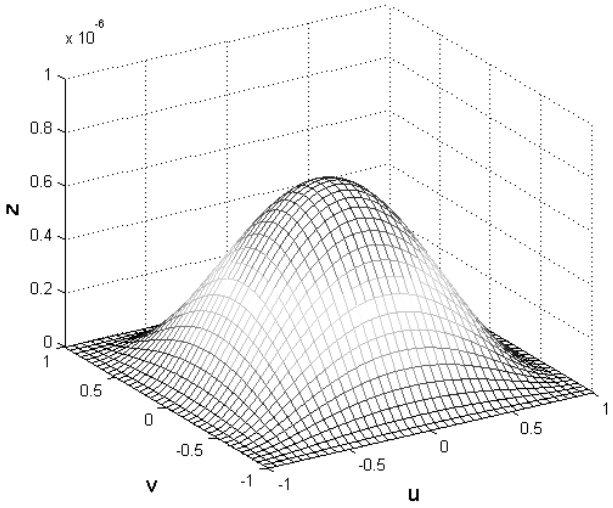


**Figure 1-14: Membrane topography for *R*=1.**

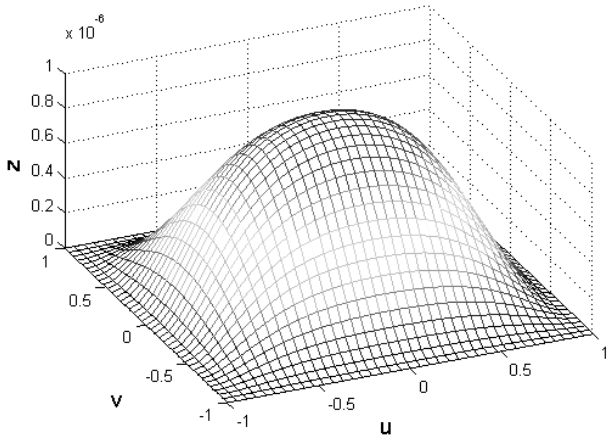


**Figure 1-15: Membrane topography for *R*=2.**

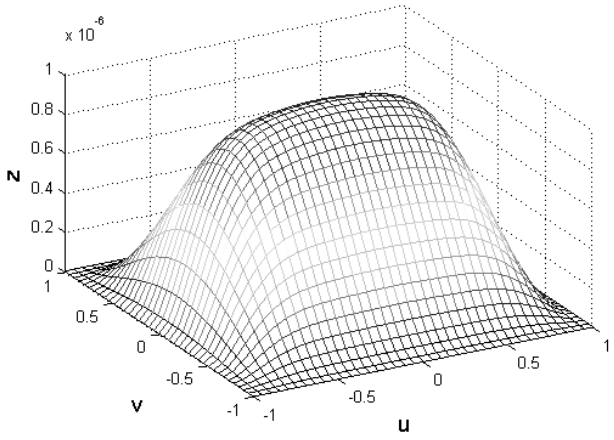


**Figure 1-16: Membrane topography for *R*=3.**

The most important parameter is the maximal deflection, which exists in the membrane centre. Let us go back to Equation 1-31 and calculate the maximal deflection of the membrane $w_{max}$. When $u$=0 and $v$=0 (membrane centre), we get:

$$w_{\max} = K_{00}$$ **Equation 1-37**

Then, we can transform Equation 1-31 into the form:

$$w(u,v) = w_{\max}\left(1-u^2\right)^2\left(1-v^2\right)^2\sum_{i,j=0}^{n}k_{ij}u^{2i}v^{2j}$$ **Equation 1-38**

where:

$$k_{ij} = \frac{K_{ij}}{K_{00}}$$ **Equation 1-39**

First, we will analyse the deflection of the square membrane without residual stress due to various values of pressure.

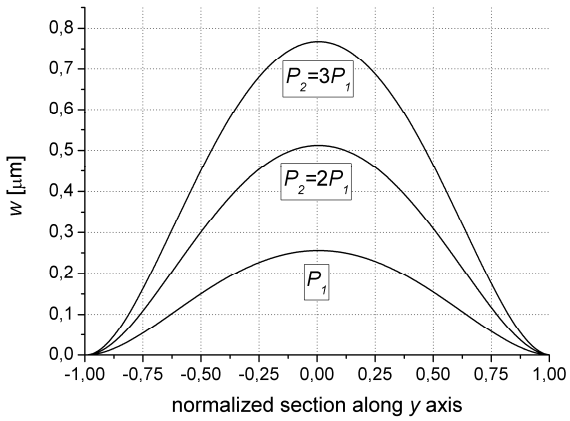


**Figure 1-17: Square membrane deflection under the various pressures.**

It can be seen that the maximal deflection is directly proportional to the pressure and the membrane form is always the same. Thus the coefficients $k_{ij}$ from Equation 1-38) describe the normalized membrane form, which is dependent only on anisotropy coefficient [66]. Values of these coefficients for isotropic material, silicon <100>, silicon <110> and various membrane ratios are presented in Table 1-2 and are similar to those found in the literature [67][66][65]. However, simulations showed that the membrane form is also dependent on residual stress, more precisely on ratio $(\sigma_0 h)/D$. Figure 1-18 illustrates this difference between membrane forms:

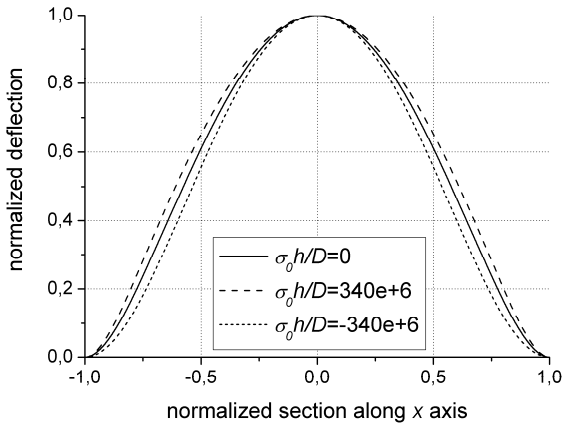


**Figure 1-18: Square membrane forms for various values of residual stress.**

In the example a 300 μm × 300 μm × 5 μm silicon membrane with 100 MPa of residual stress in tension and compression was simulated. The difference between the forms is significant, but the stress value is relatively high. In structures in which the residual stress is not desired, its value is often much smaller. Then, the normalized form of the membrane can be used. However, one should not omit this phenomenon, especially when the membrane is less rigid or when the stress distribution within the membrane is very important (it will be explained in section 1.2.3.7).

As it was shown earlier, the membrane response to the load depends on membrane ratio *R*. When this ratio increases, the membrane surface also increases which results in larger deflection of the membrane. Figure 1-19 shows an interesting dependence:

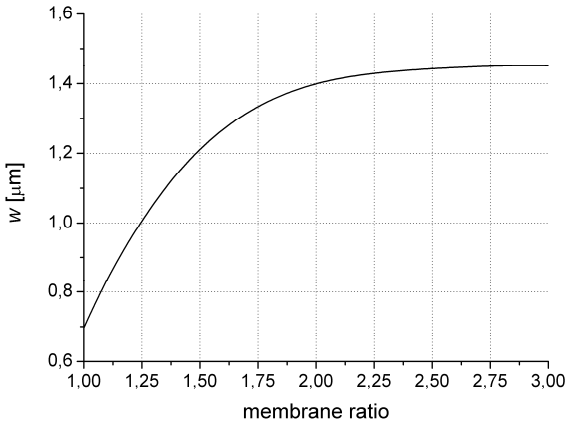


**Figure 1-19: Membrane deflection versus the membrane ratio *R*.**

It can be seen that the deflection stabilizes for membrane ratio close to 3. Thus, the use of membrane with greater ratio is not effective. These kinds of membranes are called long rectangular membrane and as a limit one assumes the ratio equal to 4 [68].

**Table 1-2: Values of coefficients $k_{ij}$.**

| Material | Isotropic | | | Silicon <100> | | | Silicon <110> | | |
|---|---|---|---|---|---|---|---|---|---|
| Membrane ratio | $R$=1 | $R$=2 | $R$=3 | $R$=1 | $R$=2 | $R$=3 | $R$=1 | $R$=2 | $R$=3 |
| $k_{00}$ | 1 | 1 | 1 | 1 | 1 | 1 | 1 | 1 | 1 |
| $k_{10}$ | 0.2604 | 0.026176 | 0.0058193 | 0.30804 | 0.04206 | 0.0087489 | 0.21394 | 0.013422 | 0.0050028 |
| $k_{20}$ | 0.0061114 | -0.0043596 | 0.00011688 | 0.02363 | -0.0074972 | -0.00050118 | -0.0062246 | -0.0012725 | 0.00041255 |
| $k_{01}$ | 0.2604 | 1.2398 | 1.7158 | 0.30804 | 1.1778 | 1.5418 | 0.21394 | 1.3025 | 1.9056 |
| $k_{11}$ | 0.23313 | 0.23099 | -0.13122 | 0.21464 | 0.27828 | -0.051871 | 0.27005 | 0.16597 | -0.22366 |
| $k_{21}$ | 0.17577 | 0.035689 | -0.039898 | 0.25236 | 0.098709 | -0.053211 | 0.097826 | -0.020533 | -0.023228 |
| $k_{02}$ | 0.0061114 | 0.56294 | 3.0631 | 0.02363 | 0.71585 | 3.1003 | -0.0062246 | 0.41328 | 3.0122 |
| $k_{12}$ | 0.17577 | 0.56157 | 1.4007 | 0.25236 | 0.47013 | 1.3129 | 0.097826 | 0.69938 | 1.5084 |
| $k_{22}$ | -0.41853 | 0.0031656 | 0.13207 | -0.72156 | -0.08051 | 0.21606 | -0.10302 | 0.080058 | 0.050627 |

### 1.2.3.7. Stress distribution

Having calculated the membrane deflection, one can determine the stress distribution within the membrane. Using the Hooke's law (Equation A-10), definition of strain and taking into consideration the assumption of thin plates that there is no displacement in *z* axis, the stress components are expressed with following formulas:

$$\sigma_x(x,y,z) = -\frac{Ez}{(1-\nu^2)}\left(\frac{\partial^2 w(x,y)}{\partial x^2} + \nu\frac{\partial^2 w(x,y)}{\partial y^2}\right)$$
$$\sigma_y(x,y,z) = -\frac{Ez}{(1-\nu^2)}\left(\nu\frac{\partial^2 w(x,y)}{\partial x^2} + \frac{\partial^2 w(x,y)}{\partial y^2}\right) \qquad \textbf{Equation 1-40}$$
$$\sigma_{xy}(x,y,z) = -2Gz\frac{\partial^2 w(x,y)}{\partial x \partial y}$$

It can be seen that the maximal absolute value of stress is found on the membrane surfaces and stress is changing linearly in *z* axis. The middle plane is not stressed as a result of the thin plate theory assumption. In estimating the total stress within the material, one uses the von Mises stress which is a weighted mean of stress components:

$$\sigma_{vM} = \sqrt{\frac{1}{2}\left[(\sigma_x-\sigma_y)^2 + (\sigma_y-\sigma_z)^2 + (\sigma_z-\sigma_x)^2 + 6(\sigma_{xy}^2+\sigma_{yz}^2+\sigma_{zx}^2)\right]} \qquad \textbf{Equation 1-41}$$

Discarding null $\sigma_z$, $\sigma_{zx}$ and $\sigma_{yz}$ components, we get:

$$\sigma_{vM} = \sqrt{\frac{1}{2}\left[(\sigma_x-\sigma_y)^2 + \sigma_x^2 + \sigma_y^2 + 6\sigma_{xy}^2\right]} \qquad \textbf{Equation 1-42}$$

The von Mises stresses for various membrane ratios are presented in Figure 1-20 and Figure 1-21:

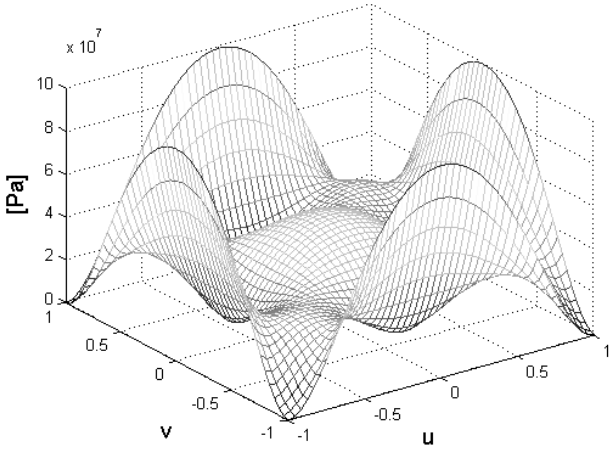


**Figure 1-20: Stress distribution for square membrane.**

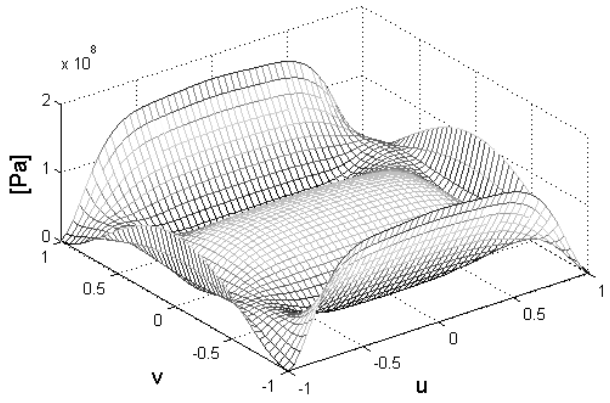


**Figure 1-21: Stress distribution for rectangular membrane with *R*=3.**

In square membrane the maximal stress is in the middle of edges and in the membrane centre is by about half time smaller. For the membrane with ratio higher than 1, the maximal stress is in the middle of the longer edge. In the membrane centre, the stress is also by about half time smaller but it is comparable with the maximal value of the stress for square membrane. This fact is very important in piezorezistive membrane-based sensors in which gauges are placed in the centre of the rectangular membrane instead of edges of square membrane.

Let us now consider an existence of the residual stress. Its value is simply added to the *x* and *y* components of the stress:

$$\sigma_x(x,y,z) = -\frac{Ez}{(1-\nu^2)}\left(\frac{\partial^2 w(x,y)}{\partial x^2} + \nu\frac{\partial^2 w(x,y)}{\partial y^2}\right) + \sigma_0$$

$$\sigma_y(x,y,z) = -\frac{E}{(1-\nu^2)}\left(\nu\frac{\partial^2 w(x,y)}{\partial x^2} + \frac{\partial^2 w(x,y)}{\partial y^2}\right) + \sigma_0$$

**Equation 1-43**

As it was mentioned earlier, the residual stress changes the membrane form on which the stress of the deflected membrane depends. To illustrate this, in Figure 1-22 we plotted the distribution of $\sigma_x$ along *x* axis resulting from square membrane bending (with conditions which allow obtaining the same maximal deflection) for various values of ratio $(\sigma_0 h)/D$ (which correspond with Figure 1-18):

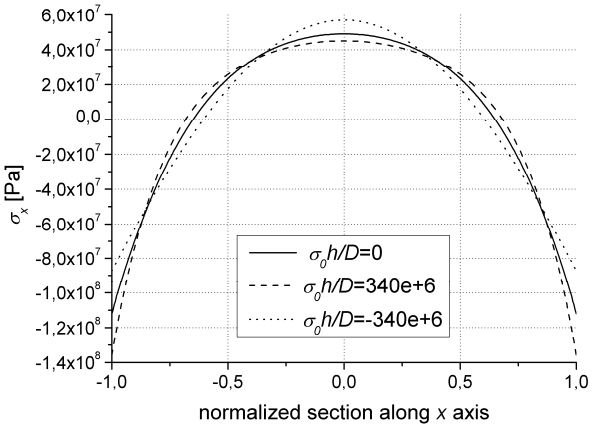


**Figure 1-22: $\sigma_x$ in square membrane for various values of residual stress.**

One can remark, that the difference reaches 16% in the centre and 22% on the edge. Even if the residual stress is relatively high in this case, the deviation can be significant for much smaller values of residual stress. The influence of residual stress increases with the membrane ratio. The same characteristic was plotted for the membrane with $R$=3 (Figure 1-23).

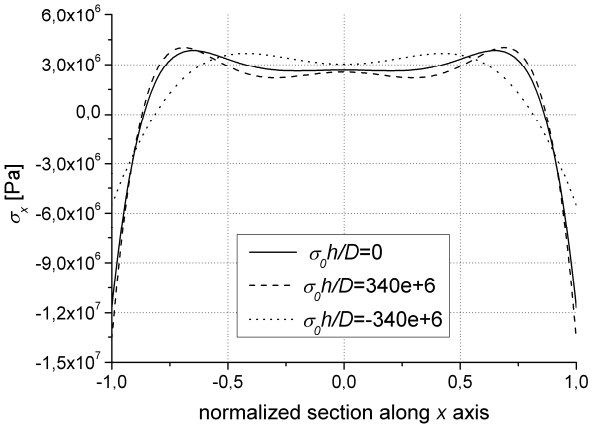


**Figure 1-23: $\sigma_x$ in rectangular membrane with $R$=3 for various values of residual stress.**

The difference is about 14% in the membrane centre. On its edge for tensile stress remains the same. However, in case of compression the deviation raises up to 47%. If we compare the stress along the shorter section (Figure 1-24), the difference reaches 20% in the centre and 30% on the edge. It has to be remarked that the curve for the membrane in tension is incorrect from the centre to the maximal value. It is caused by insufficient number of coefficients $k_{ij}$. However, the values in the centre and outside this range are correct what was verified with FEM simulation.

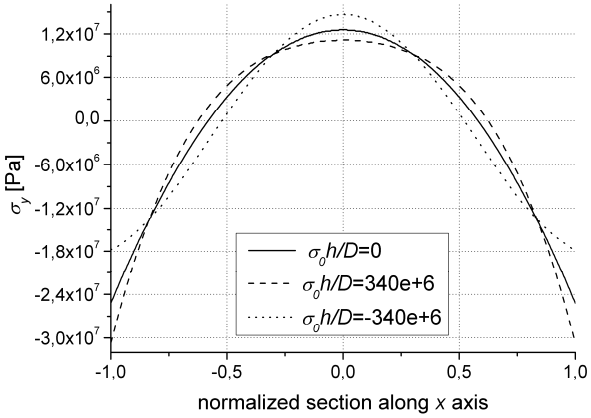


**Figure 1-24: $\sigma_y$ in rectangular membrane with $R$=3 for various values of residual stress.**

We can summarize, that the residual stress has significant influence on the stress value especially for high membrane ratios. Even if the residual stress is relatively small, the deviation might be significant and the use of the normalized coefficient $k_{ij}$ will produce a serious error.

## 1.2.4. Circular membrane

Remark: The theory, solution and behaviour of bent circular membrane are similar to the rectangular membranes. Thus, some points will be described shortly or omitted. For more information refer to the paragraph 1.2.3.

### 1.2.4.1. Membrane bending by laterally distributed load

In modelling of circular membrane of radius $R_0$, we use cylindrical coordinates with origin placed in the middle of the membrane (Figure 1-25):

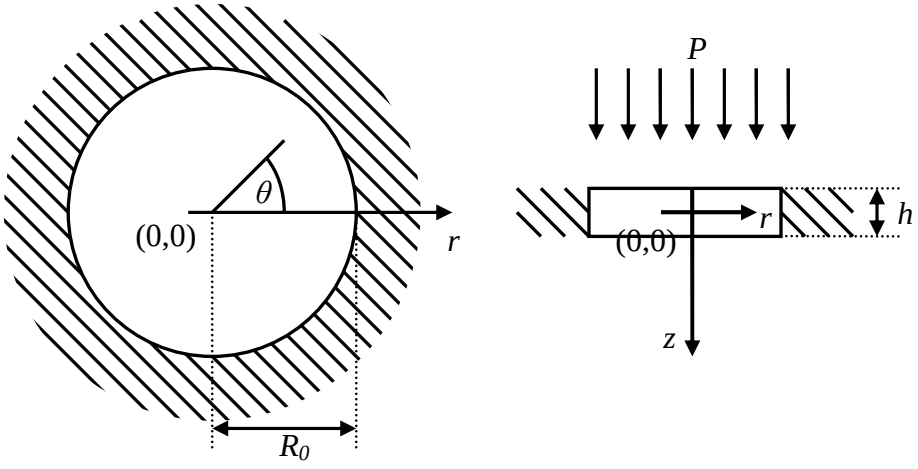


**Figure 1-25: Definition of geometric parameters. Top view is on the left and section on the right.**

The external pressure $P$ is distributed over the whole membrane. The equation of equilibrium of the loaded membrane for small deflections, assuming that the deflection $w$ does not depend on angle $\theta$, is as follows [48]:

$$D\left(\frac{\partial^4 w_1(r)}{\partial r^4}+\frac{2}{R_0}\frac{\partial^3 w_1(r)}{\partial r^3}-\frac{1}{R_0^2}\frac{\partial^2 w_1(r)}{\partial r^2}+\frac{1}{R_0^3}\frac{\partial w_1(r)}{\partial r}\right)=P \qquad \textbf{Equation 1-44}$$

It can be seen that Equation 1-44 is not dependent on material anisotropy. One assumes that anisotropy has influence only on maximal membrane deflection and in case of orthotropy Equation 1-44 takes the following form [49]:

$$\frac{3+\alpha}{4}D\left(\frac{\partial^4 w_1(r)}{\partial r^4}+\frac{2}{R_0}\frac{\partial^3 w_1(r)}{\partial r^3}-\frac{1}{R_0^2}\frac{\partial^2 w_1(r)}{\partial r^2}+\frac{1}{R_0^3}\frac{\partial w_1(r)}{\partial r}\right)=P \qquad \textbf{Equation 1-45}$$

or using Laplace operator in polar coordinates [50]:

$$\frac{3+\alpha}{4}D\Delta^2 w_1(r)=P \qquad \textbf{Equation 1-46}$$

### 1.2.4.2. Residual stress

The residual stress can be expressed as force acting transversally and uniformly on the membrane edge (Figure 1-26):

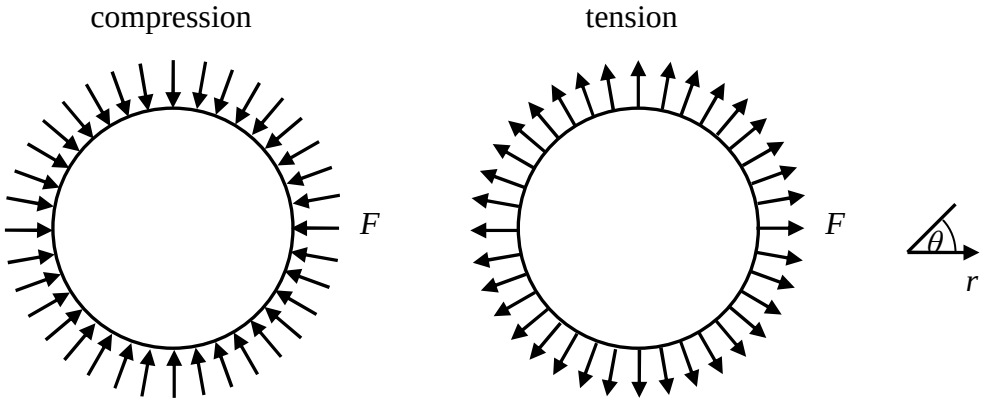


**Figure 1-26: Compressive and tensile residual stresses in circular membrane.**

Thus, the force is independent on angle and the term describing the residual stress is as follows [50]:

$$\sigma_0 h\left(\frac{\partial^2 w_1(r)}{\partial r^2}+\frac{1}{R_0}\frac{\partial w_1(r)}{\partial r}\right)=\sigma_0 h\Delta w_1(r) \qquad \textbf{Equation 1-47}$$

### 1.2.4.3. Initial deflection

For circular membrane, the same rules take effect as for rectangular membrane (see paragraph 1.2.3.3).

### 1.2.4.4. Classical equation of equilibrium

Combining the equation of membrane bending, the term describing the existence of residual stress and taking into account the initial deflection of the membrane, we get the final equation of equilibrium:

$$\frac{3+\alpha}{4} D\Delta^2 w_1(r) + \sigma_0 h \Delta w(r) = P \qquad \textbf{Equation 1-48}$$

To simplify the calculations, the deflection $w_1$ is replaced with the deflection $w$:

$$w_1 = w - w_0 \qquad \textbf{Equation 1-49}$$

Then, the equation of equilibrium has only one unknown $w$:

$$\frac{3+\alpha}{4} D\Delta^2 \left(w(r) - w_0(r)\right) + \sigma_0 h \Delta w(r) = P \qquad \textbf{Equation 1-50}$$

### 1.2.4.5. Solution for circular membrane

The solution of Equation 1-50 is similar as for rectangular membrane. The integration limit $\Omega$ is $[0, r]\times[0, 2\pi]$. We assume that the membrane is perfectly clamped on its edge. Thus, the boundary conditions are as follows [47]:

$$\begin{aligned} &w(R_0) = 0 \\ &\left.\frac{\partial w}{\partial z}\right|_{R_0} = 0 \end{aligned} \qquad \textbf{Equation 1-51}$$

Equation 1-50 can be expressed without dimension using the following transformation:

$$u = \frac{r}{R_0} \qquad \textbf{Equation 1-52}$$

Then, the integration limit $\Omega$ becomes non-dimensional $[0, 1]\times[0, 2\pi]$ and Equation 1-50 takes the following form:

$$\begin{aligned} &\frac{3+\alpha}{4}\frac{D}{R_0^4}\left(\frac{\partial^4\left(w-w_0\right)}{\partial u^4} + \frac{2}{u}\frac{\partial^3\left(w-w_0\right)}{\partial u^3} - \frac{1}{u^2}\frac{\partial^2\left(w-w_0\right)}{\partial u^2} + \frac{1}{u^3}\frac{\partial\left(w-w_0\right)}{\partial u}\right) + \\ &\quad + \frac{\sigma_0 h}{R_0^2}\left(\frac{\partial^2 w}{\partial u^2} + \frac{\partial w}{\partial u}\right) = P \end{aligned} \qquad \textbf{Equation 1-53}$$

We assume that the initial deflection $w_0$ can be expressed as an additional pressure $P_{w0}$:

$$P_{w0} = \frac{3+\alpha}{4}\frac{D}{R_0^4}\left(\frac{\partial^4 w_0}{\partial u^4} + \frac{2}{u}\frac{\partial^3 w_0}{\partial u^3} - \frac{1}{u^2}\frac{\partial^2 w_0}{\partial u^2} + \frac{1}{u^3}\frac{\partial w_0}{\partial u}\right) \qquad \textbf{Equation 1-54}$$

Then, Equation 1-53 is:

$$\frac{3+\alpha}{4}\frac{D}{R_0^4}\left(\frac{\partial^4 w}{\partial u^4} + \frac{2}{u}\frac{\partial^3 w}{\partial u^3} - \frac{1}{u^2}\frac{\partial^2 w}{\partial u^2} + \frac{1}{u^3}\frac{\partial w}{\partial u}\right) + \frac{\sigma_0 h}{R_0^2}\left(\frac{\partial^2 w}{\partial u^2} + \frac{\partial w}{\partial u}\right) = P + P_{w0} \qquad \textbf{Equation 1-55}$$

We predict the solution in cylindrical coordinates similar to this as for rectangular membrane:

$$w(u)=\sum_{i=0}^{n}K_i\varphi_i,\qquad \varphi_i=(1-u^2)^2u^{2i} \qquad \textbf{Equation 1-56}$$

limiting the number of terms to two ($n$=1). Then, the system of Galerkin equations reads:

$$\iint_{\Omega}\frac{3+\alpha}{4}\frac{D}{R_0^4}\left(\frac{\partial^4 w}{\partial u^4}+\frac{2}{u}\frac{\partial^3 w}{\partial u^3}-\frac{1}{u^2}\frac{\partial^2 w}{\partial u^2}+\frac{1}{u^3}\frac{\partial w}{\partial u}\right)\varphi_i u\,du\,d\theta+$$
$$+\iint_{\Omega}\frac{\sigma_0 h}{R_0^2}\left(\frac{\partial^2 w}{\partial u^2}+\frac{\partial w}{\partial u}\right)\varphi_i u\,du\,d\theta=\iint_{\Omega}(P+P_{w0})\varphi_i u\,du\,d\theta,\qquad i=0,1 \qquad \textbf{Equation 1-57}$$

Substituting Equation 1-56 into Equation 1-57 and calculating the integrals, we get the system of linear equations in matrix form (see APPENDIX C.2):

$$\frac{3+\alpha}{4}\frac{D}{R_0^4}\mathbf{A_1K}+\frac{\sigma_0 h}{R_0^2}\mathbf{A_2K}=(P+P_{w0})\mathbf{B} \qquad \textbf{Equation 1-58}$$

Coefficients of matrices $\mathbf{A_1}$, $\mathbf{A_2}$ and vector $\mathbf{B}$ are presented in APPENDIX D.2. The vector $\mathbf{K}$ is calculated as follows:

$$\mathbf{K}=\left(\frac{3+\alpha}{4}\frac{D}{R_0^4}\mathbf{A_1}+\frac{\sigma_0 h}{R_0^2}\mathbf{A_2}\right)^{-1}(P+P_{w0})\mathbf{B} \qquad \textbf{Equation 1-59}$$

The unknown pressure $P_{w0}$ is calculated using the normalized coefficients $k_i$ (see next paragraph) and solving Equation 1-54, which is reduced to the following form:

$$P_{w0}=\frac{3+\alpha}{4}\frac{D}{R_0^3}\mathbf{A_1KB}^{-1} \qquad \textbf{Equation 1-60}$$

### 1.2.4.6. Membrane deflection

The typical graphical representation of the membrane deflection described by Equation 1-56 is presented in Figure 1-27:

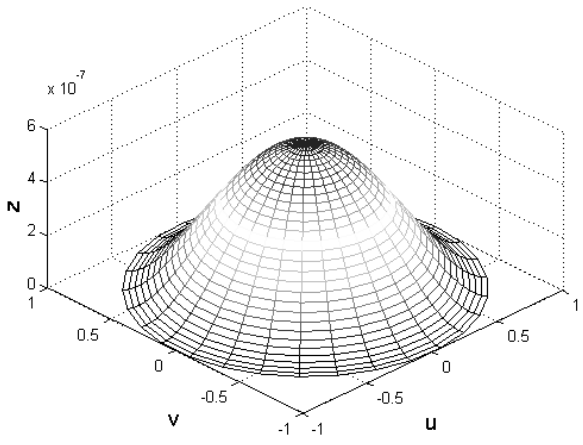


**Figure 1-27: Circular membrane topography.**

The maximal deflection is calculated from Equation 1-56 substituting $u$=0 (membrane centre):

$$w_{\max} = K_0 \qquad \textbf{Equation 1-61}$$

Then, we can transform Equation 1-56 into the form:

$$w(u) = w_{\max}\left(1-u^2\right)^2 \sum_{i=0}^{n} k_i u^{2i} \qquad \textbf{Equation 1-62}$$

where:

$$k_i = \frac{K_i}{K_0} \qquad \textbf{Equation 1-63}$$

The membrane behaviour is the same as for rectangular membrane. The maximal deflection is directly proportional to the applied pressure. Then the coefficients $k_i$ describe the normalized membrane form. Furthermore, calculations of these coefficients for the membrane without the residual stress showed that the coefficient $k_2$ is equal to 0 and the function of membrane deflection takes the following form (the same as in [51]):

$$w(u) = w_{\max}\left(1-u^2\right)^2 \qquad \textbf{Equation 1-64}$$

However, the residual stress changes the membrane form and the coefficient $k_2$ is necessary unless the stress is relatively small (see paragraph 1.2.3.6).

### 1.2.4.7. Stress distribution

In cylindrical coordinates, according to the Hooke's law, the stress can be expressed with the following formula:

$$\sigma(r,\theta,z) = -\frac{Ez}{(1-\nu^2)}\frac{\partial^2 w(r)}{\partial r^2} \qquad \textbf{Equation 1-65}$$

The stress is independent on the angle, similarly to the deflection. As the stress has only one component, the von Mises stress can be expressed as an absolute value of this component. The typical stress distribution is shown in Figure 1-28:

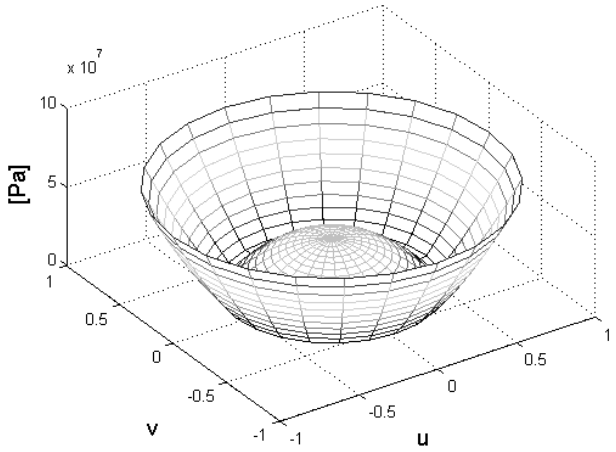


**Figure 1-28: Stress distribution in circular membrane.**

The maximal stress is at the membrane edge and in the centre is about half time smaller similarly than for square membrane.

The existence of residual stress is taken into consideration by adding it to the stress induced from membrane bending:

$$\sigma(r,\theta,z) = -\frac{Ez}{(1-\nu^2)}\frac{\partial^2 w(r)}{\partial r^2} + \sigma_0 \qquad \textbf{Equation 1-66}$$

It changes the membrane form and has similar influence on stress distribution as for square membrane (see paragraph 1.2.3.7).

## 1.2.5. Membrane buckling

Buckling is a phenomenon when the body undergoes the displacement transverse to the load. In case of a membrane, the buckling occurs due to compressive stress (Figure 1-29).

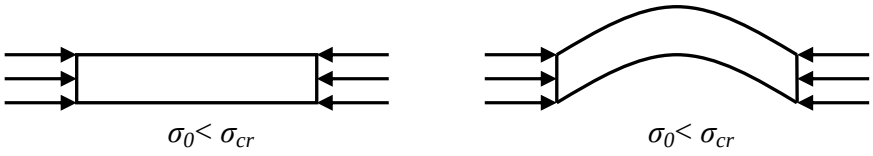


**Figure 1-29: Membrane buckling due to compressive residual stress.**

In investigation of membranes buckling, the energy method can be used [45]. If the work done by compressive forces is smaller then the strain energy of membrane bending for any form of lateral bending, the flat form of the membrane is stable. If this work becomes larger, the flat form is no more stable and the membrane will buckle producing an initial deflection. Equation 1-67 allows the calculation of critical load $\sigma_{cr}$:

$$-\frac{1}{2}\iint_s \sigma_{cr} h \Delta w(x,y) = \frac{1}{2}\iint_s D h^3 \Delta\Delta w(x,y) \qquad \textbf{Equation 1-67}$$

According to [70], the thin plates theory for small deflections cannot be used in calculation of the deflection of buckled membranes. Thus, we will only focus shortly on the behaviour of buckled membranes and on finding the critical load which defines the model limitation.

The behaviour of the buckled membrane can be investigated using the theory for large deflections. The pressure response remains the same with the exception of the switching effect. The buckled membrane has two stable positions: -*w* and *w*. The initial membrane position depends on structure asymmetry. The applied pressure changes the membrane strain energy [70]. When the pressure exceeds the critical value, only one stable position exists. Because of this fact, when the critical pressure is applied in opposite direction than the membrane deflection, it jumps to the stable position (Figure 1-30). This phenomenon, used e.g. in switches [71], may be used in verifying if the membrane is buckled.

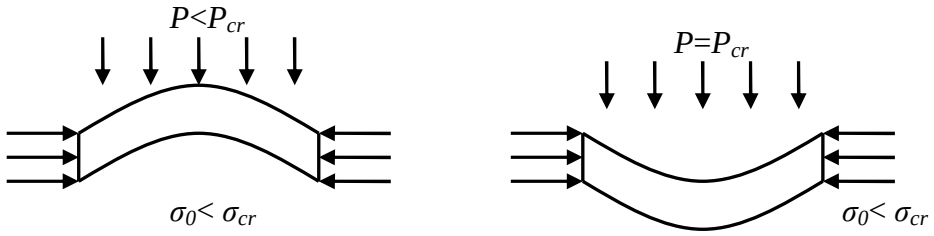


**Figure 1-30: Switching effect of buckled membrane.**

## 1.2.6. Reduced model

The classical model is not convenient in use. It needs calculation of elements in matrices. Furthermore, it is highly dependent on function describing the membrane form, which should contain appropriate number of terms. Then, this number determines the size of matrices. Finally, each change of resulting function needs the recalculation of matrix coefficients. Thus, it is desirable to use some other simpler model. Many works has been done in this field, especially during investigation of residual stress using the bulge test technique [74][75]. The idea is to use the membrane property that its deflection depends linearly on uniformly applied pressure. If we analyze Equation 1-17, one can see that the term describing the residual stress is similar to the one describing the membrane rigidity and should also be linear. Then, the relation maximal deflection versus applied pressure can be expressed as follows [76]:

$$C_1 \frac{D}{b^4} w_{1\_\max} + C_2 \frac{\sigma_0 h}{b^2} w_{1\_\max} = P \qquad \textbf{Equation 1-68}$$

where $w_{1\_max}$ is the maximal change of membrane deflection due to applied pressure, $C_1$ and $C_2$ are coefficients of proportionality. Both coefficients are dependent on membrane ratio $R$ and the first one also on coefficient of anisotropy. The similar equation for circular membrane can be written:

$$\frac{3+\alpha}{4} C_1 \frac{D}{R_0^4} w_{1\_\max} + C_2 \frac{\sigma_0 h}{R_0^2} w_{1\_\max} = P \qquad \textbf{Equation 1-69}$$

where in this case, the coefficients of proportionality are constants. In calculation of coefficient C1 and C2, the classical model is used, so the precision depends on the function of membrane deflection. We have performed the calculations using the function from Equation 1-31 and Equation 1-56 for rectangular and circular membrane, respectively. The results are presented in Table 1-3:

**Table 1-3: Values of coefficient $C_1$ and $C_2$.**

| Coefficient | | $C_1$ | | | $C_2$ |
|---|---|---|---|---|---|
| Material | | Isotropic | Silicon <100> | Silicon <110> | - |
| $b/a$ | 1 | 792.449 | 866.36 | 728.75 | 15.35 |
| | 1.5 | 455.894 | 488.32 | 427.76 | 11.42 |
| | 2 | 394.552 | 410.58 | 380.48 | 10.34 |
| | 2.5 | 382.591 | 389.44 | 376.51 | 9.88 |
| | 3 | 380.325 | 381.98 | 378.35 | 9.55 |
| Circular | | 64 | | | 4.45 |

Values correspond to those found in the literature for isotropic square membrane [77], rectangular membranes [78] and circular membranes [51]. Going further, we can simply take into the consideration the initial deflection of the membrane $w_{0\_max}$:

$$C_1 \frac{D}{b^4} w_{1\_\max} + C_2 \frac{\sigma_0 h}{b^2} \left( w_{1\_\max} + w_{0\_\max} \right) = P \qquad \textbf{Equation 1-70}$$

Then, one can introduce the total deflection in the centre of the membrane $w_{max}$:

$$C_1 \frac{D}{b^4} w_{\max} + C_2 \frac{\sigma_0 h}{b^2} w_{\max} = P + P_{w0\_\max} \qquad \textbf{Equation 1-71}$$

where $P_{w0\_max}$ is the pressure producing the maximal initial deflection and is calculated as follows:

$$P_{w0\_\max} = C_1 \frac{D}{b^4} w_{0\_\max} \qquad \textbf{Equation 1-72}$$

The same procedure can be applied to the circular membrane, which yields:

$$\frac{3+\alpha}{4}C_1\frac{D}{R_0^4}w_{\max}+C_2\frac{\sigma_0 h}{R_0^2}w_{\max}=P+P_{w0\_\max} \quad \textbf{Equation 1-73}$$

$$P_{w0\_\max}=\frac{3+\alpha}{4}C_1\frac{D}{R_0^4}w_{\max} \quad \textbf{Equation 1-74}$$

It has to be remarked that the reduced model operates only on the maximal deflection. Thus, it is not possible to obtain the membrane form and normalized membrane form has to be used. As it was mentioned earlier, the residual stress can significantly affect the results (e.g. stress calculation), so the reduced model can be used for relatively small residual stress. In other cases, it should be verified with the classical model.

### 1.2.6.1. Membrane buckling

The reduced model can be also used in finding the critical load, which causes membrane buckling. If we go back to Equation 1-71, its left-hand side has to be always positive. Thus, the buckling occurs when this part of equation is equal to zero. The critical residual stress is calculated as follows:

$$\sigma_{cr}=-\frac{C_1}{C_2}\frac{D}{hb^2} \quad \textbf{Equation 1-75}$$

Calculating the critical load for isotropic square membrane we get similar value as in [72][73]. For circular membrane the critical residual stress is equal to:

$$\sigma_{cr}=-14.38\frac{3+\alpha}{4}\frac{D}{hR_0^4} \quad \textbf{Equation 1-76}$$

and is similar to the formula obtained in [45][79].

### 1.2.6.2. Model normalization

To simplify the further notation, we will introduce a membrane constant $k_{mem}$ (equivalent of spring constant) given by:

$$k_{mem}=C_1\frac{D}{b^4}+C_2\frac{\sigma_0 h}{b^2} \quad \textbf{Equation 1-77}$$

for rectangular membrane and:

$$k_{mem}=\frac{3+\alpha}{4}C_1\frac{D}{R_0^4}+C_2\frac{\sigma_0 h}{R_0^2} \quad \textbf{Equation 1-78}$$

for circular membrane. We introduce also a pressure $P_h$ given by:

$$P_h=P+P_{w0\_\max} \quad \textbf{Equation 1-79}$$

Then, the normalized equation in reduced model is as follows:

$$k_{mem} w_{\max} = P_h \qquad \textbf{Equation 1-80}$$

## 1.2.7. Classical vs. reduced model

To prove that the reduced model gives accurate results, a comparison with the classical model for various conditions was performed. Figure 1-31 presents the characteristics $w_{max}$=f($P$) for a silicon square membrane without and with compressive and tensile residual stress:

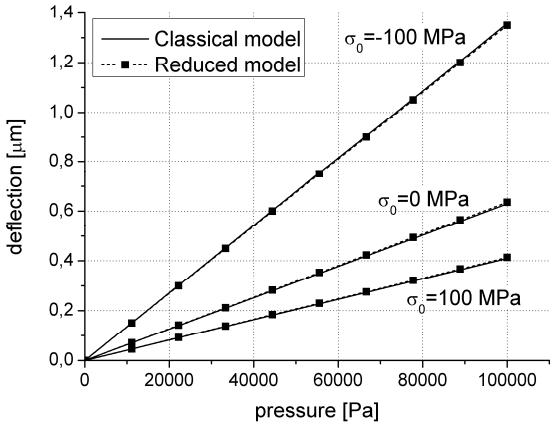


**Figure 1-31: Comparison between classical and reduced model.**

The differences are negligible and are caused by numerical rounding. Similar results can be obtained for other membrane forms and material orientations. Thus, the approximation of membrane equation by linear functions is a good alternative especially when only maximal deflection is needed.

# 1.3. Electrostatic actuation

## 1.3.1. Rectangular membrane

### 1.3.1.1. Classical equation of equilibrium

Now, we will consider a rectangular membrane with dimensions of length *a*, width *b* (*b*≥*a*) and thickness *h*, placed in Cartesian coordinates system with the origin (0,0) in the middle of the membrane and an parallel electrode of gap spacing *d* as shown in Figure 1-32:

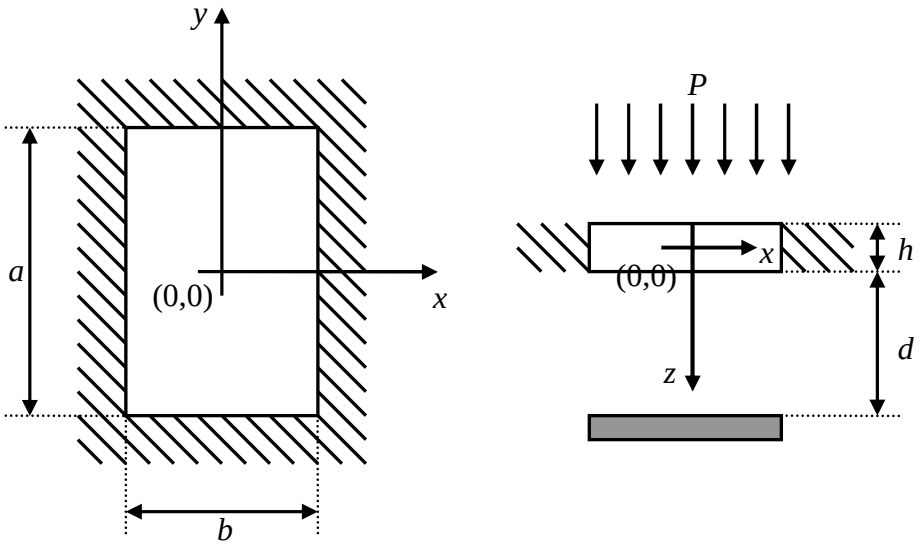


**Figure 1-32: Definition of geometric parameters. Top view is on the left and section on the right.**

The external pressure *P* is distributed over the whole membrane and the dimensions of the bottom electrode are the same as for the membrane. When the voltage *V* is applied between the electrodes, the membrane deflects due to external pressure and electrostatic pressure. Then, using Equation 1-19 and definition of electrostatic pressure [80], the equation of equilibrium takes the following form:

$$D\Delta\Delta\big(w(x,y)-w_0(x,y)\big)+\sigma_0 h\Delta w(x,y)=P+\varepsilon\frac{V^2}{2\big(d-w(x,y)\big)^2} \qquad \textbf{Equation 1-81}$$

It can be seen, that the electrostatic pressure depends on the position of the membrane. It is uniformly distributed only when the membrane is flat. When, the membrane is deformed in the direction of the electrode, the electrostatic pressure is the highest in its centre and the smallest on its edges.

### 1.3.1.2. Solution

The integration limit Ω is [-*a*/2, *a*/2]×[-*b*/2, *b*/2]. We assume that the membrane is perfectly clamped on its edges. Thus, the boundary conditions are as follows [47]:

$$w(\partial\Omega) = 0$$
$$\left.\frac{\partial w}{\partial z}\right|_{\partial\Omega} = 0 \qquad \textbf{Equation 1-82}$$

where dΩ are points on membrane edges. Equation 1-81 can be expressed without dimension, using the following transformation:

$$u = \frac{2x}{a}$$
$$v = \frac{2y}{b} \qquad \textbf{Equation 1-83}$$
$$R = \frac{b}{a}$$

The integration limit Ω becomes then non-dimensional [-1, 1]×[-1, 1] and Equation 1-81 takes the following form:

$$D\frac{16}{a^2b^2}\left(R^2\frac{\partial^4(w-w_0)}{\partial u^4}+2\alpha\frac{\partial^4(w-w_0)}{\partial u^2\partial v^2}+\frac{1}{R^2}\frac{\partial^4(w-w_0)}{\partial v^4}\right)+$$
$$+\sigma_0 h\frac{4}{ab}\left(R\frac{\partial^2 w}{\partial x^2}+\frac{1}{R}\frac{\partial^2 w}{\partial y^2}\right)=P+\varepsilon\frac{V^2}{2(d-w)^2} \qquad \textbf{Equation 1-84}$$

Replacement of the initial deflection $w_0$ with the pressure $P_{w0}$ (Equation 1-23) yields:

$$D\frac{16}{a^2b^2}\left(R^2\frac{\partial^4 w}{\partial u^4}+2\alpha\frac{\partial^4 w}{\partial u^2\partial v^2}+\frac{1}{R^2}\frac{\partial^4 w}{\partial v^4}\right)+\sigma_0 h\frac{4}{ab}\left(R\frac{\partial^2 w}{\partial u^2}+\frac{1}{R}\frac{\partial^2 w}{\partial v^2}\right)=$$
$$=P+P_{w0}+\varepsilon\frac{V^2}{2(d-w)^2} \qquad \textbf{Equation 1-85}$$

#### *Method I*

We predict the solution with the function described by Equation 1-31. Then, the system of Galerkin equations can be written as follows:

$$\iint_\Omega D\frac{16}{a^2b^2}\left(R^2\frac{\partial^4 w}{\partial u^4}+2\alpha\frac{\partial^4 w}{\partial u^2\partial v^2}+\frac{1}{R^2}\frac{\partial^4 w}{\partial v^4}\right)\varphi_{ij}\,du dv+$$
$$+\iint_\Omega \sigma_0 h\frac{4}{ab}\left(R\frac{\partial^2 w}{\partial u^2}+\frac{1}{R}\frac{\partial^2 w}{\partial v^2}\right)\varphi_{ij}\,du dv \qquad \textbf{Equation 1-86}$$
$$=\iint_\Omega (P+P_{w0})\varphi_{ij}\,du dv+\iint_\Omega \varepsilon\frac{V^2}{2(d-w)^2}\varphi_{ij}\,du dv,\qquad i,j=0,1,2$$

Substituting Equation 1-31 into Equation 1-86 and calculating the integrals, we get the system of linear equations in matrix form (see APPENDIX C.1):

$$D\frac{16}{a^2b^2}\mathbf{A_1K}+\sigma_0 h\frac{4}{ab}\mathbf{A_2K}=\left(P+P_{w0}\right)\mathbf{B}+\varepsilon\frac{V^2}{2}\mathbf{B_1} \qquad \textbf{Equation 1-87}$$

Coefficients of matrices $\mathbf{A_1}$, $\mathbf{A_2}$ and vector $\mathbf{B}$ are the same as in solution presented in paragraph 1.2.3.5 and are presented in APPENDIX D.1. The vector matrix $\mathbf{K}$ is calculated as follows:

$$\mathbf{K}=\left(D\frac{16}{a^2b^2}\mathbf{A_1}+\sigma_0 h\frac{4}{ab}\mathbf{A_2}\right)^{-1}\left(\left(P+P_{w0}\right)\mathbf{B}+\varepsilon\frac{V^2}{2}\mathbf{B_1}\right) \qquad \textbf{Equation 1-88}$$

As the initial deflection is not an effect of electrostatic force, the pressure $P_{w0}$ can be calculated from Equation 1-36 using the normalized coefficients $k_{ij}$ from Table 1-2 and the coefficient $K_{00}$ (equal to $w_0$).

The last unknown is the matrix $\mathbf{B_1}$ which consist of following elements:

$$\iint_{\Omega}\frac{1}{\left(d-w\right)^2}\varphi_{i,j}\,du\,dv \qquad \textbf{Equation 1-89}$$

As one can see, this integral is dependent on membrane deflection (it partially represents the electrostatic pressure). Thus, to solve this inconvenience, the solution has to be iterative. In the first iteration the membrane is deformed due to external pressure and/or initial deflection ($\mathbf{K}(1)$), the electrostatic pressure is calculated by integration of Equation 1-89 and new membrane position is obtained ($\mathbf{K}(n+1)$), which is the new starting position. This procedure is repeated until the solution converges. The procedure of calculation is shown in Figure 1-33:

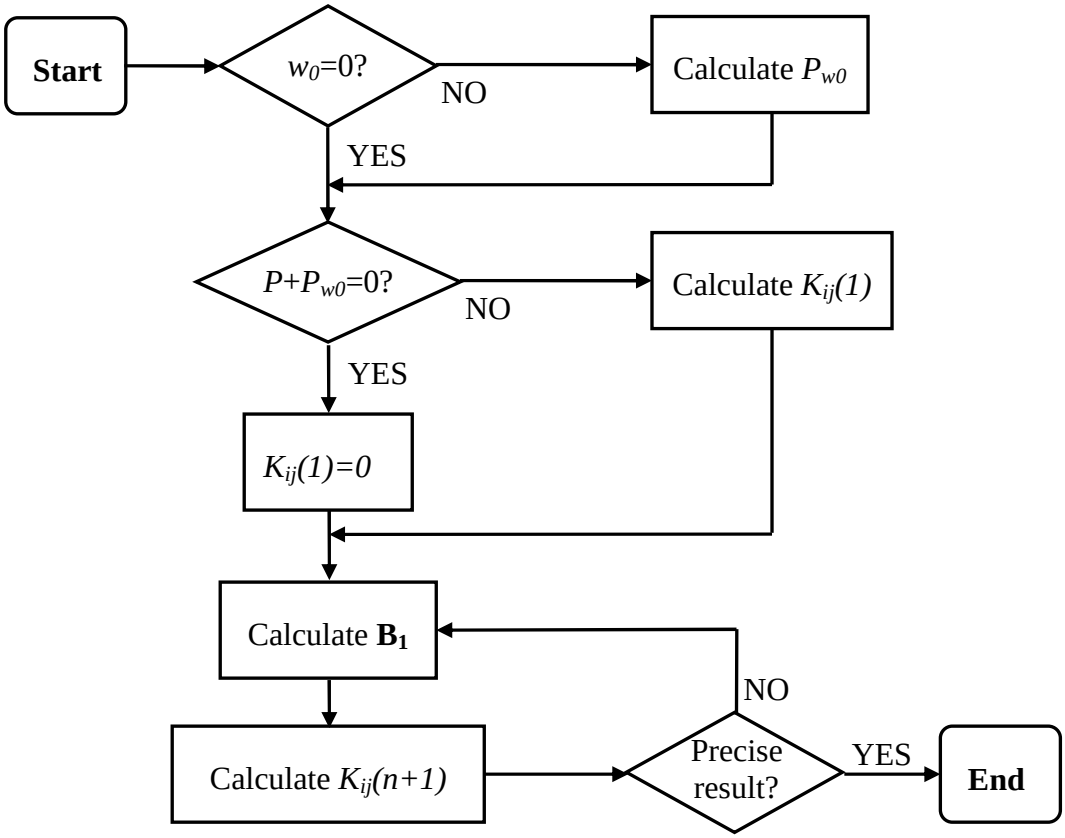


**Figure 1-33: Procedure of calculation for electrostatic pressure.**

The most inconvenient step in this procedure is the calculation of matrix $\mathbf{B_1}$. There is no analytical solution for integral from Equation 1-89, thus it has to be calculated numerically. As the membrane function is the complex polynomial function, it takes a lot of time. Therefore, an alternative solution method may be useful.

### *Method II*

The right-hand side of Equation 1-85 has inconvenient denominator. To simplify the calculation of this equation, the denominator can be removed (what is usually used e.g. in FEM method) by transforming the equation into the following form:

$$D\frac{16}{a^2b^2}\left(R^2\frac{\partial^4 w}{\partial u^4}+2\alpha\frac{\partial^4 w}{\partial u^2\partial v^2}+\frac{1}{R^2}\frac{\partial^4 w}{\partial v^4}\right)(d-w)^2+ \\ +\sigma_0 h\frac{4}{ab}\left(R\frac{\partial^2 w}{\partial u^2}+\frac{1}{R}\frac{\partial^2 w}{\partial v^2}\right)(d-w)^2=(P+P_{w0})(d-w)^2+\varepsilon\frac{V^2}{2} \quad \textbf{Equation 1-90}$$

Then the solution is similar as in first method, which yields to Equation 1-88. Unfortunately, due to transformation of equation of equilibrium, the matrices $\mathbf{A_1}$, $\mathbf{A_2}$ and vector $\mathbf{B}$ have to be recalculated. Furthermore, each of their element contains an integral of deflection function in square what makes the calculations difficult and analytical solution is difficult to derive.

### 1.3.1.3. Membrane deflection

Firstly, we will analyze the influence of applied voltage on maximal membrane deflection without external pressure. Figure 1-34 shows exemplary characteristics for various membrane ratios:

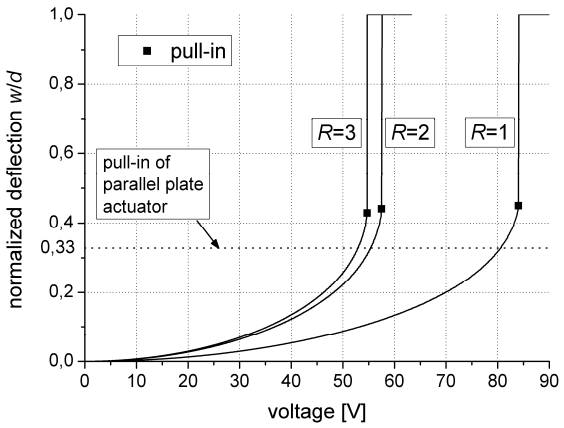


**Figure 1-34: Membrane deflection versus applied voltage.**

It can be seen that the pull-in effect occurs for much larger deflection than for parallel plate actuator (see paragraph 1.1). Square membrane is unstable for normalized deflections larger than 0.46. For rectangular membrane it slightly drops and for $R$=3 is 0.44. As the membrane deflection increases with membrane ratio, the pull-in voltage consequently lowers. One can also see the stabilization of this voltage.

As it was mentioned earlier, the distribution of electrostatic pressure over the deflected membrane is not uniform. Thus, the applied voltage should have an effect on the membrane form. Figure 1-35 presents the forms of square membrane for various voltages:

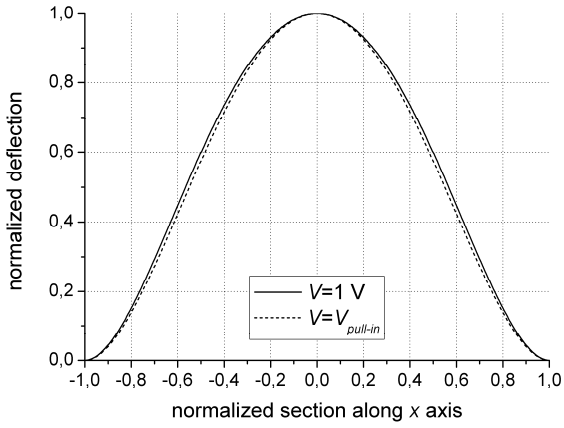


**Figure 1-35: Square membrane forms for various voltages.**

The membrane form changes with applied voltage, however the difference is not relatively large and can be neglected, thus one can use the normalized coefficients $k_{ij}$ from table Table 1-2 to describe the membrane form. When the membrane ratio increases, the influence of the voltage is more significant, especially along the longer dimension. Figure 1-36 shows membrane forms for ratio $R$=3:

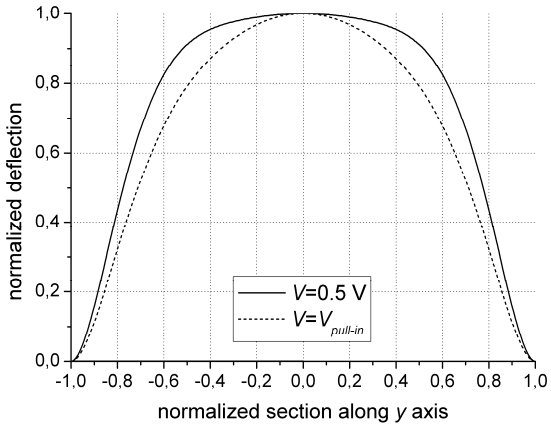


**Figure 1-36: Membrane forms for *R*=3 and various voltages.**

Comparing the forms along the longer section, one can see that the difference cannot be neglected and normalized coefficients $k_{ij}$ should not be used.

Let us now take into consideration the external pressure. The membrane is then closer to the bottom electrode and the electrostatic force is larger. Thus, the operational range shortens what is shown in Figure 1-37:

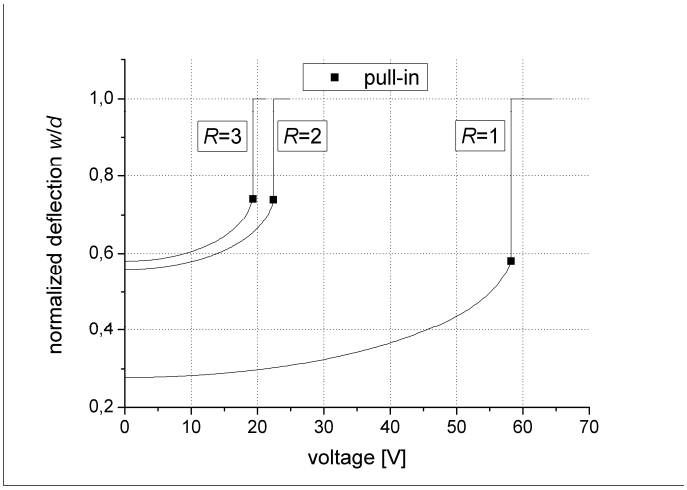


**Figure 1-37: Membrane deflection versus applied voltage with applied external pressure (atmospheric).**

As the range of voltages that can be applied is smaller, the influence of electrostatic force on membrane form is reduced. However, it is still significant what is shown in Figure 1-38:

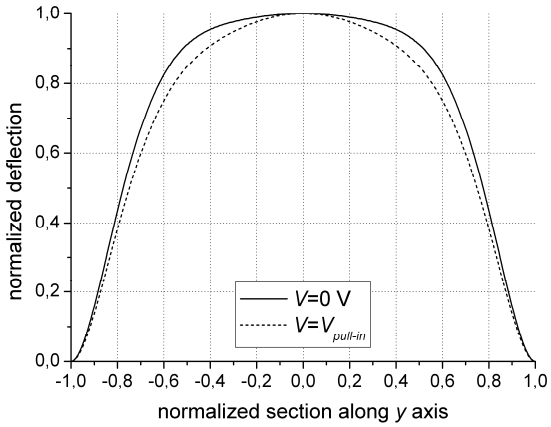


**Figure 1-38: Membrane forms for *R*=3, external pressure and various voltages.**

### 1.3.1.4. Stress distribution

In the previous paragraph, it was shown that the electrostatic pressure has a significant influence on the membrane form. Thus, the stress distribution within the membrane will be also different than for uniform pressure. Following comparisons show the difference between stress distributions calculated for normalized (using coefficients from Table 1-2) and real form of the membrane for pull-in voltage. In the case of a square membrane, the stress is overestimated by 11% on the edge and underestimated by 9% in the centre as shown in Figure 1-39. For the membrane with ratio *R*=3, the difference reaches 46% on the edge and -12% in the centre. Furthermore, the shape of the stress curve is no longer the same (Figure 1-40)

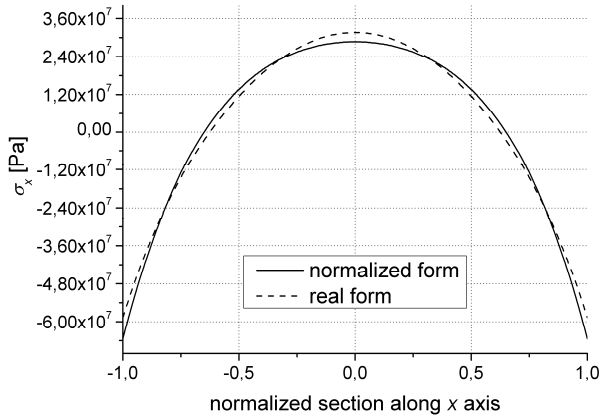


**Figure 1-39: $\sigma_x$ in square membrane for pull-in voltage.**

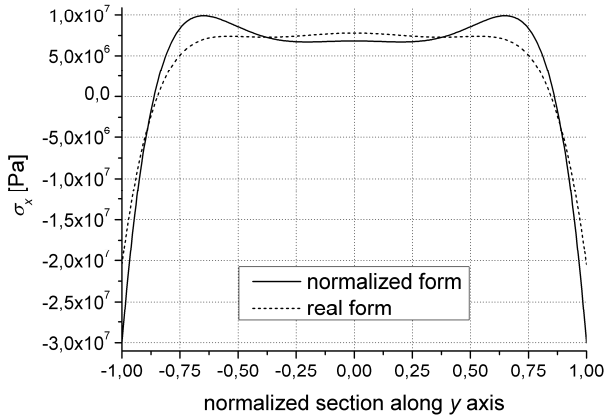


**Figure 1-40: $\sigma_y$ in rectangular membrane with $R$=3 for pull-in voltage.**

Summarizing, the function describing the membrane form with exact coefficients $k_{ij}$ has crucial influence on calculation of stress within the membrane actuated electrostatically. The use of normalized coefficient leads to serious errors, especially for high membrane ratios.

### 1.3.1.5. Capacitance

The electrostatic actuator has another important parameter, which is the capacitance. By definition, the capacitance of a parallel plate capacitor is expressed with the following formula:

$$C = \varepsilon \frac{S}{d} \qquad \textbf{Equation 1-91}$$

where $S$ is a surface of the plate, $d$ is a distance between the plates and $\varepsilon$ is the permittivity of the space between the plates. In case of membrane-based actuator, the distance varies and Equation 1-91 takes the following form:

$$C = \varepsilon \iint_S \frac{1}{\left(d - w(x,y)\right)} \partial x \partial y \qquad \textbf{Equation 1-92}$$

Usually, the bottom electrode is insulated by a thin oxide layer. When its thickness is much smaller than the distance between the electrodes, the total capacitance can be approximated by Equation 1-92. The typical function of the capacitance versus the applied voltage is shown in Figure 1-41:

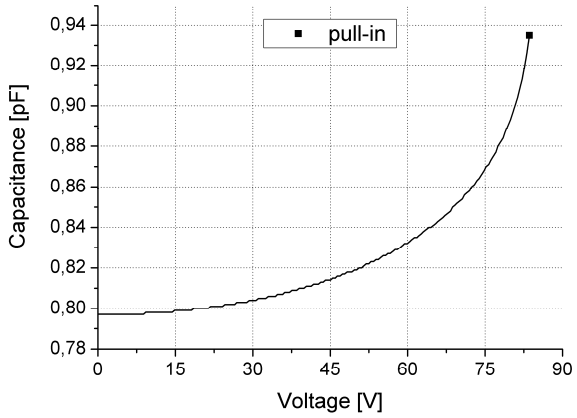


**Figure 1-41: Typical capacitance function versus applied voltage for square membrane.**

The similar function can be plotted for other membrane ratios. It is worth to remark that the capacitance is almost independent from function describing the membrane form. Several simulations have shown that the use of normalized coefficient $k_{ij}$ produce the difference smaller than 1% in the worst case. Thus, if only capacitance has to be calculated, one can use the normalized membrane form without precision loss.

## 1.3.2. Circular membrane

### 1.3.2.1. Classical equation of equilibrium and its solution

In case of electrostatic actuation, the equation of equilibrium of circular membrane (Equation 1-50) takes the following form:

$$\frac{3+\alpha}{4} D\Delta^2\left(w(r)-w_0(r)\right)+\sigma_0 h\Delta w(r)=P+\varepsilon\frac{V^2}{2\left(d-w(r)\right)^2} \qquad \textbf{Equation 1-93}$$

The integration limit Ω is $[0, r]\times[0, 2\pi]$. We assume that the membrane is perfectly clamped on its edge. Thus, the boundary conditions are as follows [47]:

$$w(R_0)=0$$
$$\left.\frac{\partial w}{\partial z}\right|_{R_0}=0 \qquad \textbf{Equation 1-94}$$

Equation 1-93 can be expressed without dimension using the following transformation:

$$u=\frac{r}{R_0} \qquad \textbf{Equation 1-95}$$

Then, the integration limit Ω becomes non-dimensional $[0, 1]\times[0, 2\pi]$ and Equation 1-93 takes the following form:

$$\frac{3+\alpha}{4}\frac{D}{R_0^4}\left(\frac{\partial^4(w-w_0)}{\partial u^4}+\frac{2}{u}\frac{\partial^3(w-w_0)}{\partial u^3}-\frac{1}{u^2}\frac{\partial^2(w-w_0)}{\partial u^2}+\frac{1}{u^3}\frac{\partial(w-w_0)}{\partial u}\right)+ \\ +\frac{\sigma_0 h}{R_0^2}\left(\frac{\partial^2 w}{\partial u^2}+\frac{\partial w}{\partial u}\right)=P+\varepsilon\frac{V^2}{2(d-w)^2} \qquad \textbf{Equation 1-96}$$

Replacement of the initial deflection $w_0$ with the pressure $P_{w0}$ (Equation 1-54) yields:

$$\frac{3+\alpha}{4}\frac{D}{R_0^4}\left(\frac{\partial^4 w}{\partial u^4}+\frac{2}{u}\frac{\partial^3 w}{\partial u^3}-\frac{1}{u^2}\frac{\partial^2 w}{\partial u^2}+\frac{1}{u^3}\frac{\partial w}{\partial u}\right)+ \\ +\frac{\sigma_0 h}{R_0^2}\left(\frac{\partial^2 w}{\partial u^2}+\frac{\partial w}{\partial u}\right)=P+P_{w0}+\varepsilon\frac{V^2}{2(d-w)^2} \qquad \textbf{Equation 1-97}$$

We predict the solution with the function described by Equation 1-56. Then, the system of Galerkin equations reads:

$$\iint_\Omega \frac{3+\alpha}{4}\frac{D}{R_0^4}\left(\frac{\partial^4 w}{\partial u^4}+\frac{2}{u}\frac{\partial^3 w}{\partial u^3}-\frac{1}{u^2}\frac{\partial^2 w}{\partial u^2}+\frac{1}{u^3}\frac{\partial w}{\partial u}\right)u\varphi_i u\,du\,d\theta+ \\ +\iint_\Omega \frac{\sigma_0 h}{R_0^2}\left(\frac{\partial^2 w}{\partial u^2}+\frac{\partial w}{\partial u}\right)\varphi_i u\,du\,d\theta= \qquad \textbf{Equation 1-98} \\ =\iint_\Omega (P+P_{w0})\varphi_i u\,du\,d\theta+\iint_\Omega \varepsilon\frac{V^2}{2(d-w)^2}\varphi_i u\,du\,d\theta,\quad i=0,1$$

Substituting Equation 1-56 into Equation 1-98 and calculating the integrals, we get the system of linear equations in matrix form (see APPENDIX C.2):

$$\frac{3+\alpha}{4}\frac{D}{R_0^4}\mathbf{A_1}\mathbf{K}+\frac{\sigma_0 h}{R_0^2}\mathbf{A_2}\mathbf{K}=(P+P_{w0})\mathbf{B}+\varepsilon\frac{V^2}{2}\mathbf{B_1} \qquad \textbf{Equation 1-99}$$

Coefficients of matrices $\mathbf{A_1}$, $\mathbf{A_2}$ and vectors $\mathbf{B}$, $\mathbf{B_1}$ are presented in APPENDIX D.2. The matrix $\mathbf{K}$ is calculated as follows:

$$\mathbf{K}=\left(\frac{3+\alpha}{4}\frac{D}{R_0^4}\mathbf{A_1}+\frac{\sigma_0 h}{R_0^2}\mathbf{A_2}\right)^{-1}\left((P+P_{w0})\mathbf{B}+\varepsilon\frac{V^2}{2}\mathbf{B_1}\right) \qquad \textbf{Equation 1-100}$$

The unknown pressure $P_{w0}$ is calculated using the normalized coefficients $k_i$ (see next paragraph) and solving Equation 1-54, which is reduced to the following form:

$$P_{w0}=\frac{3+\alpha}{4}\frac{D}{R_0^4}\mathbf{A_1}\mathbf{K}\mathbf{B}^{-1} \qquad \textbf{Equation 1-101}$$

As the initial deflection is not an effect of electrostatic force, the pressure $P_{w0}$ can be calculated from Equation 1-54 using the normalized function of membrane deflection from Equation 1-64 and the coefficient $K_{00}$ (equal to $w_0$).

The procedure of calculation of the matrix **K** is the same as shown in Figure 1-33 and the unknown matrix $\mathbf{B_1}$ has to be also calculated numerically. However, it takes less time than in case of rectangular membrane due to simpler function of membrane form.

#### 1.3.2.2. Membrane deflection, stress distribution and capacitance

The influence of electrostatic pressure on behaviour of circular membrane is similar as for square membrane. Thus, we will only define the capacitance in cylindrical coordinates. For more information refer to paragraphs 1.3.1.3-1.3.1.5.

The capacitance for electrostatic actuator based on circular membrane in cylindrical coordinates is given with Equation 1-102:

$$C = \varepsilon \iint_S \frac{r}{(d - w(r))} \partial r \partial \theta \qquad \textbf{Equation 1-102}$$

### 1.3.3. Membrane pull-in

Very often, information about the stable range (up to pull-in point) of operation is needed. There is no direct method for calculating the pull-in voltage and deflection using classical model. Thus, one has to perform an iterative procedure in which the starting point (V) is set and the convergence of solution is examined to determine the direction of voltage sweeping (Figure 1-42). The key is to choose the proper starting point and to use a good algorithm to calculate the new point. However, to obtain desired precision, several iterations has to be performed which is usually very time consuming, especially for rectangular membranes.

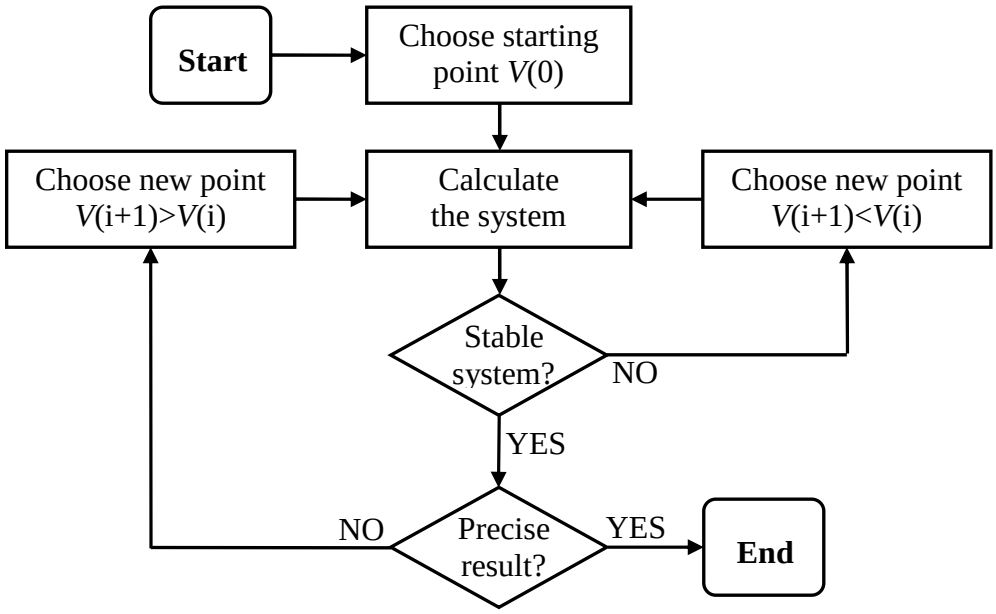


**Figure 1-42: Procedure of pull-in point calculation.**

## 1.3.4. Electrode modelling

In previous paragraphs, we have assumed that the bottom electrode has the same dimensions as the membrane and is flat. Very often, when the bottom electrode is deposited on the substrate (e.g. electrode made of aluminium), its dimensions are smaller than the membrane. Furthermore, the electrode could take other forms in order to increase the electrostatic force. Both these features will be analyzed in terms of modelling using classical model.

Let us consider the actuator from Figure 1-32 but now, the bottom electrode has dimensions of length $a_e$ and width $b_e$ and is placed under the membrane as shown in Figure 1-43:

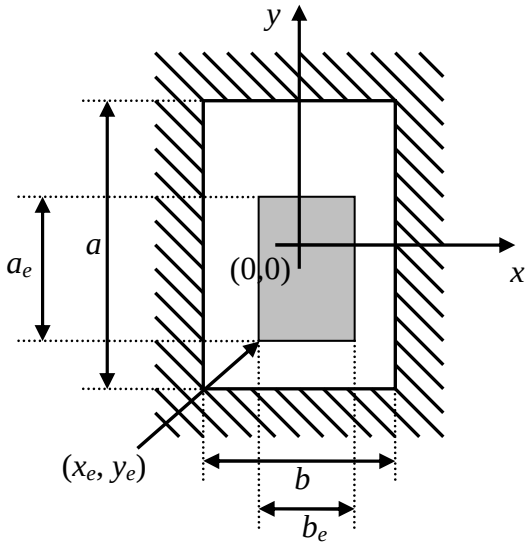


**Figure 1-43: Electrode dimensions and its placement under the membrane.**

where $(x_e, y_e)$ indicate the coordinates of one electrode corner. Then, the electrostatic pressure is acting only on the part of the membrane located above the electrode. On the other part, the electrostatic pressure is equal to zero. Then, taking into consideration the system of Galerkin equations (Equation 1-86), the terms describing the influence of electrostatic pressure change their integration limits [81]. For the electrode described above, the new non-dimensional integration limit $\Omega_e$ is:

$$\Omega_e = \left[\frac{2}{a}x_e, \frac{2}{a}(x_e + a_e)\right] \times \left[\frac{2}{b}x_e, \frac{2}{b}(y_e + b_e)\right] \qquad \textbf{Equation 1-103}$$

Now we will modify the electrode shape. Let us take the actuator from Figure 1-32 with the bottom electrode having variable height as shown in Figure 1-44:

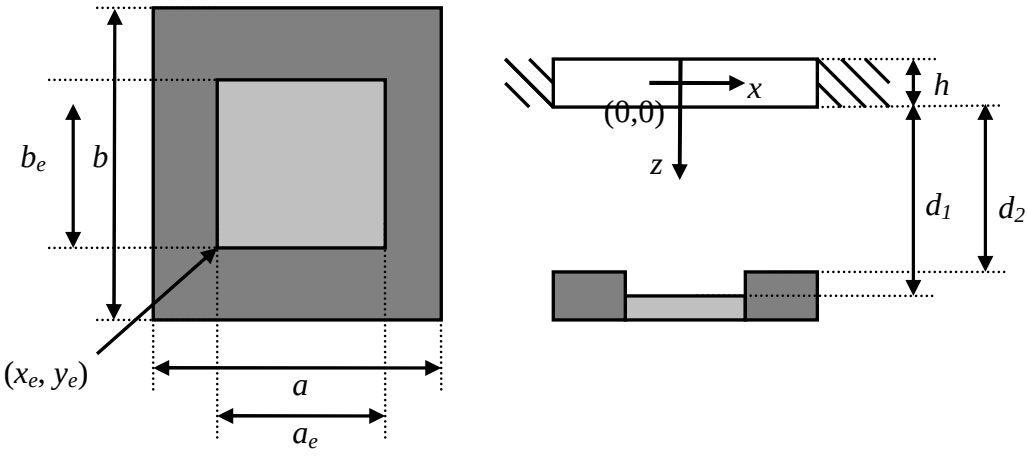


**Figure 1-44: Actuator with bottom electrode having variable height.**

Then, the electrostatic pressure has different value depending on the position on the membrane, consequently the terms of Equation 1-86, describing the influence of electrostatic pressure, have to be divided into two terms as follows:

$$\iint_{\Omega_1} \varepsilon \frac{V^2}{2(d_1 - w)^2}\ {}_{i,j}\, dudv + \iint_{\Omega_2} \varepsilon \frac{V^2}{2(d_2 - w)^2}\ {}_{i,j}\, dudv \qquad \textbf{Equation 1-104}$$

where non-dimensional integration limits are:

$$\Omega_1 = \left[\frac{2}{a}x_e, \frac{2}{a}(x_e + a_e)\right] \times \left[\frac{2}{b}x_e, \frac{2}{b}(y_e + b_e)\right] \qquad \textbf{Equation 1-105}$$
$$\Omega_2 = \Omega - \Omega_1$$

In general case, the classical model allows solving the system for any electrode dimensions and shapes. This reduces only to proper calculation of matrix $\mathbf{B_1}$. Furthermore, it does not affect the calculation time as matrix $\mathbf{B_1}$ has to be always calculated numerically.

## 1.3.5. Reduced model

It has been mentioned earlier that the classical model is inconvenient in use. In case of electrostatic actuation, it is also very time consuming. So, a good idea would be to use the reduced model, which is much faster because it is based on solving a simple algebraic equation. The principle is the same as the one presented for uniform pressure. The model neglects the membrane shape and operates only on its maximal deflection. Then, using the definition of electrostatic pressure and Equation 1-80, we get:

$$k_{mem} w_{\max} = P_h + \varepsilon \frac{V^2}{2(d - w_{\max})^2} \qquad \textbf{Equation 1-106}$$

The solution of this equation is quite simple. One can eliminate the denominator, which leads to the third-order equation, or use an iterative solution, which is more convenient in use. We assume that the deflection on the right-hand side is known. At first iteration it is equal to $w_{0\_max}$. Then, the new value of deflection is calculated from linear equation, which is the new starting point at the next iteration. This procedure is repeated until the solution converges. To verify the precision of this approach, we compared it with the classical model for square membrane without external pressure by plotting the deflection versus applied voltage. The results of this comparison are presented in Figure 1-45:

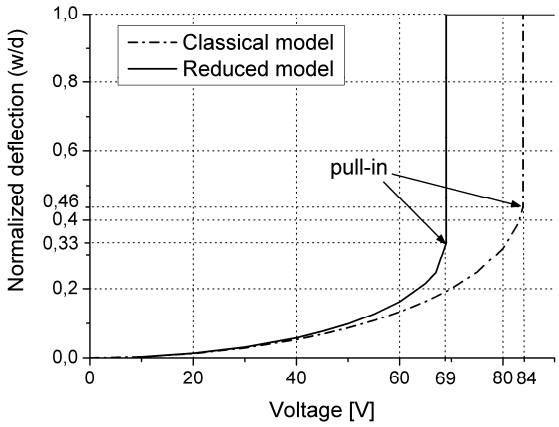


**Figure 1-45: Comparison between classical and reduced model for electrostatic actuation.**

It can be seen, that the reduced model overestimates the deflection, which causes that the pull-in voltage is smaller than the one obtained with the classical model. Furthermore, the normalized pull-in deflection is equal to 1/3 that is the same value as for parallel plate actuator. This value can indicate the reason of these results. Let us analyze the term from Equation 1-106 describing the electrostatic pressure. Its value corresponds to the electrostatic pressure in the centre of the membrane. As the reduce model assumes that the load is uniform over the whole membrane, the electrostatic pressure is then constant independently from position on the membrane. This condition is true only for flat membrane. When the membrane is deformed, the electrostatic pressure is smaller depending on how close it is to the membrane edge. Thus, the effective value of electrostatic pressure is overestimated. It is worth to remark that the reduced model gives acceptable result only for very small voltages in relation to pull-in voltage. However, due to its simplicity, it is often used in membrane actuation [82].

## 1.3.6. Calculation time

In previous paragraphs, we have compared the classical and reduced model for electrostatic actuation in term of precision. It was shown that the reduced model could be used only for specific conditions (actuation voltage much smaller than pull-in voltage). Generally, its precision is poor (usually 30% of mismatch), so we obtain an unacceptable result. It seems that this model should be rejected. However, it has one very important feature, which should be taken into consideration. In this paragraph we will compare both models in terms of calculation time.

Both model were used in MATLAB® environment, which allows time measurement of procedure execution. We will analyze the calculation time for uniform pressure and for

electrostatic pressure. In the case of electrostatic pressure one has to check if the convergence is dependent on applied voltage. Table 1-4 presents the number of iterations needed to obtain the precise result.

**Table 1-4: Number of iteration for various conditions.**

| Membrane | | $V<<V_{pull-in}$ | $V=V_{pull-in}$ |
|---|---|---|---|
| Rectangular | $R$=1 | 5 | 53 |
| | $R$=3 | 5 | 142 |
| Circular | | 5 | 37 |

Thus, to obtain a reliable result of comparison, one has to consider the worst case. Firstly, we will measure the execution time of one point. The results are presented in Table 1-5:

**Table 1-5: Calculation time in seconds of one point for various conditions.**

| Membrane | | Classical model | | | Reduced model | | |
|---|---|---|---|---|---|---|---|
| | | $V$=0 | $V<<V_{pull-in}$ | $V=V_{pull-in}$ | $V$=0 | $V<<V_{pull-in}$ | $V=V_{pull-in}$ |
| Rectangular | $R$=1 | 0.011 | 0.934 | 4.012 | <0.001 | | |
| | $R$=3 | 0.011 | 0.965 | 20.191 | | | |
| Circular | | 0.001 | 0.011 | 0.128 | | | |

It can be seen that the classical model is highly dependent on simulation conditions. Simulations for uniform pressure are fast and last about 10 milliseconds. When iterative process is executed, the time calculation rapidly increases. Although for circular membrane the simulations are quite fast due to simpler analytical description, in case of rectangular membrane they need several seconds, especially near the pull-in voltage. The reduced model is much faster because in each case the time of calculation was not larger than 1 millisecond. Going further, the advantage of reduced model is more noticeable when the full characteristic is needed. Table 1-6 presents the calculation time of 50 points, which allow plotting the membrane deflection versus applied voltage in range from 0 to $V_{pull-in}$.

**Table 1-6: Calculation time in seconds of 50 points for various conditions.**

| Membrane | | Classical model | Reduced model |
|---|---|---|---|
| Rectangular | $R$=1 | 65.283 | 0.048 |
| | $R$=3 | 145.843 | 0.056 |
| Circular | | 1.697 | 0.042 |

The classical model needs more than one minute in case of rectangular membrane as opposed to the reduced model that performs the calculations in about 50 milliseconds. The last comparison concerns the calculation of pull-in voltage (Table 1-7).

**Table 1-7: Calculation time in seconds of pull-in voltage for various conditions.**

| Membrane | | Classical model | Reduced model |
|---|---|---|---|
| Rectangular | $R$=1 | 152.789 | ≈0 |
| | $R$=3 | 145.843 | |
| Circular | | 1.697 | |

As it was mentioned earlier, using classical model, one has to use the iterative procedure. Thus, the calculations take a lot of time contrary to the reduced model, which uses the simple analytical formula. Of course, the algorithm which uses classical model might be much faster, however it will still be slower than the reduced model.

All above-mentioned facts indicate that the classical model is very slow in comparison to the reduced model and may be very inconvenient for the designer. Let us consider e.g. the optimization, where the number of points necessary to find the optimal value reaches thousands or even more. Then, this phase would last several hours, which is not promising result. Therefore, much faster reduced model would be a good alternative if its precision was similar to the one of classical model. In the next paragraph, the methodology of the classical model correction will be presented.

## 1.3.7. Correction of reduced model

It was shown that the reduced model provides erroneous results due to the assumption that the electrostatic pressure is uniformly distributed on the membrane. Thus, we will start with correction of this parameter.

Let us take the term describing the electrostatic pressure from Equation 1-106. This term correspond to the average electrostatic pressure. Then, if the electrostatic pressure varies depending on the membrane position, its average value $P_{e\_av}$ should be smaller that the value used in reduced model:

$$P_{e\_av} = \frac{1}{S}\iint_S \varepsilon \frac{V^2}{2(d-w)^2}\partial x \partial y \qquad \textbf{Equation 1-107}$$

It is intuitive to introduce the effective membrane deflection $w_{eff}$, which will correct the electrostatic pressure value (Figure 1-46):

$$w_{eff} = Aw_{\max}$$ **Equation 1-108**

where $A$ is a coefficient of correction.

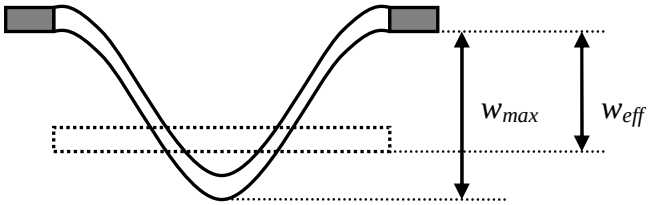


**Figure 1-46: Definition of effective membrane deflection.**

Then, the electrostatic pressure is as follows:

$$P_e = \varepsilon \frac{V^2}{2\left(d - w_{eff}\right)^2}$$ **Equation 1-109**

As the average electrostatic pressure highly depends on membrane form, firstly, we will focus on the pull-in point. Then, combining Equation 1-106 and Equation 1-109 and knowing the exact value of pull-in deflection from the classical model, we can easily calculate the coefficient $A$ using the following relation:

$$A = \frac{k_{mem} d}{3k_{mem} w_{pull-in} - 2P_h}$$ **Equation 1-110**

It can be seen that this coefficient has to be individually determined for each membrane shape (circular and rectangular), each value of anisotropy coefficient and each value of pressure $P_h$ normalized to the maximal applicable uniform pressure $P_{max}$ defined by Equation 1-111:

$$P_{\max} = k_{mem} d$$ **Equation 1-111**

Then, we verified the effectiveness of this correction by plotting the deflection curve versus the applied voltage for square membrane (Figure 1-47).

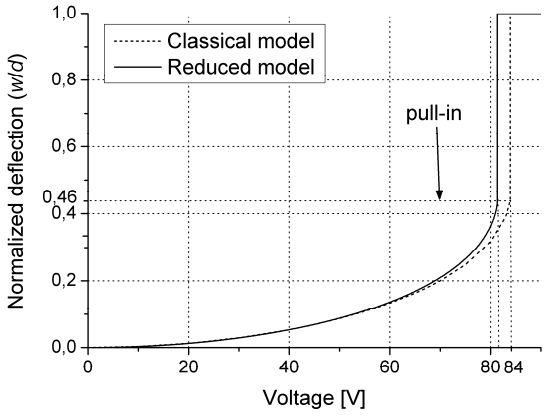


**Figure 1-47: Comparison between classical and reduced model corrected with coefficient *A*.**

It can be seen that now the reduced model matches with the classical model for the value of pull-in deflection. However, the pull-in voltage is still different. Thus, the model has to be corrected by using another coefficient. Considering the fact that the normalized pull-in deflection is dependent only on value of coefficient *A*, we can introduce a coefficient *B* as shown in Equation 1-112 non-affecting the pull-in deflection.

$$P_e = B\varepsilon \frac{V^2}{2\left(d - Aw_{\max}\right)^2} \qquad \textbf{Equation 1-112}$$

Substituting this term into Equation 1-106 and knowing the exact value of pull-in voltage from classical model, the coefficient *B* can be simply calculated as follows:

$$B = \frac{8}{27} \frac{\left(k_{mem} d - P_h A\right)^3}{\varepsilon k^2 A V_{pull-in}^2} \qquad \textbf{Equation 1-113}$$

Similarly as coefficient *A*, the coefficient *B* depends on membrane shape, coefficient of anisotropy and pressure $P_h$ normalized to the maximal pressure $P_{max}$. The results of this correction are presented in Figure 1-48:

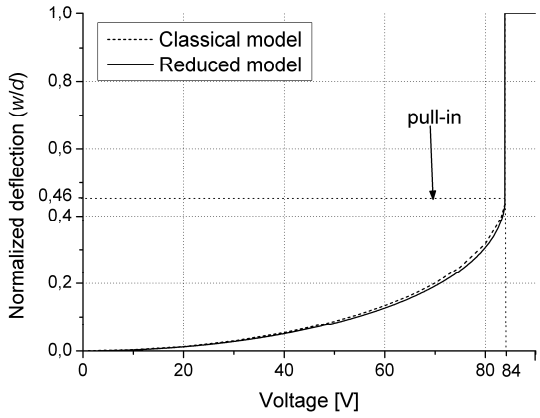


**Figure 1-48: Comparison between classical and reduced model corrected with coefficients *A* and *B*.**

Comparison shows that the correction is sufficient, the pull-in voltage and deflection fully correspond to the values from classical model. However, one can see some discrepancy between the curves below the pull-in point. It is an effect of changing membrane form with applied voltage. Then, the average electrostatic pressure is not exactly inversely proportional to $\left(d - w_{eff}\right)^2$. As a result, the electrostatic pressure has to be dependent on voltage normalized to pull-in voltage. One can achieve this through the modification of coefficient *B* or direct correction of the membrane deflection generated with electrostatic force. We used the second method. Fortunately, the simulations show that the function correcting the deflection does not depend on membrane shape and coefficient of anisotropy. It varies only with pressure $P_h$ normalized to $P_{max}$ as shown in Figure 1-49.

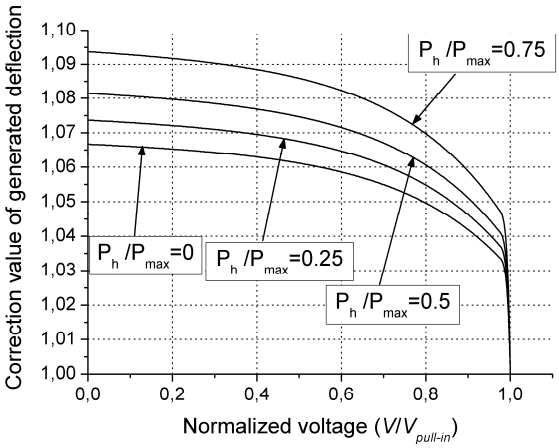


**Figure 1-49: Function correcting the deflection generated electrostatically.**

### 1.3.7.1. Complete corrected reduced model

In the previous paragraph, we developed the analytical model of electrostatic membrane-based actuator, which is the combination of the reduced and classical model. To summarize, we will gather all information needed to use this model.

The corrected reduced model uses the following relation:

$$k_{mem} w_{\max} = P_h + B\varepsilon \frac{V^2}{2(d - Aw_{\max})^2} \qquad \textbf{Equation 1-114}$$

where $k_{mem}$ is the membrane-spring constant described with Equation 1-77 or Equation 1-78 and coefficients from Table 1-3, $A$ and $B$ are the coefficients of correction (Table 1-8), $P_h$ is the sum (Equation 1-79) of the uniform pressure and the pressure corresponding to the initial deflection (Equation 1-72 or Equation 1-74) and $P_{max}$ is the maximal applicable uniform pressure (Equation 1-111). The solution of Equation 1-114 may be iterative. In the first iteration one assumes that the deflection on the right-hand side of the equation is known and one calculates the new value of the deflection, which is the starting point in next iteration. This process is repeated until the solution converges. The last step is to correct the obtained deflection using the function from Figure 1-49. The complete procedure is presented in Figure 1-50:

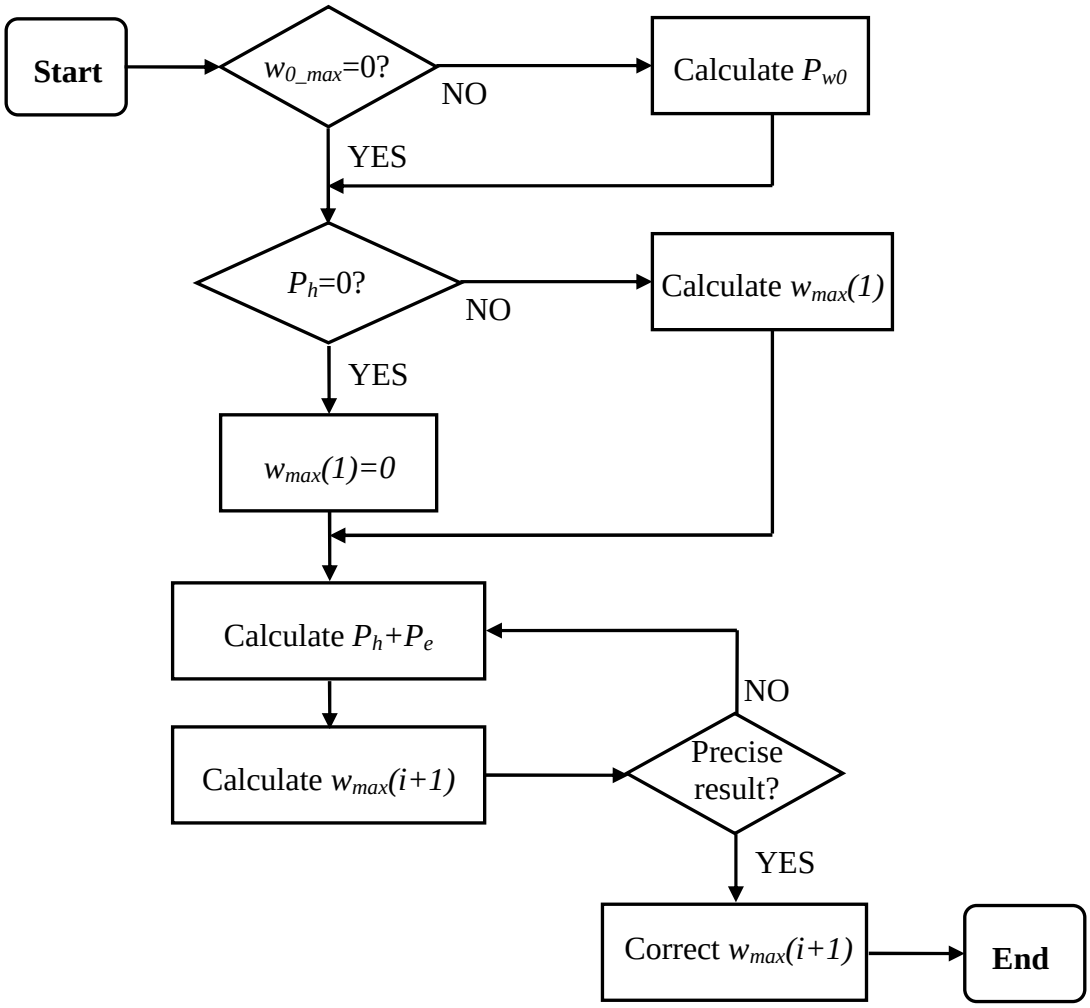


**Figure 1-50: Procedure of calculation for electrostatic pressure using corrected reduced model.**

The pull-in voltage and deflection are calculated directly using following formulas:

$$V_{pull-in} = \sqrt{\frac{8}{27}\frac{\left(k_{mem}d - P_h A\right)^3}{ABk^2\varepsilon}} \qquad \textbf{Equation 1-115}$$

$$w_{pull-in} = \frac{1}{3}\frac{d}{A} + \frac{2}{3}\frac{P_h}{k_{mem}} \qquad \textbf{Equation 1-116}$$

Going further, the reduced model operates only on the maximal membrane deflection. Thus, to get the membrane form and stress distribution, the function from Equation 1-38 or Equation 1-62 with coefficients from Table 1-2 can be used. In fact, the normalized function of membrane deflection may produce serious errors in specific conditions, so the results should be verified with classical model.

**Table 1-8: Values of coefficients *A* and *B* for various conditions.**

| Material | | Isotropic | | | | | | Silicon <100> | | | | | | Silicon <110> | | | | | |
|---|---|---|---|---|---|---|---|---|---|---|---|---|---|---|---|---|---|---|---|
| $\frac{P_h}{P_{max}}$ | Coefficient | Circular | *b*/*a* | | | | | Circular | *b*/*a* | | | | | Circular | *b*/*a* | | | | |
| | | | 1 | 1.5 | 2 | 2.5 | 3 | | 1 | 1.5 | 2 | 2.5 | 3 | | 1 | 1.5 | 2 | 2.5 | 3 |
| 0 | *A* | 0.75 | 0.724 | 0.725 | 0.739 | 0.752 | 0.760 | 0.751 | 0.725 | 0.726 | 0.738 | 0.751 | 0.758 | 0.747 | 0.719 | 0.727 | 0.739 | 0.757 | 0.776 |
| | *B* | 0.936 | 0.941 | 0.959 | 0.979 | 1 | 1.015 | 0.937 | 0.943 | 0.959 | 0.976 | 0.991 | 1.004 | 0.933 | 0.944 | 0.955 | 0.983 | 1.005 | 1.01 |
| 0.25 | *A* | 0.801 | 0.773 | 0.774 | 0.79 | 0.803 | 0.812 | 0.803 | 0.774 | 0.776 | 0.788 | 0.802 | 0.81 | 0.799 | 0.768 | 0.777 | 0.79 | 0.809 | 0.829 |
| | *B* | 0.870 | 0.874 | 0.891 | 0.91 | 0.929 | 0.943 | 0.871 | 0.876 | 0.891 | 0.907 | 0.921 | 0.933 | 0.866 | 0.878 | 0.888 | 0.914 | 0.934 | 0.938 |
| 0.5 | *A* | 0.863 | 0.833 | 0.834 | 0.851 | 0.865 | 0.875 | 0.864 | 0.834 | 0.836 | 0.849 | 0.864 | 0.873 | 0.860 | 0.827 | 0.837 | 0.851 | 0.871 | 0.893 |
| | *B* | 0.748 | 0.752 | 0.766 | 0.782 | 0.799 | 0.811 | 0.749 | 0.753 | 0.766 | 0.78 | 0.792 | 0.802 | 0.745 | 0.755 | 0.763 | 0.786 | 0.803 | 0.807 |
| 0.75 | *A* | 0.942 | 0.909 | 0.91 | 0.928 | 0.944 | 0.955 | 0.944 | 0.910 | 0.912 | 0.927 | 0.943 | 0.952 | 0.937 | 0.903 | 0.913 | 0.929 | 0.951 | 0.974 |
| | *B* | 0.517 | 0.519 | 0.529 | 0.54 | 0.552 | 0.560 | 0.519 | 0.520 | 0.529 | 0.538 | 0.547 | 0.554 | 0.513 | 0.521 | 0.527 | 0.543 | 0.555 | 0.557 |

### 1.3.7.2. Limitations

It has to be emphasized that the corrected reduced model has some limitations. Starting at the beginning, the model is based on the theory of thin plates for small deflections. The ratio $R_h$ is then limited in range from 10 to 80 and the ratio $w/h$ should not exceed 0.3.

Second, the next limitation results from the assumption that the membrane is perfectly clamped on its edges. The real clamping is not considered in analytical models due to difficulty of finding the exact function of membrane deflection and the dependence of substrate surrounding the membrane on the results. The influence of clamping conditions will be analyzed in next paragraph in which the comparison with FEM simulation will be discussed.

Third, the most important limitation of the reduced model is that it operates only on maximal membrane deflection. Thus, it is not possible to calculate the function describing the membrane form. The normalized function can only be used in specific conditions e.g. for respectively small value of residual stress. Then, the error is relatively small and does not exceed 10% in stress distribution in the worst case. If the residual stress is larger, the calculated membrane form significantly differs from the real form producing more than 50% discrepancy in stress distribution in some cases. Thus, the normalized function should be used with caution and one should verify the results with the classical model.

Fourth, it should be remarked that the model has a limitation concerning the initial position of the membrane. If we look at Table 1-8, one can see that the coefficients are given for positive values of ratio $P_h/P_{max}$. This means that the membrane, due to uniform pressure, should be flat or deformed towards the bottom electrode. In other words, the total deflection (including the initial deflection) of the membrane under the uniform pressure (without electrostatic pressure) has to be positive or equal to zero. In other case, the correction of the model is no longer valid and the results may be erroneous.

Finally, the last limitation concerns the electrode shape. As the reduced model does not use an integration limit, there is no direct possibility to change the electrode shape. It can be taken into consideration indirectly by introducing a coefficient correcting the term describing the electrostatic pressure. In paragraph 2.1.2.2 we will try to determine the values of this coefficient.

## 1.4. Analytical model vs. FEM simulation

In previous paragraphs we presented the analytical model of electrostatic actuator. Now, we will focus on an other, commonly used approach, which is a simulation using finite element method (FEM). We will present the principle of modelling using this technique. Then we will point to its advantages and drawbacks. Next, we will compare both methods in order to verify the developed analytical model. Finally, we will present the dedicated tool written in MATLAB® which allows the complete simulation on electrostatic membrane-based actuator using the reduced model. As a FEM simulator we will use ANSYS® environment.

### 1.4.1. FEM model

Modelling of electrostatic membrane-based actuators requires two domains to be taken into account: mechanical and electrical. In mechanical domain a membrane as a solid structure with applied mechanical loads is simulated. In FEM there is no restriction in shapes. One can simulate a circular or rectangular membrane and other more complex shapes. In our case, the typical model for square membrane is shown in Figure 1-51:

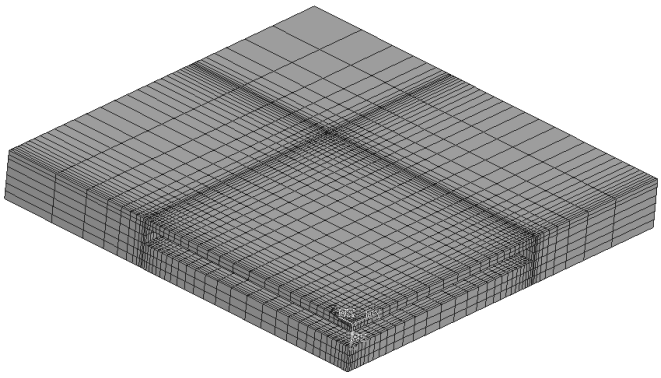

**Figure 1-51: The FEM model of a square membrane. The distance between the membrane and the substrate was enlarged to obtain legible image.**

As one of the FEM features is symmetry, one can reduce the model to only one quarter of the membrane. In structure meshing we used the element SOLID186 that supports the anisotropy. As one can see the division of the structure was made to obtain the best precision in weak points of the membrane such as its edge and centre. Furthermore, the membrane division was set experimentally through the recurrent decrease until the results remain stable. This allows obtaining the division as small as possible what leads to reduction of calculation time. To obtain trustworthy results, the model consists of substrate surrounding the membrane. Its dimensions are comparable to the membrane in *xy* coordinates but its thickness is a few times

larger. This should correspond fairy well to the real conditions. Substrate division was maximally decreased, as the results in this region are not necessary. The most important part in FEM simulation is the choice of clamping conditions. The proper clamp of the structure has to correspond to those in real structures. One can specify the following types of clamping (Figure 1-52) [83]:

a) Perfect clamping – the membrane is fixed on its edges
b) Real clamping 1 – the structure is fixed on the bottom surface of the substrate
c) Real clamping 2 – the structure is fixed only in one point

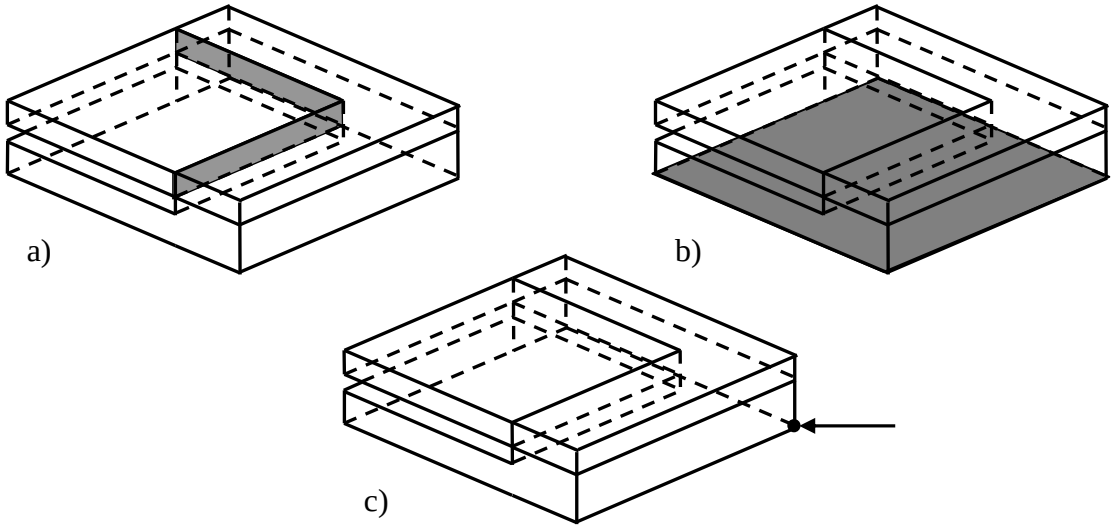


**Figure 1-52: Types of structure clamping.**

The first one is the same condition, as the one used in analytical model. It is the worst case of all because it does not exist in real devices. It can only be used to verify the analytical models. The second one is much more reliable because the membrane is not directly fixed and the substrate reacts to the applied load. In the third one the substrate is free and bends with the membrane. For further simulation we will use the perfect clamping to verify and estimate the accuracy of the analytical model and the real clamping 1 to estimate the influence of clamping conditions. The chosen real clamping type matches most the clamping observed in fabricated samples.

The electrical domain is used to simulate the structure under the electrical load. In case of electrostatic force, we need a virtual element, which realizes the coupling between the mechanical and electrical domain. This feature is supported by the transducer element (TRANS126) which allows applying the electrical voltage $V$ on edges of mechanical gap distance $d$ with permittivity $\varepsilon$ [84]. Then, this element coupled with nodes of the bottom membrane surface produces the electrostatic force acting on the membrane, which depends on

element voltage and gap distance (Figure 1-53). The area, which contains the nodes linked with transducer element, forms the electrode. Thus, one can easily change the electrode shape and gap distance.

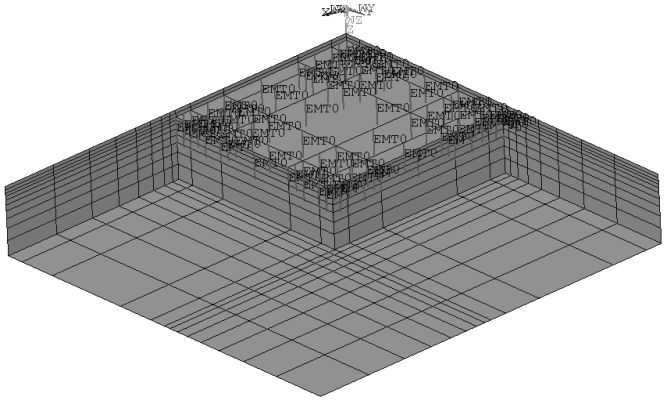

**Figure 1-53: The FEM model of a square membrane with transuder elements (EMT0). Membrane division was decreased and the substrate beneath the membrane was removed to obtain legible image.**

The complete FEM model seems to be simple. However, it should be remarked that the model has to be reconstructed each time when the membrane and electrode dimensions change. The only parameter whose variation does not require the model reconstruction is the voltage. When the exact structure dimensions are known, one can simply change the voltage and perform the simulation once again. However, the design process usually needs finding the optimal dimension of the structure and then the FEM simulation becomes more complicated resulting in larger calculation time.

## 1.4.2. Comparison

We performed the simulations of a rectangular (900 μm × 300 μm × 5 μm) and square (300 μm × 300 μm × 5 μm) silicon membranes with a bottom electrode of gap distance 1μm. We will investigate the influence of uniform pressure, residual stress and voltage using the perfect clamping of the membrane (marked as FEM1 on graphs) to verify the analytical model and the real clamping (FEM2) to investigate the influence of clamping conditions on the membrane behaviour. All results will be compared with those obtained with the analytical model (AM) with the remark that we will not use the normalized membrane form. Finally, we will compare the simulation time. In comparison we omitted the circular shape of the membrane, as it is very similar in behaviour to the square membrane.

### 1.4.2.1. Uniform pressure

We will now compare the results for the load of uniform pressure. Figure 1-54 and Figure 1-55 show the curves of maximal deflection versus applied pressure.

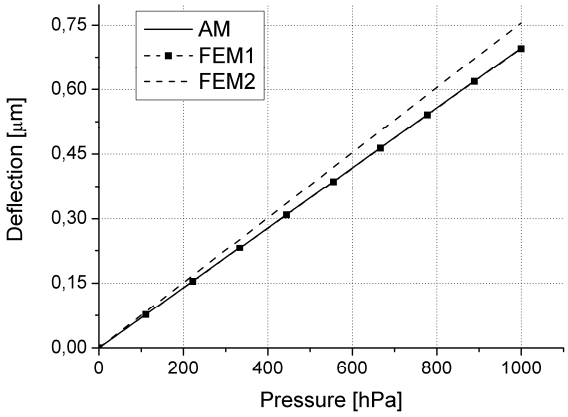


**Figure 1-54: Comparison of deflection for square membrane loaded with uniform pressure.**

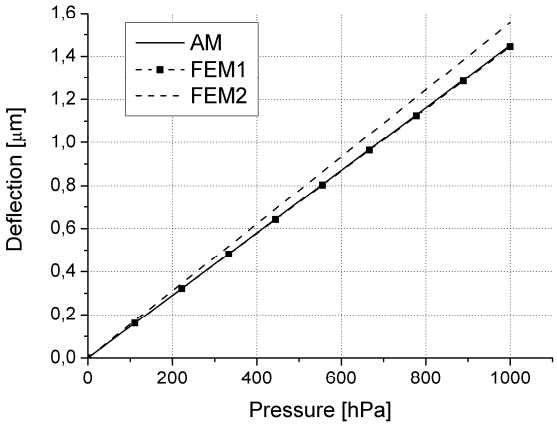


**Figure 1-55: Comparison of deflection for rectangular membrane loaded with uniform pressure.**

The analytical model gives almost the same results as FEM using the perfect clamping. The real clamping has significant influence on membrane deflection, which is 8% larger for both membranes. It indicates that the stress within the membrane will also be different. However, one should verify the membrane form as the substrate can also deform. Figure 1-56 and Figure 1-57 show the stress distribution along the longer section for square and rectangular membrane.

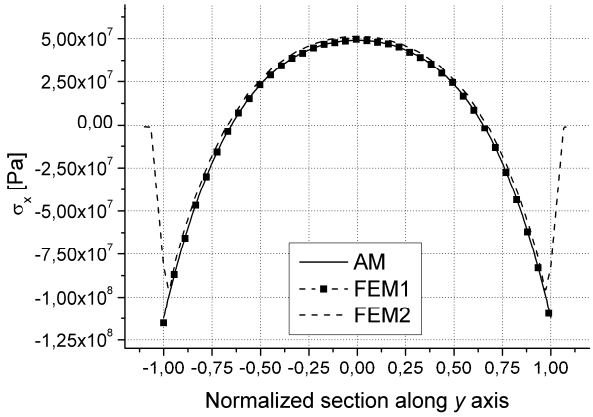


**Figure 1-56: Comparison of $\sigma_x$ for square membrane loaded with uniform pressure.**

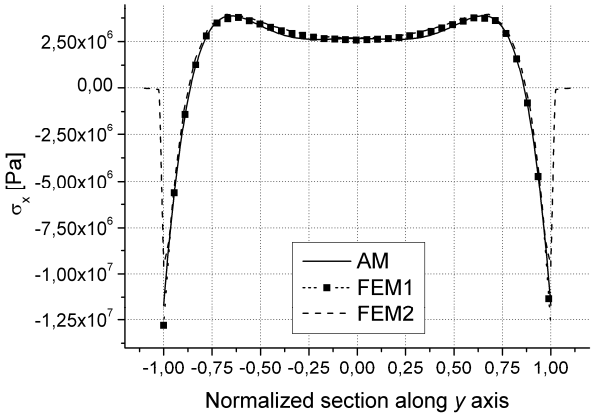


**Figure 1-57: Comparison of $\sigma_x$ for rectangular membrane loaded with uniform pressure.**

Comparison between the analytical model and FEM using perfect clamping shows that the results match almost perfectly. The difference is less than 1%. It proves that the analytical approach is correct and the function describing the membrane form has sufficient precision. The influence of real clamping is not significant in the middle of the membrane where the difference does not exceed 5%. Near the membrane edge the membrane form is different resulting in up to 22% overestimation in stress using real clamping. This shows the most important drawback of the analytical model, which should not be ignored.

### 1.4.2.2. Residual stress

Now, we will compare the results from simulations of the membrane with 100 MPa in tension and compression. The maximal deflection of the square membrane is shown in Figure 1-58 and Figure 1-59:

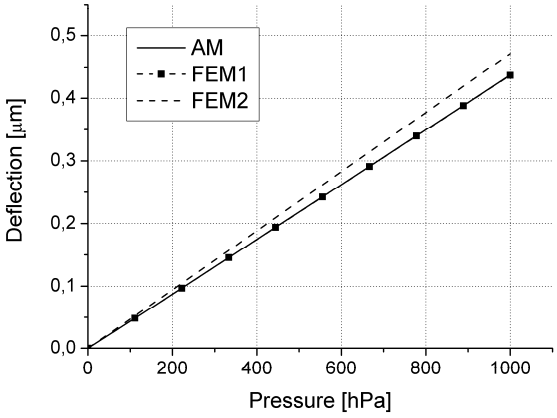


**Figure 1-58: Comparison of the deflection for square membrane in tension loaded with uniform pressure.**

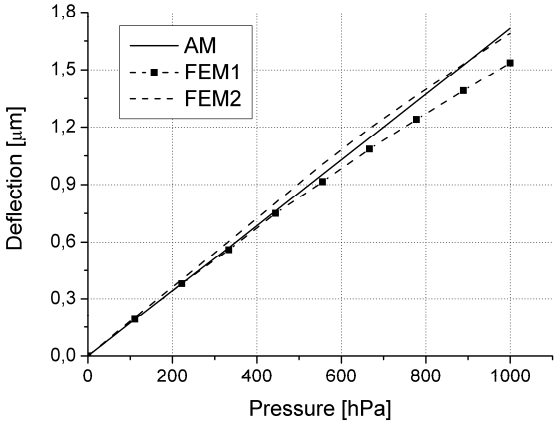


**Figure 1-59: Comparison of the deflection for square membrane in compression loaded with uniform pressure.**

In case of tension, the results are similar as for the membrane without residual stress. The analytical model gives comparable results to those from FEM with perfect clamping and are underestimated by 8% in comparison to real clamping. In case of compression for small pressures the dependence is quite the same. For larger values the characteristic obtained with FEM is no longer linear. It is caused by the use of analysis applicable for large displacements (it is needed to perform the simulation with applied residual stress) as the ratio $w/h$ is close to 0.3. The simulations of rectangular membrane were omitted, as the influence of residual stress is quite the same.

### 1.4.2.3. Voltage

In comparison of electrostatic actuation, we will focus on the maximal deflection of the membrane. Figure 1-60 and Figure 1-61 show the characteristics of the deflection versus applied voltage.

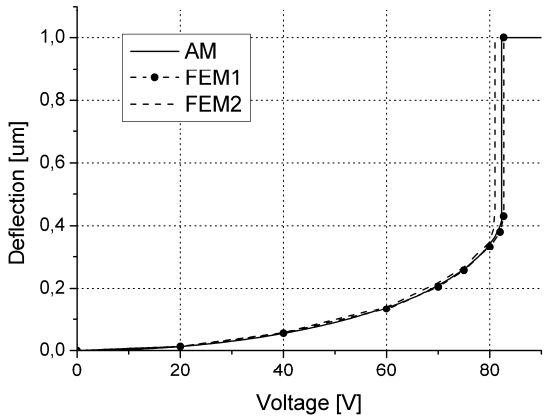


**Figure 1-60: Comparison of the deflection versus applied voltage for square membrane.**

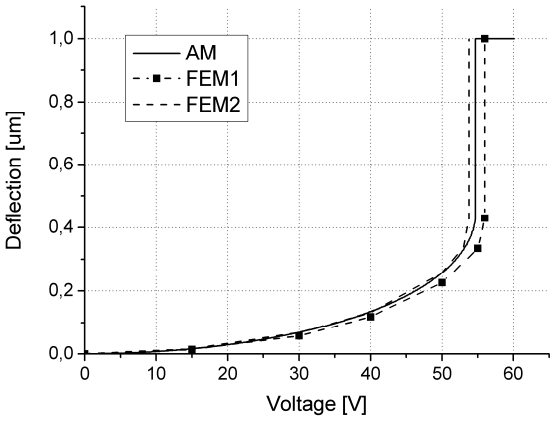


**Figure 1-61: Comparison of the deflection versus applied voltage for rectangular membrane.**

The results from analytical model are very close to those from FEM with perfect clamping. They are underestimated by 1% for square membrane and 3% for rectangular. The real clamping has moderate affect on the deflection. The pull-in voltage is smaller by about 4% for square membrane and 10% for rectangular membrane in comparison with perfect clamping. One can state that the influence of clamping is less significant for electrostatic actuation that for the hydrostatic one. Thus, we plotted the same characteristics for membranes initially deflected by hydrostatic pressure (Figure 1-62 and Figure 1-63):

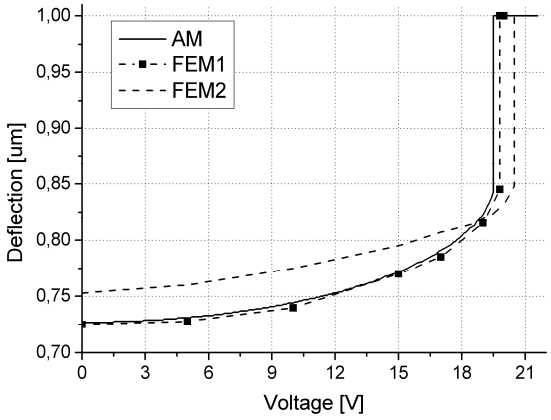


**Figure 1-62: Comparison of the deflection versus applied voltage for square membrane initially deflected.**

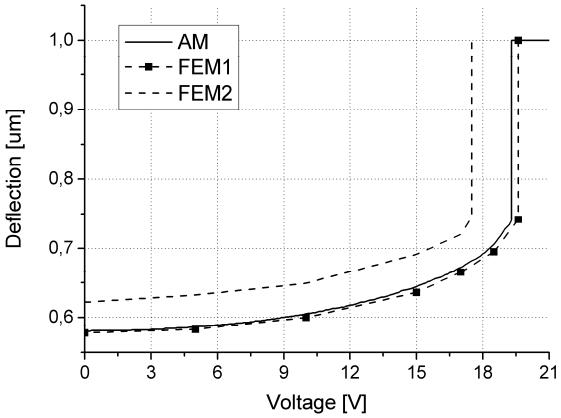


**Figure 1-63: Comparison of the deflection versus applied voltage for rectangular membrane initially deflected.**

For square membrane the characteristic for real clamping is more flattened which causes that the initial underestimation turns into the overestimation of pull-in voltage by 5%. In rectangular membrane the curves shapes are quite similar and 10% underestimation remains the same in the wide range of applied voltages. It is worth to remark that in both cases the analytical results match those obtained from FEM with perfect clamping.

The last thing worth to compare is the stress distribution in the worst case, which occurs for the pull-in voltage and without the hydrostatic pressure. We plotted $\sigma_x$ the along the central section of the longer side:

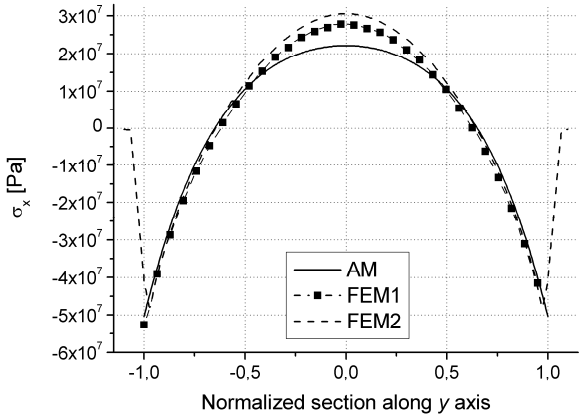


**Figure 1-64: Comparison of $\sigma_x$ for square membrane and pull-in voltage.**

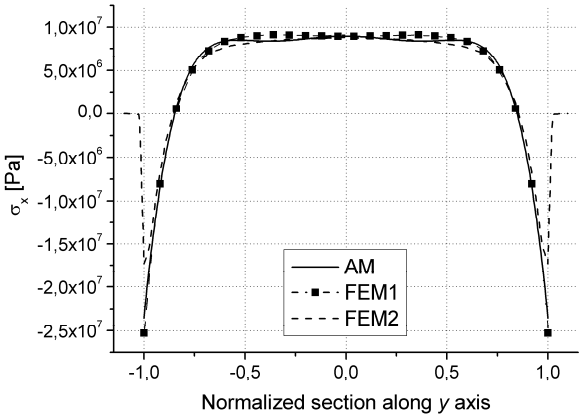


**Figure 1-65: Comparison of $\sigma_x$ for rectangular membrane and pull-in voltage.**

In both cases one can observe conformity between analytical model and FEM with perfect clamping where the difference is less than 3%. The real clamping has significant influence near the membrane edge where the use of perfect clamping overestimates the stress by 20% for square membrane and 26% for rectangular membrane.

All shown comparisons prove that the results obtained with the analytical model are comparable with those from FEM simulator. The difference in maximal deflection is less than 3%. Furthermore, comparison of stress distribution shows that the function chosen to describe the membrane form has good precision. In some cases, it can produce some artefacts that can be neglected. Going further, the influence of real clamping depends on initial conditions. In some cases the difference is relatively small, in others is significant. Thus, it should be always taken into consideration and the analytical model should be verified with FEM simulator.

#### 1.4.2.4. Simulation time

As we performed all needed simulations to verify the analytical model and estimate the incertitude of several assumptions on results, which simplify the model, let us compare the simulation time. We will compare the mechanical simulation and coupled electro-mechanical simulation separately. The time obtained for FEM simulations concerns the script execution (creating 3-D model, meshing and solving). The results of measurements are presented in Table 1-9:

**Table 1-9: Comparison of simulation between analytical model and FEM simulation (time in seconds).**

| Type of simulation | Mechanical | Electro-mechanical | | |
|---|---|---|---|---|
| | One point | One point | 50 points | Pull-in point |
| Analytical model | ≈0 | <0.001 | 0.048 | ≈0 |
| FEM simulator | ≈5 | ≈27 | ≈357 | ? |

The mechanical simulation is relatively fast and takes a few seconds. The electro-mechanical simulation lasts longer due to fact that some time is needed to create transducer elements and calculation procedure is iterative. It needs about half a minute. It is not much considering that the FEM simulation is very precise. However, simulation time is getting more significant if we need a full characteristic of the device. Then, at least six minutes needed by FEM simulation are incomparable to 50 milliseconds needed in analytical calculations. Moreover, if we would like to perform an optimization, we would need several hours to accomplish this task. Thus, it would be desired to perform such tasks with analytical model in tens of seconds with similar results. The last comparison deals with finding the pull-in point. Using the FEM simulator one has to perform an iterative simulation guessing each new starting point. Therefore, we did not measure the time for this task but it is sure that it takes much more time than simple calculation using analytical model.

### 1.4.3. Dedicated simulation tool

All above-mentioned facts prove that the analytical model is a good alternative for simulating membrane-based actuators. As this approach, considering all specified features, assumptions and limitations, will be used instead of FEM simulator, it is desirable to create some graphical interface, which will be simple and intuitive in use and will give the results in a clear form. In order to create such a tool, a numerical computing environment and programming language MATLAB® was used. The main window of written tool is presented in Figure 1-66:

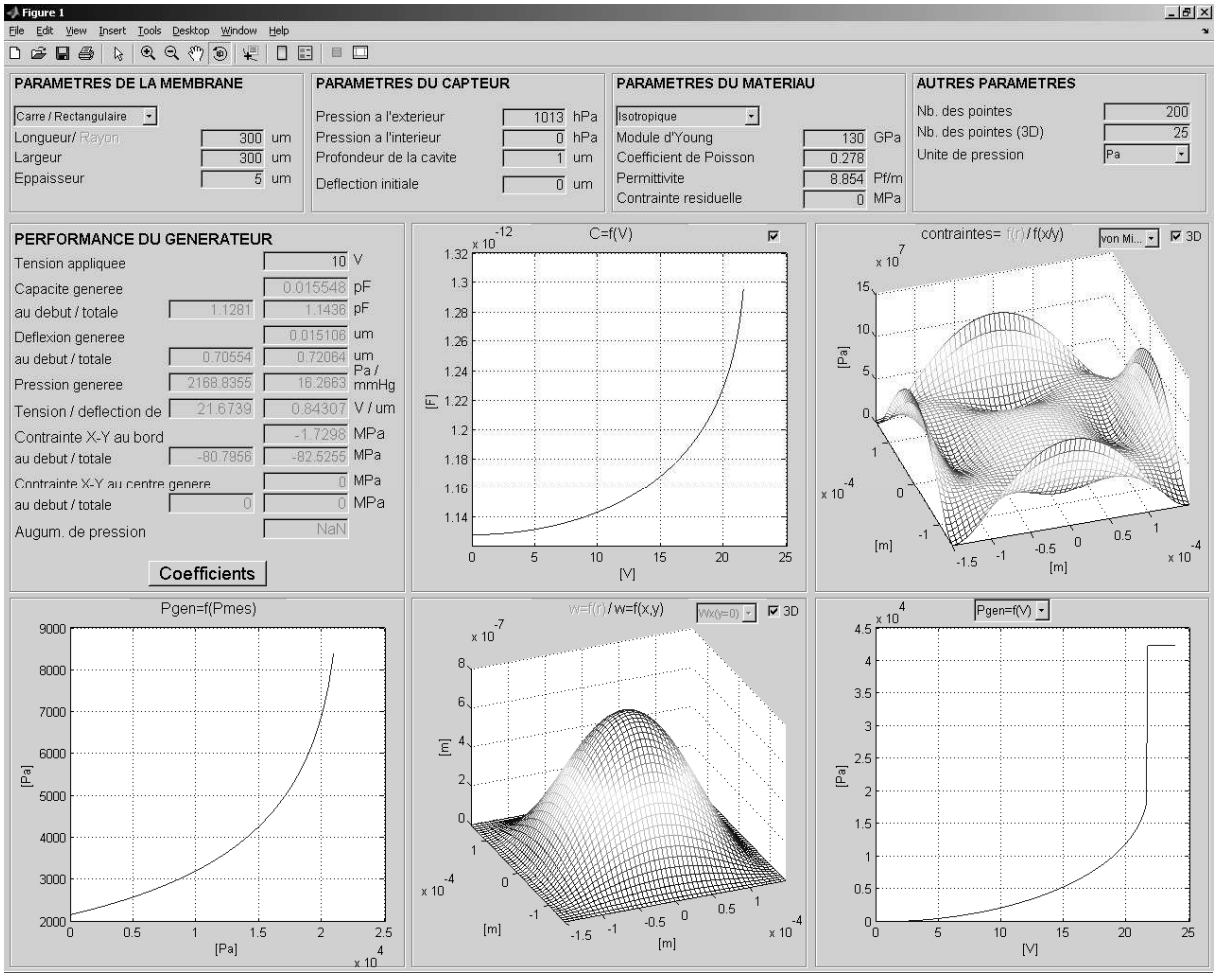


**Figure 1-66: Main window of the simulation tool in ®MATLAB GUI.**

It can be divided into three main parts. The upper part is dedicated to define the following parameters of:

- membrane – its shape (circular and rectangular with membrane ratio up to 3), dimensions and initial deflection
- surroundings – pressure above and below the membrane
- bottom electrode – its gap distance and permittivity of space
- material – its kind such as silicon <100>, <110> and fully definable isotropic, residual stress including the calculation of the maximal stress (buckling).

The parameters such as the membrane dimensions and hydrostatic pressure can be set without any restrictions concerning the specific ratios. In the tool all coefficients and other functions were approximated using the MATLAB® built-in curve fitting tool. All functions are presented in APPENDIX E.

The second part is dedicated to the results. One can specify the most important characteristics which are plotted in figures:

- capacitance versus the applied voltage

- stress distribution ($\sigma_x$, $\sigma_y$, $\sigma_{von\_mises}$) within the membrane (top surface) in 3-D plot or 2-D plot along the central section of each side
- form of the deflected membrane in 3-D plot or 2-D plot along the central section of each side
- total membrane deflection versus applied voltage
- membrane deflection generated electrostatically versus applied voltage
- pressure generated electrostatically versus applied voltage
- pressure generated electrostatically versus applied hydrostatic pressure

Furthermore, the tool allows extracting the exact value from the curves. The left part is dedicated to the results calculated for one user-defined voltage, which are useful in estimating the device performance.

As one can see, the presented tool is very simple in use. The user needs only to specify the basic parameters and all results are automatically listed and plotted. Furthermore, all results can be transformed to the other form as the tool is written in numerical computing program. Finally, its most important advantage is the calculation time, which usually takes no more than a few seconds including data processing and visualization.

Chapter 2

# Optimization and statistical approach

## 2.1. Optimization

The previous chapter fully described the methodology of modelling of electrostatic membrane-based actuators and related issues to this. The complete model allows estimating the device performance from defined input parameters. In design phase, the most important question is: what values of these parameters should be taken into account to obtain desired performance of the device? It is more critical if we take into the consideration the fact that its proper definition affects the number of cycles needed to experimentally verify the assumptions and the project time needed to fabricate the device which fulfils the requirements. In this chapter we will focus on a method allowing shortening of the project duration, which is the optimization. Next, we will focus on the issues related to the fabrication with the help of statistical analysis.

### 2.1.1. Design path

Let us focus on the design path of a device (Figure 2-1). The main tasks remain still the same. At the beginning, the project requirements are defined and verified if it is possible to carry out the project. Then, the simulations are performed and verified experimentally. If the result meets the requirements the process is finished. In other case (what usually happens), the second step has to be performed once again until the results are satisfactory.

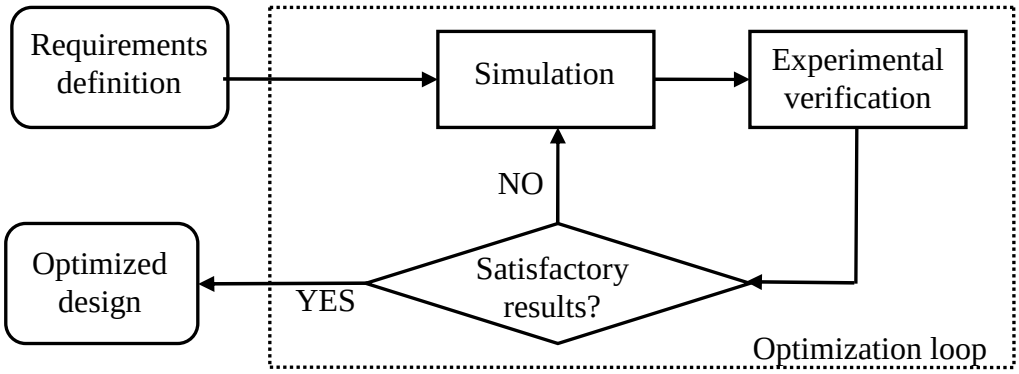


**Figure 2-1: Classical design path.**

As one can see, the simulation and verification process can be named, as an optimization loop that is critical is whole design path. Each repetition results in increase of project duration and its costs. Therefore, many works have been done in order to increase the effectiveness of the design path. The most inconvenient phase is experimental verification which is time consuming and expensive. It would be desirable to perform the fabrication only once. Today, it is possible thanks to FEM simulators, which are constantly improved providing us with

more and more reliable results. Then, the optimization loop consists only of simulation phase and the number of experimental verifications can be radically decreased (Figure 2-2).

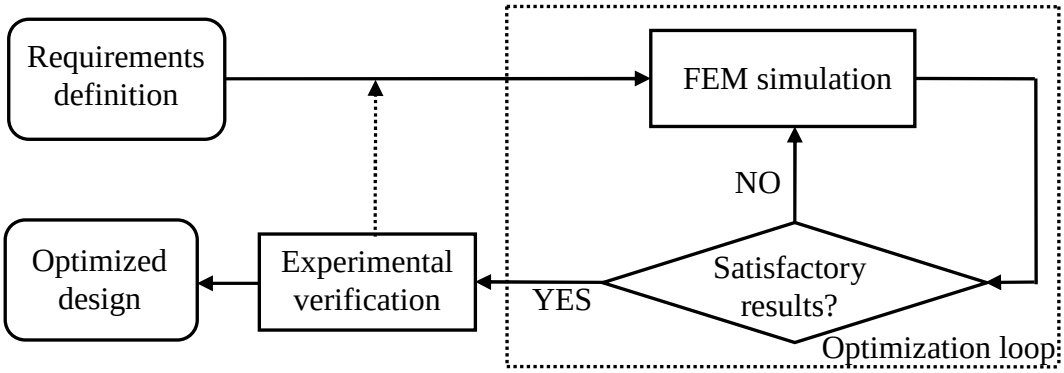


**Figure 2-2: Optimized design path.**

Let us consider our electrostatic actuator. As it was mentioned in the previous chapter, the FEM simulation is not relatively fast if we are talking about the repetitive simulation. The optimization loop can last several hours assuming that nothing goes wrong. Thus, the simulation phase is now a bottleneck in the design path. Let us analyse the use the analytical model instead of the FEM simulator. We are able to perform on optimization phase in a few minutes obtaining accurate results taking into account all phenomena supported with analytical model. Then, we can simply perform one simulation using FEM to verify the results, as the analytical model does not support the real clamping. Even, if the results are not satisfactory, we can simply tune up input parameters and repeat the procedure “wasting” a few minutes, not a few hours. In next sections, we will describe the optimization phase more precisely and we will show how to use the analytical model (Figure 2-3).

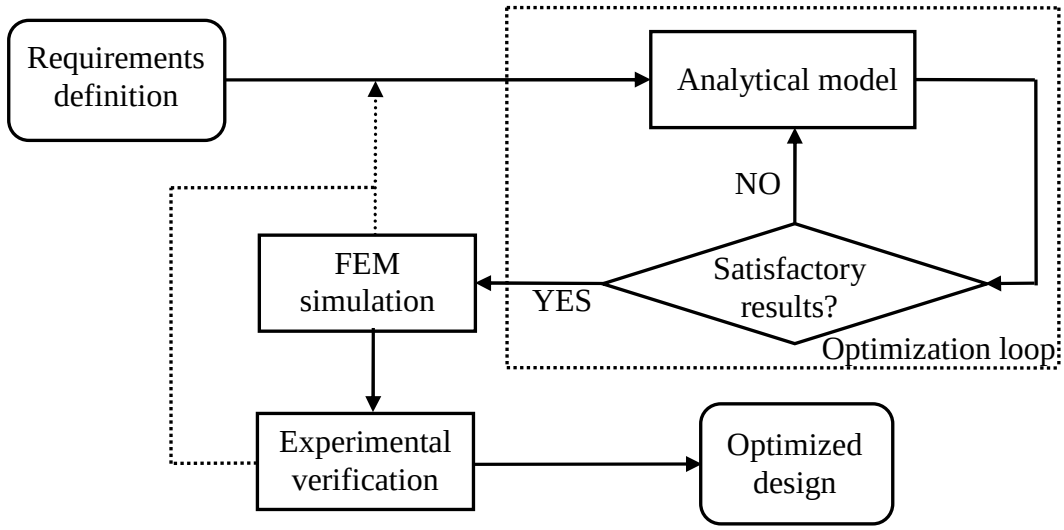


**Figure 2-3: Design path using analytical model.**

## 2.1.2. Principles

In mathematical sense, the optimization refers to the study of problems in which one seeks to minimize the function by systematically choosing the values of variables from within an allowed set. Let us consider the function $y$=f($x$) from Figure 2-4:

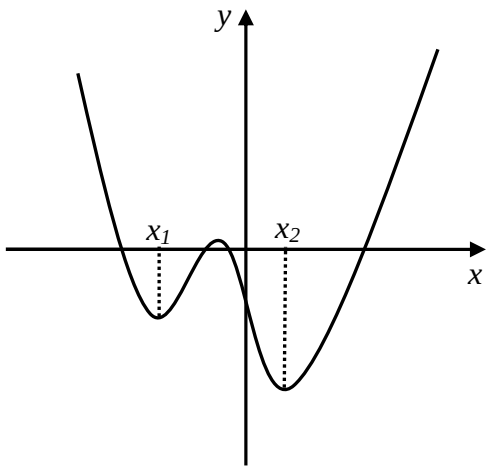


**Figure 2-4: Exemplary function.**

The $x$ value is an argument of function f($x$) which is optimized in order to find its minimal value. As the function has one variable, the optimization is one-dimensional. If the set of argument is undefined (all real values), the value of argument that we are looking for is equal to $x_2$. This type of optimization is called unconstrained [85]. The optimization algorithms are not perfect. They always need a starting point from which they start the procedure [86]. If one set the proper starting point, one will find the global minimum of the function. In other case, the local minimum can be found such as the point $x_1$ in our example. In engineering applications, the unconstrained, one-dimensional optimizations are rare. Usually, they depend on many parameters whose sets are defined by e.g. project requirements or technological process. In solving of this type of problems, a sequential quadratic programming can be used [87][88][89], which is supported by MATLAB® environment.

Now we will focus on optimization of electrostatic actuator. The optimization process can be simply performed as the device is described with a mathematical function using the analytical model. This function need to be optimized. Let us then define the actuator output parameters and discuss its input parameters, which can be used in optimization.

### *Output parameters*

- Generated deflection ($w_{gen}$) – the change of the membrane deflection due to applied voltage.

- Generated pressure ($P_{gen}$) – the equivalent of hydrostatic pressure, which causes the same membrane deflection as the applied voltage.
- Generated stress ($\sigma_{gen}$) – the change of the stress within the membrane due to applied voltage. We will be operating on difference $\sigma_x$- $\sigma_y$ in the membrane centre and on its edge what is mainly used in piezorezistive pressure sensors [69].
- Generated capacitance ($C_{gen}$) – the change of the capacitance between the membrane and the bottom electrode due to applied voltage.
- Generated volume ($Vol_{gen}$) – the change of the volume due to applied voltage. It is a basic parameter used in description of micro-pumps [90].
- Pull-in voltage ($V_{pull\text{-}in}$) – The voltage that causes the collapse of the membrane. The main parameter which defines the device operational range [91]. However, this parameter may be considered as the input parameter when it defines the gap distance (see paragraph below).

### *Input parameters*

Note that not all of actuator parameters, may be taken in optimization process.

- Material properties ($E$, $\nu$, $\alpha$) – The choice of material is usually made at the beginning of the project and is conditioned by project requirements. So, they will not be taken into consideration in optimization.
- Hydrostatic pressure ($P$) – The pressure between the membrane and the electrode is conditioned by technological process and type of application. The external pressure depends on environment in which the device will be used. Simulations showed that the best performance of an actuator is obtained when the membrane is initially flat. Thus, it is desirable to design an actuator without applied hydrostatic pressure. Due to this fact, this parameter will not be taken into account in further optimization.
- Membrane initial deflection ($w_0$) – this parameter depends on fabrication process (excluding buckling). Similarly to the above, this parameter will be omitted.
- Residual stress ($\sigma_0$) – this parameter also depends on fabrication process. Although there are methods to apply the specified value of residual stress [70], this parameter will not be taken into account. Generally, the compressive residual stress results in better performance, as the membrane is less stiff. The stress in tension has the opposite effect.
- Voltage ($V$) – the influence of this parameter on the device performance is obvious (according to the definition of electrostatic pressure). The larger voltage is applied, the better performance is obtained. Thus, this parameter will be omitted in optimization.

- Membrane shape – the choice between the circular and rectangular membrane depends on the designer needs.
- Membrane dimensions ($R_0$, $b$, $R$, $h$) – in optimization, the radius, the length of shorter edge, the membrane ratio and thickness will be taken into consideration.
- Gap distance ($d$) – the most important parameter. According to the definition of electrostatic pressure, the distance between electrodes should be as small as possible. Usually, there is no one value, which will be optimal for each case. As the membrane stiffness depends on its dimensions, the same applied voltage produces different membrane deflections. Thus, the gap distance should be recalculated every time what causes that the use of computer is required. In optimal case, the distance should be such that the pull-in voltage is a little bit larger than the voltage operational range.

Having all parameters defined, we can visualize the optimization process for electrostatic actuator as shown in Figure 2-5:

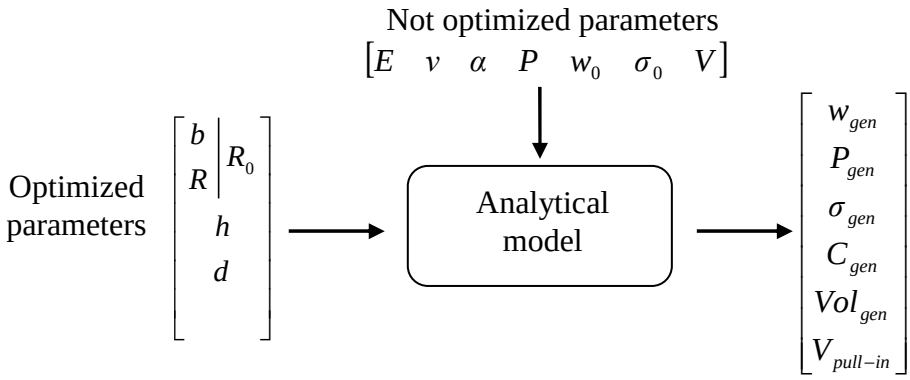


**Figure 2-5: Model of electrostatic actuator used in optimization.**

The function describing the actuator has three (circular membrane) or four (rectangular membrane) independent parameters and seven constants. On output it generates seven parameters describing the actuator behaviour. Fortunately, if we look closer at the output parameters, we can see that all of them are derivative of the deflection. Furthermore, usually only one of these parameters is important for a device used in a specific application. Thus, we can look upon them as independent, so the optimization remains as a one-objective problem.

### 2.1.2.1. Optimization tool

All above-mentioned facts were used to construct the tool performing the optimization process. The tool uses the same features of MATLAB® environment as the simulation tool. The main window of the tool is presented in Figure 2-6:

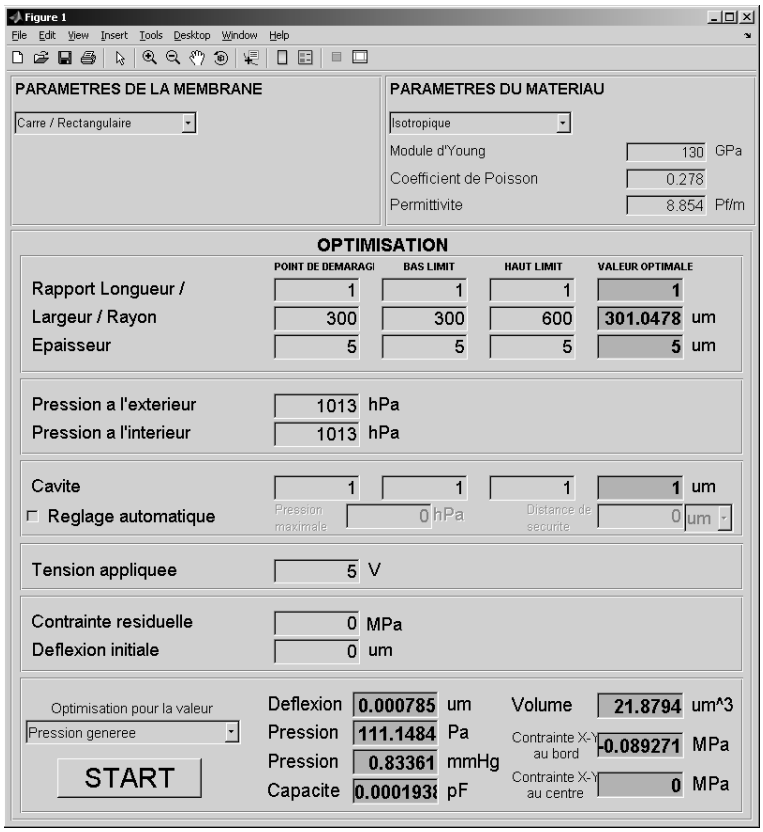


**Figure 2-6: Main window of the optimization tool in ®MATLAB GUI.**

The use of the tool is very simple. One has to define the constant parameters, set the lower and upper boundries of design variables and choose the output parameter, which is to be optimized. Then, the optimization procedure can be initialized and in a few second the results are presented on the screen. Furthermore, the tool allows manually defining the starting point for each variable. It has to be remarked that each procedure should be repeated for different starting points to verify if the optimization procedure has stopped at the global minimum for defined variable sets.

The last important matter concerns the performance of the tool. The typical optimization phase including all variables for rectangular membrane lasts about a few seconds. This value corresponds to the average of several runs performed for different starting points. If we take into consideration the fact that each procedure should be verified with FEM simulation and a few repetitions will be performed to get the exact results, the total optimization phase should take a few minutes. When compared to several hours needed for the optimization using FEM simulations, it is fairly obvious that the analytical model is more convenient in such task.

### 2.1.2.2. Electrode dimensions

In previous paragraphs we concerned on an actuator, which consists of flat bottom electrode with the same dimension as the membrane. It was caused by limitations of the reduced model i.e. the inability to change the electrode parameters. In this paragraph, we will try to estimate how much we can gain or loose by modifying the electrode. Firstly, we will analyze the influence of its size. According to the definition of electrostatic force, the larger electrode is, the larger force is. Thus, one should design the actuator with an electrode of the same dimensions as a membrane. Sometimes, due to fabrication process it is not possible e.g. when the electrode is deposited on a substrate. Then, the electrode "covers" less then 100% of membrane surface. Figure 2-7 shows the loss in performance versus the electrode surface normalized to the surface of the square membrane:

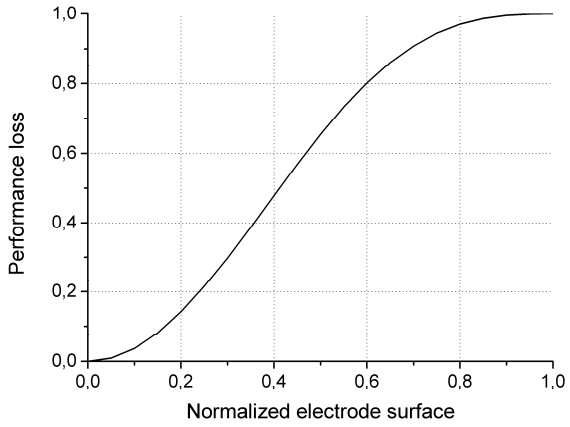


**Figure 2-7: Performance loss versus normalized electrode surface.**

It can be seen that for electrodes, which cover 80% of the membrane surface or more, the loss in performance is less than 3% and can be neglected. If for some reasons the electrode is smaller, the performance significantly decreases and this fact has to be taken into account.

Now, let us consider the electrode form. When the flat electrode is placed in optimal distance from the membrane, the maximal electrostatic pressure occurs only in the centre of the membrane. The optimal case is when the electrode has the same form as the membrane in the entire operational range. Such a form is difficult to fabricate, so we will simulate also the simpler design, which is a 3-steps electrode as shown in Figure 2-8 (steps width ratio is 4:3:3).

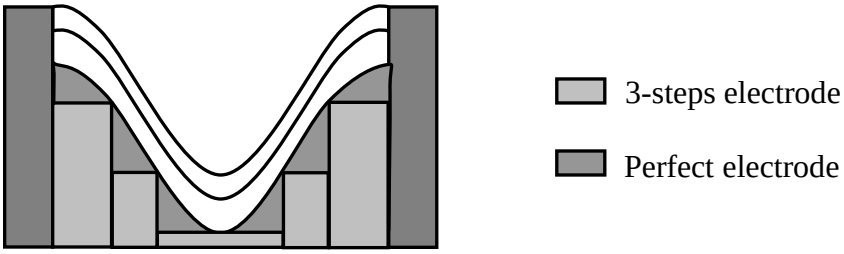


**Figure 2-8: Electrode designs.**

We performed the simulations for the square membrane without hydrostatic pressure and under the atmospheric pressure. In both cases, the electrode centre was placed at the same level. The gain in performance in the ratio to the flat electrode is shown in Table 2-1:

**Table 2-1: Gain in actuator performance in the ratio to the flat electrode.**

| Electrode | $P_h$=0 | $P_h$=$P_{atm}$ |
|---|---|---|
| Flat | 0% | 0% |
| 3-steps | 34% | 46% |
| Perfect | 123% | 524% |

One can see that the electrostatic actuation is much larger than for flat electrode, even for the 3-step electrode. Of course, the simulated gain by more than 100% is hard to obtain. Nevertheless a good design can significantly improve the performance. It has to be remarked that obtained values are valid only in shown example and might be different in other cases. The idea was only to show the possible benefits from modifying the electrode form.

## 2.2. Statistical approach

In previous chapter, we described the optimization phase, which gives us the optimal values of input parameters. If we fabricate the device using these values, we should obtain the desired device performance. Is it really possible? The answer is no if we take into the consideration the fact that the fabrication process is not perfect. The desired results may not be achieved as the equipment has some inaccuracy and some errors could be made by a human. Furthermore, some specified number of structures is fabricated at the same time. As the equipment does not have perfect reproducibility, the performance of each structure will be different. Thus, one should take into account all possible uncertainties and errors. In this paragraph, we will show how to use the analytical model to perform such an analysis.

### 2.2.1.1. Principles

Let us consider a simple function of one variable for which we found an optimal value. If we know its uncertainty, we can simply estimate the dispersion of the function value from derivative calculation [92]. However, this information is useless because it determines only the range in which the function value varies. For us, the most important information is its distribution, which allows estimating the number of devices having some specified performance. Thus, we need to define the distribution of input parameter, in other words to define the probability of occurrence of values from the specific range. For further discussion, we will use a uniform distribution and the most important in theory of probability the normal (Gaussian) distribution [93]. Both distributions are shown in Figure 2-9:

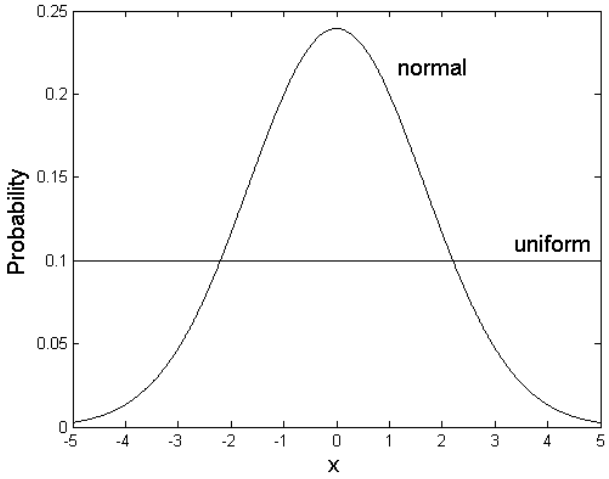


**Figure 2-9: Uniform and normal distribution.**

The probability function for uniform distribution has following form:

$$f(x) = \begin{cases} \dfrac{1}{x_2 - x_1}, & x \in < x_1, x_2 > \\ 0, & x < x_1 \text{ and } x > x_2 \end{cases}$$ **Equation 2-1**

and for normal distribution:

$$f(x) = \frac{1}{\sigma\sqrt{2\pi}} \exp\left( -\frac{(x-\mu)^2}{2\sigma^2} \right), \qquad -\infty < x < \infty$$ **Equation 2-2**

where $\sigma$ is a standard deviation and $\mu$ is an expected value. As one can see the normal distribution is determined in the whole set of real numbers. If we would like to set the range, we can use the three-sigma rule and set the limits as $< \mu - 3\sigma, \mu + 3\sigma >$. Then, almost all (99.7%) of the values lie within this range. Now, we need to specify the number of values in the set to get the reliable results. Figure 2-10 shows the expected value of the set versus the number of elements:

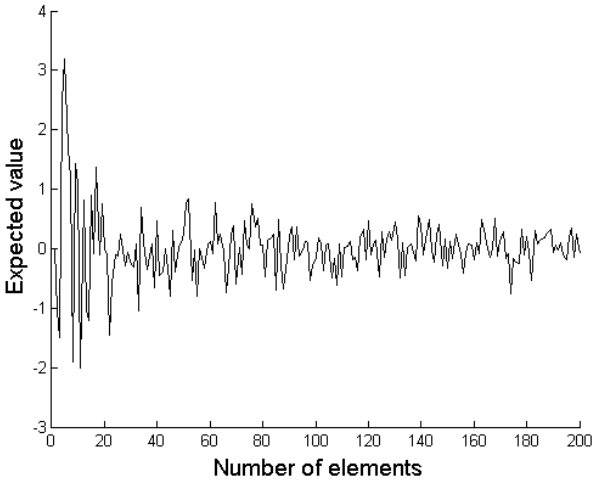


**Figure 2-10: Expected value for different number of elements in set.**

One can state that the expected value stabilizes for about 40 elements in set using the built-in MATLAB® function.

Having defined the distribution function, we can now describe the methodology of performing the statistical analysis. If we have defined the distribution of input parameters, we need to calculate the output values for each value from the set of input parameters to obtain the information about its distribution. Thus, it is desired to use a tool which is relatively fast. In case of our electrostatic actuator, the ideal solution is to use the developed analytical model, which can perform such an analysis in less than one second. Furthermore, we can significantly increase the number of elements in the set of input parameters and the analysis will take only a few seconds. This fact is very important e.g. when we need to estimate the

performance of structures fabricated in one cycle in which their amount is counted in hundreds or thousands.

### 2.2.1.2. Sources of uncertainties and errors

To determine the distribution of actuator input parameters, more precisely their maximal possible deviation, we need to study the source of this phenomenon. First, we will take into the consideration the membrane thickness. In our fabrication process, we use SOI wafers. The advantage of this solution is that we can choose the exact value of silicon thickness, which creates the membrane. Then, we can simply remove the bulk and the oxide using selective etching. Nevertheless, the wafers available on the market are also imperfect. The SOI wafer fabrication needs some specific actions that induce some uncertainties resulting in non-uniform thickness of silicon layer. As an example we will show the specification of wafers delivered by a vendor. They performed the thickness measurement in seven points on each of 11 SOI wafers. The results of such measurements are shown on Figure 2-11:

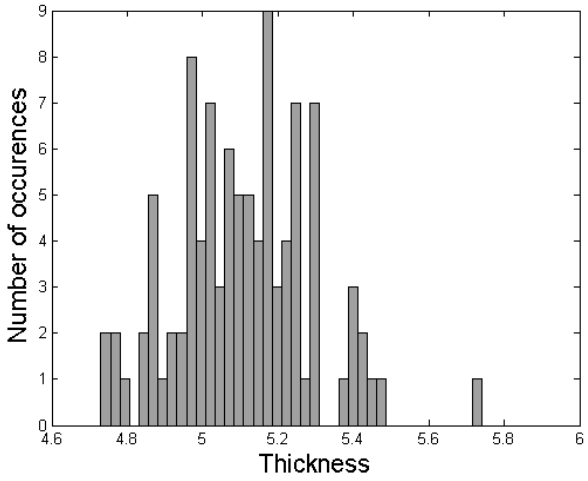


**Figure 2-11: Histogram of thickness (µm) distribution on SOI wafers.**

All wafers were specified as 5 µm ± 0.5 µm. From measurements, we obtained the expected value of 5.11 µm with standard deviation of 0.18 µm. This fact cannot be neglected as the membrane stiffness highly depends on its thickness (in cube). Then, the performance of the device on one wafer will be dependent on its position and the device might even be not operational. This shows why the statistical analysis is so important.

The next problem concerns the membrane length and width. They may vary due to inaccuracy during the masks fabrication and the photolithography used in transferring the membrane pattern into the wafer. The machines used in these processes are not perfect an

have some precision which may induce a dispersion in dimensions of transferred shapes. One has to be remarked that the alignment in photolithography made by a human has no affect on membrane dimensions. The photolithography is performed only once during membrane fabrication, so the alignment inaccuracy causes only the position shift of the membranes on the wafer.

The next factor, which has an effect on the actuator performance, is the gap distance. The cavity is formed by thermal oxidation on the silicon substrate. Although this process is well known and controllable, obtaining the exact desired thickness of the oxide layer on the whole wafer is not possible.

The last parameters, which cause the dispersion of actuator performance, are the residual stress and the initial deflection of the membrane. However, it is very hard to estimate the dispersion of these parameters as they strongly depend on quality of processed wafers, conditions during the fabrication and other factors. It can be determined only experimentally for each process separately.

Taking into consideration all above-mentioned facts, we have estimated the dispersion of all parameters for the fabrication process performed in LAAS. The values are presented in Table 2-2:

**Table 2-2: Dispersion of input parameters in fabrication process.**

| Input parameter | Maximal error |
|---|---|
| Membrane length | ±2 μm |
| Membrane width | ±2 μm |
| Membrane thickness | ±0.5 μm |
| Cavity depth | ±0.005 μm |
| Residual stress | ±5 MPa |
| Initial membrane deflection | ±0.05 μm |

Having all parameters defined, it is desirable to know which parameter has the strongest influence on the actuator performance. To obtain such information, we performed the simulations with one parameter that varies (normal distribution) and others set as constants for each above-mentioned parameter. The expected value $\mu$ and standard deviation $\sigma$ of generated pressure are presented in Table 2-3:

**Table 2-3: Expected value and standard deviation of generated pressure for each input parameter.**

| Input parameter | $\mu$ [Pa] | $\sigma$ [Pa] |
|---|---|---|
| Membrane length/width | 1859.21 | 47.48 |
| Membrane thickness | | 953.53 |
| Cavity depth | | 11.68 |
| Residual stress | | 52.35 |
| Membrane initial deflection | | 54.15 |

As one can see, almost all input parameters may slightly change the performance (standard deviation smaller than 3% of expected value). Most devices should fulfil the requirements even if the restrictions in performance are high. The most critical parameter is the membrane thickness whose standard deviation is almost 50% of expected value. It has to be remarked that in case of electrostatic actuator the greatly increased performance is also undesirable. As the cavity depth is uniform on whole wafer, the range of applied voltage will shorten significantly resulting in uselessness of the device. Thus, it is safe to say that the production yield will be very low and one has to use the SOI wafers because of high uniformity of their thickness. Of course, the results might be different for other conditions. The aim of this simulation was only to show how strong may be the influence of parameter dispersion on the actuator performance.

### 2.2.1.3. Statistical tool

Consequently, the tool allowing the statistical simulation was written in ®MATLAB environment. The main window is presented in Figure 2-12:

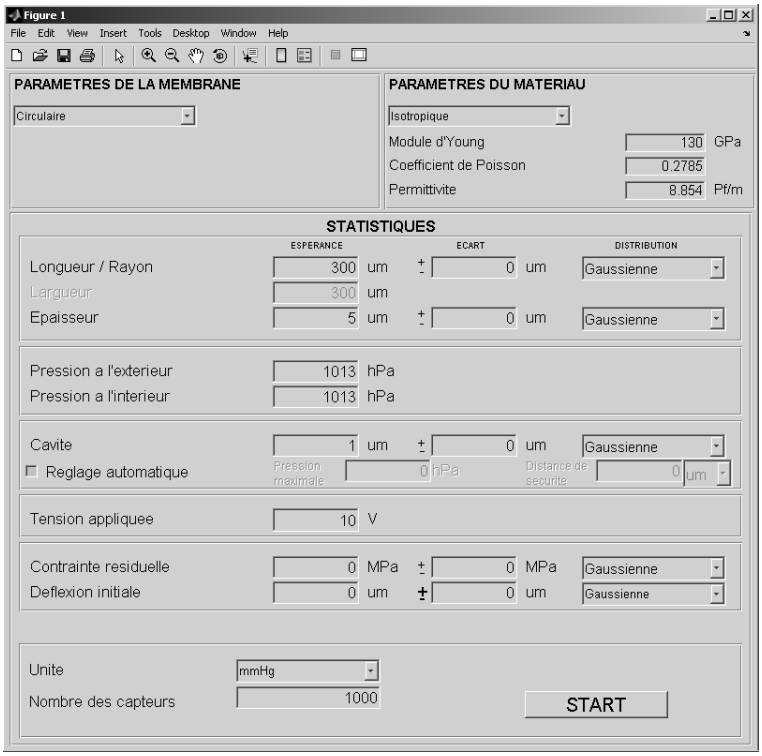


**Figure 2-12: Main window of statistical tool in MATLAB® GUI.**

It allows defining the desired value of each input parameter and their maximal dispersion and type of distribution. The results are shown on additional figures, which consist of the histogram and its basic parameters: the expected value (EX) and standard deviation (STD). The histograms are created for all input and output parameters. The typical histogram is shown in Figure 2-13:

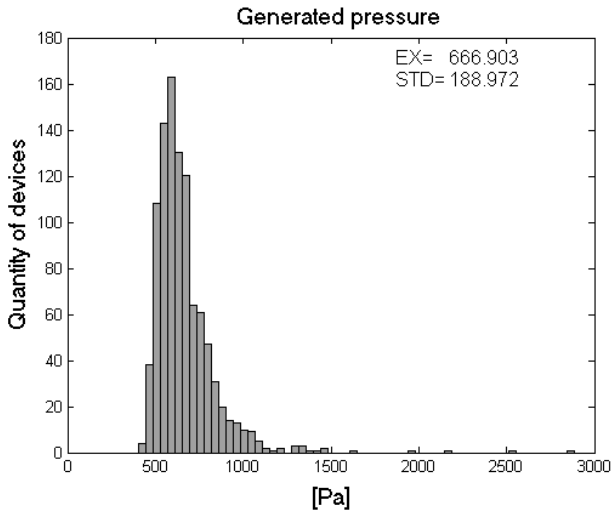


**Figure 2-13: Typical histogram of generated pressure obtained from statistical simulation.**

Let us describe a little bit the information contained in the histogram. The above histogram results from simulation performed for the set of one thousand elements, the number which corresponds to the quantity of devices on one wafer. The expected value of generated pressure

(667 Pa) gives us the information about the “average” performance of the device. It has to be remarked that this value may not correspond to the most probable value. In our case, 160 devices generate about 615 Pa. The standard deviation describes the dispersion of output parameter. A low standard deviation indicates that all data points are very close to the expected value, while large standard deviation indicates that the data are spread out over the large range of values. In our case a value of 189 Pa is relatively high as it is equal to about one third of the expected value. One can suppose that most of devices will have a performance in range of EX±STD. This information is useful in estimating the number of devices, which fulfil our requirements. E.g. we define that the minimum generated pressure should be 500 Pa and the minimum pull-in voltage should be higher than 40 V. Then, we get approximately 740 devices that meet these requirements. Thus, we can easily estimate the production yield and calculate the production cost. Furthermore, the distribution of output parameters and knowledge of the influence of input parameters allows improving the design.

The important point concerns the time needed to perform a statistical simulation. The typical simulation for the set of one thousand elements lasts about 30 seconds thanks to the analytical model. The same simulation with FEM based tool will take about 6 hours. The difference is significant so the use of analytical model is beneficial for the designer. Going further, we can compare the total time needed to perform complete simulation, which consists of behavioural analysis, optimization and statistical analysis. Using the tools based on analytical model, we need about ten to twenty minutes including all necessary repetitions and verification with FEM simulation needed to obtain the desired results. This proves that the analytical model is a better solution than the FEM simulation (in presented and similar cases), which needs about one day to perform the same task. Furthermore, the tools are easier in use, they need only to define input parameters and the calculations including the visualization of results are performed automatically.

Chapter 3

# Fabrication and characterization of test samples

## 3.1. Technological process

In order to verify the developed analytical model described in previous chapters, we will present the experimental work. Firstly, we will describe the technological process used in fabrication of electrostatic actuator. Then, we will discuss methods of measuring and consequently, the measurement setups will be presented. Finally, the experimental results will be compared to those obtained with analytical model and possible sources of mismatch will be indicated.

### 3.1.1. Fabrication steps

The complete process was performed in clean room situated in LAAS laboratory. It has to be remarked that, according to the project requirements, only structures with rectangular membranes with ratio *R* equal to 1 and 3 were fabricated. To validate the model for circular membrane, the capacitive pressure sensor, fabricated earlier in LAAS, was used. The process for this type of structure will be described separately.

Firstly, we will focus on the square and rectangular membranes. The overall chip size was set to 2000 µm × 720 µm. The membrane dimensions are then limited and for the first design (not optimized) was set to 300 µm × 300 µm for the square membrane and 900 µm × 300 µm for the rectangular membrane. In case of electrostatic actuator, the membrane cannot be fabricated using the typically used process such as KOH etching [94] and DRIE etching [95]. To allow the generation of electrostatic force, one needs the electrode beneath the membrane. Thus, one has to fabricate the membrane with a sealed cavity (vacuum) as shown in Figure 3-1.

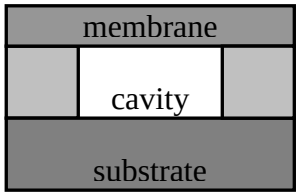


**Figure 3-1: Membrane with sealed cavity.**

The cavity can be formed by etching of sacrificial layer [96][97] or using the bonding technology [98]. In our case, when the membrane is made of silicon, the bonding technique is required. The most commonly employed techniques are anodic, intermediate-layer and direct bonding. In our work we will focus on the last technique. The important information is what kind of materials we will use in bonding.

The membrane will be made of silicon with thickness set to 5µm. It was shown in previous chapter that the variation of membrane thickness has a critical effect on membrane behaviour and should be as close as possible to the desired value. The membrane liberation by etching of silicon wafer is not a good idea as the etching process has to be well-controlled and even minor mistakes might be destructive. The better way is to use the ion-cut layer transfer [99], which allows fabricating the membrane with good thickness uniformity and small roughness of the surface. Nowadays, this process can be omitted thanks to SOI wafers available on the market that are fabricated with different thickness of silicon layer. In their production a wafer bonding technology such as smart-cut [100](similar to ion-cut layer) and SIMOX [101] technology are used which allows fabricating uniform, thin and smooth layers. Then, the membrane liberation is performed by removing the bulk (KOH or DRIE etching) and the buried oxide layer (HF etching). Both processes are highly selective, so they can be well controlled.

The choice of material used to form the bottom electrode depended on several factors. There are two possibilities: the silicon and the glass (PYREX 7740® or SD2). In case of silicon, which is a conductive material, there is no need to deposit the electrode. Furthermore, access to the electrode is easier and no canal is needed as for the glass substrate (Figure 3-2).

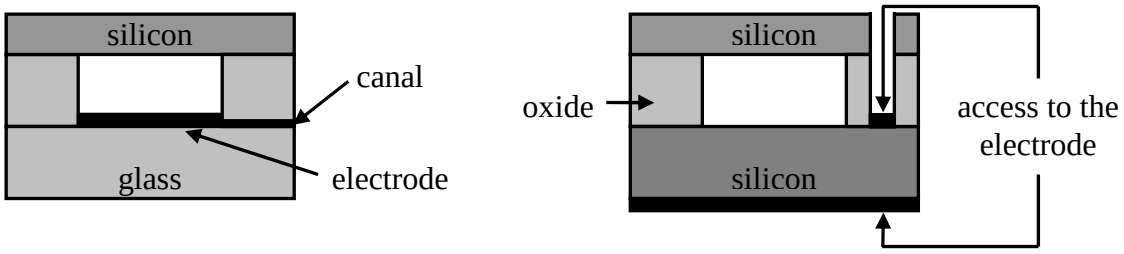


**Figure 3-2: Designs for glass and silicon substrate.**

The next problem concerns the thermomechanical stresses. The bonding process is performed at high temperature. As each material has different coefficient of thermal expansion, when the bonded structure returns to the ambient temperature, the materials shrinks resulting in appearance of undesired stress distribution within the structure. When the membrane is thick this stress may affect significantly the device operation. This problem was solved by development of the different type of the glass (SD2), which has similar coefficient of thermal expansion to the silicon resulting in significant reduction of the thermomechanical stresses (Figure 3-3). The only drawback of the silicon is the necessity of insulation between the membrane and the substrate. This induces a parasitic capacitance between the electrodes (Si-$SiO_2$-Si), which may hamper the measurement of the device capacitance.

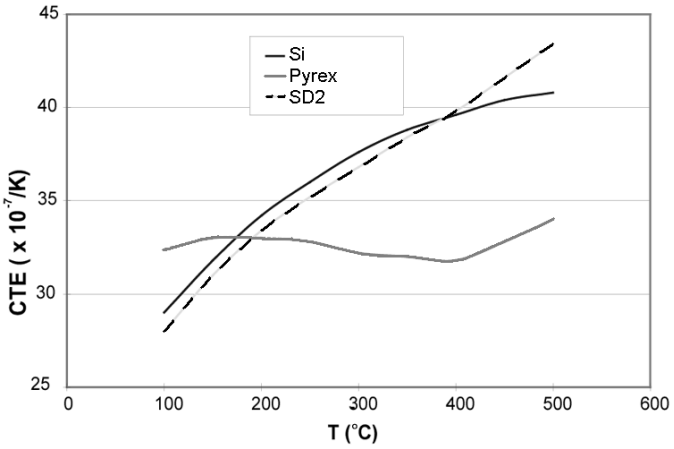


**Figure 3-3: Coefficient of thermal expansion for silicon, pyrex® and SD2 glass.**

All above-mentioned facts decided the choice of silicon as a substrate. Thus, the hydrophilic bonding between the silicon and oxide layer has to be performed which was studied in details in [102]. It has to be remarked that the wafers have to be as flat as possible and the total bow of the wafers should not exceed 5 µm [103]. At the beginning, the silicon wafer is covered with an oxide layer that contains the Si-O-Si and Si-OH (silanol) bonds. The amount of silanol groups determines the hydrophilicity of the surface. One can enhance the hydrophilicity by the most popular warm SC-1 in the solution of $NH_3$:$H_2O_2$:$H_2O$ in 1:1:5 ratio. Then, the wafers are placed in the bonding machine and the contact between them is established. The weak bonding is then created between the water molecules (Figure 3-4a). The strong bonding is obtained by applying the squeezing force and initial annealing, which causes the release of water molecules, and the bond is created by Van der Walls forces [104] (Figure 3-4b). After further annealing more water molecules are released and Si-O-Si bond is formed according to the following reaction (Figure 3-4c):

$$Si-OH \; + \; Si-OH \; \rightarrow \; Si-O-Si \; + \; H_2O \qquad \textbf{Equation 3-1}$$

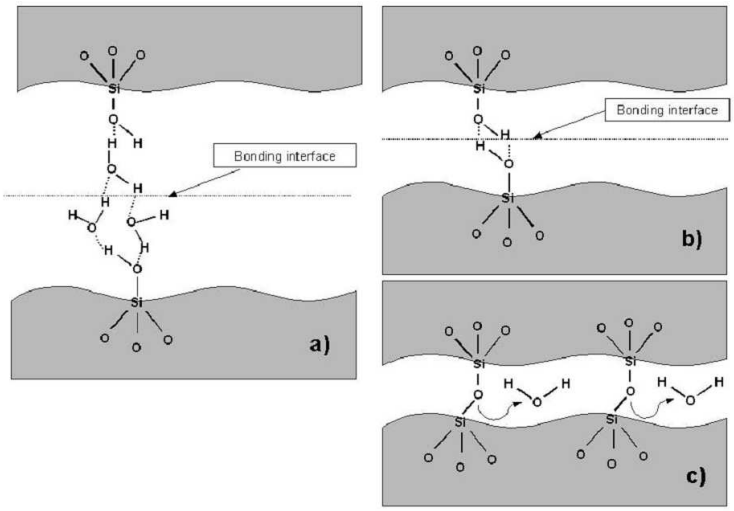


**Figure 3-4: Hydrophilic bonding: a) bonding via intermediate water molecules, b) bonding between two OH groups by Van der Walls forces, c) formation of Si-O-Si bonds.**

Now we can describe the whole fabrication process of electrostatic actuator presented in Figure 3-5. The process starts with the P-type (100) low resistivity (0.005 Ωm - 0.03 Ωm) silicon wafer (a). After the cleaning, the thermal dioxide is grown (1.28 μm or 2 μm depending on sample) (b). The cavities are formed by oxide etching process (c), which is sufficient for cavity up to 2 μm [105]. Then, the cavity bottom is protected against the short circuit with 500 Å thermally grown oxide (d). Due to project requirements, the edges of cavities are oriented in <110> direction that is the most efficient for piezorezistive sensors ($\pi_{44}$ has the highest value in P-type silicon [106]). Finally, the wafer is thermally treated in plasma $O_2$ before the bonding. The second one, N-type (100) high resistivity (3 Ωm - 6 Ωm) SOI wafer, is cleaned and warmed with SC-1 solution to make the surface hydrophilic. Both wafers are then bonded in AML-AWB bonder using direct wafer bonding (e). The process is performed in vacuum under the force of 2000 N and then annealed for 2h at 1150˚C to complete the bond. The backside oxide is etched with BHF (buffer HF) [107], the silicon bulk is removed in KOH (f) and buried oxide is etched with BHF (g) what leads to the membranes release. It has to be remarked that the membranes are deflected under the atmospheric pressure, as there is vacuum inside the cavities. Next, each cell on the wafer is separated by top silicon layer etch (h). Then, the boron implantation on top surface is performed to obtain good electrical contact (i). Openings to the substrate are created (j) and metallic contacts to both electrodes in lift-off process are made (k). This completes the whole process and the wafer is ready to cut. The complete mask used in the process is shown in APPENDIX F.

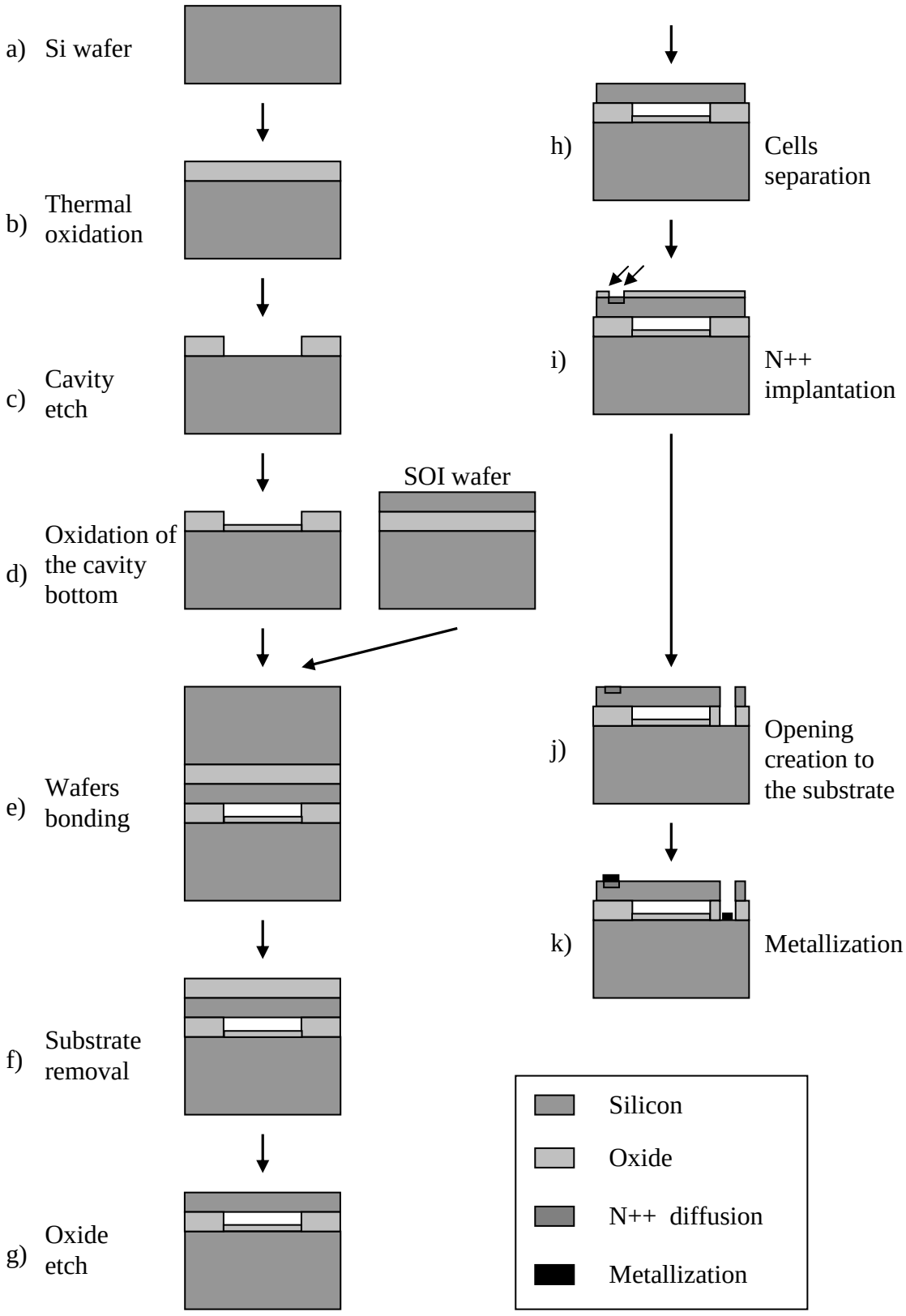


**Figure 3-5: Fabrication steps of electrostatic actuator.**

## 3.1.2. Process characterization

During the fabrication process, some parameters have to be controlled to be sure that the process is performed correctly and measured to facilitate the characterization. Now, we will focus only on the actuator based on rectangular membranes. The capacitive pressure sensor will be omitted as it was described precisely in [51] and it will be used only to validate the analytical model.

### *Wafer curvature*

As it was mentioned earlier, the wafer curvature is very important during the bonding process. To obtain a strong and correct bond, the wafers should be as flat as possible. The measurement of the wafers curvature before the bonding allows estimating correctness of this process and taking the actions to reduce too large curvatures. The measurement is performed using the mechanical profiler (Tencor stylus profiler [52] used in LAAS) along the wafer diameter as shown in Figure 3-6:

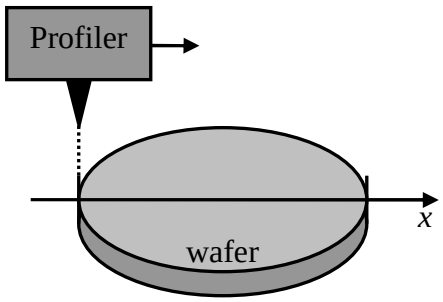


**Figure 3-6: Wafer curvature measurement principle using mechanical profiler.**

The typical obtained profile with the marked wafer bow is shown in Figure 3-7:

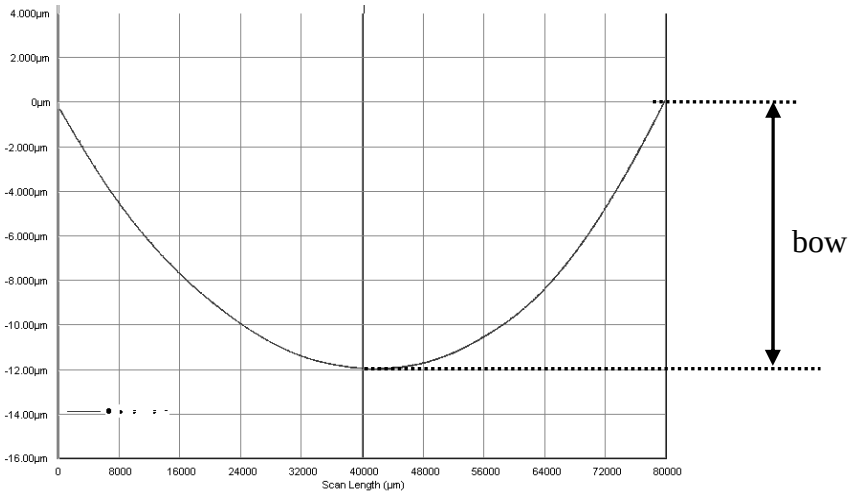


**Figure 3-7: Wafer curvature obtained from mechanical profiler.**

If the wafer bow is too large, it can be compensated by deposition of a compressive layer (e.g. silicon dioxide) or tensile layer (e.g. silicon nitride) on the proper side of the wafer:

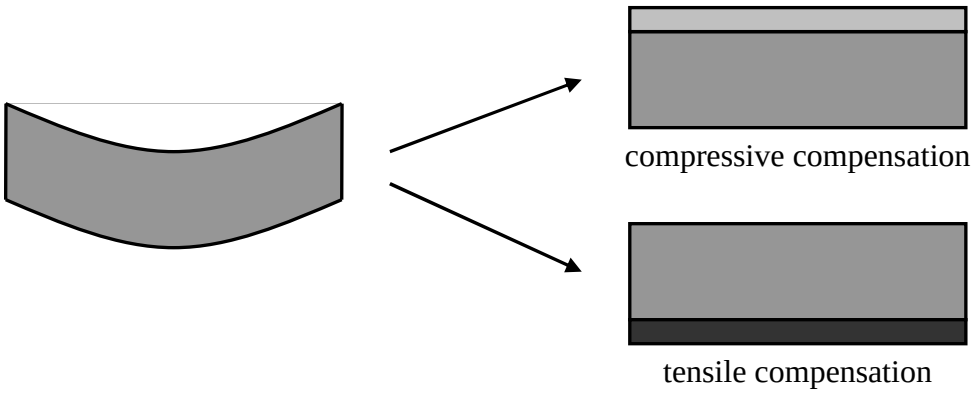


**Figure 3-8: Compensation of wafer curvature using compressive or tensile layer.**

### *Cavity depth and membrane dimensions*

After the cavity etching, one can simply measure its depth and the membrane dimensions as they correspond to the cavity size. It can be performed with mechanical profiler or optical profiler (Fogale Zoomsurf 3D [53] used in LAAS). The typical 3-D view and corresponding 2-D section of the square cavity is shown in Figure 3-9:

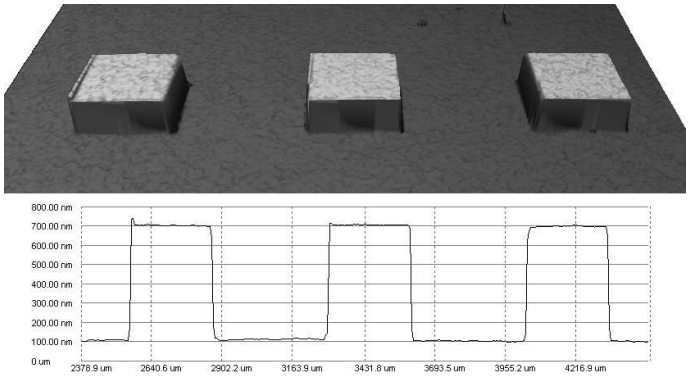


**Figure 3-9: 3-D view of square cavities and its corresponding section obtained by optical profiler.**

It has to be remarked that optical profiler does not allow measuring the cavity depth, as the reflectivity of the oxide layer depends on its thickness. Thus, the cavity depth has to be measured with mechanical profiler. Of course, all these measurements can be performed on the complete structure. However, at this stage one can stop the process if something went wrong avoiding unnecessary costs and wasting the time.

### *Bonding*

The proper bond is required to fabricate fully working device. Thus, the characterization of bond process in required. Several methods were developed such as the

bond imaging, cross-sectional analysis and bond-strength measurement. In our case, the first method is the most convenient because it is not destructive and can be used as in-process monitor. One of the imaging methods used in LAAS is an infrared transmission [109]. The typical image obtained from IR camera is presented in Figure 3-10:

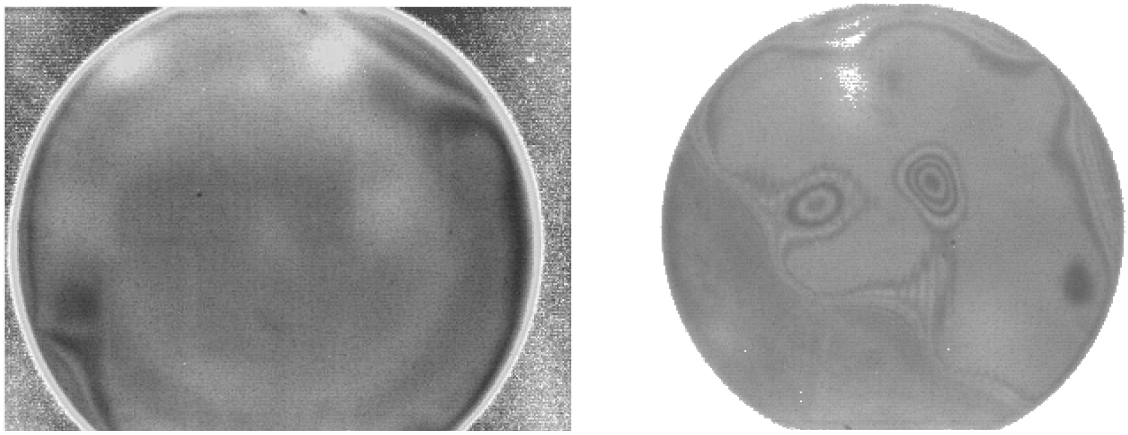

**Figure 3-10: Images of bonded wafers obtained from IR camera.**

The image of the perfectly bonded wafers should have uniform contrast (wafer on the left). Any imperfections can be found as changes in contrast (edges of both wafers). Furthermore, large unbonded regions (voids) appear as an interference pattern “Newton’s ring” (wafer on the right). The resolution of this method is one quarter of the wavelength of the IR camera, which is smaller than the resolution of other techniques such as X-rays or ultrasonic. However, the IR method is very simple and can be used directly before and after annealing.

## 3.2. Measurement set-up

In order to validate the analytical model of electrostatic actuator, some specific measurements have to be performed to verify the actuator performance. According to Equation 1-81 and Equation 1-93, the initial deflection and the residual stress has to be known to calculate the actuator performance. The experimental values can be obtained from measurements in three ways. The first one is a measurement of the mechanical response that is the deflection of the membrane. The value of maximal deflection is sufficient to obtain the values of generated deflection and pressure. For other parameters (generated stress, volume and capacitance), the membrane form is needed. One can use the calculated function describing the membrane form. However, we will also try to validate it experimentally. The second one is based on measurement of electrical response. The measurement of capacitance is much simpler but it does not give the information about the membrane form. Thus, the actuator performance has to be estimated using the calculated function describing the membrane deflection. The third one is a measurement of change in resistance. This method allows only to obtain the value of generated stress in the area, where gauges are placed. In this section, we will describe all these methods that will be used in experimental work. It has to be remarked that we performed on-wafer measurements only.

### 3.2.1. Initial deflection measurement

The measurement of initial deflection has to be performed in the environment of the pressure equal to this inside the cavity. In our case, there is a vacuum inside the cavity. To make the measurement possible, the wafer is placed inside the chamber (vacuum box) in which the vacuum is created using the pump. Then, the membrane deflection is measured using optical profiler as the chamber does not make possible to measure the electrical response (Figure 3-11). The precision of optical profiler is smaller than 10 nm, however, it is very fragile to the external vibrations, which may significantly affect on the precision.

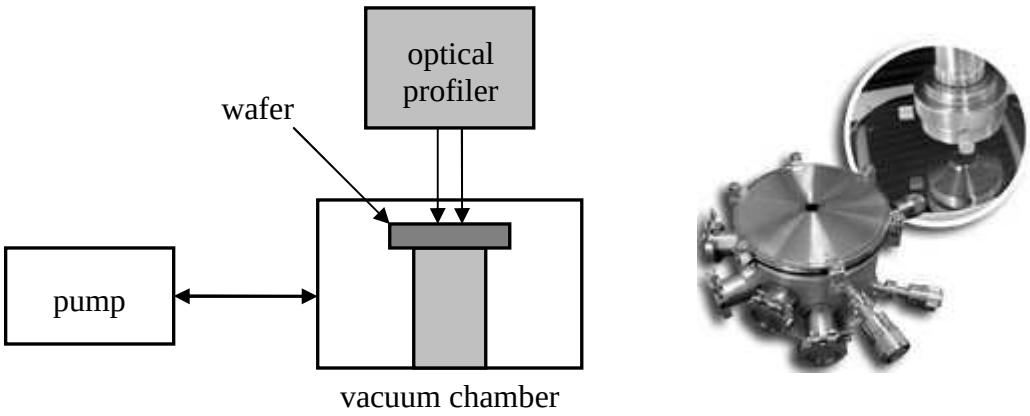


**Figure 3-11: Initial deflection measurement: the schema on the left, the photo on the right.**

The vacuum precision depends on pump performance and tightness of connections. In some cases, the proper vacuum could not be established. Thus, the initial deflection was estimated assuming that the membrane deflection is linearly dependent on applied pressure using the following formula:

$$w_{0\_\max} = w_{Pext\_\max} - P_{ext}\frac{w_{Pext\_\max} - w_{P0\_\max}}{P_{ext} - P_0} \qquad \textbf{Equation 3-2}$$

where $w_{pext\_max}$ is the membrane deflection under the atmospheric pressure, $w_{P0\_max}$ is the membrane deflection inside the chamber, $P_{ext}$ is the external pressure and $P_0$ is the pressure inside the cavity. The convention of sign for initial deflection is shown on Figure 3-12.

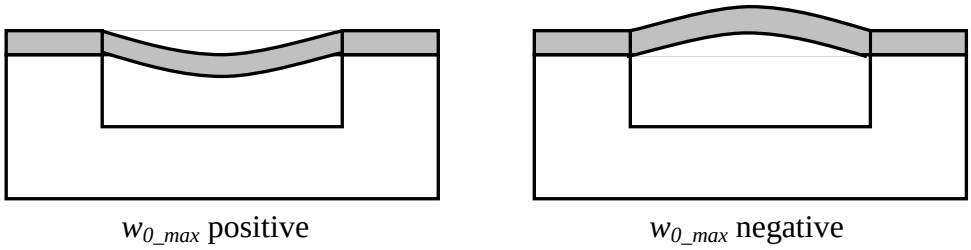


**Figure 3-12: Convention of sign for initial deflection.**

## 3.2.2. Residual stress measurement

The measurement of the residual stress is performed indirectly. One assumes that the membrane deflection is linearly dependent on the applied pressure. Then, we can measure the membrane deflection under two different pressures and use Equation 1-81 or Equation 1-93 for residual stress calculation. One can simply use the initial deflection of the membrane and measure the deflection under the atmospheric pressure. In most cases this procedure is valid. It can give incorrect results when the membrane is buckled. To avoid this, if the membrane is initially pumped (the membrane is bent into the opposite direction than the electrode), one can observe the membrane behaviour when increasing the pressure inside the chamber. If the

deflection is changing linearly, the membrane is not buckled and estimation of residual stress can be performed. If the switching effect occurs, one has to choose two points in which the membrane is bent towards the electrode.

### 3.2.3. Mechanical response measurement

The measurement is simply performed using an optical profiler. Firstly, the thickness of the membrane and cavity depth are measured using the openings made on each test structure. Then, the voltage is applied using the probes placed on the specific plots. The external pressure is equal to the atmospheric pressure, so the membrane is already bended due to hydrostatic pressure difference. The photo of the profiler and view of the sample is shown in Figure 3-13:

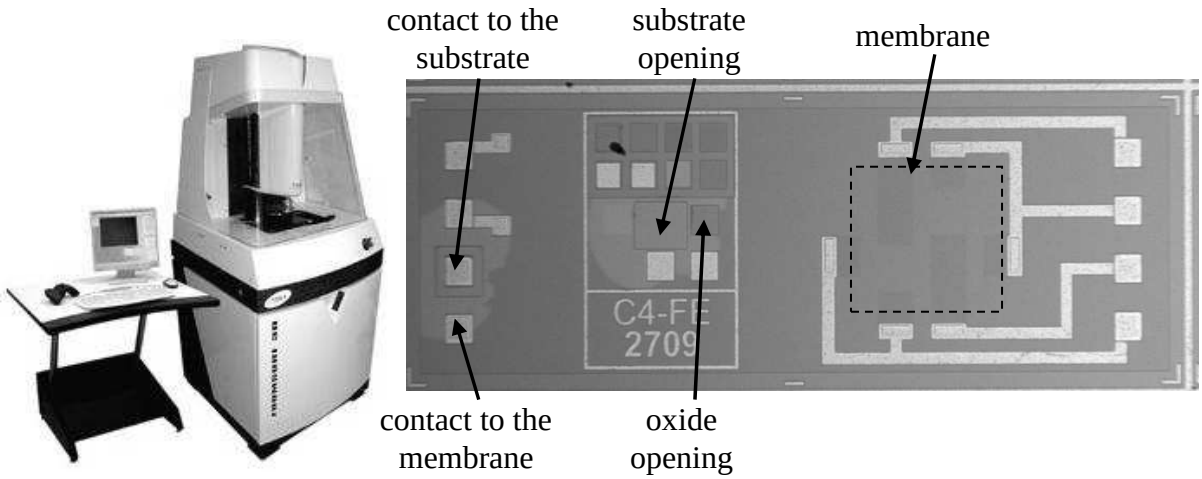


**Figure 3-13: Optical profiler on the left and test structure with marked connections on the right.**

Using obtained 3-D view of the structure, one can simply extract the maximal membrane deflection and the membrane form needed for calculation of the actuator performance.

### 3.2.4. Capacitance response measurement

The measurement of capacitance is performed using the impedance analyzer (Agilent 4294A). Using the probes, the sample contacts are connected to the analyzer, which measures the parallel capacitance of the equivalent circuit by applying the sinusoidal voltage (Figure 3-14). The analyzer allows applying the bias voltage that is used for the membrane actuation. The maximal bias voltage is 40 V, which may not be sufficient to plot the full characteristic of the actuator. In this case, a partial characteristic will be plotted only. It has to be remarked that any parasitic capacitance will also be measured. One has to take this fact into account in case of test structures fabricated on silicon substrate, as they have a parasitic capacitance Si-$SiO_2$-

Si. Thus, this measurement will be performed for structures with circular membrane only, as they have no parasitic capacitance (see paragraph 3.4).

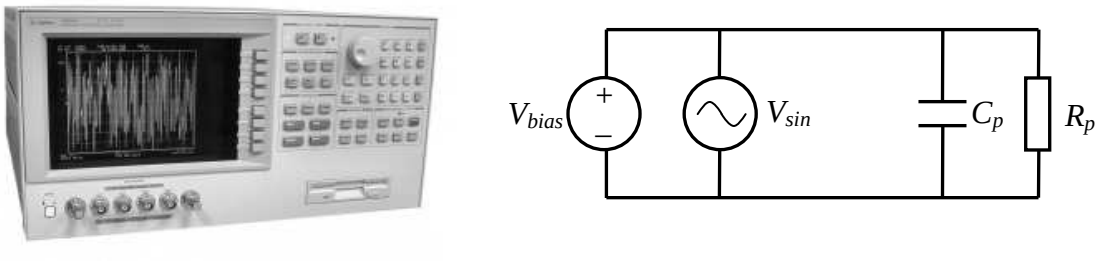


**Figure 3-14: Capacitance measurement set-up and its equivalent circuit.**

## 3.2.5. Resistance measurement

This method is the most important for the project, as it will be used in final product in autocalibration mode. The membrane is bent due to the pressure difference (external pressure equal to the atmospheric pressure). The voltage is applied using the probes placed on the specific plots. Then, the change in resistance is measured using ohmmeter (Figure 3-15). It has to be remarked that this measurement will be performed on specially designed samples with open Wheatstone bridge, which allow resistance measurement of one gauge. In final product, the output value will be the voltage, which is proportional to the resistance change of all gauges in the bridge. The gauges are placed on edges of square membrane and in the centre of rectangular membrane. Their dimensions are 40 μm × 4 μm × 0.5 μm and they have nonuniform doping profile in depth due to fabrication process. For more information refer to [111].

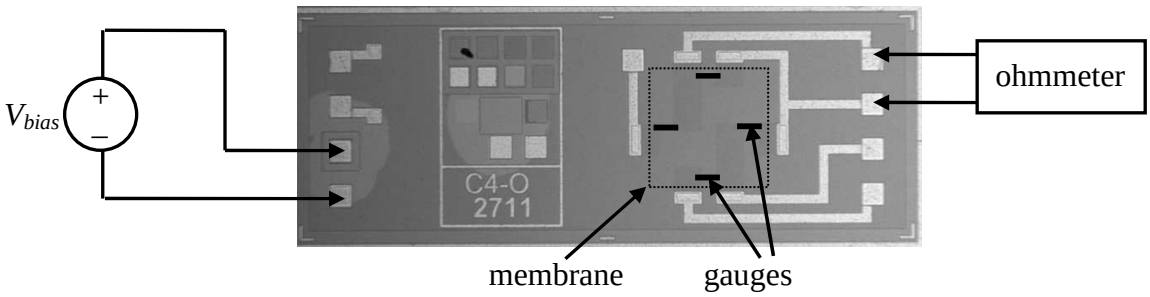


**Figure 3-15: Resistance measurement schema.**

## 3.3. Actuator performance

As it was mentioned earlier, the test structures, fabricated during this work, consist of square and rectangular ($R$=3) membranes. Thus, we will focus mostly on these structures. The structures with circular membranes will be described separately. All results obtained during measurements will be compared to those obtained with developed analytical model by calculating the relative difference between them. As the comparison of deflection in unstable zone is not reliable, the difference is calculated for voltage, which generates the same deflection or capacitance, according to the following relation:

$$\Delta V = -\frac{V_{anal} - V_{meas}}{V_{meas}}, \qquad w(V_{anal}) = w(V_{meas}), \qquad C(V_{anal}) = C(V_{meas}) \qquad \textbf{Equation 3-3}$$

where $V_{anal}$ and $V_{meas}$ are voltages obtained from calculation and measurements, respectively. Negative and positive values of the difference correspond to underestimation and overestimation, respectively. In measurements of resistance, the difference is calculated between the measured and calculated values of resistance for the same applied voltage, according to the following relation:

$$\Delta R = -\frac{R_{anal}(V) - R_{meas}(V)}{R_{meas}(V)} \qquad \textbf{Equation 3-4}$$

In calculations of resistance, two analytical models will be used: the first one, described in this dissertation, which allows calculation of the stress distribution within the membrane and the second one, described in [111], which allows calculation of resistance change in gauge due to applied stress.

### 3.3.1. Square and rectangular membranes

The structures were fabricated on five wafers using the different conditions. Firstly, the wafers have different curvatures. Some of them were compensated to obtain the surface as flat as possible. Secondly, the different bonding conditions were checked in order to obtain the best bonding strength. Finally, the temperature of annealing during the phosphor implantation may also have the influence on actuator performance. The conditions of all wafers are presented in Table 3-1. The wafers will be described separately.

**Table 3-1: Conditions used in actuators fabrication depending on wafer.**

| Wafer | 1 | 2 | 3 | 4 / 5 |
|---|---|---|---|---|
| Si bow [μm] | ⌒ 17.7 | ⌒ 12.5 | ⌣ 5.8 | ⌣ 0.7 / 0.8 |
| Si compensation | none | none | none | none |
| SOI bow [μm] | ⌒ 16.3 | ⌒ 33.2 | ⌒ 82.5 | ⌒ 83.3 / 81.2 |
| SOI compensation | none | none | $SiO_2$ (bulk side) ⌣ 1.2 | $SiO_2$ (bulk side) ⌣ 3 / 2.5 |
| Temperature of bond squeeze [˚C] | 150 | 20 | 150 | 150 |
| Temperature of implantation annealing [˚C] | 1000 | 1000 | 1200 | 1000 |
| Cavity depth [μm] | 1.25 | 1.25 | 2 | 2 |

### *Wafer 1*

The cavity depth was set to 1.25 μm (measured values were in range from 1.245 μm to 1.26 μm). Unfortunately, the cavities were to shallow and all rectangular membranes touched the electrode. Thus, only square membranes were measured. The wafer was not perfectly bonded (the characterization with IR camera was not performed) and measurement of only its one half was possible. Six structures were completely measured. Their initial deflections are presented in Table 3-2:

**Table 3-2: Measurement of initial deflection for wafer no. 1.**

| Structure | $w_0$ [nm] | Structure | $w_0$ [nm] |
|---|---|---|---|
| C3204 | -291 | C3802 | 109 |
| C3705 | -227 | C3302 | -23 |
| C4402 | 126 | C3202 | -74 |

The negative and positive values indicate that the membrane is initially pumped or deflected towards the electrode, respectively. It can be seen that the values differ significantly which may indicate that the membranes are buckled. To verify this, the external pressure was gradually increased for pumped structures. The deflection was changing linearly without the switching effect what proved that the critical residual stress was not achieved. Thus, this phenomenon has to have some other source. Probably it is an effect of improper bonding caused by inappropriate conditions or too large curvatures of the wafers. Then, the membrane thickness was measured and the values of residual stress were calculated (Table 3-3).

**Table 3-3: Membrane thickness and residual stress for wafer no. 1.**

| Structure | $h$ [μm] | $\sigma_0$ [MPa] | Structure | $h$ [μm] | $\sigma_0$ [MPa] |
|---|---|---|---|---|---|
| C3204 | 4.78 | -18 | C3802 | 4.96 | -29 |
| C3705 | 4.9 | -5 | C3302 | 4.75 | -21 |
| C4402 | 5.17 | -6 | C3202 | 4.8 | -33 |

For all structures, the membrane was in compression (what was expected), as the membranes are initially deflected (in case of tension the membrane should be initially flat). The dispersion in values of residual stress is not high and it may have a connection with bonding precision. Next, the structures were measured under the applied voltage. Figure 3-16 presents characteristics $w$=f($V$) obtained from measurements and calculation and corresponding relative difference (Equation 3-3).

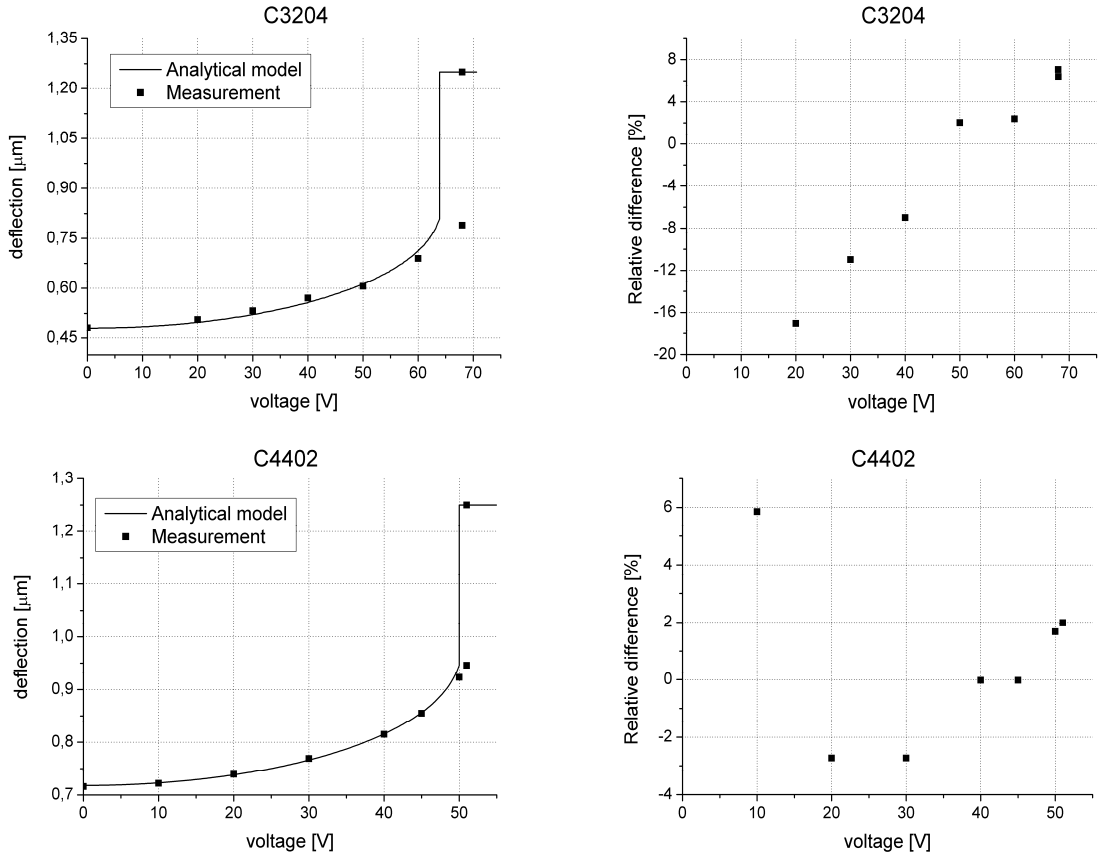

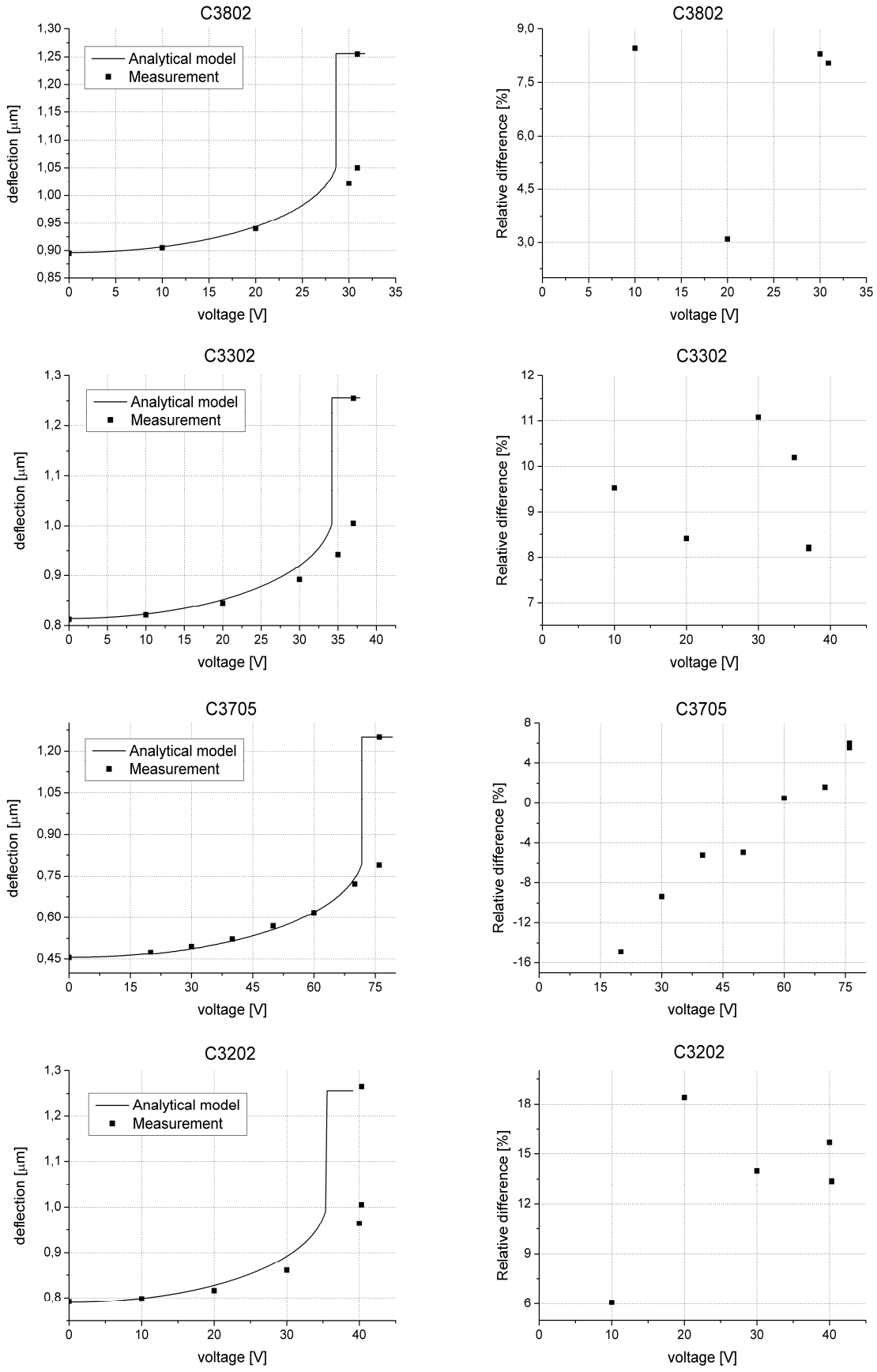


**Figure 3-16: Characteristics *w*=f(*V*) and corresponding relative difference of structures from wafer no. 1.**

The results for all structures are quite similar. For each structure, analytical model overestimates the results for voltages close to pull-in voltage (maximum 13%). The difference in the middle range depends on structure and varies from -16% to 18%. It has to be emphasized that for small voltages, which generate small deflection, the measurement error is more significant. There is no dependence of initial deflection or residual stress what means that the actuator behaviour remains still the same and can be described with analytical model with good precision.

### *Wafer 2*

The second wafer was processed similarly as the previous one except the bond squeeze that was performed in room temperature (20˚C). The wafer was characterized with IR camera after the bonding what is shown in Figure 3-17:

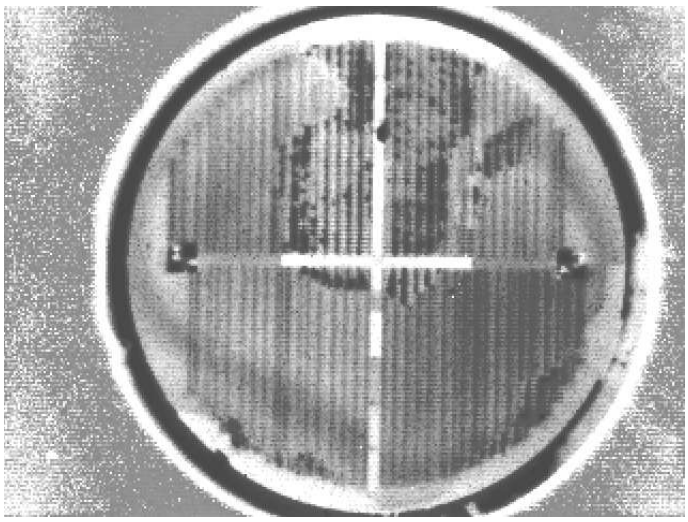

**Figure 3-17: Image from IR camera for wafer no. 2.**

The wafers were not properly bonded in the top region, which caused the destruction of the membrane layer during further processing. The other part seems to be well bonded except the wafer edge. The structures with rectangular membrane were immeasurable as the cavity depth was too small. The values of initial deflection for square membranes are shown in Table 3-4:

**Table 3-4: Initial deflection of structures for wafer no. 2.**

| Structure | $w_0$ [nm] | Structure | $w_0$ [nm] | Structure | $w_0$ [nm] |
|---|---|---|---|---|---|
| C1001 | 250 | C2404 | -330 | C5102 | 195 |
| C1201 | 247 | C2402 | 290 | C3306 | 214 |
| C1805 | -316 | C0705 | -480 | C3606 | 156 |
| C1804 | -306 | | | | |

One can observe the same effect as for previous wafer. The membranes are initially deflected in both directions and are not buckled what was experimentally verified. For further measurements only four structures were chosen as the others broke down during actuation. The membrane thickness and calculated residual stress are shown in Table 1-1:

**Table 3-5: Membrane thickness and residual stress for wafer no. 2.**

| Structure | $h$ [μm] | $\sigma_0$ [MPa] | Structure | $h$ [μm] | $\sigma_0$ [MPa] |
|---|---|---|---|---|---|
| C0705 | 4.6 | -55 | C3306 | 5.02 | -27 |
| C5102 | 5.5 | -24 | C3606 | 5.12 | -26 |

The residual stress has good reproducibility for membrane with positive initial deflection. The one initially pumped has residual stress two times larger what may be correlated together. However, the result from one sample is not sufficient to draw such a conclusion. Next, the characteristics $w$=f($V$) obtained form measurements and analytical model and corresponding relative difference (Equation 3-3) were plotted in Figure 3-18 in order to investigate the behaviour of actuators. The cavity depth varied in range from 1.278 μm to 1.291 μm.

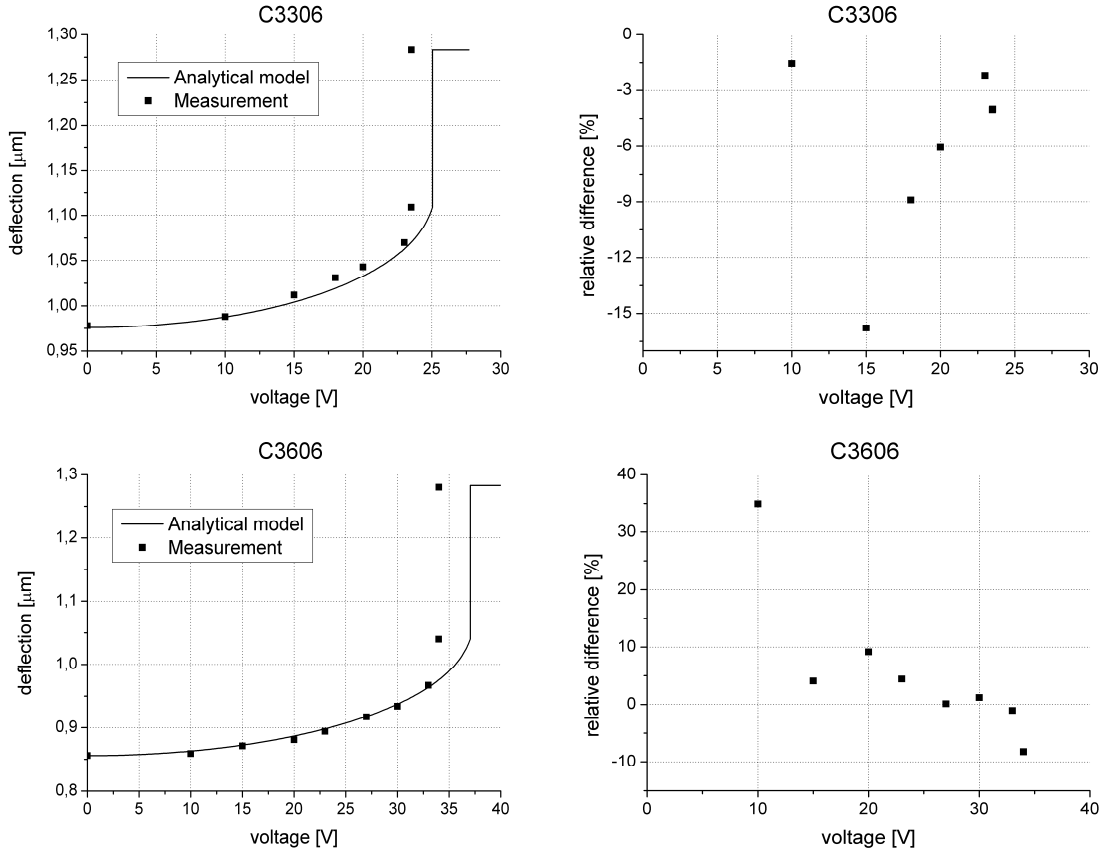

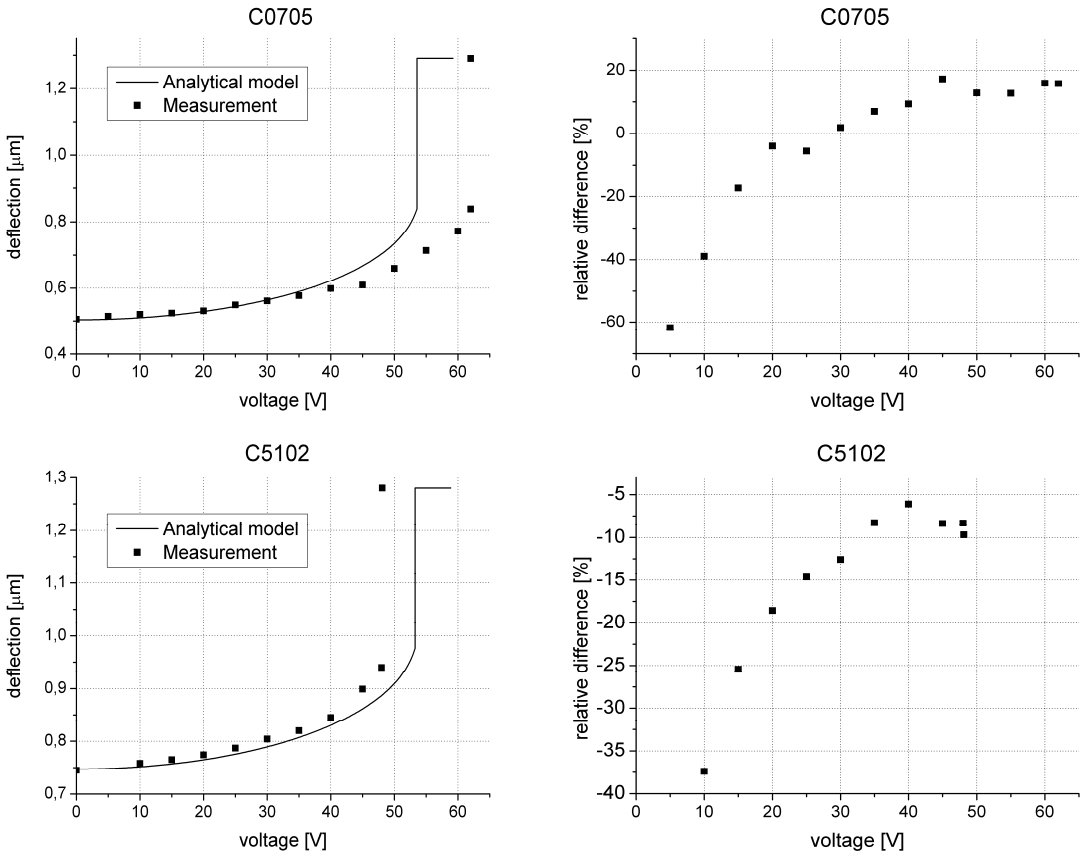


**Figure 3-18: Characteristics *w*=f(*V*) and corresponding relative difference of structures from wafer no. 2.**

For this wafer we obtained the opposite results. The calculations are now underestimated by about 10% maximum. Only for the structure with larger residual stress (C0705) the calculations are overestimated by 14% that may be caused by localization of the structure in a region of corrupted bond. For small voltages the difference is more significant and reaches 60% what is caused by higher influence of measurement error.

### *Wafer 3*

The next wafer was designed to allow measurement of rectangular membranes. Thus, the cavity depth was increased to 2 μm (measured values were in range from 1.96 μm to 2.02 μm). The wafers were quite well bonded except the edge and a few voids in the middle (Figure 3-19). The SOI wafer had to be compensated by oxide deposition on the backside, as its bow was higher than 80μm.

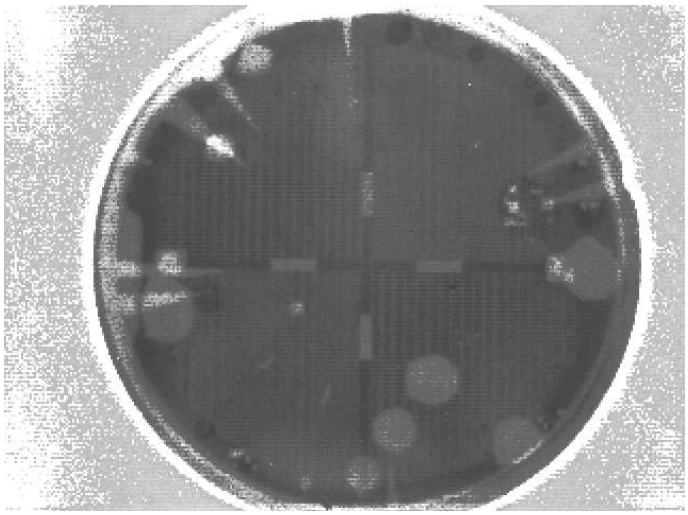

**Figure 3-19: Image from IR camera for wafer no. 3.**

Unfortunately, all rectangular membranes were deformed, as shown in Figure 3-20 (membranes under the atmospheric pressure), probably due to higher temperature of annealing. Thus, the measurement was not performed as it would be incorrect.

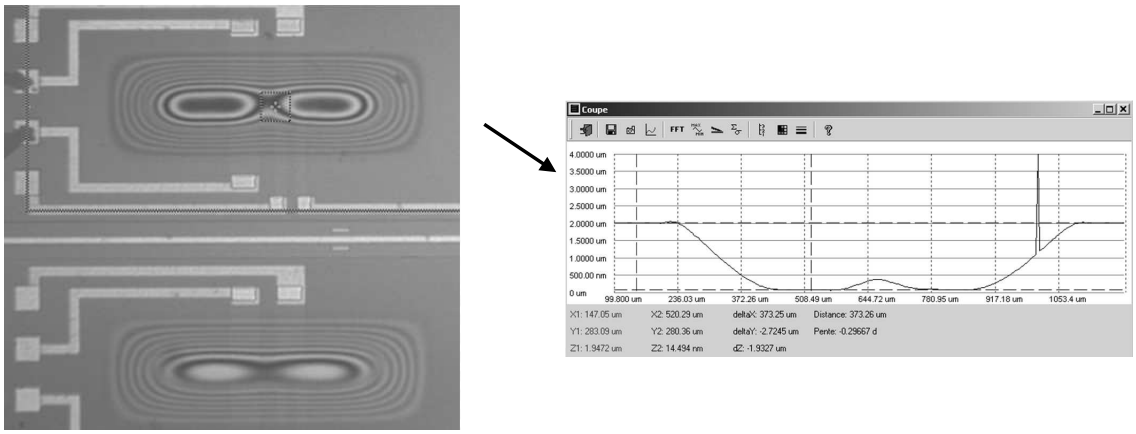


**Figure 3-20: Deformation of rectangular membranes due to higher temperature of annealing.**

Thus, only square membranes were measured. The values of initial deflection are shown in Table 3-6:

**Table 3-6: Initial deflection of structures for wafer no. 3.**

| Structure | $w_0$ [nm] | Structure | $w_0$ [nm] | Structure | $w_0$ [nm] |
|---|---|---|---|---|---|
| C0403 | -252 | C0404 | -260 | C0506 | -208 |
| C0503 | -240 | C0811 | -243 | C0806 | -173 |
| C0204 | -254 | C0306 | -222 | C0205 | -153 |

It can be seen that the results are quite reproducible. All membranes are initially pumped and the value of initial deflection oscillates in range from -150 nm to -260 nm. The measured structures were placed close to the centre of the wafer where the bonding should be proper.

Then, the membrane thickness was measured and the residual stress was calculated. The results are shown in Table 3-7:

**Table 3-7: Membrane thickness and residual stress for wafer no. 3.**

| Structure | $h$ [μm] | $\sigma_0$ [MPa] | Structure | $h$ [μm] | $\sigma_0$ [MPa] |
|---|---|---|---|---|---|
| C0503 | 5.3 | -117 | C0306 | 5.3 | -127 |
| C0204 | 5.1 | -103 | C0506 | 5.25 | -114 |
| C0404 | 5.34 | -105 | C0806 | 5.19 | -103 |
| C0811 | 5.2 | -109 | C0205 | 5.22 | -93 |

The dispersion of residual stress is very small which may prove that the bonding is correct and the structures are reproducible. It has to be remarked that the value of residual stress is three times larger than for previous wafers. It is probably caused by annealing performed at higher temperature (at 1200˚C). Next, the structures were measured under the applied voltage. Because the results were very similar, we will present characteristics only for four structures.

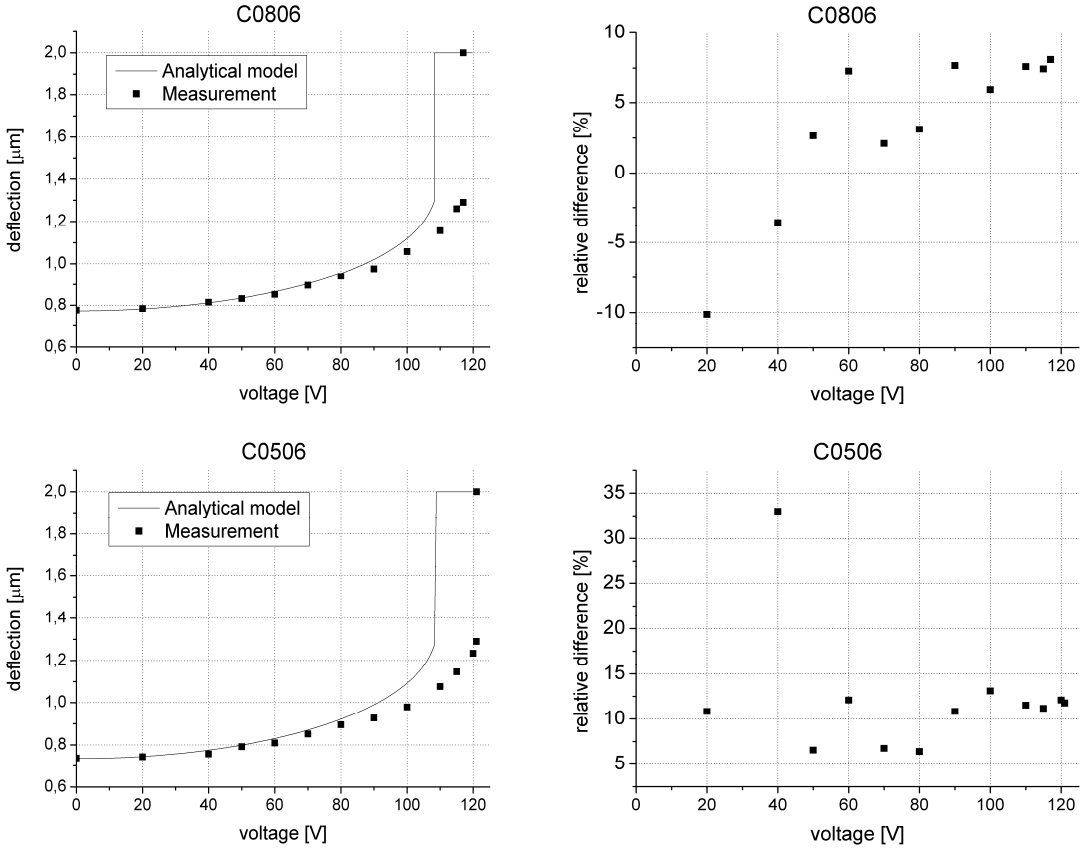

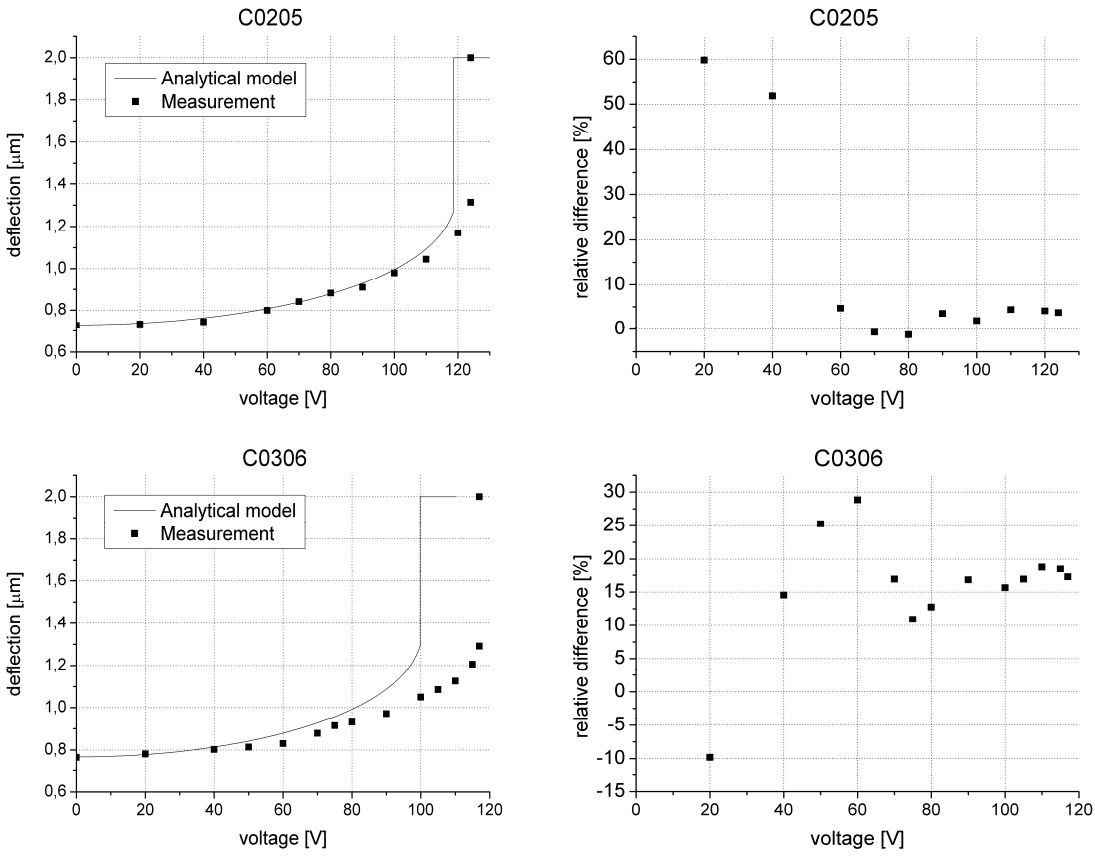


**Figure 3-21: Characteristics *w*=f(*V*) and corresponding relative difference of structures from wafer no. 3.**

The characteristics are quite similar to those obtained for wafer no.1. The calculations are overestimated by 20% maximum. For two structures (C0806 and C0205) whose residual stress is a little bit lower, the difference is significantly lower and is about 7%. It has to be remarked that even if the structures have much higher residual stress and are probably much more deformed due to conditions of fabrication process, the analytical model is still comparable to the measurements.

### *Wafer 4*

The last wafer was fabricated using the same conditions as the previous one except the temperature of annealing, which was 1000˚C. This allowed the measurement of rectangular membrane whose form seemed to be correct. The quality of bonding was the best of all measured wafers as shown in Figure 3-22:

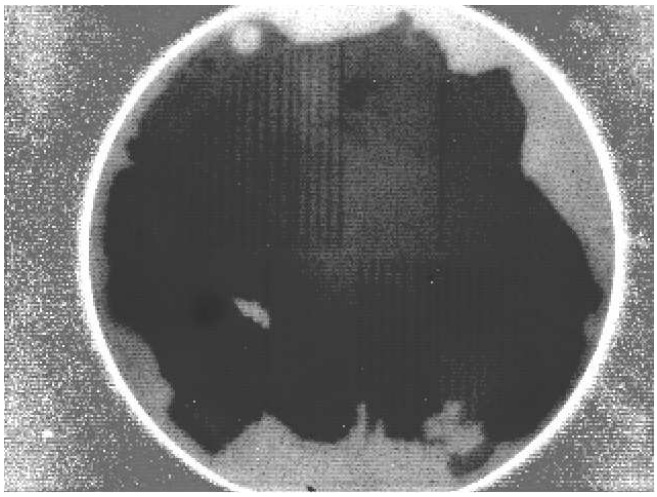

**Figure 3-22: Image from IR camera for wafer no. 4.**

As usual, the edge of the wafer is unbonded. However, the middle of the wafer is well bonded except one visible void. The results of initial deflection measurement are shown in Table 3-8 (the first letter in the structure name indicates its type: C – square membrane, R – rectangular membrane):

**Table 3-8: Initial deflection of structures for wafer no. 4.**

| Structure | $w_0$ [nm] | Structure | $w_0$ [nm] | Structure | $w_0$ [nm] | Structure | $W_0$ [nm] |
|---|---|---|---|---|---|---|---|
| R0401 | -31 | R0504 | 7 | C0101 | -132 | C0303 | -112 |
| R0301 | -183 | R0404 | 71 | C0201 | -104 | C0203 | -92 |
| R0102 | -112 | R0304 | -12 | C0301 | -116 | C0103 | -97 |
| R0202 | -136 | R0204 | 6 | C0401 | -115 | C0105 | -76 |
| R0302 | -30 | R0104 | -120 | C0501 | -101 | C0205 | -88 |
| R0402 | 11 | R0103 | -147 | C0601 | -102 | C0305 | -110 |
| R0502 | 79 | R0303 | -118 | C0603 | -107 | C0405 | -81 |
| R0602 | 64 | R0503 | 13 | C0503 | -113 | C0505 | -108 |
| R0604 | -25 | R0603 | 79 | C0403 | -108 | C0605 | -102 |

All square membranes are pumped and theirs initial deflections are close to -100 nm. For rectangular membranes the results are not reproducible. One can find the membranes deflected in both directions whit deflection varying from -180 nm to 80 nm. Probably, it is caused by higher influence of technological process quality on rectangular membranes i.e. due to plastic deformations (higher local stress value in rectangular membranes than in square ones). Next, the residual stress was calculated for some structures (Table 3-9):

**Table 3-9: Membrane thickness and residual stress for wafer no. 4.**

| Structure | $h$ [μm] | $\sigma_0$ [MPa] | Structure | $h$ [μm] | $\sigma_0$ [MPa] |
|---|---|---|---|---|---|
| R0102 | 5.28 | -32 | C0101 | 5.16 | -48 |
| R0604 | 5.35 | -29 | C0201 | 5.19 | -47 |
| R0504 | 5.4 | -28 | C0103 | 5.31 | -53 |
| R0103 | 5.39 | -33 | C0105 | 5.29 | -49 |
| R0603 | 5.4 | -30 | C0605 | 5.34 | -50 |
| R0503 | 5.4 | -31 | C0505 | 5.34 | -52 |

The dispersion in results is very small, even if the initial deflection is not reproducible, which may indicate that all structures are placed in region of uniform bond. The higher value of residual stress for square membranes may be caused by its smaller surface on which the stress is distributed. Next, the characteristic $w$=f($V$) were plotted for six structures (Figure 3-23):

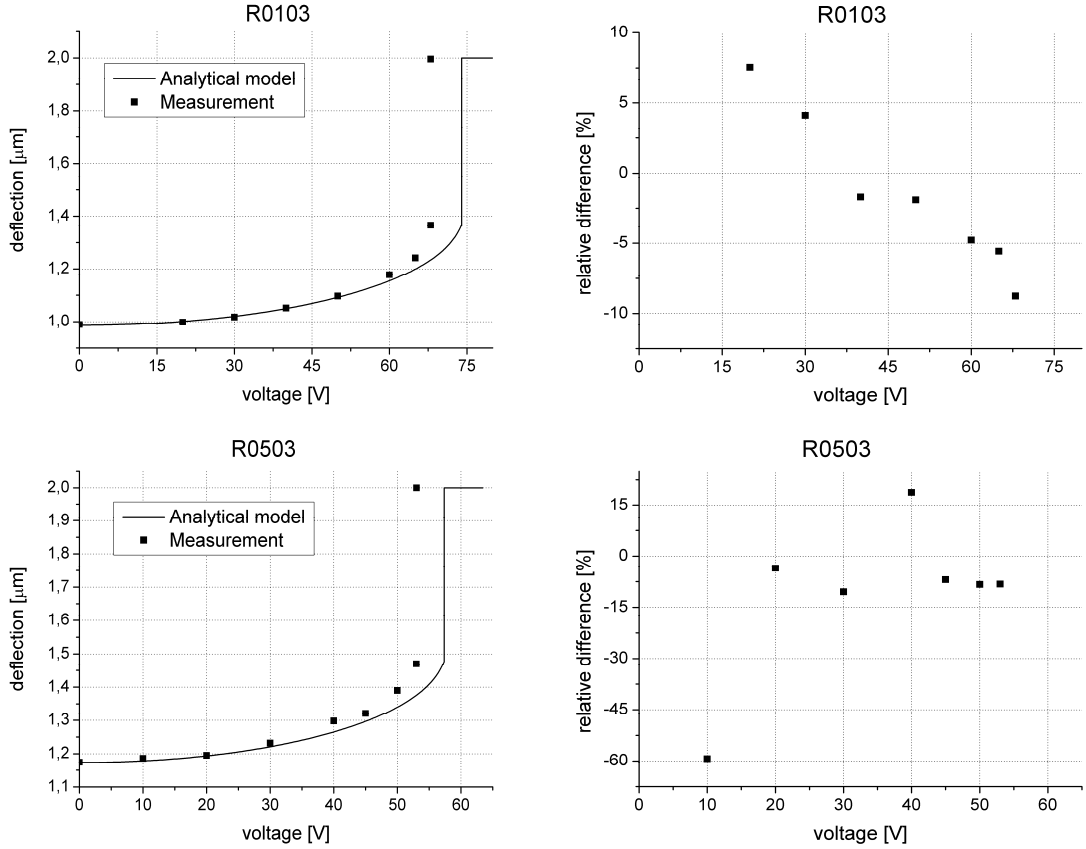

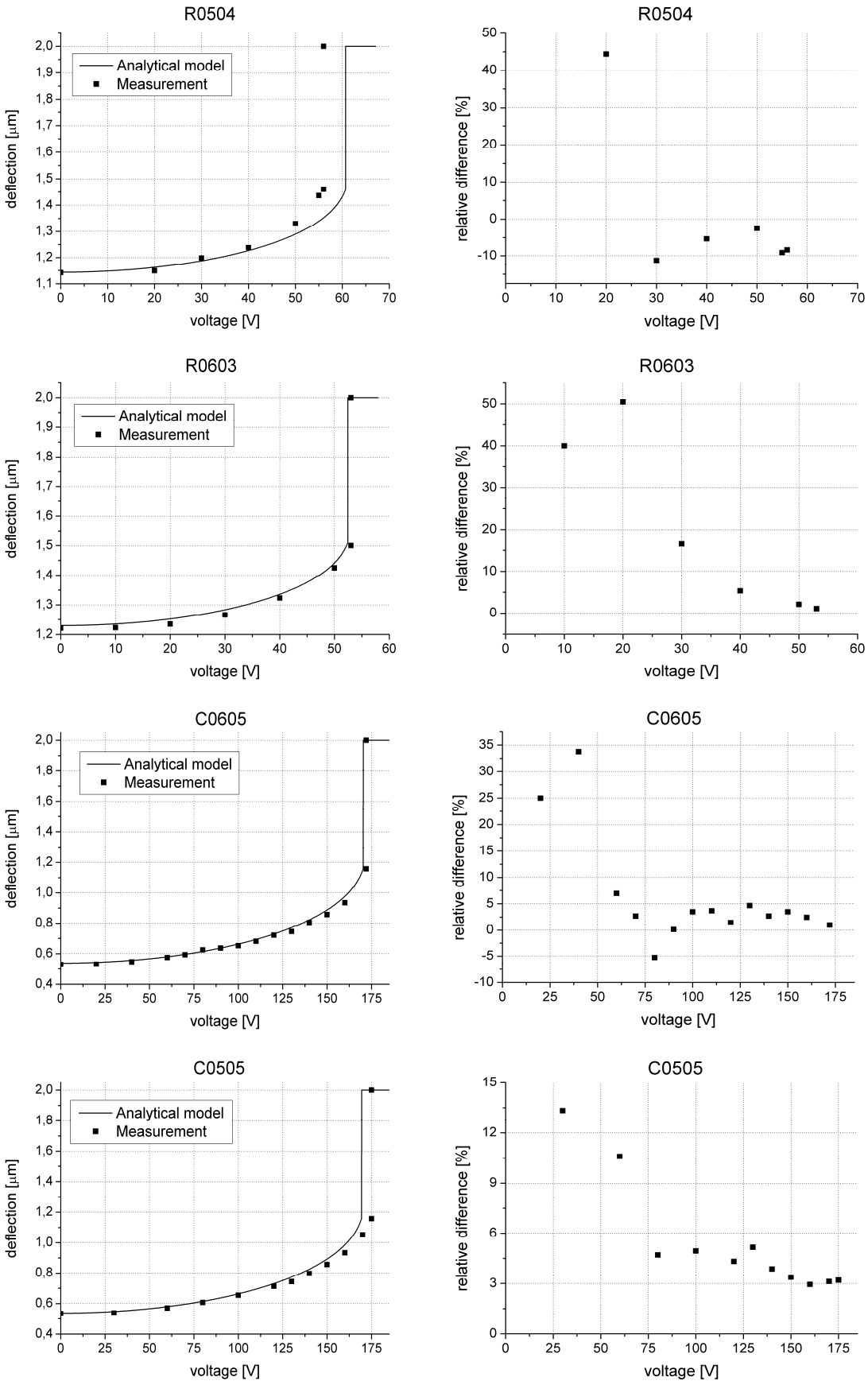


**Figure 3-23: Characteristics *w*=f(*V*) of structures from wafer no. 4.**

The results obtained for square membranes are very close to the analytical model. The calculations are overestimated by only 5% for square membranes. In case of rectangular membranes, the results are not so accordant. They are underestimated by 12% maximum what is acceptable in engineering calculations. Furthermore, the characteristics obtained for structure R0603 agrees with calculation almost perfectly (only 2% of overestimation). Thus, one can state that analytical model is precise enough also for rectangular membranes. For small voltages, the same as for structures from previous wafer, the differences are more significant and reach up to 50% due to higher influence of measurement error.

### *Membrane form*

In order to verify the membrane form, we analyzed the membrane without applied voltage and under the voltage close to the pull-in voltage. In Figure 3-24, we plotted the forms for square membrane (C0605 – wafer no.4):

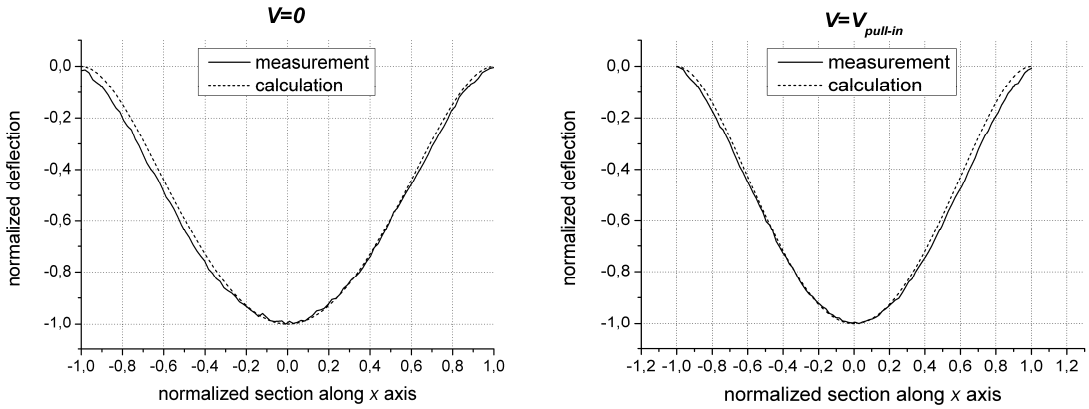


**Figure 3-24: Comparison between calculated and measured forms for square membrane.**

The forms are quite similar. The visible mismatch may be caused by use of ideal clamping in calculations. Next, we analyzed the form of rectangular membrane (R0503 – wafer no.4). The comparison is shown in Figure 3-25:

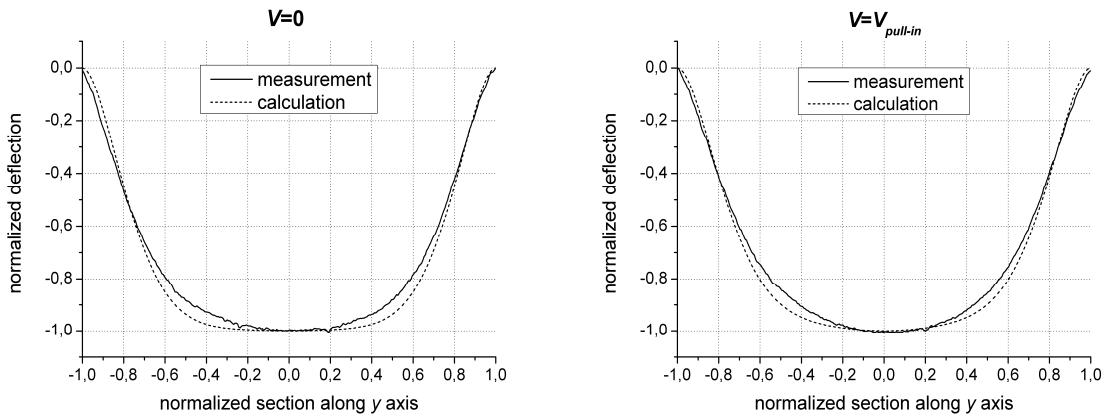


**Figure 3-25: Comparison between calculated and measured forms for rectangular membrane.**

The measured forms are not flat in the middle as those obtained from calculations. Probably, it is caused by some phenomena evolved in fabrication process that will be described in paragraph 3.3.2. In Figure 3-26, the comparison between measured forms without and with applied voltage for both types of membranes is shown.

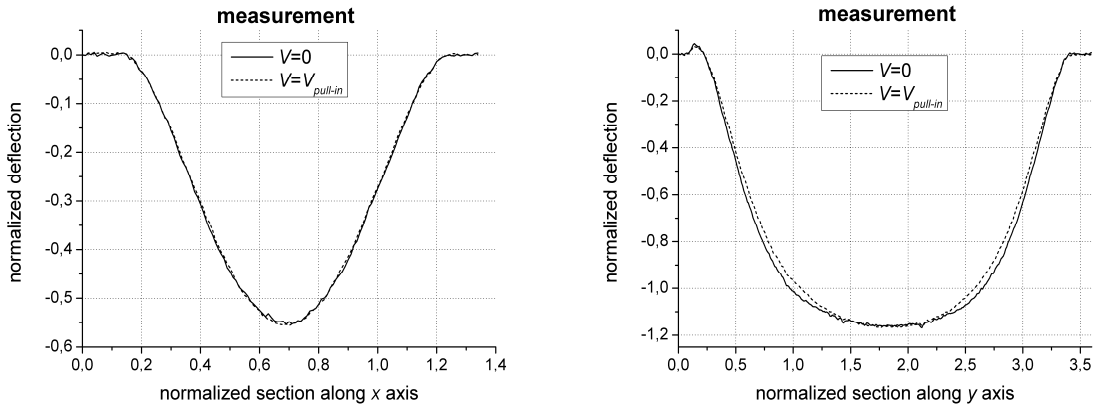


**Figure 3-26: Comparison between measured forms without and with applied voltage for square and rectangular membrane.**

As one can see, the influence of voltage is not visible for square membrane because the membrane is initially deflected under the atmospheric pressure. For rectangular membrane, the difference is visible what proves that the analytical model correctly calculates the membrane form.

### *Resistance measurement*

It can be seen in previous sections that the measurements of deflection are not precise enough for small voltages, as the generated deflections are comparable with the precision of measurement equipment. Therefore, we performed the measurements of resistance change in order to validate the model for small voltages. The structures, which allow such measurements, were fabricated on fifth wafer using similar conditions as for wafer no. 4

(Table 3-1). Two structures with square membrane were measured. Firstly, the values of initial deflection and residual stress were calculated (Table 3-10), which are similar to those obtained for wafer no. 4.

**Table 3-10: Membrane thickness, initial deflection and residual stress for wafer no. 5.**

| Structure | $h$ [μm] | $w_0$ [nm] | $\sigma_0$ [MPa] |
|---|---|---|---|
| C0203 | 5.25 | -97 | -46 |
| C2411 | 5.28 | -108 | -51 |

Then, the resistance change was measured for voltages in range of 0 V to 60 V. The characteristics for both structures and corresponding relative difference between the analytical model are shown in Figure 3-27.

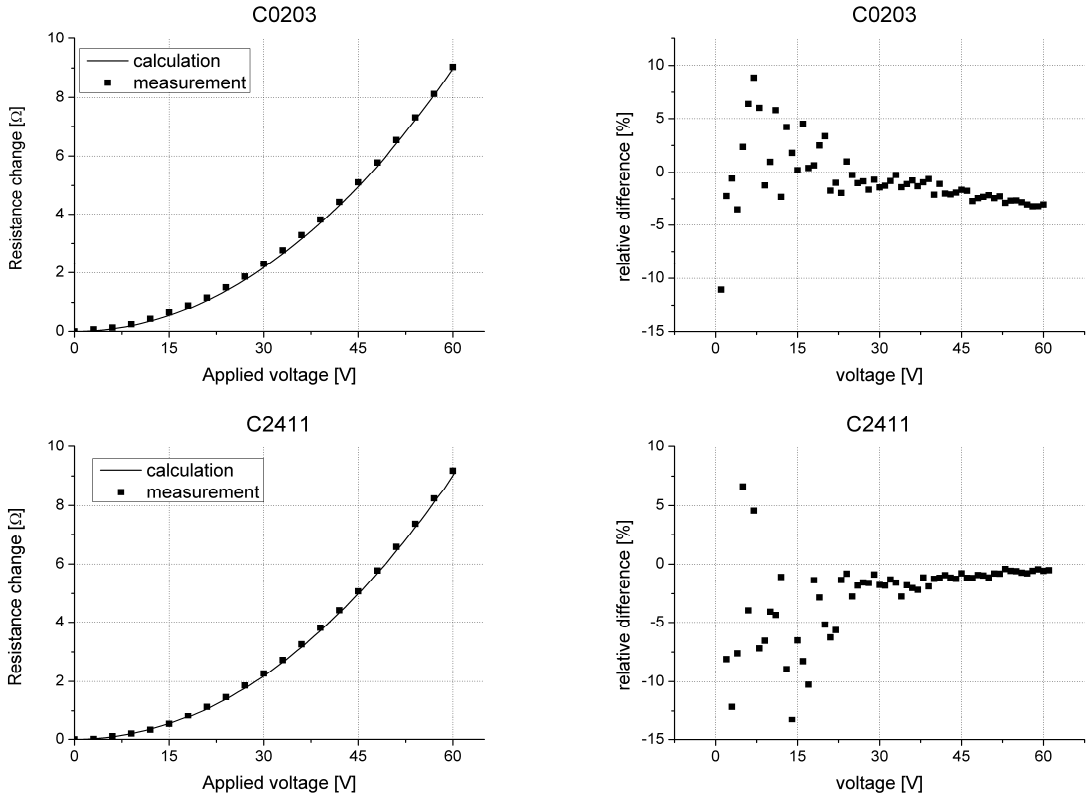


**Figure 3-27: Characteristics $\Delta R$=f($V$) of structures from wafer no. 5.**

As one can see, the results are quite similar. For high voltages, the difference is less than 3%, so it can be neglected. For small voltages (the zoom in this range is presented in Figure 3-28), which are the most interesting for the project, the dispersion is higher due to higher influence of measurement error and reaches up to 14%. It has to be emphasized also that the analytical model incorrectly calculates the stress distribution within the membrane (especially at the edge) due to unreal clamping conditions. However, the difference is usually smaller than 10%

what proves that this measurement method is more reliable than the measurement of deflection and shows that the analytical model correctly describes the membrane behaviour for small voltages also.

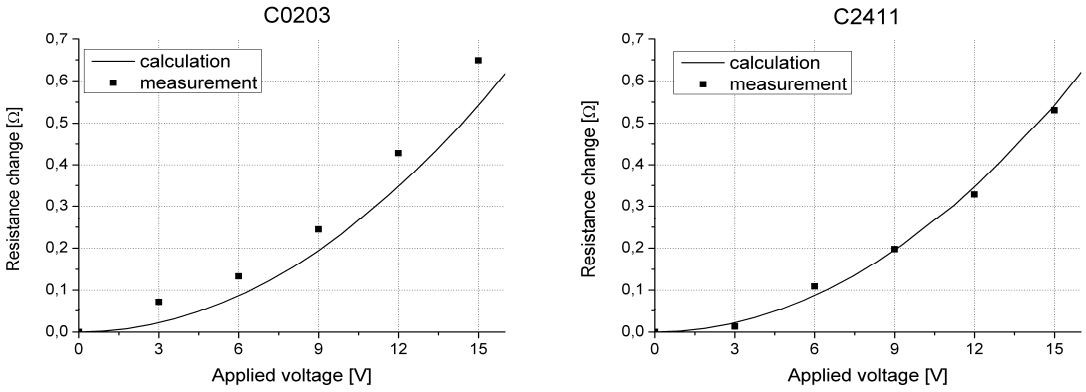


**Figure 3-28: Zoom of characteristics $\Delta R$=f($V$) of structures from wafer no. 5 for small voltages.**

## 3.3.2. Sources of errors

The results obtained during the experimental work have good agreement with the calculation for most of measured structures. Now, we will discuss the possible sources of errors for the structures with square and rectangular membranes. The first one is the precision of measuring equipment. However, the measurements showed that it is not very important when plotting the full electrical characteristics. It affects significantly only for small generated deflections which are comparable to the equipment precision. This kind of error may affect significantly on the initial deflection of the membrane also. The next one concerns the assumption that the residual stress does not change with depth of the membrane. In fact the residual stress is the highest near the border between the materials and lowers with depth. When the membrane is thin (as in our case), one can assume that the stress is uniform. In other cases, this assumption may produce incorrect results. The most significant source of errors is the fabrication process. The first phenomenon, which may occur, are plastic deformations of silicon. In our case, after the etching of SOI bulk, the membranes are bent due to pressure difference (vacuum in the cavity). The maximal value of von Mises stress is usually higher than 100 MPa and 200 MPa for square and rectangular membrane, respectively. These values are smaller than the value of yield stress given for room temperature. However, when we analyzed the fabrication steps, the structures were annealed at high temperature. According to the [110] the yield stress lowers with the temperature as shown in Figure 3-29:

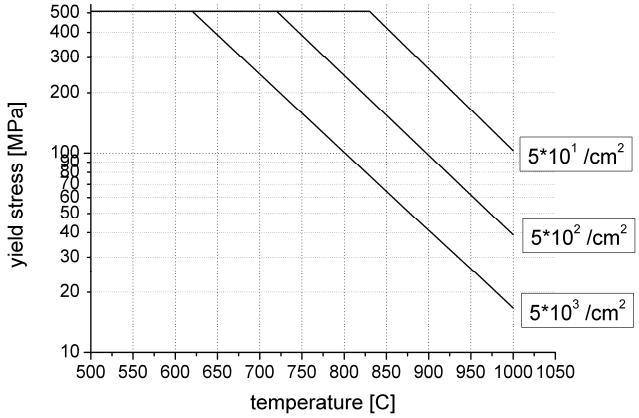


**Figure 3-29: Yield stress of silicon versus temperature for various value of dislocation density.**

Then, during annealing, the stress within the membrane exceeds the maximal stress in elastic zone producing the local plastic deformation of the membrane, especially for rectangular one. This may change the membrane form and response to the load producing serious errors. The consequences of this phenomenon were especially noticeable in rectangular membranes fabricated on wafer no. 3 and no. 4. The last important factor is the bonding process. Each imperfection may change the membrane form or induce additional residual stress. In our case, inexact bonding was observable at the membranes edges (as shown in Figure 3-30) for several structures:

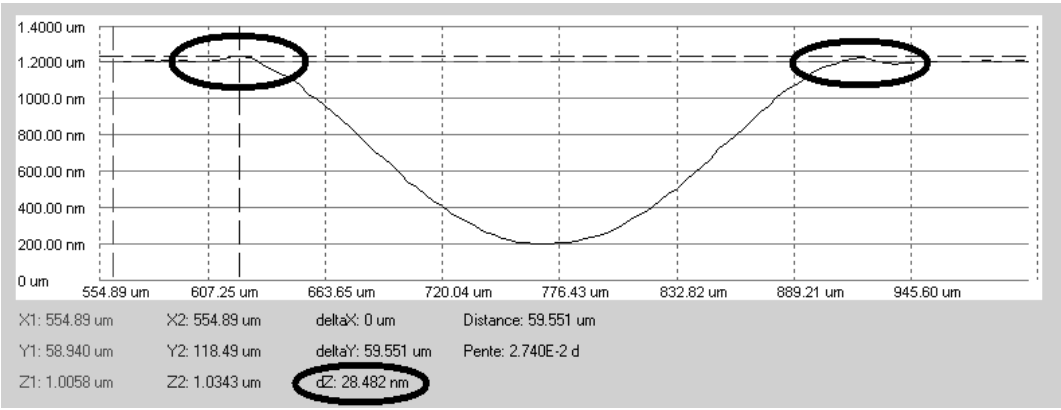


**Figure 3-30: Exemplary profile of square membrane with marked imperfection of bonding on the edges.**

Nevertheless, all above-mentioned sources of errors do not disqualify the analytical model. The results are comparable and describe the membrane behaviour well enough. Of course, the model cannot take into account all the technological phenomena. Thus, its precision could be increase only when fabrication process performed in appropriate conditions, which eliminate or reduce the influence of undesired phenomena.

## 3.4. Circular membranes

Technological process used in fabrication of capacitive pressure sensor based on the circular membrane was a little bit different. As a base of the sensor, the glass PYREX® 7740 was used, in which the cavities were formed (radius equal to 1750 μm). Then, the metallic electrode was deposited on the cavities bottoms and the contacts to the electrode were created. To avoid the short circuit, the plots were made in the glass during the cavities etching instead of oxide deposition on the electrode [108]. The glass substrate is bonded with the silicon wafer, which was next etched in KOH to liberate the membranes and create access to the electrode contacts. The thickness of the membranes was well controlled as it was set to 30 μm - 40 μm. Finally, the metallization was performed to create the contacts to the membranes. The sensor has also a canal, which causes that the pressure inside the cavity is equal to the external one. Some sensors have sealed cavity with vacuum inside. For more information please refer to [51]. The whole structure is presented in Figure 3-31:

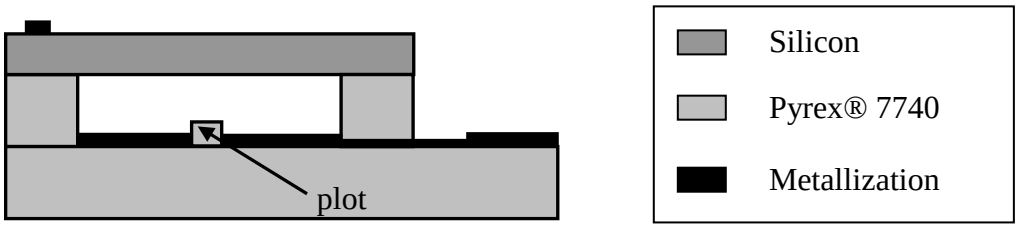


**Figure 3-31: Schema of the capacitive pressure sensor.**

In order to validate the model for circular membrane, the capacitance of test structures was measured (see paragraph 3.2.4). This method is less resistant to errors than measurement of maximal deflection as the capacitance depends also on membrane form. The measurement of membrane deflection was not precise enough due to high roughness of the membrane surface what is shown on the profile in Figure 3-32:

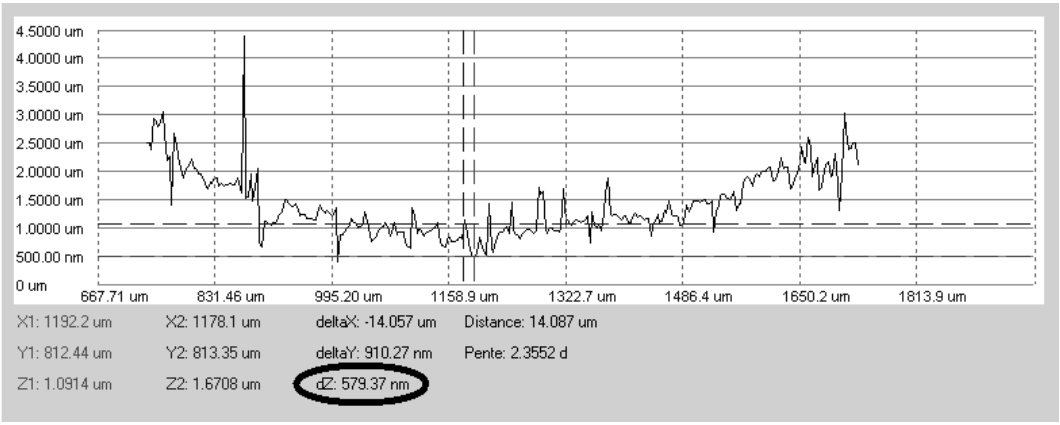


**Figure 3-32: Profile of bent circular membrane.**

In this case, the error, which is made when extracting the value, may be equal even to 580 nm. If we compare it to cavity depth, which is about 4 μm, this may produce unacceptable errors. Thus, the measurement of membrane deflection was not performed. Due to the same problem, the measurement of initial deflection was not possible. Furthermore, as the structures have open canal, it was not possible to measure the membrane response to the applied hydrostatic pressure, making impossible the calculation of residual stress. As the membrane thickness is about 30 μm to 40 μm, the average residual stress within the membrane should be much smaller then in case of structures with rectangular membrane. One can predict the tensile stress from coefficient of thermal expansion for silicon and pyrex (Figure 3-3). Then, the membranes should be initially flat. Four structures were measured whose basic parameters are presented in Table 3-11:

**Table 3-11: Parameters of structures with circular membrane.**

| Structure | *h* [μm] | d [μm] | $C_0$ measured [pF] | $C_0$ calculated [pF] | Error [%] | old measurements of $C_0$ [51] [pF] |
|---|---|---|---|---|---|---|
| p2c2-S | 32 | 3.4 | 23.796 | 23.200 | 2.6 | 23.022 |
| p5b10-L | 28 | 4.4 | 18.619 | 17.927 | 3.9 | 17.869 |
| p5b6-XL | 39 | 4.1 | 20.201 | 19.239 | 5 | 19.165 |
| p5e9-S | 37 | 4.4 | 19.127 | 17.927 | 6.7 | 18.151 |

One can see that the measured initial capacitance ($C_0$) is about 2.5% to 7% higher than the calculated one. For comparison, the results of measurements, performed in a short time after the fabrication (about 3 years ago), were shown in Table 3-11 in the last column. These results agreed with the calculation. Thus, this dispersion may be caused by ageing of the material, improper storage or humidity inside the cavity. Next, the characteristics of capacitance versus the applied voltage and corresponding relative difference (Equation 3-3) were plotted (Figure 3-33). To reduce the influence of error made during the measurement of initial capacitance, the generated capacitance will be taken into account.

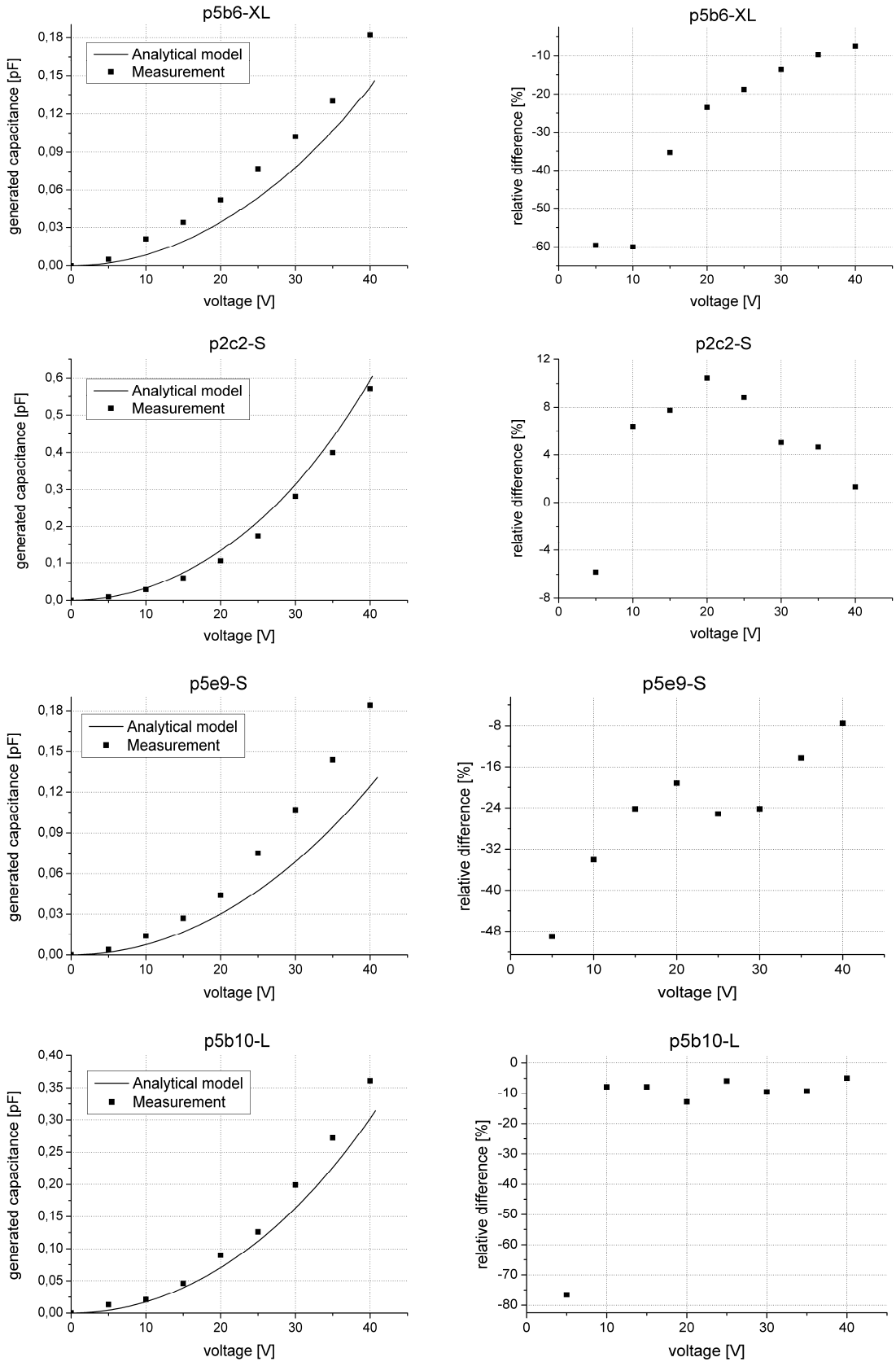


**Figure 3-33: Characteristics $C_{gen}$=f($V$) for measured circular membrane.**

The dispersion in results depends on the structure. For structure p2c2-S, we obtained good accordance (overestimation of 5%). For the other ones, the error is much higher and is 16%, 24% and 36% of underestimation, respectively. For small voltages, the difference is more significant and reaches up to 80% what is caused by higher influence of measurement error. It has to be emphasized that all these structures are not new and the membranes behaviour might change in time. Moreover, the initial deflection of the membrane (if it exists) and residual stress were not taken into account, which might induce errors in calculations.- Although the results are not sufficiently precise, one can assume that the analytical model is correct.

# Conclusions

The MEMS market grows rapidly since several years. Nowadays, it is hard to imagine life without such a technology. It is used in household devices, industry, transport and many, many more. We have a contact with it each day, we look at it and we use it, often without realizing it. Plurality of applications forced high competition on the market. The quality and functionality do not guarantee the sure success. The very important determinant is time to market. Therefore, the proper method of modelling of MEMS devices is needed in order to shorten the project duration. One can specify two basic methods: most commonly used FEM simulation and analytical calculations. The objective of this dissertation was to develop the complete and fast analytical model in order to design and optimize the electrostatic actuators and to compare it to the FEM simulation and to experimental results.

In the first chapter, the principle of electrostatic actuator was presented basing on the simplest structure made of two parallel plates. This system is nonlinear so one can observe distinctive cycles of operation that form the hysteresis. The analytical description of such system was shown also. Next, we focused on more complex structures based on a membrane (this word was used to describe a thin plate) of circular and rectangular shapes. Firstly, we described the membrane behaviour under the uniform load in terms of small deflection using the Lagrange-Newton differential equation. We took into account the phenomena such as the residual stress and initial deflection of the membrane, which usually occur during the fabrication process of MEMS devices. It has to be emphasized that these phenomena have significant influence on membrane behaviour and should not be omitted in modelling what is frequently suggested in literature. The analysis of the membrane deflection allowed reducing the model by normalizing its form. Then, one can operate only on maximal membrane deflection what simplify the calculation. Next, we analyzed the membrane behaviour with applied voltage. Using the differential equation, we observed some inconvenience in the method of solving and calculation time. In specific conditions, the calculation may last a few seconds, especially for rectangular membranes, which is not suitable if optimization phase should be short. Therefore, the reduced model is a good alternative, as it does not require the time-consuming calculation of integrals. However, the simulation showed that this model produces serious errors because it is valid only for parallel plate actuator. Nevertheless, the calculation time was the priority for us, so we decided to improve this model. Two coefficients and one correcting function were introduced into the membrane equation, which were calculated using the classical model. Then, the model generatedprovided with the correct values of maximal membrane deflection. As this model uses some simplifications, it has some limitations. Simulations showed that the form of electrostatically actuated membrane changes

with voltage. Thus, the use of normalized membrane forms may produce significant errors. We assumed that the membrane is initially flat or deflected towards the bottom electrode. In other cases the results may be erroneous. Next, the developed model was compared with the FEM simulations performed in ANSYS® environment. We obtained good conformity between these two methodologies using the assumption that the membrane is perfectly clamped on their edges. In order to obtain the results closer to reality, we performed the FEM simulation of membranes using the real clamping (with substrate). The membrane deflection is then up to 10% higher and the stress up to 20%. Higher than the prediction of analytical model. Going further, we compared the time of calculations between both analytical models and FEM simulation. The reduced analytical model is much faster, especially when a characteristic containing several points is needed. Our method perform this task in time smaller than one second, as opposed to classical model and FEM simulation which need dozen of seconds and a few minutes, respectively. Moreover, we described the electrode modelling and its possibility of adaptation in each method. Finally, we created the simulation tool based on developed analytical model in MATLAB® environment that allows simulating the user-defined electrostatic actuator made of isotropic material and commonly used silicon in <100> and <110> directions. The tool provides all necessary parameters and characteristics, which fully describe the actuator performance. It has to be remarked that although this tool is a good alternative to the FEM simulation, it should not replace the classical approach. Thus, each time the results should be verified with FEM simulation.

In the second chapter, the design paths of actuator were described. We started from classical path, which is based on hand-made calculation and experimental verification. As this method is inconvenient and requires high costs, the computer-based modelling became a standard. This approach significantly reduces the project duration and cost, as the number of runs of experimental phase was significantly limited. However, the execution time of FEM simulation is still a bottleneck, which may affect project duration. Therefore, we proposed to use the developed analytical model that allows performing several simulations in a few seconds providing accurate results. Then, the optimization phase, which usually needs hundreds of runs, lasts no more than a few minutes instead of many hours when using FEM method. Finally, the tool that performs the optimization phase in fully automated way was written in MATLAB.

Next, the advantages of developed analytical model were used in order to simulate the fabrication process. It is almost impossible to achieve an ideal conformity between analytical simulation and experimental results. The wafers used in fabrication are not identical, the

equipment has limited precision, the process introduces some uncertainties and some errors could be made by a human. All these facts causes that the fabricated structures might have different performance that may not meet project requirements. Thus, the statistical simulation is very helpful especially in estimating the production yield, which has direct influence on project costs. As this simulation also requires several runs, the use of analytical model is desired. Consequently, the statistical tool was written in MATLAB.

In the last chapter, the experimental results were compared to the analytical model in order to verify them. Firstly, we described the fabrication process used in LAAS laboratory and the methods of its characterization. Next, the measurement set-up and methods of estimating the basics parameters of actuator that were used in estimation of actuator performance were shown. Finally, the experimental results were presented. The structures were fabricated on five wafers under different conditions. Each wafer was characterized in order to verify the correctness of bonding. Then, the electrical characteristics of structures with square and rectangular membrane were plotted and compared with the results obtained from analytical model. We have obtained good agreement with the theory. The difference depended on structure and did not exceed 20%. Usually, it was oscillating around 10% and for some structures the results were very close to the theory. Several factors might have caused this mismatch, such as the model inaccuracy, problems during fabrication and some undesired phenomena e.g. plastic deformation. Furthermore, the higher dispersions for small voltages were effect of higher influence of measurement error what was proved by performing the measurement of resistance change. Additionally, the capacitive pressure sensors with circular membrane were measured in order to validate the model for this kind of membranes

The work presented in this dissertation showed that the analytical modelling is a good alternative to the FEM simulation. Due to its simplicity, it is much faster what can be especially noticeable during the optimization phase. However, its simplification causes that the range of use is significantly limited. Some of its limitations could be removed by increasing the number of parameters, but it will of course increase the calculation time. As a future work, one can envision add the possibility of simulation for large deflection of the membrane and the possibility of changing the electrode form. The most significant limitation of the developed model are the clamping conditions. The comparison showed that the difference might reach up to 20% what cannot be neglected. Thus, it is desirable to implement the real clamping into the analytical model. One cannot forget that some phenomena cannot be described using this approach. It concerns especially the thermomechanical stresses. The developed model takes into consideration only the result of thermal treatment, i.e. the value of

average residual stress remaining in the material, contrary to the FEM method, which allows the simulation of thermal treatment process. Thus, the analytical model should not be the indispensable tool in the design process. It may be used as a basic method. However, all results should be verified with the FEM simulation. Nevertheless, the analytical modelling is a powerful simulation method of MEMS devices.

The benefits of the work presented in this dissertation will be exploited in CAPTAM project. The aim of the project is to optimize the piezoresistive pressure sensor, which integrates the electrostatic pressure generator. Thus, the optimization has to be coupled in order to obtain the desired sensitivity of the sensor and performance of the generator. Therefore, the developed analytical model will be very helpful in such numerically complex task.

# Appendices

# *APPENDIX A. Material properties*

## A.1 Mechanical properties

The main property of all solid materials is their elasticity [31]. When some external force, producing stress σ, is applied on the material, it deforms in such a way that after removing this force, the material returns to its original shape. The amount of deformation is called strain $\varepsilon$. Elasticity comes from atomic interaction in a crystal structure of the body. When there are no external forces, atoms are arranged in such a way, that the energy is minimal. The energy between two neighbouring atoms is shown in Figure A-1:

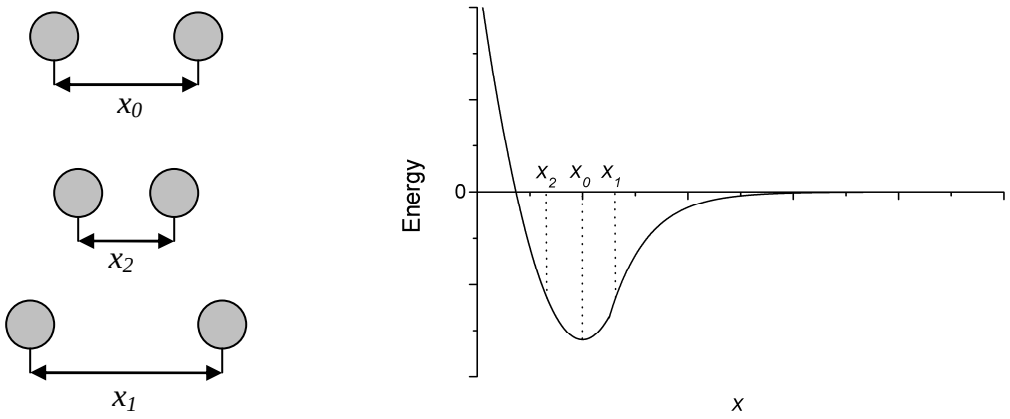


**Figure A-1: Energy between two neighbouring atoms versus the distance between them.**

The distance $x_0$ between atoms corresponds to the equilibrium state where the energy is minimal. When some external force is applied on the body, atoms are rearranged as shown in Figure A-2:

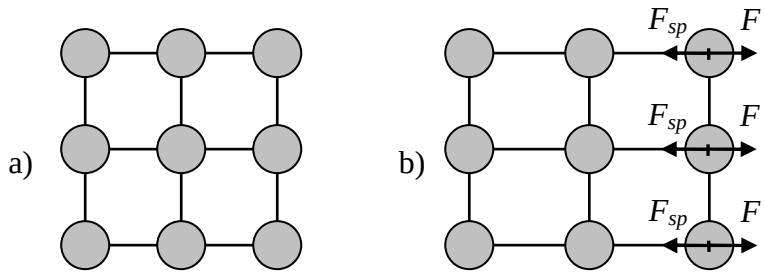


**Figure A-2: Crystal structure: a) without external force applied, b) with external force applied.**

The change of distance between atoms results in change of interaction energy. If the strain is relatively small, the energy is proportional in square to the distance between atoms (Figure A-1). Then, the energy can be expressed with the following formula:

$$E(x_1) = E(x_0) + \frac{(x_1 - x_0)^2}{2}\left(\frac{\partial^2 E}{\partial x^2}\right)_{x_0}$$ **Equation A-1**

The force of atoms interaction (spring force) in position $x_1$ is:

$$F_{sp} = -\frac{\partial E(x_1)}{\partial x_1} = -2(x_1 - x_0)\left(\frac{\partial^2 E}{\partial x^2}\right)_{x_0} = -k_{sp}(x_1 - x_0)$$ **Equation A-2**

where $k_{sp}$ is a spring constant. Thus, the external force, inversely directed to the spring force of atoms, is directly proportional to the atoms displacement.

If we consider a body with applied external force and introduce the stress and strain definitions:

$$\sigma = \frac{F}{S}$$ **Equation A-3**

$$\varepsilon = \frac{\Delta l}{l}$$ **Equation A-4**

where $\Delta l$ is an elongation, $l$ is a body length and $S$ is a transversal section of the body, the relation between the stress and strain can be expressed by a Hooke's law:

$$\sigma = E\varepsilon$$ **Equation A-5**

This is the fundamental expression describing the linear elasticity of material assuming that the elastic body is homogeneous and continuously distributed over its volume.

In general case, when working in three-dimensional stress state (Figure A-3), the Hooke's law takes the following form:

$$\sigma_{ij} = c_{ijkl}\varepsilon_{kl}, \qquad i, j, k, l = 1,2,3$$ **Equation A-6**

where $c_{ijkl}$ is a tensor of a 9×9 stiffness matrix **C**, $\sigma_{ij}$ is a tensor of a 9-elements vector **σ** and $\varepsilon_{kl}$ is a tensor of a 9-elements vector **ε**.

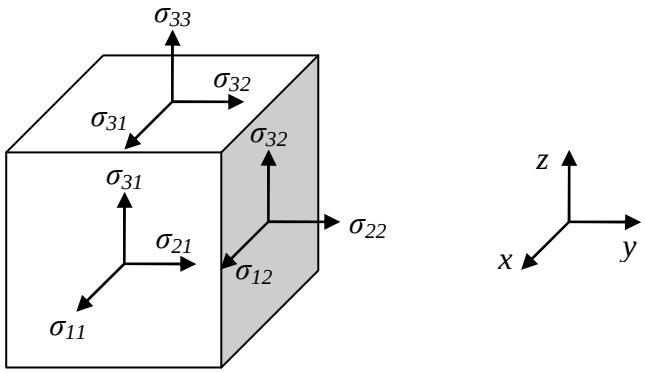


**Figure A-3: The components of stress acting on the sides of the element.**

Due to symmetry of stress tensor $\sigma_{ij}$, strain tensor $\varepsilon_{kl}$ and stiffness tensor $c_{ijkl}$:

$$\sigma_{ij} = \sigma_{ji}$$
$$\varepsilon_{ij} = \varepsilon_{ji} \qquad \textbf{Equation A-7}$$
$$c_{ijkl} = c_{jikl},\ c_{ijkl} = c_{ijlk},\ c_{ijkl} = c_{klij}$$

and introducing the following change of indexes:

$$\begin{bmatrix} 11 \\ 22 \\ 33 \\ 23,32 \\ 13,31 \\ 12,21 \end{bmatrix} = \begin{bmatrix} 1 \\ 2 \\ 3 \\ 4 \\ 5 \\ 6 \end{bmatrix} \qquad \textbf{Equation A-8}$$

Equation A-6 reduces to the following equation:

$$\sigma_i = c_{ij}\varepsilon_j, \qquad i, j = 1...6 \qquad \textbf{Equation A-9}$$

## A.2 Silicon properties

Silicon is a common material used today in construction of electronic devices due to its great electrical properties. However, the main advantages of silicon are its mechanical properties that allow its use in fabrication of micromechanical systems [32]. We can list the following silicon properties:

- high Young's modulus comparable to steel
- low density
- wide range of linear elasticity
- high yield stress
- low thermal expansion
- melting point at 1410ºC

The other important feature is that the atoms in crystalline silicon are arranged in a diamond lattice structure. The cubic symmetry simplifies the calculations because the stiffness matrix from Equation A-9 has 12 nonzero elements and only three differently valued elements [33]. Then, the matrix form of Hooke's law for silicon takes the following form (stiffness form):

$$\begin{bmatrix} \sigma_1 \\ \sigma_2 \\ \sigma_3 \\ \sigma_4 \\ \sigma_5 \\ \sigma_6 \end{bmatrix} = \begin{bmatrix} c_{11} & c_{12} & c_{12} & 0 & 0 & 0 \\ c_{12} & c_{11} & c_{12} & 0 & 0 & 0 \\ c_{12} & c_{12} & c_{11} & 0 & 0 & 0 \\ 0 & 0 & 0 & c_{44} & 0 & 0 \\ 0 & 0 & 0 & 0 & c_{44} & 0 \\ 0 & 0 & 0 & 0 & 0 & c_{44} \end{bmatrix} \cdot \begin{bmatrix} \varepsilon_1 \\ \varepsilon_2 \\ \varepsilon_3 \\ \varepsilon_4 \\ \varepsilon_5 \\ \varepsilon_6 \end{bmatrix} \qquad \textbf{Equation A-10}$$

where:

$$c_{11} = E\frac{1-v}{(1+v)(1-2v)}$$
$$c_{12} = E\frac{v}{(1+v)(1-2v)} \qquad \textbf{Equation A-11}$$
$$c_{44} = G$$

$E$ is a Young's modulus, $v$ is a Poisson ratio and $G$ is a shear modulus. Poisson ratio $v$ determines the ratio of the relative transverse strain to the relative axial strain:

$$v = -\frac{\varepsilon_3}{\varepsilon_1} = -\frac{\varepsilon_2}{\varepsilon_1} \qquad \textbf{Equation A-12}$$

Hooke's law can be also written in compliance form:

$$\begin{bmatrix}\varepsilon_1\\ \varepsilon_2\\ \varepsilon_3\\ \varepsilon_4\\ \varepsilon_5\\ \varepsilon_6\end{bmatrix} = \begin{bmatrix} s_{11} & s_{12} & s_{12} & 0 & 0 & 0\\ s_{12} & s_{11} & s_{12} & 0 & 0 & 0\\ s_{12} & s_{12} & s_{11} & 0 & 0 & 0\\ 0 & 0 & 0 & s_{44} & 0 & 0\\ 0 & 0 & 0 & 0 & s_{44} & 0\\ 0 & 0 & 0 & 0 & 0 & s_{44}\end{bmatrix} \cdot \begin{bmatrix}\sigma_1\\ \sigma_2\\ \sigma_3\\ \sigma_4\\ \sigma_5\\ \sigma_6\end{bmatrix} \qquad \textbf{Equation A-13}$$

where:

$$s_{11} = \frac{1}{E}$$
$$s_{12} = -\frac{v}{E} \qquad \textbf{Equation A-14}$$
$$s_{44} = \frac{1}{G}$$

As the crystal structure of silicon is not isotropic (Figure A-4), its properties depend on a direction.

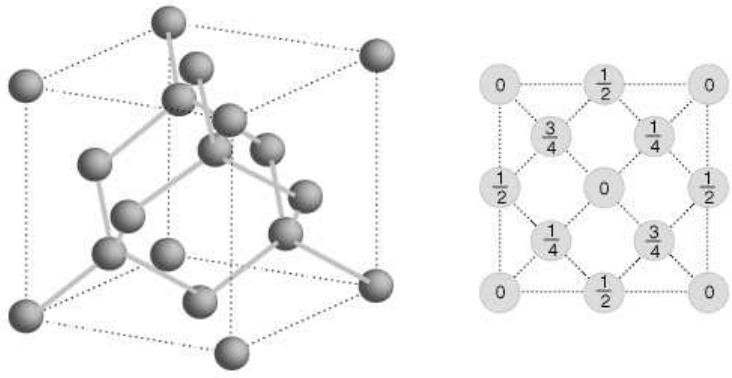


**Figure A-4: Arrangement of the silicon atoms in a unit cell. Numbers indicate the height of the atom above the base of the cube as a fraction of the cell dimension.**

Then, a coefficient of anisotropy $\alpha$ can be introduced [34]:

$$\alpha = v + \frac{2G\left(1 - v^2\right)}{E}$$ **Equation A-15**

Usually, silicon is cut in (100) plane. The values of Young's modulus, shear modulus and Poisson ratio, depending on crystallographic direction, are shown in Figure A-5, Figure A-6 and Figure A-7 [35]:

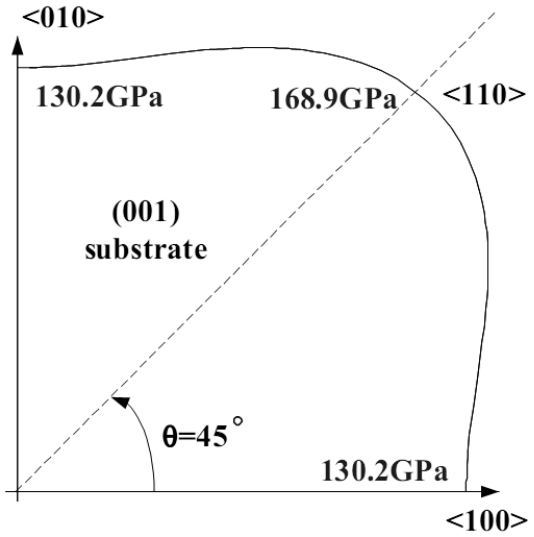


**Figure A-5: Young's modulus in silicon cut in (100) plane.**

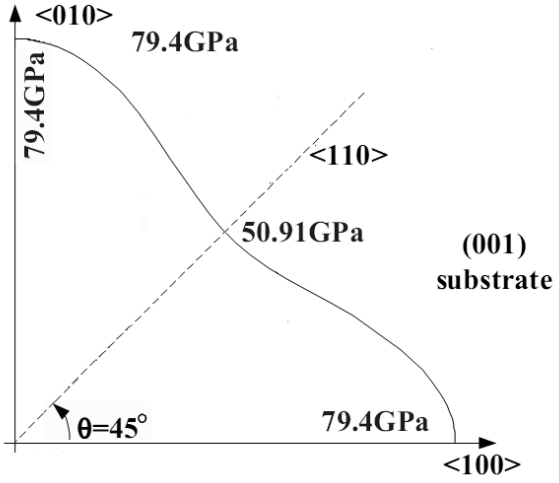


**Figure A-6: Shear modulus in silicon cut in (100) plane.**

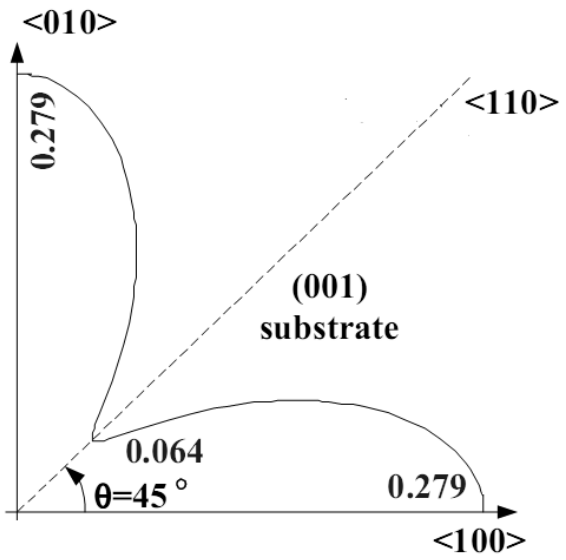


**Figure A-7: Poisson ratio in silicon cut in (100) plane.**

As one can see, the anisotropy of silicon has specific feature that mechanical properties are the same in perpendicular directions (e.g. <100> and <010>). This kind of anisotropy is called orthotropy. The basic mechanical properties of silicon for the most popular directions are shown in Table A-1.

**Table A-1: Mechanical properties of silicon in plane (100) for different directions.**

| Direction | E [GPa] | G [GPa] | ν | α |
|---|---|---|---|---|
| <100> | 130,2 | 79,4 | 0,279 | 1,403 |
| <110> | 168,9 | 50,9 | 0,064 | 0,664 |

## A.3 Isotropic material

If the material is isotropic (mechanical properties are the same in all directions), the coefficient of anisotropy is equal to 1. Then, the elements of stiffness and compliance matrix in Hooke's law are as follows:

$$c_{11} = E\frac{1-v}{(1+v)(1-2v)}, \qquad s_{11} = \frac{1}{E}$$
$$c_{12} = E\frac{v}{(1+v)(1-2v)}, \qquad s_{12} = -\frac{v}{E} \qquad \textbf{Equation A-16}$$
$$c_{44} = \frac{E}{2(1+v)}, \qquad s_{44} = \frac{2(1+v)}{E}$$

# *APPENDIX B. Derivation of equilibrium equation of membrane bending*

## B.1 Rectangular membrane

We consider a thin plate made of anisotropic material. The relation between the stress and strain components can be represented by the following equations:

$$\begin{aligned}\sigma_x &= E_x^{'}\varepsilon_x + E^{''}\varepsilon_y \\ \sigma_y &= E_y^{'}\varepsilon_y + E^{''}\varepsilon_x \\ \sigma_{xy} &= G\varepsilon_{xy}\end{aligned} \qquad \textbf{Equation B-1}$$

where $E^{'}_x$, $E^{'}_y$, $E^{''}$, G are constants needed to characterize the elastic properties of a material. We assume that linear elements perpendicular to the middle plane (*xy* plane) of the plate before bending remain straight and normal to the deflection surface of the plate after bending. Hence the strain components are expressed with the following relations [41]:

$$\begin{aligned}\varepsilon_x &= -z\frac{\partial^2 w}{\partial x^2} \\ \varepsilon_y &= -z\frac{\partial^2 w}{\partial y^2} \\ \varepsilon_{xy} &= -2z\frac{\partial^2 w}{\partial x \partial y}\end{aligned} \qquad \textbf{Equation B-2}$$

The corresponding stress components are:

$$\begin{aligned}\sigma_x &= -z\left(E_x^{'}\frac{\partial^2 w}{\partial x^2} + E^{''}\frac{\partial^2 w}{\partial y^2}\right) \\ \sigma_y &= -z\left(E_y^{'}\frac{\partial^2 w}{\partial y^2} + E^{''}\frac{\partial^2 w}{\partial x^2}\right) \\ \sigma_{xy} &= -2Gz\frac{\partial^2 w}{\partial x \partial y}\end{aligned} \qquad \textbf{Equation B-3}$$

The bending and twisting moments are then:

$$\begin{aligned}M_x &= \int_{-h/2}^{h/2} z\sigma_x = -\left(D_x\frac{\partial^2 w}{\partial x^2} + D_1\frac{\partial^2 w}{\partial y^2}\right) \\ M_y &= \int_{-h/2}^{h/2} z\sigma_y = -\left(D_y\frac{\partial^2 w}{\partial y^2} + D_1\frac{\partial^2 w}{\partial x^2}\right) \\ M_{xy} &= \int_{-h/2}^{h/2} z\sigma_{xy} = -2D_{xy}\frac{\partial^2 w}{\partial x \partial y}\end{aligned} \qquad \textbf{Equation B-4}$$

where:

$$D_x = \frac{E_x^{'} h^3}{12}, \qquad D_y = \frac{E_y^{'} h^3}{12}, \qquad D_1 = \frac{E^{''} h^3}{12}, \qquad D_{xy} = \frac{Gh^3}{12}$$ **Equation B-5**

The differential equation of equilibrium of plate under the load is as follows [41]:

$$\frac{\partial^2 M_x}{\partial x^2} - 2\frac{\partial^2 M_{xy}}{\partial x \partial y} + \frac{\partial^2 M_y}{\partial y^2} = -P$$ **Equation B-6**

Combining Equation B-4 and Equation B-6 we get:

$$D_x \frac{\partial^4 w}{\partial x^4} - 2H \frac{\partial^4 w}{\partial x^2 \partial y^2} + D_y \frac{\partial^4 w}{\partial y^4} = P$$ **Equation B-7**

where:

$$H = D_1 + 2D_{xy}$$ **Equation B-8**

In case of orthotropy we have:

$$E_x^{'} = \frac{E}{1-\nu^2}, \qquad E_y^{'} = \frac{E}{1-\nu^2}, \qquad E^{''} = \frac{\nu E}{1-\nu^2}, \qquad G = \frac{(\alpha - \nu)E}{2(1-\nu^2)}$$ **Equation B-9**

which leads to the final equation describing the membrane bending:

$$D\left(\frac{\partial^4 w}{\partial x^4} - 2\alpha \frac{\partial^4 w}{\partial x^2 \partial y^2} + \frac{\partial^4 w}{\partial y^4}\right) = P$$ **Equation B-10**

# *APPENDIX C. Solution of equilibrium equation*

## C.1 Rectangular membrane

We start with Equation 1-85:

$$D\frac{16}{a^2b^2}\left(R^2\frac{\partial^4 w}{\partial u^4}+2\alpha\frac{\partial^4 w}{\partial u^2\partial v^2}+\frac{1}{R^2}\frac{\partial^4 w}{\partial v^4}\right)+\sigma_0 h\frac{4}{ab}\left(R\frac{\partial^2 w}{\partial u^2}+\frac{1}{R}\frac{\partial^2 w}{\partial v^2}\right)= \\ = P+P_{w0}+\varepsilon\frac{V^2}{2(d-w)^2} \qquad \textbf{Equation C-1}$$

We predict the solution as follows:

$$w(u,v)=\sum_{i,j=0}^{n}K_{ij}\varphi_{ij}, \qquad \varphi_{ij}=\left(1-u^2\right)^2u^{2i}\left(1-v^2\right)^2v^{2j} \qquad \textbf{Equation C-2}$$

Then, the system of Galerkin equations reads:

$$\iint_\Omega D\frac{16}{a^2b^2}\left(R^2\frac{\partial^4 w}{\partial u^4}+2\alpha\frac{\partial^4 w}{\partial u^2\partial v^2}+\frac{1}{R^2}\frac{\partial^4 w}{\partial v^4}\right)\varphi_{ij}\,dudv+\iint_\Omega\sigma_0 h\frac{4}{ab}\left(R\frac{\partial^2 w}{\partial u^2}+\frac{1}{R}\frac{\partial^2 w}{\partial v^2}\right)\varphi_{ij}\,dudv= \\ =\iint_\Omega\left(P+P_{w0}\right)\varphi_{ij}\,dudv+\iint_\Omega\varepsilon\frac{V^2}{2(d-w)^2}\varphi_{ij}\,dudv, \qquad i,j=0,1,2 \qquad \textbf{Equation C-3}$$

Substituting Equation C-2 into Equation C-3 we get:

$$D\frac{16}{a^2b^2}K_{11}\iint_\Omega\left(R^2\frac{\partial^4\varphi_{11}}{\partial u^4}+2\alpha\frac{\partial^4\varphi_{11}}{\partial u^2\partial v^2}+\frac{1}{R^2}\frac{\partial^4\varphi_{11}}{\partial v^4}\right)\varphi_{ij}dudv+D\frac{16}{a^2b^2}K_{33}\iint_\Omega\left(R^2\frac{\partial^4\varphi_{33}}{\partial u^4}+2\alpha\frac{\partial^4\varphi_{33}}{\partial u^2\partial v^2}+\frac{1}{R^2}\frac{\partial^4\varphi_{33}}{\partial v^4}\right)\varphi_{ij}dudv+$$

$$+\sigma_0 h\frac{4}{ab}K_{11}\iint_\Omega\left(R\frac{\partial^2\varphi_{11}}{\partial u^2}+\frac{1}{R}\frac{\partial\varphi_{11}}{\partial v^2}\right)\varphi_{ij}dudv+\sigma_0 h\frac{4}{ab}K_{33}\iint_\Omega\left(R\frac{\partial^2\varphi_{33}}{\partial u^2}+\frac{1}{R}\frac{\partial\varphi_{33}}{\partial v^2}\right)\varphi_{ij}dudv= \quad \textbf{Equation C-4}$$

$$=\left(P+P_{w0}\right)\iint_\Omega\varphi_{ij}dudv+\varepsilon\frac{V^2}{2}\iint_\Omega\frac{1}{\left(d-w\right)^2}\varphi_{ij}dudv,\qquad i,j=0,1,2$$

Then, we can rewrite the above equation into the matrix form:

$$D\frac{16}{a^2b^2}\mathbf{A_1K}+\sigma_0 h\frac{4}{ab}\mathbf{A_2K}=\left(P+P_{w0}\right)\mathbf{B}+\varepsilon\frac{V^2}{2}\mathbf{B_1} \quad \textbf{Equation C-5}$$

where matrices $\mathbf{A_1}$, $\mathbf{A_2}$ and vectors $\mathbf{B}$, $\mathbf{B_1}$ have following form:

$$\mathbf{A_1}=\begin{bmatrix}\iint_\Omega\left(R^2\frac{\partial^4\varphi_{11}}{\partial u^4}+2\alpha\frac{\partial^4\varphi_{11}}{\partial u^2\partial v^2}+\frac{1}{R^2}\frac{\partial^4\varphi_{11}}{\partial v^4}\right)\varphi_{11}dudv & \cdots & \iint_\Omega\left(R^2\frac{\partial^4\varphi_{33}}{\partial u^4}+2\alpha\frac{\partial^4\varphi_{33}}{\partial u^2\partial v^2}+\frac{1}{R^2}\frac{\partial^4\varphi_{33}}{\partial v^4}\right)\varphi_{11}dudv\\ \cdots & \cdots & \cdots\\ \cdots & \cdots & \cdots\\ \iint_\Omega\left(R^2\frac{\partial^4\varphi_{11}}{\partial u^4}+2\alpha\frac{\partial^4\varphi_{11}}{\partial u^2\partial v^2}+\frac{1}{R^2}\frac{\partial^4\varphi_{11}}{\partial v^4}\right)\varphi_{33}dudv & \cdots & \iint_\Omega\left(R^2\frac{\partial^4\varphi_{33}}{\partial u^4}+2\alpha\frac{\partial^4\varphi_{33}}{\partial u^2\partial v^2}+\frac{1}{R^2}\frac{\partial^4\varphi_{33}}{\partial v^4}\right)\varphi_{33}dudv\end{bmatrix} \quad \textbf{Equation C-6}$$

$$\mathbf{A_2}=\begin{bmatrix}\iint_\Omega\left(R\frac{\partial^2\varphi_{11}}{\partial x^2}+\frac{1}{R}\frac{\partial^2\varphi_{11}}{\partial y^2}\right)\varphi_{11}dudv & \cdots & \iint_\Omega\left(R\frac{\partial^2\varphi_{33}}{\partial x^2}+\frac{1}{R}\frac{\partial^2\varphi_{33}}{\partial y^2}\right)\varphi_{11}dudv\\ \cdots & \cdots & \cdots\\ \cdots & \cdots & \cdots\\ \iint_\Omega\left(R\frac{\partial^2\varphi_{11}}{\partial x^2}+\frac{1}{R}\frac{\partial^2\varphi_{11}}{\partial y^2}\right)\varphi_{33}dudv & \cdots & \iint_\Omega\left(R\frac{\partial^2\varphi_{33}}{\partial x^2}+\frac{1}{R}\frac{\partial^2\varphi_{33}}{\partial y^2}\right)\varphi_{11}dudv\end{bmatrix} \quad \textbf{Equation C-7}$$

$$\mathbf{B} = \begin{bmatrix} \iint_{\Omega} \varphi_{11} du dv \\ \cdots \\ \cdots \\ \iint_{\Omega} \varphi_{33} du dv \end{bmatrix}$$ **Equation C-8**

$$\mathbf{B_1} = \begin{bmatrix} \iint_{\Omega} \frac{1}{(d-w)^2} \varphi_{11} du dv \\ \cdots \\ \cdots \\ \iint_{\Omega} \frac{1}{(d-w)^2} \varphi_{33} du dv \end{bmatrix}$$ **Equation C-9**

## C.2 Circular membrane

We start with Equation 1-97:

$$\frac{3+\alpha}{4}\frac{D}{R_0^4}\left(\frac{\partial^4 w}{\partial u^4}+\frac{2}{u}\frac{\partial^3 w}{\partial u^3}-\frac{1}{u^2}\frac{\partial^2 w}{\partial u^2}+\frac{1}{u^3}\frac{\partial w}{\partial u}\right)+\frac{\sigma_0 h}{R_0^2}\left(\frac{\partial^2 w}{\partial u^2}+\frac{\partial w}{\partial u}\right)=P+P_{w0}+\varepsilon\frac{V^2}{2(d-w)^2}$$ **Equation C-10**

We predict the solution as follows:

$$w(u)=\sum_{i=0}^{n} K_i \varphi_i, \qquad \varphi_i = (1-u^2)^2 u^{2i}$$ **Equation C-11**

Then, the system of Galerkin equations reads:

$$\iint_{\Omega}\frac{3+\alpha}{4}\frac{D}{R_0^4}\left(\frac{\partial^4 w}{\partial u^4}+\frac{2}{u}\frac{\partial^3 w}{\partial u^3}-\frac{1}{u^2}\frac{\partial^2 w}{\partial u^2}+\frac{1}{u^3}\frac{\partial w}{\partial u}\right)\varphi_i u du d\theta+\iint_{\Omega}\frac{\sigma_0 h}{R_0^2}\left(\frac{\partial^2 w}{\partial u^2}+\frac{\partial w}{\partial u}\right)\varphi_i u du d\theta=$$

$$=\iint_{\Omega}(P+P_{w0})\varphi_i u du d\theta+\iint_{\Omega}\varepsilon\frac{V^2}{2(d-w)^2}\varphi_i u du d\theta,\qquad i=0,1$$

**Equation C-12**

Substituting Equation C-11 into Equation C-12 we get:

$$\frac{3+\alpha}{4}\frac{D}{R_0^4}K_1\iint_{\Omega}\left(\frac{\partial^4\varphi_1}{\partial u^4}+\frac{2}{u}\frac{\partial^3\varphi_1}{\partial u^3}-\frac{1}{u^2}\frac{\partial^2\varphi_1}{\partial u^2}+\frac{1}{u^3}\frac{\partial\varphi_1}{\partial u}\right)\varphi_i u du d\theta+\frac{3+\alpha}{4}\frac{D}{R_0^4}K_2\iint_{\Omega}\left(\frac{\partial^4\varphi_2}{\partial u^4}+\frac{2}{u}\frac{\partial^3\varphi_2}{\partial u^3}-\frac{1}{u^2}\frac{\partial^2\varphi_2}{\partial u^2}+\frac{1}{u^3}\frac{\partial\varphi_2}{\partial u}\right)\varphi_i u du d\theta+$$

$$+\frac{\sigma_0 h}{R_0^2}K_1\iint_{\Omega}\left(\frac{\partial^2\varphi_1}{\partial u^2}+\frac{\partial\varphi_1}{\partial u}\right)\varphi_i u du d\theta+\frac{\sigma_0 h}{R_0^2}K_2\iint_{\Omega}\left(\frac{\partial^2\varphi_2}{\partial u^2}+\frac{\partial\varphi_2}{\partial u}\right)\varphi_i u du d\theta=$$

$$=(P+P_{w0})\iint_{\Omega}\varphi_i u du d\theta+\varepsilon\frac{V^2}{2}\iint_{\Omega}\frac{1}{(d-w)^2}\varphi_i u du d\theta,\qquad i=0,1$$

**Equation C-13**

Then, we can rewrite the above equation into the matrix form:

$$\frac{3+\alpha}{4}\frac{D}{R_0^4}\mathbf{A_1}\mathbf{K}+\frac{\sigma_0 h}{R_0^2}\mathbf{A_2}\mathbf{K}=(P+P_{w0})\mathbf{B}+\varepsilon\frac{V^2}{2}\mathbf{B_1}$$

**Equation C-14**

where matrices $\mathbf{A_1}$, $\mathbf{A_2}$ and vectors $\mathbf{B}$, $\mathbf{B_1}$ have following form:

$$\mathbf{A_1}=\begin{bmatrix}\iint_{\Omega}\left(\frac{\partial^4\varphi_1}{\partial u^4}+\frac{2}{u}\frac{\partial^3\varphi_1}{\partial u^3}-\frac{1}{u^2}\frac{\partial^2\varphi_1}{\partial u^2}+\frac{1}{u^3}\frac{\partial\varphi_1}{\partial u}\right)\varphi_1 u du d\theta & \iint_{\Omega}\left(\frac{\partial^4\varphi_2}{\partial u^4}+\frac{2}{u}\frac{\partial^3\varphi_2}{\partial u^3}-\frac{1}{u^2}\frac{\partial^2\varphi_2}{\partial u^2}+\frac{1}{u^3}\frac{\partial\varphi_2}{\partial u}\right)\varphi_1 u du d\theta\\ \iint_{\Omega}\left(\frac{\partial^4\varphi_1}{\partial u^4}+\frac{2}{u}\frac{\partial^3\varphi_1}{\partial u^3}-\frac{1}{u^2}\frac{\partial^2\varphi_1}{\partial u^2}+\frac{1}{u^3}\frac{\partial\varphi_1}{\partial u}\right)\varphi_2 u du d\theta & \iint_{\Omega}\left(\frac{\partial^4\varphi_2}{\partial u^4}+\frac{2}{u}\frac{\partial^3\varphi_2}{\partial u^3}-\frac{1}{u^2}\frac{\partial^2\varphi_2}{\partial u^2}+\frac{1}{u^3}\frac{\partial\varphi_2}{\partial u}\right)\varphi_2 u du d\theta\end{bmatrix}$$

**Equation C-15**

$$\mathbf{A_2} = \begin{bmatrix} \iint_{\Omega}\left(\frac{\partial^2\varphi_1}{\partial u^2}+\frac{\partial\varphi_1}{\partial u}\right)\varphi_1 u\,du\,d\theta & \iint_{\Omega}\left(\frac{\partial^2\varphi_2}{\partial u^2}+\frac{\partial\varphi_2}{\partial u}\right)\varphi_1 u\,du\,d\theta \\ \iint_{\Omega}\left(\frac{\partial^2\varphi_1}{\partial u^2}+\frac{\partial\varphi_1}{\partial u}\right)\varphi_2 u\,du\,d\theta & \iint_{\Omega}\left(\frac{\partial^2\varphi_2}{\partial u^2}+\frac{\partial\varphi_2}{\partial u}\right)\varphi_2 u\,du\,d\theta \end{bmatrix}$$ **Equation C-16**

$$\mathbf{B} = \begin{bmatrix} \iint_{\Omega}\varphi_1 u\,du\,d\theta \\ \iint_{\Omega}\varphi_2 u\,du\,d\theta \end{bmatrix}$$ **Equation C-17**

$$\mathbf{B_1} = \begin{bmatrix} \iint_{\Omega}\frac{1}{(d-w)^2}\varphi_1 u\,du\,d\theta \\ \iint_{\Omega}\frac{1}{(d-w)^2}\varphi_2 u\,du\,d\theta \end{bmatrix}$$ **Equation C-18**

Remark: the integration of variable $\theta$ is not necessary as for all terms in Equation C-13 it has the same value of $2\pi$. In further calculation this integration will be omitted.

# *APPENDIX D. Coefficients of matrices* $\mathbf{A_1}$, $\mathbf{A_2}$ *and vector* **B**

## D.1 Rectangular membrane

$$\mathbf{A_1} = \begin{bmatrix} a1_{1111} & \dots & a1_{3311} \\ \dots & \dots & \dots \\ a1_{1133} & \dots & a1_{3333} \end{bmatrix}, \qquad a1_{ijkl} = a1_{klij}$$

$$a1_{1111} = \frac{32768}{11025}\frac{4\alpha R^2 + 7R^4 + 7}{R^2} \qquad a1_{1211} = \frac{32768}{121275}\frac{11R^4 + 7}{R^2} \qquad a1_{1311} = -\frac{32768}{4729725}\frac{52\alpha R^2 - 143R^4 + 63}{R^2}$$

$$a1_{2111} = \frac{32768}{121275}\frac{7R^4 + 11}{R^2} \qquad a1_{2211} = \frac{32768}{121275}\frac{R^4 + 1}{R^2} \qquad a1_{2311} = \frac{32768}{4729725}\frac{13R^4 + 9}{R^2}$$

$$a1_{3111} = -\frac{32768}{4729725}\frac{52\alpha R^2 - 63R^4 - 143}{R^2} \qquad a1_{3211} = \frac{32768}{4729725}\frac{9R^4 + 13}{R^2} \qquad a1_{3311} = \frac{32768}{156080925}\frac{52\alpha R^2 + 99R^4 + 99}{R^2}$$

$$a1_{1212} = \frac{32768}{1576575}\frac{52\alpha R^2 + 429R^4 + 21}{R^2} \qquad a1_{1312} = \frac{32768}{4729725}\frac{56\alpha R^2 + 689R^4 + 21}{R^2} \qquad a1_{2112} = \frac{32768}{121275}\frac{R^4 + 1}{R^2}$$

$$a1_{2212} = \frac{32768}{525525}\frac{13R^4 + 1}{R^2} \qquad a1_{2312} = \frac{32768}{52026975}\frac{689R^4 + 33}{R^2} \qquad a1_{3112} = \frac{32768}{4729725}\frac{9R^4 + 13}{R^2}$$

$$a1_{3212} = \frac{32768}{52026975}\frac{52\alpha R^2 + 297R^4 + 33}{R^2} \qquad a1_{3312} = \frac{32768}{156080925}\frac{56\alpha R^2 + 477R^4 + 33}{R^2}$$

$$a1_{1313} = \frac{32768}{80405325}\frac{612\alpha R^2 + 10931R^4 + 147}{R^2} \qquad a1_{2113} = \frac{32768}{4729725}\frac{13R^4 + 9}{R^2} \qquad a1_{2213} = \frac{32768}{52026975}\frac{689R^4 + 33}{R^2}$$

$$a1_{2313} = \frac{32768}{884458575}\frac{10931R^4 + 231}{R^2} \qquad a1_{3113} = \frac{32768}{156080925}\frac{52\alpha R^2 + 99R^4 + 99}{R^2} \qquad a1_{3213} = \frac{32768}{156080925}\frac{-56\alpha R^2 + 477R^4 + 33}{R^2}$$

$$a1_{3313} = -\frac{32768}{11497961475}\frac{2652\alpha R^2 - 32793R^4 - 1001}{R^2} \qquad a1_{2121} = \frac{32768}{1576575}\frac{52\alpha R^2 + 21R^4 + 429}{R^2}$$

$$a1_{2221} = \frac{32768}{525525}\frac{R^4 + 13}{R^2} \qquad a1_{2321} = \frac{32768}{52026975}\frac{-52\alpha R^2 + 33R^4 + 297}{R^2}$$

$$a1_{3121} = \frac{32768}{4729725}\frac{56\alpha R^2 + 21R^4 + 689}{R^2} \qquad a1_{3221} = \frac{32768}{52026975}\frac{33R^4 + 689}{R^2} \qquad a1_{3321} = \frac{32768}{156080925}\frac{-56\alpha R^2 + 33R^4 + 477}{R^2}$$

$$a1_{2222} = \frac{32768}{17342325}\frac{52\alpha R^2 + 99R^4 + 99}{R^2} \qquad a1_{2322} = \frac{32768}{52026975}\frac{56\alpha R^2 + 159R^4 + 99}{R^2} \qquad a1_{3122} = \frac{32768}{52026975}\frac{33R^4 + 689}{R^2}$$

$$a1_{3222} = \frac{32768}{52026975}\frac{56\alpha R^2 + 99R^4 + 159}{R^2} \qquad a1_{3322} = \frac{32768}{2029052025}\frac{784\alpha R^2 + 2067R^4 + 2067}{R^2}$$

$$a1_{2323} = \frac{32768}{3832653825}\frac{2652\alpha R^2 + 10931R^4 + 3003}{R^2} \qquad a1_{3123} = \frac{32768}{156080925}\frac{-56\alpha R^2 + 33R^4 + 477}{R^2} \qquad a1_{3223} = \frac{32768}{2029052025}\frac{784\alpha R^2 + 2067R^4 + 2067}{R^2}$$

$$a1_{3323} = \frac{32768}{11497961475}\frac{2856\alpha R^2 + 10931R^4 + 4823}{R^2} \qquad a1_{3131} = \frac{32768}{80405325}\frac{612\alpha R^2 + 147R^4 + 10931}{R^2}$$

$$a1_{3231} = \frac{32768}{884458575}\frac{231R^4 + 10931}{R^2} \qquad a1_{3331} = -\frac{32768}{11497961475}\frac{2652\alpha R^2 - 1001R^4 - 32793}{R^2}$$

$$a1_{3232} = \frac{32768}{3832653825}\frac{2652\alpha R^2 + 3003R^4 + 10931}{R^2} \qquad a1_{3332} = \frac{32768}{11497961475}\frac{2856\alpha R^2 + 4823R^4 + 10931}{R^2}$$

$$a1_{3333} = \frac{32768}{11497961475}\frac{1836\alpha R^2 + 4501R^4 + 4501}{R^2}$$

$$\mathbf{A_2} = \begin{bmatrix} a2_{1111} & \dots & a2_{3311} \\ \dots & \dots & \dots \\ a2_{1133} & \dots & a2_{3333} \end{bmatrix}, \qquad a2_{ijkl} = a2_{klij}$$

$$a2_{1111} = -\frac{65536}{33075}\frac{R^2+1}{R} \qquad a2_{1211} = -\frac{65536}{363825}\frac{1}{R} \qquad a2_{1311} = -\frac{65536}{14189175}\frac{13R^2+9}{R}$$

$$a2_{2111} = -\frac{65536}{363825}R \qquad a2_{2211} = 0 \qquad a2_{23111} = \frac{65536}{12006225}R$$

$$a2_{3111} = \frac{65536}{14189175}\frac{-13R^2+9}{R} \qquad a2_{3211} = \frac{65536}{12006225}\frac{1}{R} \qquad a2_{3311} = \frac{65536}{52026975}\frac{R^2+1}{R}$$

$$a2_{1212} = -\frac{65536}{4729725}\frac{13R^2+3}{R} \qquad a2_{1312} = -\frac{65536}{14189175}\frac{14R^2+3}{R} \qquad a2_{2112} = 0$$

$$a2_{2212} = -\frac{65536}{4002075}R \qquad a2_{2312} = -\frac{65536}{22297275}2R \qquad a2_{3112} = \frac{65536}{12006225}\frac{1}{R}$$

$$a2_{3212} = \frac{65536}{52026975}\frac{-3R^2+1}{R} \qquad a2_{3312} = \frac{65536}{2029052025}\frac{-42R^2+13}{R} \qquad a2_{1313} = -\frac{65536}{80405325}\frac{51R^2+7}{R}$$

$$a2_{2113} = \frac{65536}{12006225}R \qquad a2_{2213} = -\frac{65536}{22297275}2R \qquad a2_{2313} = -\frac{65536}{17342325}R$$

$$a2_{3113} = \frac{65536}{52026975}\frac{R^2+1}{R} \qquad a2_{3213} = \frac{65536}{2029052025}\frac{-42R^2+13}{R} \qquad a2_{3313} = \frac{65536}{34493884425}\frac{-459R^2+91}{R}$$

$$a2_{2121} = -\frac{65536}{4729725}\frac{3R^2+13}{R} \qquad a2_{2221} = -\frac{65536}{4002075}\frac{1}{R} \qquad a2_{2321} = \frac{65536}{52026975}\frac{R^2-3}{R}$$

$$a2_{3121} = -\frac{65536}{14189175}\frac{3R^2+14}{R} \qquad a2_{3221} = -\frac{65536}{22297275}\frac{2}{R} \qquad a2_{3321} = \frac{65536}{2029052025}\frac{13R^2-42}{R}$$

$$a2_{2222} = -\frac{65536}{17342325}\frac{R^2+1}{R} \qquad a2_{2322} = -\frac{65536}{676350675}\frac{14R^2+13}{R} \qquad a2_{3122} = -\frac{65536}{22297275}\frac{2}{R}$$

$$a2_{3222} = -\frac{65536}{676350675}\frac{13R^2+14}{R} \qquad a2_{3322} = -\frac{65536}{289864575}\frac{2\left(R^2+1\right)}{R} \qquad a2_{2323} = -\frac{65536}{11497961475}\frac{153R^2+91}{R}$$

$$a2_{3123} = \frac{65536}{2029052025}\frac{13R^2-42}{R} \qquad a2_{3223} = -\frac{65536}{289864575}\frac{2\left(R^2+1\right)}{R} \qquad a2_{3222} = -\frac{65536}{34493884425}\frac{153R^2+98}{R}$$

$$a2_{3131} = -\frac{65536}{80405325}\frac{7R^2+51}{R} \qquad a2_{3231} = -\frac{65536}{17342325}\frac{1}{R} \qquad a2_{3331} = \frac{65536}{34493884425}\frac{91R^2-459}{R}$$

$$a2_{3232} = -\frac{65536}{11497961475}\frac{91R^2+153}{R} \qquad a2_{3332} = -\frac{65536}{34493884425}\frac{98R^2+153}{R} \qquad a2_{3333} = -\frac{65536}{547521975}\frac{R^2+1}{R}$$

$$\mathbf{B} = \begin{bmatrix} b_{11} \\ \cdots \\ \cdots \\ b_{33} \end{bmatrix}, \qquad b_{ij} = b_{ji}$$

$$b_{11} = \frac{256}{255} \qquad b_{12} = \frac{256}{1575} \qquad b_{13} = \frac{256}{4725} \qquad b_{22} = \frac{256}{11025} \qquad b_{23} = \frac{256}{33075} \qquad b_{33} = \frac{256}{99225}$$

## D.2 Circular membrane

$$\mathbf{A_1} = \begin{bmatrix} \frac{64}{6} & \frac{64}{24} \\ \frac{64}{24} & \frac{64}{15} \end{bmatrix} \qquad \mathbf{A_2} = \begin{bmatrix} \frac{4}{6} & -\frac{4}{60} \\ -\frac{4}{60} & -\frac{4}{60} \end{bmatrix} \qquad \mathbf{B} = \begin{bmatrix} \frac{1}{6} \\ \frac{1}{24} \end{bmatrix}$$

# *APPENDIX E. Approximations used in simulation tool*

## E.1 Rectangular membrane

Remark: The values of coefficients *A* and *B* correspond to $P_h$=0.

***Isotropic material***

$$\frac{1}{C_1} = -0.00004659R^5 + 0.0003788R^4 - 0.0007573R^3 - 0.001322R^2 + 0.006302R - 0.003293$$

$$C_2 = 99.49e^{-3.072R} + 11.4e^{-0.05929R}$$

$$A = 0.01355R^5 - 0.1272R^4 + 0.4466R^3 - 0.7161R^2 + 0.5252R + 0.5818$$

$$B = 0.003951R^5 - 0.03543R^4 + 0.1047R^3 - 0.09497R^2 + 0.00325 + 0.6995$$

***Silicon <100>***

$$\frac{1}{C_1} = -0.00005015R^5 + 0.0004504R^4 - 0.001252R^3 + 0.000216R^2 + 0.004196R - 0.002406$$

$$C_2 = 85.16e^{-2.895R} + 11.02e^{-0.04876R}$$

$$A = 0.01442R^5 - 0.142R^4 + 0.5305R^3 - 0.9271R^2 + 0.7637R + 0.4852$$

$$B = 0.003474R^5 - 0.03273R^4 + 0.1063R^3 - 0.1298R^2 + 0.06518 + 0.6706$$

***Silicon <110>***

$$\frac{1}{C_1} = -0.00003953R^5 + 0.0002684R^4 - 0.00009365R^3 - 0.003211R^2 + 0.008744R - 0.004296$$

$$C_2 = 126.3e^{-3.386R} + 12.05e^{-0.07828R}$$

$$A = 0.009812R^5 - 0.101R^4 + 0.401R^3 - 0.7563R^2 + 0.6933R + 0.472$$

$$B = 0.001522R^5 - 0.01218R^4 + 0.01511R^3 + 0.08061R^2 - 0.1638R + 0.7576$$

## E.2 Factors taking into consideration $P_h/P_{max}$ ratio for coefficients *A* and *B*

$$A = A\left[0.087025\left(\frac{P_h}{P_{\max}}\right)^3 + 0.048799\left(\frac{P_h}{P_{\max}}\right)^2 + 0.256113\left(\frac{P_h}{P_{\max}}\right) + 1\right]$$

$$B = B\left[-1.31689\left(\frac{P_h}{P_{\max}}\right)^4 + 1.36291\left(\frac{P_h}{P_{\max}}\right)^3 - 0.9221\left(\frac{P_h}{P_{\max}}\right)^2 - 0.11704\left(\frac{P_h}{P_{\max}}\right) + 1\right]$$

## E.3 Approximation of function correcting the deflection

$$\begin{cases} w = (w - w_0)\left[1 + \left(-0.0006059e^{4.015\frac{V}{V_{pull-in}}} + 0.0673e^{-0.04965\frac{V}{V_{pull-in}} + 0.0673}\right)\left(0.000001072e^{14.55\frac{P_h}{P_{\max}}} + e^{0.3964\frac{P_h}{P_{\max}}}\right)\right] + w_0, & V < 0.978V_{pull-in} \\ w = (w - w_0)\left[1 + \left(-0.034472\left(\frac{V}{V_{pull-in}}\right)^{154.7} + 0.034472\right)\left(0.000001072e^{14.55\frac{P_h}{P_{\max}}} + e^{0.3964\frac{P_h}{P_{\max}}}\right)\right] + w_0, & V > 0.978V_{pull-in} \end{cases}$$

# APPENDIX F. Mask used in fabrication of electrostatic actuator

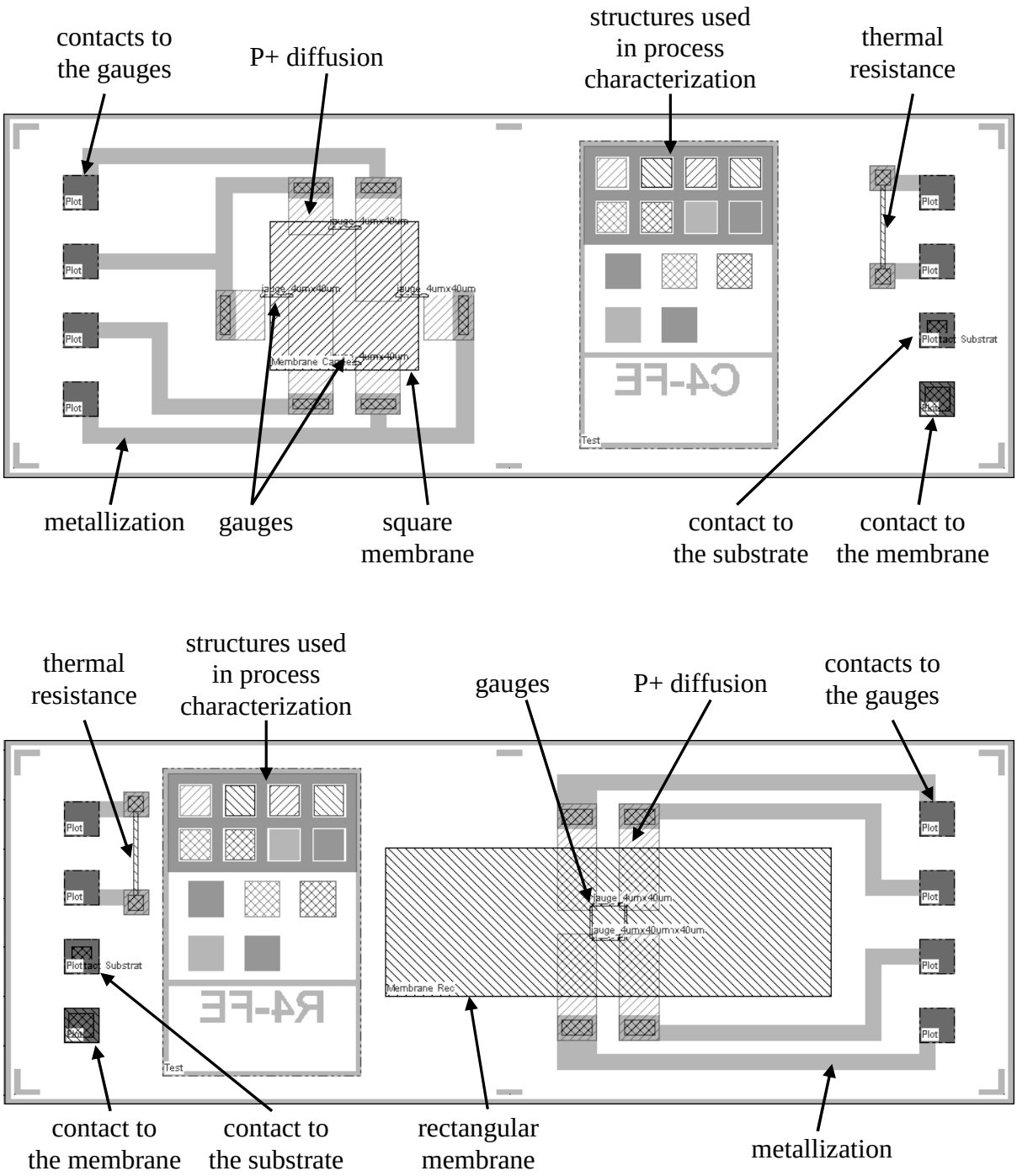


**Figure F-1: Masks used in fabrication of samples with square (top) and rectangular (bottom) membranes.**



- 164 -

# References

[1] H. C. Nathanson et al.
The Resonant Gate Transistor
*IEEE Transaction on Electron Devices, 1967, vol. 14, no. 3, pp 117-133*

[2] M. Mehregany, S. Roy
Introduction to MEMS
*Microengineering Aerospace Systems, 2000, Aerospace Press*

[3] H. C. Nathanson, R. A. Wickstrom
A resonant-gate silicon surface transistor with high Q bandpass properties
*Applied Physics Letters 7, 84 (1965)*

[4] H.C. Lima, B. Schulkina, M.J. Pulickala
Flexible membrane pressure sensor
*Sensors and Actuators A: Physical, 2005, vol. 119, no. 2, pp. 332-335*

[5] A. Ettouhami, N. Zahid, M. Elbelkacemi
A novel capacitive pressure sensor structure with high sensitivity and quasi-linear response
*Comptes Rendus Mécanique, 2004, vol. 332, no. 2, pp. 141-146*

[6] P. Gaucher, D. Eichner
Piezoelectric bimorph cantilever for actuating and sensing applications
*Journal de physique. IV, European Meeting on Integrated Ferroelectrics No2, 1998, vol. 8, no 9, pp. Pr9.235-Pr9.238*

[7] T. Itoh, T. Ohashi
Piezoelectric cantilever array for multiprobe scanning force microscopy
*Proceeding of IEEE MEMS '96, 1996, pp. 451-455*

[8] P. Robert, D. Saias
Integrated RF-MEMS switch based on a combination of thermal and electrostatic actuation
*Proceeding of TRANSDUCERS Conference, Solid-State Sensors, Actuators and Microsystems, 2003, Vol. 2,pp. 1714- 1717*

[9] D. Niarchos
Magnetic MEMS: key issues and some applications
*Sensors and Actuators A: Physical, vol. 109, no. 1-2, pp. 166-173*

[10] H. A. C. Tilmans, E. Fullin
A fully-packaged electromagnetic microrelay
*Proceeding of IEEE Micro Electro Mechanical Systems Conference, 1999, pp. 25-30*

[11] C. R. Dauwalter, J. C. Ha
A high performance magnetically suspended MEMS spinning wheel gyro
*Position Location and Navigation Symposium, 2004, pp. 70-77*

[12] T. Lalinský
Thermal actuation of a GaAs cantilever beam
*Journal of Micromechanics and Microengineering, vol. 10, pp. 293-298*

[13] C. Niezrecki, D. Brei, S. Balakrishnan, A. Moskalik
Piezoelectric actuation: State of the art
*The Shock and vibration digest, 2001, vol. 33, no. 4, pp. 269-280*

[14] H. Kahn
The TiNi shape-memory alloy and its applications for MEMS
*Journal of Micromechanics and Microengineering, vol. 8, pp. 213-221*

[15] H. Lin, C. Ho
Optical pressure transducer
*Review of scientific instruments, 1993, vol. 64, no. 7, pp. 1999-2002*

[16] J. D. Zook, D. W. Bums
Optically Excited Self-resonant Strain Transducers
*Proceeding of Solid-State Sensors and Actuators Conference, 1995, vol.: 2, pp. 600-603*

[17] A. Fargas Marquès, R. Costa Castelló, A. M. Shkel
Modelling the electrostatic actuation of MEMS: state of the art 2005
*Universitat Politecnica de Catalunya, 2005*

[18] P. Attia, M. Boutry , A. Bosseboeuf, P. Hesto
Fabrication and characterization of electrostatically driven silicon microbeams
*Journal of Microelectronics, 1998, vol. 29, no. 9, pp. 641-644*

[19] T. Juneau, K. Unterkofler
Dual-axis optical mirror positioning using a nonlinear closed-loop controller
*Proceeding of Solid-State Sensors, Actuators and Microsystems Conference, 2003, vol. 1, pp. 560- 563*

[20] P. B. Chu, P. R. Nelson
Dynamics of polysilicon parallel-plate electrostatic actuators
*Sensors and Actuators A: Physical, 1996, vol. 52, no. 1-3, pp. 216-220*

[21] T. A. Roessig, R. T. Howe
Surface-micromachined resonant accelerometer
*Proceeding of Solid State Sensors and Actuators Conference, 1997, vol.2, pp. 859-862*

[22] M. M. Teymoori, E. A. Abbaspour-Sani
A novel electrostatic micromachined pump for drug delivery systems
*Proceeding of IEEE Semiconductor Electronics Conference, 2002, pp. 105- 109*

[23] T. N. Juneau
Micromachined Dual Input Axis Rate Gyroscope
*PhD Thesis, University of California, Berkeley, 1997*

[24] R. K. Gupta, S. D. Senturia
Pull-in time dynamics as a measure of absolute pressure
*Proceeding of IEEE Micro Electro Mechanical Systems Workshop, 1997, pp. 290-294*

[25] J. M. Huanga, A. Q. Liu
Mechanical characterization of micromachined capacitive switches: design consideration and experimental verification
*Sensors and Actuators A: Physical, vol. 108, no. 1-3, pp. 36-48*

[26] N. Blanc, J. Brugger, N. F. de Rooij
Scanning force microscopy in the dynamic mode using microfabricated capacitive sensors
*Journal of Vacuum Science and Technology B, 1996, vol. 14, no. 2, pp. 901-905*

[27] O. Francais
Analysis of an Electrostatic Microactuator with the help of Matlab simulink transient and frequency characteristics
*Technical Proceedings of the 2000 International Conference on Modeling and Simulation of Microsystems, Chapter 6, pp. 281-284*

[28] E. Durand
Électrostatique – Tome II
Masson et C$^{ie}$ Editeurs, (Paris, 1966)

[29] B. Artz, L.Cathey,
A finite element method for determining structural displacements resulting from electrostatic forces
*IEEE Solid-State Sensor and Actuator Workshop, June 1992, pp. 190 – 193*

[30] A. Rollier, B Legrand
The stability and pull-in voltage of electrostatic parallel-plate actuators in liquid solutions
*Journal of Micromecanics and Microengineering, 2006, vol. 16, no. 4, pp. 794-801*

[31] E. Landau, F. Lifshitz
Theory of elasticity, 2$^{nd}$ edition
Pergamon Press, (1970)

[32] K. Petersen
Silicon as a mechanical material
*Proceedings of the IEEE, May 1982, vol. 70, no. 5, pp. 420-457*

[33] J. F. Nye
Physical properties of crystal
Oxford University Press, (London, 1957)

[34] C. Plantier
Etude de faisabilité de capteurs de pression piezorezistifs a jauges en silicium polycrytalline
*PhD Thesis, Université Paul Sabatier, Toulouse, 1992*

[35] J. Wortman, R. Evans
Young's modulus, Shear modulus and Poisson ration in Silicon and Germanium
*Journal of Applied Physics, Jan 1965, voll. 36, no. 1, pp. 153-156*

[36] E. R. Olivas
Finite element analysis of metallic thin window: An iterative process
*IEEE Proceeding of Particle Accelerator Conference, Jun 2007, pp. 551-553*

[37] J. T. Cannon, S. Dostrovsky
The evolution of dynamics : vibration theory from 1687 to 1742
Springer, (New York, 1981)

[38] D. Boyajian, D. Weggel, S. Chen
Instituting seminal teaching-datums: examples from plate and shell theory
*World Transactions on Engineering and Technology Education, 2006, vol.5, no.1,pp. 73-76*

[39] C. P. Heins
Applied plate theory for the engineer
Lexington Books, (Mains 1976)

[40] E. Ruggiero
Modeling and Control of SPIDER Satellite Components
*PhD Thesis, Virginia Polytechnic Institute and State University, Blacksburg, July 2005*

[41] S. Timoshenko, S. Woinowsky-Kreiger
Theory of plates and shells, 2nd edition
McGraw-Hill, (New York, 1959)

[42] E. Ventsel, T. Krauthammer
Thin Plates & Shells: Theory, Analysis, & Applications
Marcel Dekker Inc., (New York, 2001)

[43] O. Kopacz, K. Krawczyk
Wykłady z teorii sprężystości
Politechnika Poznańska, (Poznań 2002/2003)

[44] S. G. Lekhtniski
Anisotropic plates
Gordon and Breach Science Publishers, (New York, 1968)

[45] S. Timoschenko, J. Gere
Theory of elastic stability
McGraw-Hill, (New York, 1963)

[46] S. Lee, T. Tanaka
Sensitivity of Ultrasonic Sensor Structures Having Multilayer Diaphragm Structure
*Japanese Journal of Applied Physics, 2004, vol. 43, pp. L1534-L1536*

[47] A. W. Leissa
Vibration of plates
Acoustical Society of Amer, (1993)

[48] P. N. Ratier
Simulation du comportement des capteurs de pression capacitifs microélectroniques
*PhD Thesis, Institut National des Sciences Appliquées, Toulouse, 1993*

[49] Y. Ohasi
Bending of a thin elliptic plate of an orthotropic material under uniform lateral load
*Journal of Applied Mathematics and Physics (ZAMP), 1952, vol. 3, no. 3, pp. 212-224*

[50] E. Yamaguchi
Basic theory of plates and elastic stability
Structural engineering handbook
CRC Press LLC, 1999

[51] M. Al Bahri
Influence de la température sur le comportement statique et dynamique des capteurs de pression capacitifs au silicium
*PhD Thesis, Institut National des Sciences Appliquées de Toulouse, Toulouse, 2005*

[52] KLA Tencor
Tencor stylus profiler manual
*http://www.kla-tencor.com*

[53] Fogale Nanotech
Zoomsurf 3D optical profiler manual
*http://www.fogale.fr*

[54] Analyse et Similitude Dimensionnelles
Encyclopedia Universalis
vol. 5, 13th publication

[55] O. Francais, I. Dufour
Energy-Based Solution Method for the Global Behavior of Diaphragms under Pneumatic and Electrostatic Pressure
*Technical Proceedings of the 1998 International Conference on Modeling and Simulation of Microsystems, California, pp. 298-303*

[56] M. Mehregany, M. Allen
The use of micromachined structures for the measurement of mechanical properties and adhesion of thin films
*IEEE 1986 Solid-State Sensors Workshop, Jun 1986*

[57] J. Pan, P. Lin
Verification of FEM analysis of load-deflection methods for measuring mechanical properties of thin films
*Technical Digest IEEE Solid-State Sensors and Actuators Workshop, 1990, pp. 70-73*

[58] D. Maier-Schneider
A new analytical solution for the load-deflection of square membranes
*Journal of Microelectromechanical Systems, 1995, vol. 4, no. 4, pp. 238-241*

[59] F. Kerrour, F. Hobar
A novel numerical approach for the modelling of the square shaped silicon membrane
*Journal Semiconductors, Physics, Quantum Electronics and Optoelectronics, 2006, vol. 9, no.4, pp. 52,57*

[60] W. Ko, M. Bao
A high sensitivity integrated circuit capacitive pressure transducer
*IEEE Journal of Transaction on Electron Devices, 1982, vol. ED-29, no. 1, pp. 48-56*

[61] J.J. Vlassak, W.D. Nix
A new bulge test technique for the determination of Young's modulus and Poisson's ratio of thin films
*Journal of Materials Research, vol. 7, no. 12, pp. 3242-3249*

[62] G. Blasquez, Y. Naciri
Static response of capacitive pressure sensor with square or rectangular silicon diaphragm
*Revue de Physique Appliquée, Vol. 22/7 (1987), pp. 505-510*

[63] O. Francais, I. Dufour
Normalized abacus for the global behavior of diaphragms: pneumatic, electrostatic, piezoelectric or electromagnetic actuation
*Journal of Modeling and Simulation of Microsystems, 1999, vol. 1, no. 2, pp. 149-160*

[64] A. Ern, J.-L. Guermond
Theory and Practice of Finite Elements
Springer, (2004)

[65] N. Ben Moussa
Conception, modélisation et réalisation d'un capteur de pression capacitif microélectronique
*PhD Thesis, Universite Paul Sabatier, Toulouse, 1985*

[66] Y. Naciri
Contribution a l'etude de capteurs de pression capacitifs miniaturises
*PhD Thesis, Universite Paul Sabatier, Toulouse, 1986*

[67] C. S. Sander, J. W. Knutti
A monolithic capacitive pressure sensor with pulse-period output
*IEEE Transactions on Electron Devices, 1980, vol. 27, no. 5, pp. 927- 930*

[68] R. Hohlfelder
Bulge and blister testing of thin films and their interfaces
*PhD Thesis, Stanford University, USA, 1998*

[69] Y. Lee, H. Seo, A. Kawamura
Compensation Method Of Offset And Its Temperature Drift In Silicon Piezoresistive Pressure Sensor Using Double Wheatstone-bridge Configuration
*Proceeding of Solid-State Sensors and Actuators Conference, Eurosensors IX and Transducer '95, 1995, vol. 2, pp. 570-573*

[70] D. S. Popescu
Buckled membranes for microstructures
*IEEE Proceeding of Microelectromechanical Systems, 1994, pp. 188-192*

[71] M. A. Huff, A. D. Nikolich, M. A. Schmidt
A threshold pressure switch utilizing plastic deformation of silicon
*Proceeding of Solid-State Sensors and Actuators, San Francisco, Jun 1991, pp. 177-180*

[72] D. S. Popescu, D. C. Dascalu
Silicon active microvalves using buckled membranes in actuation
*Proceeding of Solid-State Sensors and Actuators, 1995, Eurosensors IX, Transducers'95, vol. 2, pp. 305-308*

[73] X. Ding, W. Ko
A study on silicon-diaphragm buckling
*Proceeding of IEEE Solid-State Sensor and Actuator Workshop, 1990, USA, pp. 128-131*

[74] O.Tabata, K.Kawahata
Mechanical property measurements of thin films using load deflection of composite rectangular membranes
*Sensors and Actuators, 1989, vol.20, pp. 135-141*

[75] Y. Xiang, X. Chen, J.J. Vlassak
Plane-strain bulge test for thin films
*Journal of Materials Research, vol. 20, no. 9, pp. 2360-2370*

[76] H. K. Lee, S. H. Ko
Mechanical properties measurement of silicon nitride thin films using the bulge test
*Proceeding of MicroMechanics Europe Workshop, Guimaraes, Portugal, Sep 2007, pp. 95-98*

[77] M. Bao, Y. Wang
Analysis and design of a four-terminal silicon pressure sensor at the centre of a diaphragm
*Sensors and Actuators, 1987, vol.12, pp.49-56*

[78] W. C. Young, R. G. Budynas
Roark's Formulas for Stress and Strain, 2nd edition
McGraw-Hill, (New York, 2002)

[79] H. Luoa, C. Pozrikidis
Buckling of a pre-compressed or pre-stretched membrane in shear flow
*International Journal of Solids and Structures, vol. 44, no. 24, 2007, pp. 8074-8085*

[80] A. Fargas Marquès, R. Costa Castelló, A. M. Shkel
Modelling the electrostatic actuation of MEMS: state of the art 2005
*Universitat Politècnica de Catalunya. Institut d'Organització i Control de Sistemes Industrials*

[81] O. Français, I. Dufour
Enhancement of elementary displaced volume with electrostatically actuated diaphragms: application to electrostatic micropumps
*Journal of Micromechanics and Microengineering, 2000, vol. 10, no. 2 , pp. 282-286*

[82] O. Français, I. Dufour
Analytical static modelling and optimization of electrostatic micropumps
*Journal of Micromechanics and Microengineering, 1997, vol. 7, pp. 183-185*

[83] X. Chauffleur
Modélisation par la méthode des éléments finis du comportement thermomécanique de capteurs de pression capacitifs et piezorezistfs en silicium
*PhD Thesis, Universite Paul Sabatier, Toulouse, 1998*

[84] M. Gyimesi, D. Ostergaard
Electro-Mechanical Transducer for MEMS Analysis in ANSYS
*Proceeding of the Modeling and Simulation of Microsystems Conference (MSM1999), 1999, pp. 270*

[85] R. Fletcher
Practical Methods of Optimization
John Wiley and Sons, (New York, 1987)

[86] P. E. Gill, W. Murray, M. H. Wright
Practical Optimization
Academic Press, (London, 1981)

[87] M. C. Biggs
Constrained Minimization Using Recursive Quadratic Programming in Towards Global Optimization
L.C.W. Dixon and G.P. Szergo, (North-Holland, 1975)

[88] S. P. Han
A Globally Convergent Method for Nonlinear Programming
*Journal of Optimization Theory and Applications, 1977, vol. 22, p. 297*

[89] M. J. D. Powell
The Convergence of Variable Metric Methods for Nonlinearly Constrained Optimization Calculations in Nonlinear Programming 3
Academic Press, (London, 1978)

[90] D. J. Laser, J. G. Santiago
A review of micropumps
*Journal of Micromechanics and Microengineering, 2004, vol. 14, no. 6, pp. R35-R64*

[91] Y. Huang, E. Haeggstrom
Collapsed regime operation of capacitive micromachined ultrasonic transducers based on wafer-bonding technique
*IEEE Symposium on Ultrasonics, 2003, vol. 2, pp.1161 – 1164*

[92] M. Grabe
Measurement Uncertainties in Science and Technology
*Springer, (2005)*

[93] T. T. Soong
Fundamentals of probability and statistics for engineering
John Wiley and Sons, (New York, 2004)

[94] C. Bergenstof Nielsen, C. Christensen
Particle Precipitation in connection with KOH etching of Silicon
*Journal of the Electrochemical Society, 2004, 151 (5), pp. G338-42*

[95] R. P. Manginell, G. C. Frye-Mason
Microfabrication of membrane-based devices by deep-reactive ion etching (DRIE) of silicon
*United States. Department Of Energy. Office Of Scientific and Technical Information, 2001*

[96] K. Klasten, N. Kordas
Capacitive pressure sensor with monolithically integrated CMOS readout circuit for high temperature applications
*Sensors and Actuators A: Physical Volumes 97-98, 1 Apr 2002, pp. 83-87*

[97] A. S. Ergun, Y. Huang
Capacitive micromachined ultrasonic transducers : Fabrication technology
*IEEE transactions on ultrasonics, ferroelectrics, and frequency, 2005, vol. 52, no. 12, pp. 2242-2258*

[98] M. A. Huff, A. D. Nikolich, M. A. Schmidt
Design of sealed cavity microstructures formed by silicon wafer bonding
*Journal of Microelectromechanical Systems, 1993, vol. 2, no. 2, pp. 74-81*

[99] C. Yun, N.W. Cheung
Fabrication of silicon and oxide membranes over cavities using ion-cut layer transfer
*Journal of Microelectromechanical Systems, 2000, vol. 9, no. 4, pp. 474-477*

[100] G. Celler, M. Wolf
Smart Cut
*SOITEC 2003*

[101] J. Blake
SIMOX (Separation by Implantation of Oxygen)
*Encyclopedia of Science & Technology*

[102] T. Suni
Direct wafer bonding for MEMS and microelectronics
*PhD Thesis, 2006, Helsinki University of Technology, Espoo, Finland*

[103] M. A. Schmidt
Wafer-to-wafer bonding for microstructure formation
*Proceedings of the IEEE, 1998, vol. 86, no. 8, pp. 1575-1585*

[104] U. Gosele, M. Aleje

Semiconductor wafer bonding. A flexible approach to materialscombinations in microelectronics; micromechanics andoptoelectronics

*Proceeding of Semiconductor Conference CAS '97, 1997, Sinaia, Romania, vol. 1,pp. 23-32*

[105] Y. Huang

Fabricating Capacitive Micromashined Ultrasonic Transducers with Wafer-Bonding Technology

*Journal of .Microelectromechanical Systems, 2003, vol. 12, no.2, pp. 128-137*

[106] A. Boukabache

Conception modélisation et réalisation d'un capteur de pression piezoresistif a faible dérive thermique

*PhD Thesis, Université de Constantine, Toulouse, 1993*

[107] M. Y. Sim, S. Gleixner

Studying the Etch Rates and Selectivity of SiO2 and Al in BHF Solutions

*University/Government/Industry Microelectronics Symposium, 2006, pp. 225-228*

[108] M. Al Bahri

Capteur de pression capacitif protégé contre les court-circuits

*Revue Internationale d'Héliotechnique, 2004, no. 30, pp.39-41*

[109] H. Takagi, R. Maedaa

Wafer-scale spontaneous bonding of silicon wafers by argon-beam surface activation at room temperature

*Sensors and Actuators A: Physical, 2003, vol. 105, no. 1, pp. 98-102*

[110] J. R. Patel, A. R. Chaudhuri

Macroscopic Plastic Properties of Dislocation-Free Germanium and Other Semiconductor Crystals. I. Yield Behavior

*Journal of Applied Physics, 1963, vol. 34, no. 9, pp. 2788-2799*

[111] M. Olszacki

Modeling and optimization of the piezoresistive pressure sensors

*PhD Thesis, Institut National des Sciences Appliquées de Toulouse, Technical University of Lodz, 2009*

# Publications

C. Maj, M. Olszacki, M. Al. Bahri, P. Pons, A. Napieralski, „Analytical Method of Strain Gauge-Based Pressure Sensor Design”*, Technical Digest of Micromechanics Europe 2007 workshop (MME 2007), Guimaraes, Portugal. pp. 75-79., September 2007*

M. Olszacki, C. Maj, M. Al. Bahri, P. Pons, A. Napieralski, „Optimization of Strain Gauge Profile Using Analytical Approach for Pressure Sensor Application”*, Technical Digest of Micromechanics Europe 2007 workshop (MME 2007), Guimaraes, Portugal pp. 79-83., September 2007*

M. Olszacki, C. Maj, M. Al. Bahri, D. Peyrou, F. Kerrour, P. Pons, A. Napieralski, „A multi-domain piezoresistive pressure sensor design tool based on analytical models”*, Technical Digest of EUROSIME 2008 conference, Freiburg, Germany, pp. 524-528., April 2008*

M. Olszacki, C. Maj, M. Al. Bahri, P. Pons, A. Napieralski, „Computer Aided Optimization Tool for MEMS Pressure Sensor Design”*, Proceedings of EUROSENSORS 2008 conference, Dresden, Germany, pp. 47-50., September 2008*

M. Olszacki, C. Maj, M. Al. Bahri, P. Pons, A. Napieralski, „The Fabrication Yield Prediction for Piezoresistive MEMS Pressure Sensors Using Dedicated Statistical Tool”*, Technical Digest of Micromechanics Europe 2008 workshop (MME 2008), Aachen, Germany, September 2008*

C. Maj, M. Olszacki, M. Al. Bahri, P. Pons, A. Napieralski, „Analytical Model of Electrostatic Membrane-Based Actuators”*, Proceeding of EUROSIME 2009 conference, Delft, Netherlands, April 2009*

M. Olszacki, C. Maj, M. Al. Bahri, P. Pons, J-C. Marrot, A. Napieralski, „The Effect of Parasitic Boron Doping on P-Type Piezoresistors”*, Proceeding of EUROSENSORS 2009 conference, pp. 65, Lausanne, Switzerland, September 2009*

C. Maj, M. Olszacki, M. Al. Bahri, P. Pons, E. Scheid, A. Napieralski, „Parasitic phenomena in electrostatic actuators based on sealed cavity fabricated with wafer-bonding technique”*, Proceeding of EUROSENSORS 2009 conference, pp. 153, Lausanne, Switzerland, September 2009*

C. Maj, M. Olszacki, M. Al. Bahri, P. Pons, L. Buscayrol, A. Napieralski, „Optimization of electrostatic membrane-based actuators and characterization of technological process using analytical model”, *Proceeding of Micromechanics Europe 2009 (MME2009) workshop, Toulouse, France, September 2009*

M. Olszacki, C. Maj, M. Al. Bahri, P. Pons, A. Napieralski, „Experimental verification of TCR coefficients for uniformly doped resistors”*, Proceeding of Micromechanics Europe 2009 (MME2009) workshop, Toulouse, France, September 2009*

A. Napieralski, M. Szermer, K. Szaniawski, M. Olszacki, C. Maj, „Aktuatory i sensory w technologii MEMS jako mikroelektromaszynowe elementy mechatroniki”*, Przegląd elektrotechniczny (Electrical review), no. 09/2009, Sigma-NOT, Warsaw, Poland, September 2009*

Cezary MAJ thesis

# Modelling and optimization of electrostatic membrane-based actuators

**Abstract.** This dissertation is concerned with an analytical modelling and optimization of electrostatic membrane-based actuators. An analytical model of a thin, perfectly clamped, silicon membrane bending described with Lagrange/Newton equation for small deflections is presented taking into account parasitic phenomena like residual stress and initial deflection of a membrane. Responses for uniform pressure are obtained with Galerkin method and are studied in order to describe the membrane's behaviour with a reduced model. Both models are analyzed in the case of electrostatic actuation and are compared in terms of precision, range of use, calculation time and easiness of use in the optimization process. The reduced model is then corrected to be fully applicable for hydrostatic and electrostatic actuation without significant precision loss and is compared with FEM simulations performed with ANSYS®. Obtained results allow defining the model advantages and disadvantages. Next, the analytical model is used to determine the influence of input parameters on actuator behaviour and to perform an optimization phase for various applications. Furthermore, statistical simulations are presented which are useful in the estimation of the influence of parameters dispersion, resulting for example from the technological process, on the device behaviour. All simulations are performed using dedicated tools written in MATLAB®. Finally, the fabrication and the characterization of test structures performed in LAAS-CNRS are described which allows the validation of the developed analytical model.
**Keywords.** MEMS, electrostatic actuation, modelling, optimization

---

Thèse de Cezary MAJ

# Modélisation et optimisation des actionneurs électrostatiques basés sur la membrane

**Résumé.** Ce mémoire concerne la modélisation analytique et l'optimisation d'actionneurs électrostatique basés sur une membrane. Le modèle analytique de fléchissement de la membrane mince de silicium, parfaitement encastrée, décrit par l'équation Lagrange/Newton pour les petites déflexions est présentée en prenant sur compte des phénomènes comme les contraintes résiduelles et les déflexions initiales de la membrane. Les réponses pour la pression uniforme sont obtenues grâce à la méthode de Galerkin et sont étudiées pour décrire le comportement de la membrane avec un modèle réduit. Les deux modèles sont analysés pour l'actionnement électrostatique et sont comparés sur le plan de la précision, le gamme d'usage, le temps des calculs et le facilité d'usage en phase d'optimisation. Puis, le modèle réduit est corrigé pour être complètement applicable pour un actionnement hydrostatique et électrostatique sans perte de précision et est comparé avec la simulation FEM réalisée dans l'ANSYS®. Les résultats obtenus permettent de déterminer les avantages et les inconvénients du modèle. En suite, le modèle analytique est utilisé pour développer un outil d'optimisation et de statistique sous MATLAB®. Ce dernier permet d'estimer l'influence de la dispersion des paramètres technologiques sur le comportement des actionneurs. Finalement la fabrication et la caractérisation de structures de tests ont été réalisées au LAAS-CNRS et ont permis la validation du modèle analytique.
**Mot clés.** MEMS, actuation électrostatique, modélisation, optimisation

Rozprawa doktorska Cezarego MAJ

# Modelowanie i optymalizacja mikrosystemów sterowanych siłą elektrostatyczną opartych na membranie

**Streszczenie.** Niniejsza rozprawa doktorska dotyczy modelowania analitycznego i optymalizacji mikrosystemów sterowanych siłą elektrostatyczną opartych na membranie. Zaprezentowany został model analityczny ugięcia idealnie zaczepionej, cienkiej, krzemowej membrany opisany równaniem Lagrange'a/Newton'a dla małych wychyleń, który uwzględnia zjawiska takie jak naprężenie rezydualne oraz ugięcie początkowe membrany. Odpowiedzi dla jednolicie rozłożonego ciśnienia zostały otrzymane dzięki metodzie Galerkin'a oraz przeanalizowane w celu opisu membrany modelem zredukowanym. Oba modele zostały użyte do opisu membrany pod ciśnieniem elektrostatycznym i porównane ze względu na dokładność, zakres użycia, czas obliczeń oraz prostotę wykorzystania w fazie optymalizacji. Następnie model zredukowany został skorygowany tak, by był całkowicie użyteczny dla wymuszenia hydrostatycznego i elektrostatycznego bez utraty dokładności i został porównany z symulacją FEM wykonaną w środowisku ANSYS®. Otrzymane wyniki pozwoliły określić zalety i wady opracowanego modelu. Dodatkowo, model analityczny został wykorzystany w dedykowanych narzędziach napisanych w środowisku MATLAB® do symulacji strukturalnej, optymalizacji i symulacji statystycznej. Ten ostatni pozwala na oszacowanie wpływu rozrzutu parametrów technologicznych na wydajność mikrosystemu. Ostatecznie, w laboratorium LAAS-CNRS, zostały wyprodukowane i scharakteryzowane struktury testowe, co umożliwiło zweryfikowanie opracowanego modelu analitycznego.
**Słowa kluczowe.** MEMS, sterowanie elektrostatyczne, modelowanie, optymalizacja